REPORT UAG-105

WORLD DATA CENTER A
for
Solar-Terrestrial Physics

COMPUTER AIDED PROCESSING OF IONOGRAMS AND IONOSONDE RECORDS

Proceedings of Session G5 at the XXVth General Assembly of the International Union of Radio Science (URSI)
Lille, France, August 28-September 5, 1996

March 1998

NATIONAL GEOPHYSICAL DATA CENTER

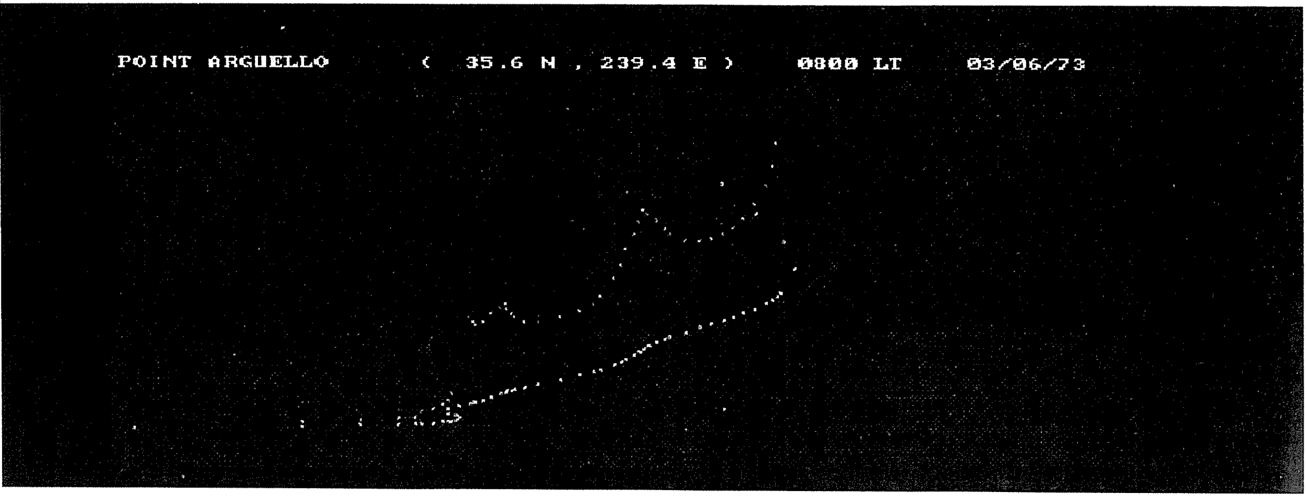

WORLD DATA CENTER-A

COORDINATION OFFICE

World Data Center-A: Coordination Office
National Academy of Sciences
2101 Constitution Avenue, NW
Washington, D.C. 20418, U.S.A.
Tel: 202-334-3368
WWW: http://www.ngdc.noaa.gov/wdcmain.html

ATMOSPHERIC TRACE GASES

World Data Center-A: Atmospheric Trace Gases
Carbon Dioxide Information Analysis Center
Oak Ridge National Laboratory
Oak Ridge, Tennessee 37831-6335, U.S.A.
Tel: 615-574-0390 (fax:-2232)

GLACIOLOGY

World Data Center-A: Glaciology (Snow and Ice)
Cooperative Institute for Research in Environmental
Sciences, Campus Box 449
University of Colorado
Boulder, Colorado 80309, U.S.A.
Tel: 303-492-5171 (fax:-2468)
Email: brekke@kyros.colorado.edu
WWW: http://nsidc.colorado.edu

MARINE GEOLOGY AND GEOPHYSICS

World Data Center-A: Marine Geology and
Geophysics
National Geophysical Data Center
NOAA, E/GC3
325 Broadway
Boulder, Colorado 80303, U.S.A.
Tel: 303-497-6141 (fax:-6513)
Email: info@ngdc.noaa.gov
WWW: http://www.ngdc.noaa.gov

METEOROLOGY

World Data Center-A: Meteorology
National Climatic Data Center
NOAA, E/CC
Federal Building
Asheville, North Carolina 28801, U.S.A
Tel: 704-271-4682 (fax:-4246)
Email: orders@ncdc.noaa.gov
WWW: http://www.ncdc.noaa.gov

OCEANOGRAPHY

World Data Center-A: Oceanography
National Oceanographic Data Center
NOAA/NESDIS, E/OC23
1825 Connecticut Avenue, NW
Universal Building, Room 409
Washington, D.C. 20235, U.S.A.
Tel: 202-606-4507 (fax:-4586)
Email: wdca@nodc.noaa.gov
WWW: http://www.nodc.noaa.gov

PALEOCLIMATOLOGY

World Data Center-A: Paleoclimatology
National Geophysical Data Center
NOAA, E/GC
325 Broadway
Boulder, Colorado 80303, U.S.A.
Tel: 303-497-6146 (fax:-6513)
Email: info@ngdc.noaa.gov
WWW: http://www.ngdc.noaa.gov

REMOTELY SENSED LAND DATA

World Data Center-A: Remotely Sensed Land Data
U.S. Geological Survey
EROS Data Center
Sioux Falls, South Dakota 57198, U.S.A.
Tel: 605-594-6142 (fax:-6150)

ROCKETS AND SATELLITES

World Data Center-A: Rockets and Satellites
National Space Science Data Center
NASA/Goddard Space Flight Center,Code 633
Greenbelt, Maryland 20771, U.S.A.
Tel: 301-286-6695 (fax:-0587)
WWW: http://nssdc.gsfc.nasa.gov

ROTATION OF THE EARTH

World Data Center-A: Rotation of the Earth
TSEO, U.S. Naval Observatory
Washington, D.C. 20392-5100, U.S.A.
Tel: 202-653-1509 (fax:-0587)

SEISMOLOGY

World Data Center-A: Seismology
National Earthquake Information Center
U.S. Geological Survey, P.O. Box 25046
Denver Federal Center, Mail Stop 967
Denver, Colorado 80225, U.S.A.
Tel: 303-273-8440

SOLAR-TERRESTRIAL PHYSICS

World Data Center-A: Solar-Terrestrial Physics
National Geophysical Data Center
NOAA, E/GC2
325 Broadway
Boulder, Colorado 80303, U.S.A.
Tel: 303-497-6324 (fax:-6513)
Email: info@ngdc.noaa.gov
WWW: http://www.ngdc.noaa.gov

SOLID-EARTH GEOPHYSICS

World Data Center-A: Solid Earth Geophysics
National Geophysical Data Center
NOAA, E/GC1
325 Broadway
Boulder, Colorado 80303, U.S.A.
Tel: 303-497-6521 (fax:-6513)
Email: info@ngdc.noaa.gov
WWW: http://www.ngdc.noaa.gov

World Data Center-A was established in the United States under the auspices of the National Academy of Sciences. WDC-A is operated with national resources, but follows ICSU guidelines. The National Academy of Sciences has overall responsibility through the Geophysics Research Forum and its Committee on Geophysical Data. WDC-A consists of a Coordination Office and nine sub-centers at scientific institutions in various parts of the United States. Most WDC-A sub-centers are at corresponding national data centers, whose large national collections are available through the WDC-A sub-centers.

Organizations wishing to contribute data or establish exchange agreements should contact the appropriate World Data Center-A.

WORLD DATA CENTER A
for
Solar-Terrestrial Physics

REPORT UAG-105

COMPUTER AIDED PROCESSING OF IONOGRAMS AND IONOSONDE RECORDS

Proceedings of Session G5 at the XXVth General Assembly of the International Union of Radio Science (URSI) Lille, France, August 28-September 5, 1996

Edited by

Phil Wilkinson
IPS Radio and Space Services
P.O. Box 5606, West Chatswood
NSW 2057, Australia

March 1998

Published by
World Data Center A for Solar-Terrestrial Physics
National Geophysical Data Center
325 Broadway, Boulder, CO 80303 USA

COMPUTER AIDED PROCESSING OF IONOGRAMS AND IONOSONDE RECORDS

Proceedings of Session G5
at the XXVth General Assembly of the International Union of Radio Science (URSI)

TABLE OF CONTENTS

Introduction

This collection of papers forms the bulk of the papers that were presented, either orally or as Poster papers, at the 1996 Lille URSI General Assembly session G5 sponsored by the URSI Commission G Working Group, INAG (Ionosonde Network Advisory Group).

Over the last decade, or more, there have been significant changes in the way ionosonde records are handled. This has been brought about by increased use of computers in all stages of data collection and processing. In UAG-104 (Ionosonde Networks and Stations, 1995) the scope of these changes was evident. While there are still long term issues for data archiving, the weight of effort is currently spent on developing methods for real time analysis of data. This is reflected in the papers in this volume. The two key changes are: computer scaling of ionograms and much greater use of oblique sounding networks, both of which depend on real time computer processing. While much greater use is being made of ionosonde records, the systems are dedicated to specific, real time objectives. There is a danger that archive data will be lost. First, real time applications will not necessarily have facilities for storing archival data and second, oblique systems may replace conventional vertical incidence sounders. While oblique ionograms can offer useful information, vertical incidence records are easier to interpret unambiguously. As greater emphasis is placed on real time, computer generated data, less resources will be spent on manual validation. It is already evident that much of the archival data is now computer processed and often real time observations are the only source of data from networks. Hopefully, this trend will reverse as groups become familiar with their new environments and can catch up on manual archival data validation programs.

In the present volume, papers cover a wide range of topics. The questions of how we process ionosonde data for research work (Wright), and whether scaling offers the necessary insights we now need (Juren) are followed by several papers looking at computer processing of vertical incidence (Jodogne, Tripathi, Grosov, Ilyin, Tsai) and oblique incidence (Redding, Kurkin, Zherebstov) ionograms, including applications of oblique records (Goodman). Some of the methods, and errors inherent in handling these electron density profiles, are considered (Denisenko, Gordienko). As greater emphasis is placed on applications, there will be increasing interest in signal statistics for the additional information they offer about the ionosphere (Denisenko, Afraimovich). Having obtained data from ionosondes, there are many possibilities for extending our understanding. Methods for predicting the ionosphere (Poole), tracking changes (Feichter, Gulyaeva, Gordienko), understanding processes (Shirochkov), and constructing morphologies (Soicher) are some of the many ways of exploiting these valuable data sets.

Archiving, validation and refinement of computer methods should be part of an integrated development program of shared information and knowledge. Can we share computer scaling methods at the code level; can we make use of signal characteristics better; will computer methods handle known problems in electron density analysis and, most important for long term purposes, will computer generated data allow us to produce correct morphologies (e.g., spread F and sporadic E) and track long term trends in data thereby revealing climate changes in the ionosphere? If the ionosonde is to continue to make a useful contribution to our knowledge of the ionosphere, real time methods, now developing along a number of interesting lines as the papers here show, need to embrace the long term needs of the field.

Thank you to all the Referees!

I was assisted in the production of this report by several referees. The referees were:

Rod Barnes, Terry Bullett, Paul Cannon, John Caruana, David Cole, Chris Colman, Ken Davies, Chris Davis, Peter Dyson, Peter Englemann, Graham Fraser, S. V. Fridman, Ivan Galkin, John Goodman, Tamara Gulyaeva, Gerhard Hartmann, Wayne Hocking, Z. Houminer, J-C. Jodogne, V. E. Kunitsyn, D. R. Lakshmi, Bengt Lundborg, John MacDougall, Didier Monselesan, Nicholas Redding, Allon Poole, Jim Scali, John Titheridge, Yogesh Tripathi, J. -L. Tsai, Bill Wright and Bruno Zolesi.

My thanks to all these people for the time they gave. I also would like to thank Yogesh Tripathi for additional help in final preparation of the papers.

Dr Phil Wilkinson, Vice Chair, INAG
IPS Radio and Space Services, AUSTRALIA.

DATA ACQUISITION AND ANALYSIS FOR RESEARCH IONOSONDES

J. W. Wright
Svavelgatan 6, S-59338 Västervik, Sweden. Phone: +46 490 10657,
email: wright@plasma.kth.se,
also Department of Physics, University of Wales, Dyfed, SY23 3BZ Aberystwyth, UK,
and M. L. V. Pitteway
Department of Computer Science, Brunel University, Uxbridge UB8 3PH, UK

1. INTRODUCTION

Research ionosondes, as exemplified by the Dynasonde, provide an environment for radio–ionospheric studies from LF through HF. Some particulars which distinguish research ionosondes from standard monitoring instruments are summarized in Table I. The research ionosonde is the necessary platform for its own development, since improvements in measurement accuracy and efficiency, and new–parameter innovations, always require on–line tests and refinement. For monitoring instruments, however, continuity and stable observing modes are paramount. The research ionosonde plays an essential role on behalf of the monitoring instruments, to distinguish practical and useful monitoring functions. This paper describes an off–line automatic analysis system for Dynasonde recordings. Some of its features are applicable to the monitoring instrument's data and even to suitably digitized analog ionograms.

2. ORGANIZING IONOGRAM INFORMATION

As suggested by Table I, the research ionosonde (and some monitoring instruments) may present for analysis many dependent variables (e.g. R', R*, V*, X, Y, Z, Vx, Vy, Vz, Chirality, dB), each derived or deduced (Pitteway and Wright, 1992) from basic complex–amplitudes; these, in turn, are obtained versus four independent variables (time t; radio frequency f; receiving–antenna locations x, y). The two ionograms in Figure 1 illustrate simple (a) and complex (b) cases from Tromsø. The coordinates are those of conventional ionograms (R'(f), but note the use of logarithmic R' for E–region detail). Colours denote echolocations by a scheme given in the caption. For the simple ionosphere (a), automated 'scaling' is a fairly straightforward matter of distinguishing E–region from F–region; O from X echoes (easy, with measured echo chirality); and O from Z echoes (difficult). For the complex ionosphere (b), the scaling problem is not even defined suitably. The first step must be one of echo classification, by which, within suitable tolerances, the ionogram complexity may be reduced to a set of "broadband structures" (Wright, et al. 1996), far fewer in number than the echoes. We have tried 'trace–following' methods with some success, but an approach based on the principles of 'Equivalence Classes' proves to be superior in every way.

2.1 APPLICATION OF EQUIVALENCE CLASSES TO IONOGRAM SCALING

'ECLAZZ' (Press, et al. 1992, p337) is an efficient list–processing algorithm. It requires us to define, preferably within the '*RST*' principles of equivalence, a logical function testing the properties by which two echoes should be recognized as belonging to the same class; ECLAZZ applies the test to each independent echo–pair. The most natural (and naïve) approach would define as classes, bins within ranges of some of the variables mentioned above (e.g. f, R', X, Y, V*, Chirality, dB), but even 10 bins per variable is at once too coarse and (with 10^7 bins) wildly prohibitive. Instead, our definition constrains the *differences* between echoes in each pair. This offers the perhaps unexpected and very useful property that gradual and continuous changes along echo traces (e.g., those arising by simple photochemistry, wind or wave dynamics as in Figure 1a) do not usually generate class distinctions, while complex structures, as in Figure 1b, can do so. The *Transitive* property of formal *RST* equivalence is *not* demanded directly of the echo variables themselves (it would be satisfied by binning), but only of certain differences. Furthermore, we enforce transitivity locally but not globally. We are not interested in similarities between echoes of an ionogram which are widely separated in frequency, group range, or time; we do not even compare such echo pairs. Without this 'band–diagonal' feature, classification time would be an N^2 process; using it, the process is nearly linear in N (N is the number of echoes of the ionogram; it is a few hundred for monitoring ionograms, but may be many thousands for research applications). For seven variables of each pair, we define absolute values of relative differences as in Table II. Note that two sets of tolerances are used.

TABLE I: RESEARCH AND MONITORING IONOSONDES COMPARED

FEATURE	RESEARCH IONOSONDES	MONITORING IONOSONDES
How many; Where ?	Few (< 10); Research Observatories	Many (> 100); Global, 2000 km spacings
Purposes	Aeronomy; Radio & Plasma Physics	Military; Communications
Prototypes	Dynasonde. Kinesonde	Research ionosondes
Dual use: Research & Monitoring ?	Yes	No
Does Stand - Alone Research ?	Yes (esp. in developing countries)	No
Cost; Re–design Inertia	\$150k - \$300k; Small	\$70k - \$250k; Very Large
Observing program	Irregular. Innovative	Dependable. Proven
Precision: time, freq.; phase	High: (state-of-art)	Moderate: (state-of-budget)
Basic Measurements consist of:	x+iy (clocked 5 µSec)	clocked x+iy
Retained ?	Yes, within echo	No
False Echo Rejection ?	Yes (real - time)	No
System Phase Error & Gain	Calibrated to Freq. Independence	Within General Specification
Antenna System	Freq. Indep. (LPA Tx; Active Rx)	Rhombic Tx; Loop Rx
Echoes / Ionogram	2000 – 4000	200 – 400
Frequency Resolution	≥100 Hz; 0.5% typical	100 kHz typical
Phase Resolution	0.1 Degree typical	5 Degrees typical
Group Range Method, Precision	Stationary Phase; .05 km	TOA; 2.5 km
Raw Parameters	e.g. Echo Peak TOA; x+iy(t)	Coarse h′; Doppler; Echoloc., Polarization.
Deduced Parameters	Precise R′, Echolocation, V*, etc.	Same as Raw Parameters
Defined in	Software	Hardware / Firmware
Derived Parameters	N(h) profiles; Vector Velocities $\Delta N/N$; Lateral Structure; Tilts Trace Classification, Plasma-Wave parameters; Scattering Cross–sections, Atmospheric Gravity Waves, Error Bars; χ^2 Estimations.	N(h) profiles; Vector Velocities, INAG Parameters.
Disposition of Results	Within Research Teams	To WDC Data Bases

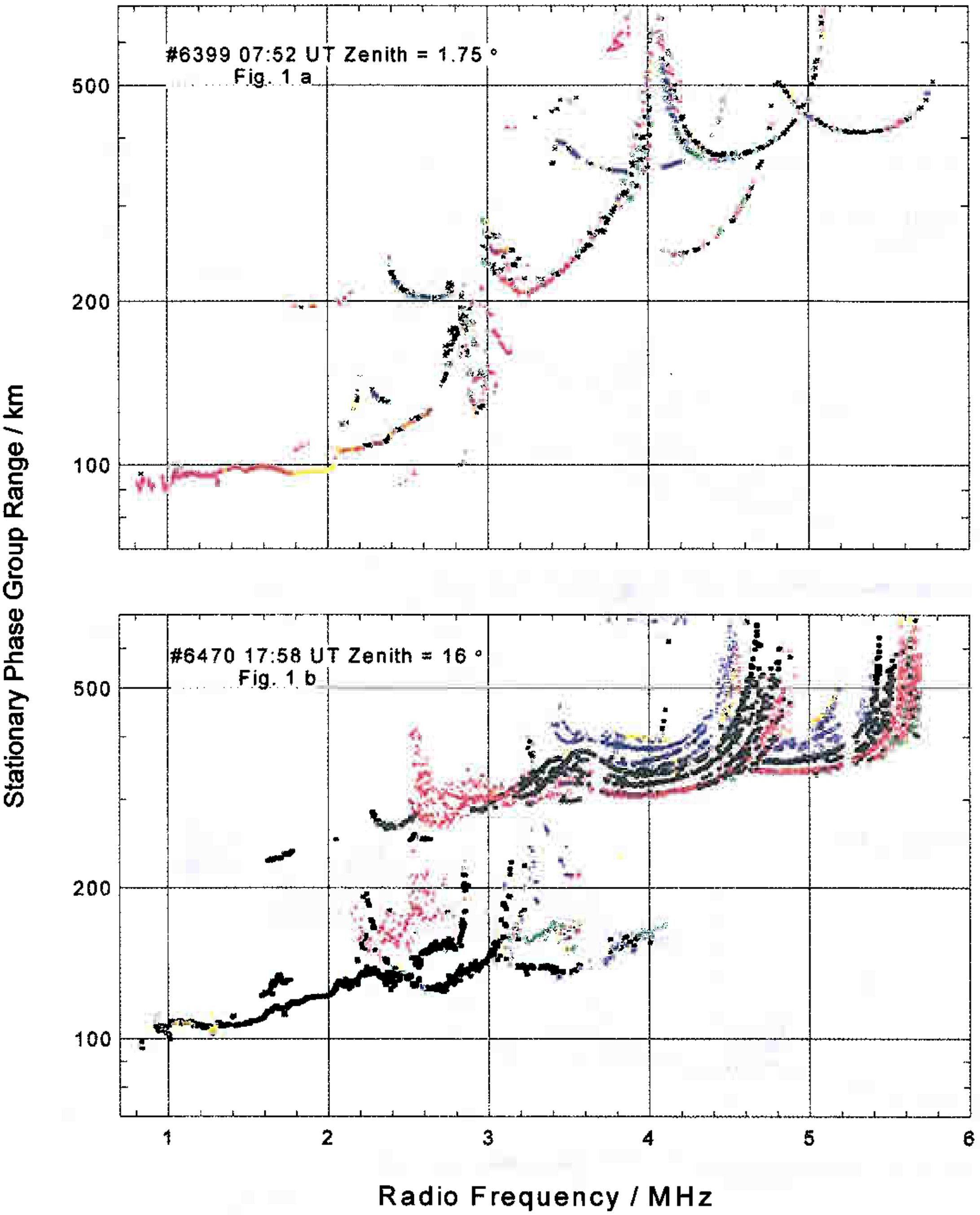

Figure 1. Typical of 243 Tromsϕ ionograms used here, from 'UKDYNA' EISCAT campaign of 22/23 May 1994. Part (a), comparatively simple R′(f) patterns, Z, O, X traces from E and F–regions. Part (b), more complex ionosphere with numerous broadband 'glints' from lateral structures. Colors denote echolocations: echoes within a zenith unit ξ (= 1.75°, part a; 16° part b) are black; echoes within ξ to 2ξ (and again, >2ξ with smaller symbols) are red in the N azimuth quadrant, yellow (E), blue (S), green (W).

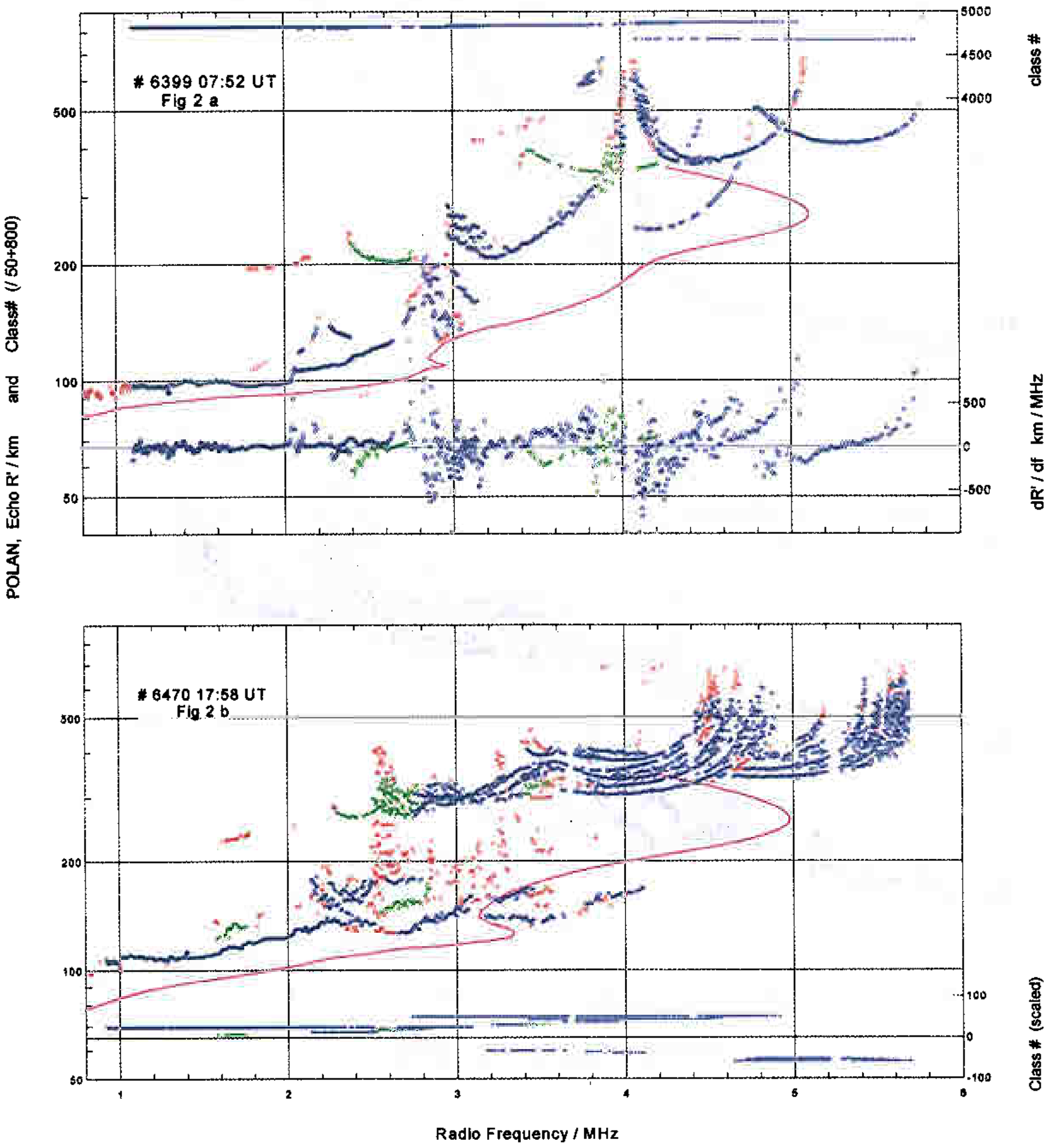

Figure 2. Same ionograms as Figure 1a,b, but showing several features of the present analysis system. Note use of logarithmic R′ scales for E–region detail. The frequency range of each 'trace' (echo class number) is shown by horizontal bars. Colors now denote classified echoes (blue); rejected classes (green); non–classed echoes (red). The derived quantity ΔR′/Δf for each classed echo appears at bottom in 1a. Continuous lines are POLAN computed profiles, after automatic selection of appropriate trace classes.

TABLE II Echo "Same – Class" Criteria and Tolerances

Echo–Pair Differences ("δ" implies absolute difference relative to mean)

Test	Definition	Close R'(f)	Open R'(f)	(Remarks)
Δf	δf	2.0 %	5.0%	(relative frequency gap)
ΔR	$\delta R'$	2.0 %	7.0%	(may extrapolate $\Delta R'/\Delta f$)
ΔX, (ΔY	$\delta X/R'$, $\delta Y/R'$	15 %	3.0%	(echolocations mag. E, N)
or ΔQ)	$\delta((Y/R'+\cos(D))*dB)$	4 %	2.0%	(***B***–field–aligned scatter)
ΔA:	δdB	15 %	10%	(relative intensity)
ΔV:	$\lvert\Delta V^*\rvert$	60	60	(Doppler, m/sec)

If *all* of the tests for an echo pair are within the "Close R'(f)" tolerances; *or,* if *all* of the tests for an echo pair are within the "Open R'(f)" tolerances, *then* the echo pair are judged to be from the same class. Using two sets of tolerances gives some adaptivity to highly variable ionospheric conditions; a single set might be satisfactory for mid–latitude conditions, or if a suitable "complexity factor" were devised for the whole ionogram. ΔQ is a special quantity to associate echoes (Z-traces, and some Spread F) dependent on scattering processes within (or normal to) magnetic field–aligned irregularities; both ΔQ and ΔY are defined, and the smaller one is tested. A test involving the echo Doppler (ΔV) is applied only in some cases.

2.2 ESTIMATION OF TRACE SLOPE, $\Delta R'/\Delta F$

Note the implied use of $\Delta R'/\Delta f$ in the ΔR test: when two echoes are judged the "same" by these tests, this new parameter is obtained as the simple (signed) difference quotient. It expresses the local slope of the R'(f) trace and has several uses, both immediate and deferred: during ECLAZZ, it aids extrapolation over small trace discontinuities or measurement gaps. Subsequently (see below), it defines analytic extrapolation for critical frequencies. It expresses the 'dispersive bandwidth' for communication channels (Fridman, et al. 1995). Used with the measured Dynasonde echo amplitudes, it may permit estimating electron collision frequencies, anomalous absorption and temperatures (Newbury, et al., 1989; also see Table III).

In Figure 2, (parts a, b correspond with Figure 1) the resulting echo classes are shown by the horizontal bars. ECLAZZ assigns, as class number, the index of its highest member in the echo list, here ordered by radio frequency. Thus the bars lie at the ordinate of the class number (perhaps proportioned here for plotting), and extend over the frequency range of the class. It is worth remarking that ECLAZZ keeps the class list "current": as each new echo in the list is considered against each echo below it in the list (*downward* from the new echo, by a trivial modification of ECLAZZ), the class list becomes updated according to whatever new associations occur. This offers potential simplification for real–time applications, and it obviates testing remote echoes. The trace slope, $\Delta R'/\Delta f$, described in the foregoing paragraph, is also plotted in Figure 2a; it is omitted from 2b because of the profusion of traces.

3. TRACE CHARACTERIZATIONS

We shall now drop the term 'class' and refer to 'traces' instead. The trace numbers are of no significance outside the analysis system, but within it they facilitate manipulations, tests and analyses of the individual traces and their constituent echoes. Among these tests, to be described below, are trace conjugacy, 'scaling' of critical frequencies, and N(h) profile inversion. The system includes some other tests (e.g. Sporadic–E and multiple–echo recognition) which are more or less obvious in method and purpose, and which shall not be described. To prepare for these tests, each trace is characterized by trace–start and trace–end mean values for the 7 parameters listed in Table II. For some parameters, mean and sigma statistics are estimated for each trace as a whole, or in segments; these are intended eventually to characterize such phenomena as Spread F (Wright, et al. 1996).

3.1 LAYER PENETRATION EXTRAPOLATIONS

For each trace, if its ending mean $\Delta R'/\Delta f > 100$ km/MHz, or its starting mean $\Delta R'/\Delta f < -100$ km/MHz, layer penetration–frequency, extrapolations are attempted. The first case refers to the asymptotic approach to infinite group retardation at a layer critical frequency. The second case refers to recovery from penetration upon reflection in a higher and more dense layer. The method of extrapolation is exact for a parabolic layer and no–field group retardation: Paul and Mackison (1981) showed that with these provisions the reciprocal slope, df/dR', considered as a function of f, decreases *linearly* to zero at the layer penetration frequency. This remains closely true with the magnetic field included; the parabolic shape is appropriate for most layers near their peak. Our method uses the trace–extremity mean reciprocal–slope, and another value a short distance inward, for a simple linear extrapolation defining the penetration frequency. Protections against wild extrapolations are applied.

3.2 TRACE CONJUGACY

We are now prepared to classify and associate the traces themselves. In accord with standard theory, at least two representations of the prevailing ionospheric structure are usually found on ionograms. Echoes of "eXtraordinary" polarization form traces which are similar to traces consisting of echoes of "Ordinary" polarization, but are displaced toward higher radio frequencies, *fx*. At high dip latitudes, such as Tromsϕ, a third representation called the "Z" trace is frequently seen. Z–traces also have O–polarization, but are displaced toward lower radio frequencies *fz*, from the corresponding O traces at *fo*. The radio frequency conjugacies are rigorously expressed in terms of the electron gyrofrequency f_H by the relationships $\sqrt{fz^2 + fz \cdot f_H} = fo = \sqrt{fx^2 - fx \cdot f_H} = fp$ where *fp* is their common plasma frequency at reflection. The Z, O and X traces are also displaced in group range at common *fp* such that, at Tromsϕ, $R'z \le R'o \le R'x$. These properties are evident in Figure 1a, where all three trace patterns occur. The *R'* displacements are not simple differences or precise ratios, as they depend on respective integrated group retardations in the profile (Paul and Smith, 1968; Titheridge, 1985, p88). However, the ratios can be characterized by approximate empirical values, which are close enough for trace recognition. At Tromsϕ, for example, $R'o/R'x \approx 0.94$, $R'z/R'o \approx 0.90$, and $R'z/R'x \approx 0.85$, at common *fp* for the *R'* in each ratio.

Three procedures, similar in their logic, consider all possible pairs of traces for O/X, Z/O, and Z/X conjugacy. For the echoes of a trace pair (i, j), the radio frequencies are shifted to tentative plasma frequencies, and the observed group–range ratios $R'i/R'j$, averaged in common *fp* bins are compared with the approximate empirical ratios. Matching trace pairs are flagged, according to their uses anticipated for subsequent applications (e.g. scaling critical frequencies, and for profile inversion). These tests could be made more sophisticated (for example, by comparing echolocation consistency), but this has not been found necessary.

4. 'SCALING' CRITICAL FREQUENCIES

E– to F–region penetration frequencies are identified by comparing traces again in pairs (i, j) selected such that the mean $R'i < 180$ km and the mean $R'j > 180$ km. The trace extremity mean frequencies (or their penetration extrapolations, if done; see above) are compared to the requirement that the end frequency of trace i and the start frequency of trace j differ by less than 10%. Only traces of common polarization chirality are compared. The minimum and maximum O–polarization penetrations are tentatively identified as fzE, and foE, respectively. A similar criterion is applied to the maximum X–chirality trace pair, for fxE. Each pair of values thus found are compared using the frequency conjugacy relations stated above. Simple and complete ionograms are adequately scaled by these steps alone, but they fail when the characteristic trace pairs are absent, or when many more than two are present, as in Figure 2b. A hierarchy of further steps is then invoked, which shall not be described in detail. They aim at identifying a value for foE by any means (for example, by conjugate calculation using fzE and/or fxE when only one or both of these can be identified); however, fzE and fxE themselves are only set non–zero when evidence for each is found.

Similarly, F–region penetrations fzF, foF, fxF are set by comparing traces in pairs (i, j) selected such that their trace–end mean *R'i* and mean $R'j > 300$ km. The trace–end frequencies (or extrapolations, if done) are compared using the conjugacy relations. Again, the aim is to get a value for foF by any means (including

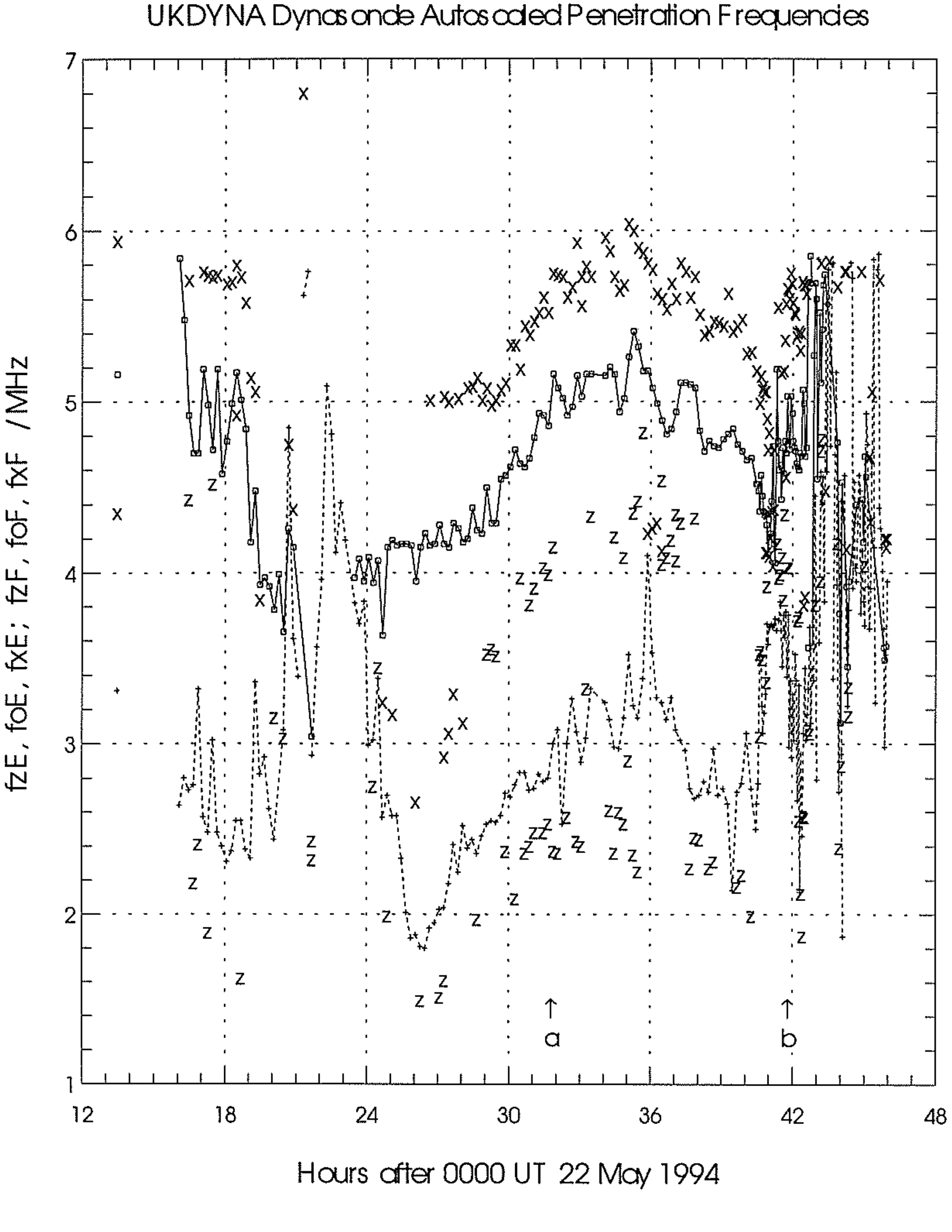

Figure 3. Time variation of E, F–layer penetration frequencies (Z, O, X modes) determined automatically by the present system, for the 243 ionograms cited for Figure 1 (12 minute intervals until hour 41; 3 minute intervals thereafter). Auroral E ionization blankets F echoes between 21 – 24 hours, and again after 43 hours. Ionogram times for Figures 1a,b and 2a,b are marked a, b.

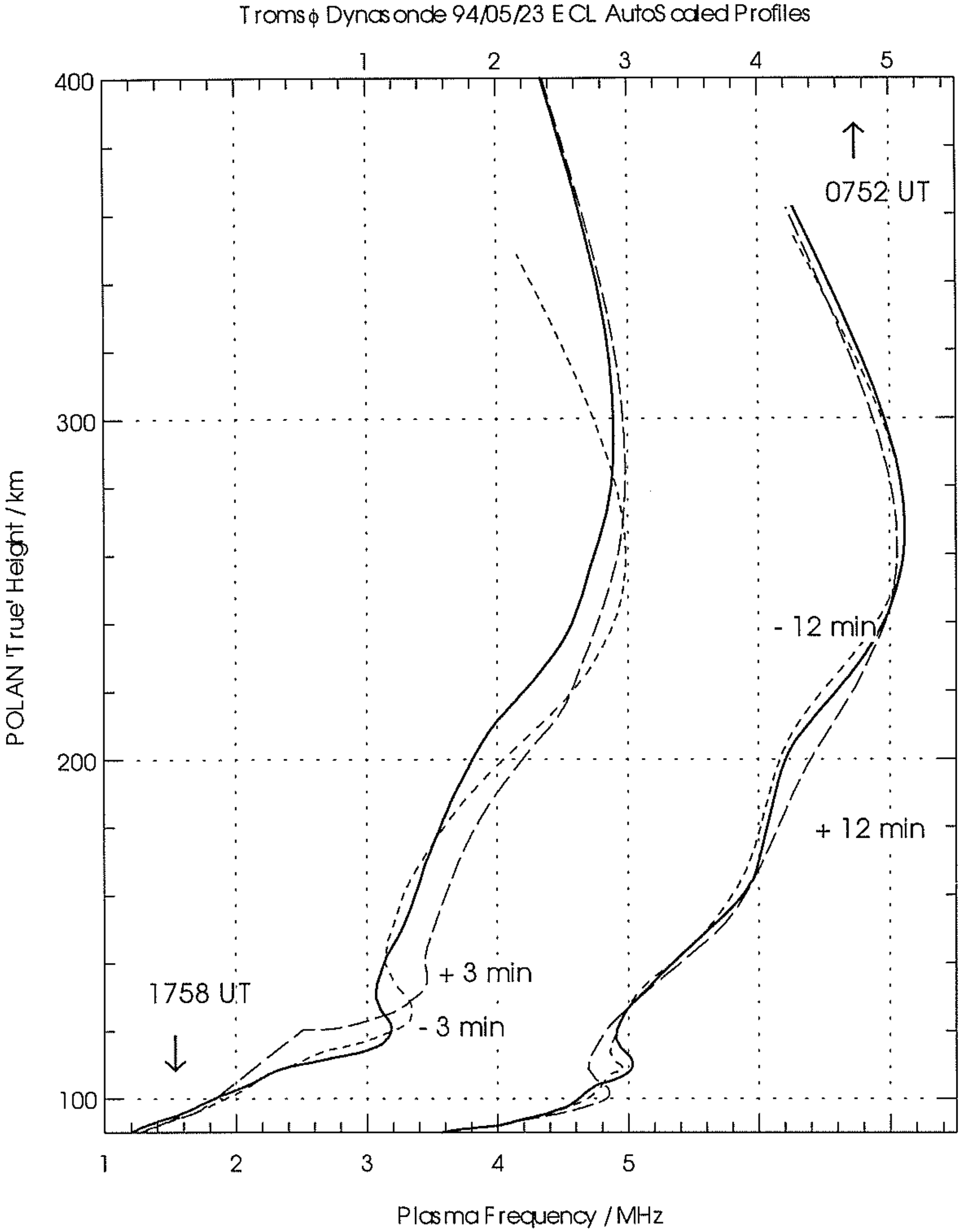

Figure 4. POLAN profiles repeated for the cases of Figures 1 and 2, and for times before and after each, to show the stability and consistency of the analyses. Each profile begins at 0.5 MHz and 70 km, well below the lowest frequency and real height of observations. X–echoes are supplied, when available, to constrain the POLAN valley solution.

conjugate calculation from fzF and/or fxF when only one or both of these can be identified); however, fzF and fxF themselves are only set non–zero when evidence for each is found.

Results of these penetration–frequency estimations are shown in Figure 3 for a 30–hour campaign from which the ionograms of Figures 1 and 2 were also taken. Two intervals of intense E–region ionization by auroral precipitation are evident (lower connected data points; hours 20 – 26, and hours 40 – 46). Between these episodes comparatively smooth variations with solar zenith angle can be seen. In the variation of foF (upper connected data points) and fxF, six oscillations of about 2 hour period are probably identifiable with atmospheric gravity wave activity. A very few failures are obvious: for example, foE has been misidentified for fzE near hours 32.5 and 39.5. No 'editing' has been applied to these results.

5. PROFILE INVERSION

Among the principle goals for this analysis system is to select data for inversion of the ionogram to an "N(h)" profile representative of the prevailing ionosphere. With the critical frequencies identified, and traces characterized by chirality, mean, starting and ending variables, it is relatively straightforward to decide which traces to use for inversion. The O–traces are first ranked according to starting frequency. Broadband traces are selected in preference to narrowband traces. More nearly zenith traces are selected when (as in Figures 1b and 2b) a choice must be made. At present, the inversion input data arrays are formatted according to the requirements of the method POLAN (Titheridge, 1985). Figures 2a,b include the resulting profiles. In Figure 4, these two profiles are repeated (heavy lines) together with 'before and after' profiles for each example, to illustrate the consistency achieved. The automatic process is remarkably stable, considering the complexity of Tromsϕ ionograms and the fact that each ionogram is analyzed entirely independently of the others. This is in contrast to an automatic inversion method previously reported (Wright, et al. 1972) by which each ionogram set windows for echo selection in the next ionogram. That tactic remains in reserve for the present system, and especially for real–time applications.

On occasions, because of intense lateral structuring of the ionosphere and the 'all–sky' view of the ionosonde, more than one profile may be appropriate to a single ionogram: see for example Wright, et al. (1988) figs 4 and 8; also Wright (1990) concerning some precautions required in highly structured conditions. The ionogram of Figure 2b would be a candidate for such treatment, but no automatic scheme for this purpose is yet implemented.

6. CONCLUDING REMARKS

This system is intended to facilitate the analysis of measurements by research ionosondes as distinguished from monitoring instruments in the introduction and by Table I. Can it nevertheless be applied to data from monitoring instruments? At temperate latitudes, and in quiet conditions everywhere, it probably can with only a few adaptations. Some modern monitoring instruments yield most of the variables used in Table II, although with less resolution. The tolerances shown there for trace discrimination, however, are not 'tight' even by monitoring instrument standards. For monitoring instruments which give only R′(f), and not echo polarization, the problem to distinguish O, X becomes similar to the O, Z problem, which is solved here by what are essentially pattern–recognition methods. Of course, all this assumes that the data are in digital form. For archived film recordings, prior tasks of scanning and echo recognition must be addressed. Scanning technology is now sufficiently mature. The method of coincidence detection used in the Dynasonde (Wright and Pitteway, 1979) should serve adequately to reject random 'noise' from scanned film ionograms. These considerations perhaps point the way to effective assimilation of the ~ 1.5×10^8 ionograms now archived on about 50,000 rolls of film (Wright and Paul, 1981).

Some remarks are appropriate concerning the present status of methods for ionogram inversion to plasma–density distributions. None of the inversion methods presently available make full use of the information available from research ionosondes, nor even from modern monitoring instruments. In supplement to the classical 'smooth', valley–corrected, peak–fitted profiles which POLAN and a few other methods yield with some success, we wish to suggest the usefulness of accommodating at least the additional features listed in Table III. References suggest potential precedents.

Finally, we remark that, as with any research ionosonde, observing methods for the Dynasonde are continually evolving. Currently, tests of an improved 8–pulse set are under way which should yield higher–

resolution echo Doppler estimates and other improvements, permitting ΔV (Table II) to play a greater role in trace discrimination.

TABLE III. Attainable New Achievements for Ionogram N(h) Inversion

Item	Input information	Aims, Remarks and References
Local Tilts	Echolocations	Correctly represent local f, h, t dependencies for AGW and other large–scale structures. >>Fresnel scale (Weixing and Jun, 1987, 1995).
'MicroScale'	δ R′; Spread F, etc.	≤ Fresnel scale (Wright and Pitteway 1996; Denisenko, et al. 1995).
Valley Improvements	Az, Ao, Ax (dB)	Improve width estimation; potentially give valley shape (A.K. Paul, unpublished remark)
	Z–echo R′(f)	Invert Z trace for B–aligned profile; (Wright, 1960)
E–peak Tn	dB(f); R′(f)o,x,z	From V_{en}. (Newbury, et al. 1989)
F–peak Te+Ti		(same)

Acknowledgments.

We are grateful to the director and staff of the Tromsϕ EISCAT installation, and in particular to Dr. M.T. Rietveld, for the Dynasonde data used here.

References

Denisenko, P.F., N.V. Nastasyina, V.I. Vodolazkin, Possibility of using ionosondes for regular observation of irregularities of electron density. *Ionosonde networks and stations*, P.J. Wilkinson (editor) UAG-104, published by World data Center A for Solar terrestrial Physics, NGDC, 325 Broadway, Boulder, CO 80303, 1995

Fridman, S.V., O.V. Fridman, K.H. Lin, K.C. Yeh and S.J. Franke. The two–frequency correlation function of the single path HF channel – Theory and comparison with the experiment. *Radio Sci. 30*, 135–147, 1995

Newbury, S.M., P.L. Dyson and A. Singh. An inversion procedure for obtaining collision frequency profiles from swept-frequency absorption measurements. *J. Atmos. Terr. Phys. 51*, 425–432, 1989

Paul, A.K. and D.L. Mackison, Scaling of the F–layer critical frequency from digital ionograms applied to observations during the solar eclipse on 26 February 1979. *J. Atmos. Terr. Phys.*, *43*, 221–224, 1981.

Paul, A.K. and G.H. Smith, Generalization of Abel's solution for both magnetoionic components in the real–height problem. *Radio Sci.* 3, 163–170, 1968..

Pitteway, M.L.V. and J.W. Wright. Toward an optimum receiving array and pulse set for the Dynasonde, *Radio. Sci.*, vol. 27, No. 4, pp. 481–490, 1992

Press, W.H., S.A. Teukolsky, W.T. Vetterling and B.P. Flannery, *Numerical Recipes in FORTRAN*, Second Edition, Cambridge University Press, Cambridge CB2 1RP UK, 1992.

Titheridge, J.E. *Ionogram analysis with the generalized program POLAN.* Report UAG–93, World Data Center A for Solar–Terrestrial Physics, U.S. Dept. of Commerce, Boulder CO 80301 USA, 1985

Vodolazkin, V.I., P.F. Denisenko, V.P. Rjanitsin, V.P. Sotsky and Yu.N. Faer, Absorption of radio waves and effective electron collision frequency in the ionosphere. *Geomag. and Aeronomy* 33, 74–83, 1993

Weixing, W., and L. Jun, Estimation of propagation parameters of non-uniform ionospheric disturbances from HF phase measurements. *Ionosonde networks and stations*, P.J. Wilkinson (editor) UAG-104, published by World data Center A for Solar terrestrial Physics, NGDC, 325 Broadway, Boulder, CO 80303, USA, 1995

Weixing, W., and L. Jun, Height profile inversion of the ionospheric movement from the observed parameters of HF radio echoes. *Chinese J. Space Sci., 7*, 85–94, 1987

Wright, J.W., A.R. Laird, D. Obitts, E.J. Violette, D.E. McKinnis, Automatic N(h, t) profiles of the Ionosphere with a digital ionosonde. *Radio Sci.* 7, 1033–1043, 1972

Wright J.W. and M.L.V. Pitteway, Real–time data acquisition and interpretation capabilities of the Dynasonde, 1. Data acquisition and real-time display. *Radio Sci.* 14, 815–825, 1979.

Wright, J.W. and A.K. Paul, *Toward global monitoring of the ionosphere in real–time by a modern ionosonde network; the geophysical requirements and technological opportunity.* NOAA Special Report; Space Environment Laboratory, Boulder CO July 1981.

Wright, J.W., R.I. Kressman, T.S. Virdi and P.N. Collis, Comparisons of EISCAT and Dynasonde ionospheric measurements: simple to moderately structured plasma densities. *J. Atmos. Terr. Phys.* 50, 405 – 421, 1988

Wright, J.W. and M.L.V. Pitteway, Toward an optimum receiving array and pulse set for the Dynasonde. *Radio Sci., 27*, 481–490, 1992

Wright, J.W., P.E. Argo and M.L.V. Pitteway, On the radiophysics and geophysics of ionogram spread F. *Radio Sci.* 31, 349–366, 1996.

Wright, J.W. Some magnetoionic phenomena of the arctic E–region. *J. Atmos. Terr. Phys.* 18, 276–289, 1960.

Wright, J.W. Ionogram inversion for a tilted ionosphere. *Radio Sci.* 26, 1175 – 1182, 1990.

A NEWCOMER'S QUESTION: "IS IT INTERESTING TO SCALE IONOGRAMS IN THE FUTURE?"

Christer Juren, Swedish Institute of Space Physics, Box 812, S-98128 Kiruna Sweden,
Phone: +46 980-79077 , Fax +46 980-79050, e-mail: christer@irf.se

ABSTRACT

The paper is based on experience gained designing an interactive system for traditional manual scaling for three ionosondes supplemented by a portable receiver. The advances in modern software and hardware facilitate user-friendly computer systems to deal with all aspects of sounding. Cheap modern high-capacity storing media can be used and there is no need to compress the data collected. With modern software techniques it is possible to build classes, which produce objects, which together with each other will extract information from the data.

As we have a long time series of traditionally scaled data sets, it is important to ensure that all new developments are compatible with past scaling, for continuity. As skilled scalers will be hard to find and finance, modern computer ideas should be brought in for displaying, interacting and calculating the required parameters directly from the original data stored in suitable formats. The scaling thus can be minimised and merely used to connect with the past data sets to study ionospheric physics.

1. THE SWEDISH IONOSONDES.

1.1 The Traditional Ionosonde at IRF.

There are three traditional ionosondes in Sweden, located in Kiruna, Lycksele and Uppsala, which run synchronously and are remotely controllable. The ionosondes are handled by the Swedish Institute of Space Physics (IRF). The peak power for each transmitter is about 1kW and the pulse length is 100 micro seconds. Both phase and amplitude are measured from the received signals. The transmitters are 15 years old while the receivers have been continuously developed and are currently 5 years old. A 30m high delta antenna is used in Kiruna for transmitting on frequencies above 3.5 MHz. For lower frequencies a 100m horizontal rhombic is used. The rhombic is pointing south and is also used for oblique sounding. In Lycksele the antennas are similar to Kiruna, but in Uppsala there are two deltas and no rhombic. The two deltas are of different heights for the two frequency bands indicated above. For receiving signals the same type of deltas are used at all places. Some experiments have been done with active antennas which are used with the portable receiver.

1.2 Computer Software And Hardware For Traditional Sounding At IRF.

Planning and construction for the current computer system, for all three stations, began in 1990. At that time, it was natural to use transputers together with their programming language Occam. Occam was, and is, a simple but sophisticated and elegant language for small grained parallel programming and was most effective for the detailed parts of the software interfacing with the hardware, which was realised in the field programmable logic Xilinx. For programming the human interface, Smalltalk was chosen. This was cutting edge software at the time and still will be for several years to come, in spite of Java! The different pieces were put together with TCP/IP and other types of message passing in accordance with Occam or more theoretically CSP (Communicating Sequential Processes).

The whole system developed as an experiment in using modern computer components in both hardware and software. The programming style also had an impact on the description of the general physical systems involved such as the ionosphere, radio wave propagation and transformation of ionograms to parameters - or scaling. The latter was important in developing a computer aided scaling system written in Smalltalk. The scaling system, a manual one, is now under revision and a reduced version, for the most commonly used parameters, is planned in Java and/or X and is intended for use by the general user on the WWW (e.g. ionograms accessed from http://www.irf.se/~ionogram/). This will be a first step towards an adaptation for the future when there are not so many skilled scalers at IRF as today and their results will be too "advanced" for the general ionospheric physicist; one of the points in this paper!

Also, access to the original individual ionograms as discrete stereograms and animations on WWW in Java and X environments have been developed.

1.3 The Data Collection And Processing For Classical Sounding At IRF.

At the beginning of each hour, a standard sounding is made at all three stations and the results are archived as digital ionograms, which are subsequently scaled to give 14 parameters. The scaling is performed in Uppsala and Lycksele for all three stations and the scaled data are stored together with the original ionograms.

The archived data can be accessed using the WWW in different forms - from FTP to interactive sessions running on X-terminals to Netscape-Java environments. Beside WWW there is a report "Ionospheric Data Sweden" which is published every month.

The ionograms are first created as bitmaps, each pixel forming a phase and amplitude pair. Each bitmap consists of 500*1024*2 bytes (1 Mbytes for each ionogram). The digital ionograms contain more information than the older photographic pictures recorded at Kiruna on 16-mm film These had about 12*10*40*40 pixels on each picture with a grey scale corresponding to, at most, 6 bits which in total gives 150 Kbytes. In Lycksele the pictures were made on a 35-mm film, which gave at most 0.5 Mbytes for each picture.

Simple scanning of the ionogram bitmaps reduces these to a data set consisting of a varying number of bytes per ionogram; 3023 to 43023 and typically about 6000 bytes. The number of bytes could be reduced to about 1000 and still represent the ionograms accurately. The data sets are saved and within 10 minutes they are accessible via WWW in interactive sessions (X-terminals or JavaOnWWW) and can be brought to the user as postscript files, which can be created when required. The postscript format is presented so that it will be an easy task to do further data processing.

The scaling which follows reduces a whole day's ionograms to 2000 bytes with the output fully accessible, like the original ionograms, on the web in addition to FTP.

2. DISSUS -- DISTRIBUTED IONOSOUNDING USING STEREOSCOPICS.

"The Swedish Ionosondes" is the overall name for the computer and radio equipment together with the software and its "patterns", interactive sessions (e.g. scaling and Internet sessions) and the future development of the whole distributed system at IRF. We are attempting to retain the traditional sounding concept but hybridising it with the latest computers and technology. The existing ionosonde transmitters at IRF and new cheaply developed receivers make it possible to do distributed sounding all over Sweden. This leads to the DISSUS concept.

- Modern computer techniques make it possible to store much information that is easily accessed and can be visualised in different ways.
- Time keeping nowadays is simple and inexpensive using GPS.
- Visualisation is old and simple but can still be used efficiently and is preferred by many people in order to summarise a lot of data for overviews. These elements form a model, called DISSUS, for sounding the ionosphere over an extended region and / or over an intervall in time.

As an example, stereoscopics, for discrete 3-D points, together with interactive animations are powerful, even for medium level graphical stations, and fit well with WWW. Here, 48 ionograms are selected from 1996, in Kiruna; for the third, 10th , 17th and 24th day in each month at 11 UT. The picture, following, is one frame from an animation running on WWW illustrating the whole year of 1996 using standard ionograms from Kiruna (http://www.irf.se/¨christer/oneYearAnimation.html). Please use crossed eyes when viewing the picture; see http://www.irf.se/christer/dissus.html and [1] for general discussions. The co-ordinate axis pointing to the right is frequency, the axis pointing upwards is virtual height and the third axis pointing into the paper is time over the year; there are seven days between each ionogram all for the same time of the day. The first ionogram, at the front, is from the third of January, 1996, at 11 UT.

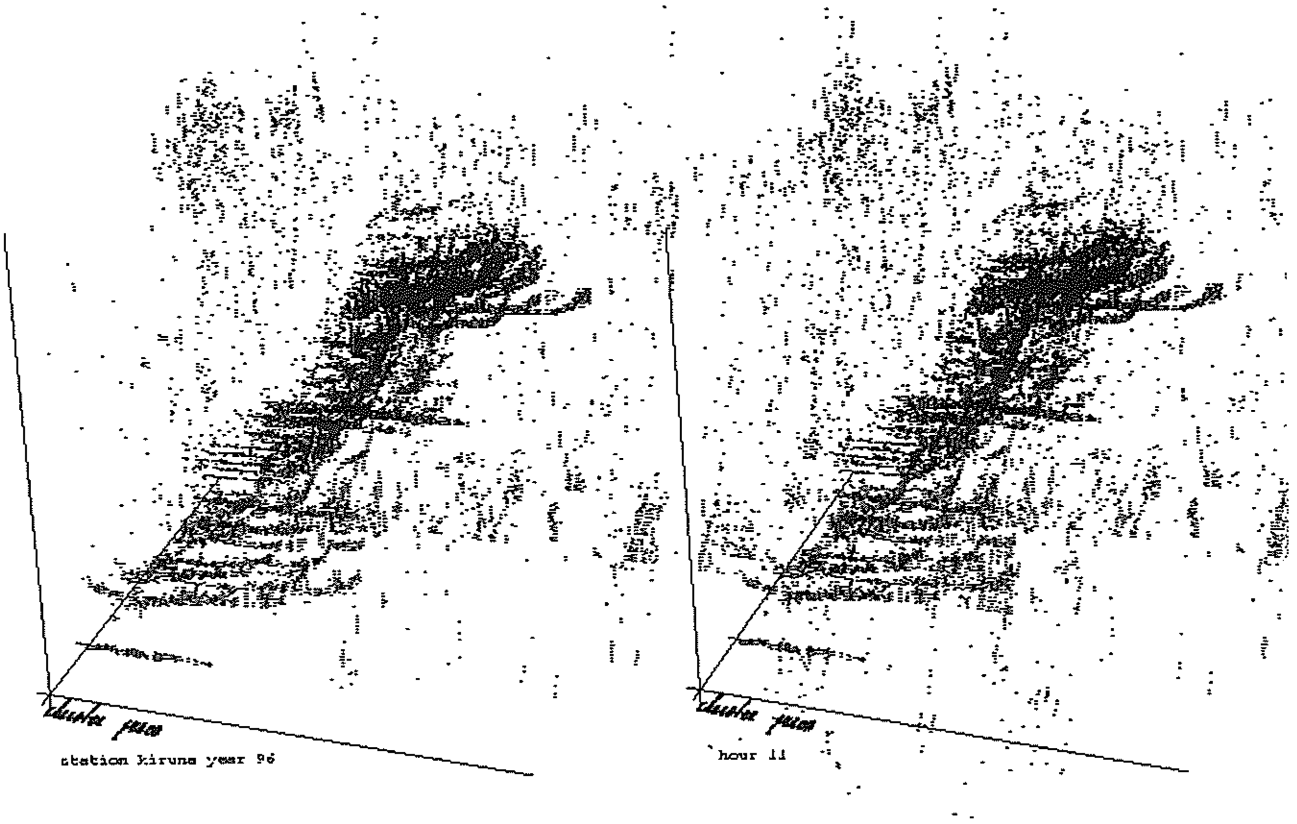

3. REDUCED SCALING: PARAMETERS FOES, FOF2 AND M(3000).

There are two types of scaling in Sweden; full scaling and reduced scaling.

Reduced scaling produces three parameters that are processed urgently each day, early in the morning, and are distributed globally as fast as possible. These parameters are foEs, foF2 and M(3000).

Full scaling is done with an accepted delay of, at most, a month and normally it should be done within a few days after the sounding.

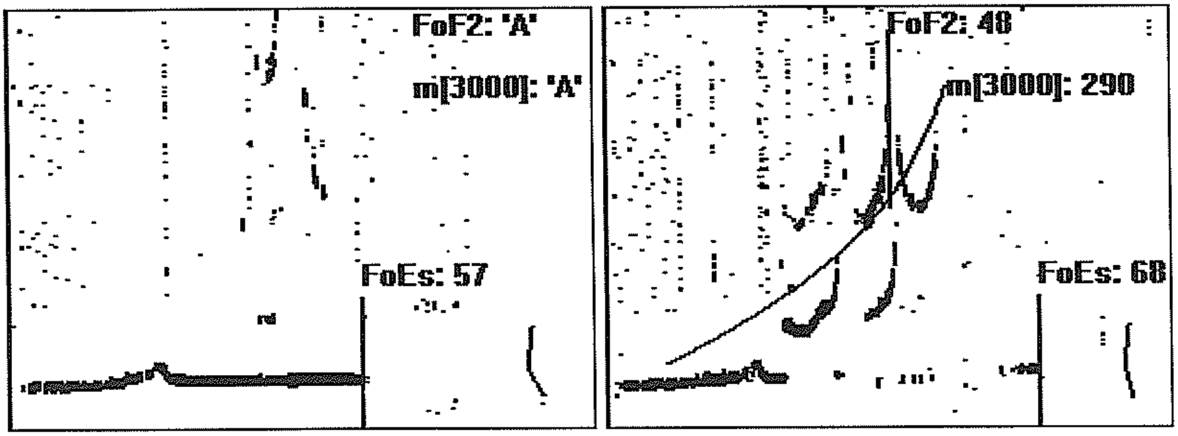

Two ionograms from Lycksele with foEs, foF2 and m(3000) indicated. They were taken at 10 and 11 UT respectively on 96.06.07.

A sample of the software code, in Smalltalk, is shown for scaling m(3000).

```
m3000
 |para aValue|
 lastSkipChar:=nil.
 aValue:= (evalResults at:’foF2’) value .
 aValue=0 ifTrue:[para:= (evalResults at:’M(3000)’
                      put:(EvalParameter newFor:’M(3000)’
                              default:nil)
                 ]
           ifFalse:[  para:=self evalMuf3000].
  para isNil ifTrue:[^nil].
  lastSkipChar=$, ifFalse:
    [para value:(para value/aValue*100 roundTo:5).
     para descriptor:(evalResults at:’foF2’)  descriptor.
     para display
    ].
"The result for m(3000) is related to foF2. The main scaling  is in the method evalMuf3000 which
support the scaler to find out the maximum usable frequency when the ordinary path is used for
communication over a 3000 km distance."
```

The sample code above illustrates the not so well known interactive program language Smalltalk at work. It should be noticed that the Smalltalk language tries to mimic the human way of communicating with a lot of objects in mind [2].

It is not a trivial task to do accurate and robust scaling, even for the simpler reduced parameter set. There are some procedures for automatic scaling but at high latitudes such systems turn out to be problematic, however it could perhaps be used [3]; but the use of a language such as Smalltalk could be a comfortable way to build interactive programs for the inspecting of the data and for going the traditional "manual" way for the scaling.

4. SUMMARY

The “Swedish Ionosondes” is an example of standard routine ionosounding which started with the IGY. DISSUS is just one example of a modern continuation of coherent ionosounding, which was experimentally started by Appleton and theoretically started, together with W. Altar, in the 1920’s. DISSUS uses a somewhat modified traditional ionosonde together with portable receivers distributed over Sweden. We plan to make and deliver scaled ionogram data together with original ionograms in suitable formats for as long as possible, but should we do continue scaling? We also plan to make it possible to do simple scaling of our ionograms on the WWW with programs in C for X-terminals and in Java, but should we? We also want to get in contact with all types of soundings in some way or another connected to the traditional ones. As a preliminary example please visit our WWW site: http://www.irf.se/~ionogram/.

References

[1] C. Juren, Vizualization of Ionosonde Data Using Discrete Ionograms, Avances in Space Research, Cospar 94, in Press.

[2] Jonathan Pletzke, Advanced Smalltalk, John Wiley & Sons, Inc (1996)

[3] J-C. J. Jodogne (This session)

MANUAL VERSUS AUTOMATIC COMPUTER PROCESSING FROM YEARS OF HOURLY DATA COMPARISON

Doc.Ing J.-C. JODOGNE,
Royal Meteorological Institute of Belgium, Av. Circulaire 3, Bruxelles, B-1180,
Belgium, email: jcjod@oma.be

ABSTRACT

The ARTIST software outputs a near real-time set of parameters from the Digisonde 256 at the station Dourbes. These parameters are organized in monthly tables with the help of the ADEP software and are recorded in a file. ADEP is also used to manually validate or correct the scaling and output in other files. For each analysed parameter, and from the comparison of simultaneous determinations, a Kendall coefficient of concordance is computed and the difference (manual minus automatic) values are divided in classes to get the related statistical frequencies. Among the analysed parameters, only fmin and h'Es show less good concordance due partly to frequently missing E-region traces.

1. BUILDING THE DATA BASE

Monitoring of the bottomside ionosphere, by teledetection of the electronic density distribution, is one of the tasks of the Dourbes ionospheric station.

In routine use since 1984, a Digisonde 256 from Lowell University, USA, fed a computer running the ARTIST software (Reinisch & Huang,1983) and recording the raw and automatically processed data. The ARTIST outputs are edited and recorded, without any human intervention, producing the automatic station monthly parameters reports. Besides this, the ADEP software (Lowell) is used to manually validate, or correct, the trace and the calculated parameters and then produce the manual station monthly parameters reports (published and available). The data base encompasses the A files (automatic data) and M files (manual data).

2. PROCEDURE

For each analysed parameter, one takes the number, **m**, of manually determined values and the number, **a**, of automatically determined values to compare with the possible maximum number of values and get the respective relative numbers. The comparison is also made between these **m** and **a** numbers and the number, **c**, of simultaneous determinations by both methods. From these determinations, the difference between the "manual" value and the "automatic" one are computed. With this set of differences, one ranks in classes and computes the statistical frequencies for each class.

Finaly, a non parametric test, the Kendall coefficient of concordance (Siegel 1956), **w** ($0 < w < 1$), is produced from the simultaneous determinations. A high, or significant, value of **w** may be interpreted as meaning that automatic and manual scaling give essentially the same result in ranking the N determinations.

3. STATISTICS

The data analysed were from_January 1992 to June 1995 and were divided in half-yearly sets of (92a, 92b,...). The following ten parameters were selected:

frequencies:	**foF2 , foF1, foEs, fmin, fminF, MufF2**
virtual heights:	**h'F, h'F2, h'Es**
M factor:	**M3000F2**

Other parameters were disregarded due to the existence of known biases in the comparison. For example, the automatic replacement of foE by the predicted value when there is no automatic determination or the fact that no manual determination of fxI was made before 1995.

The maximum number for each parameter is 24 times the number of days, or 4344 for the first half of the year (or 4368 in the case of 1992) and 4416 for the second half of the year. The relative numbers always refer to these numbers. The total number of hours for the 3.5 years is 30648.

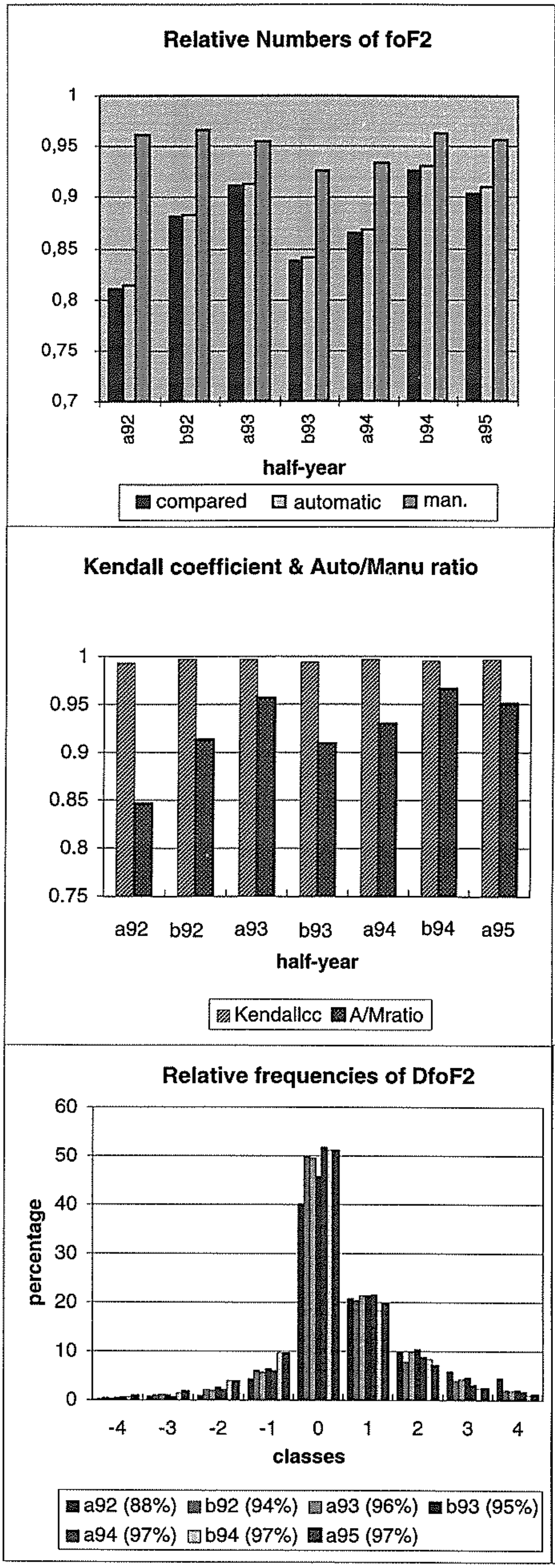
Relative Numbers of foF2

Kendall coefficient & Auto/Manu ratio

Relative frequencies of DfoF2

Fig.1a foF2 data

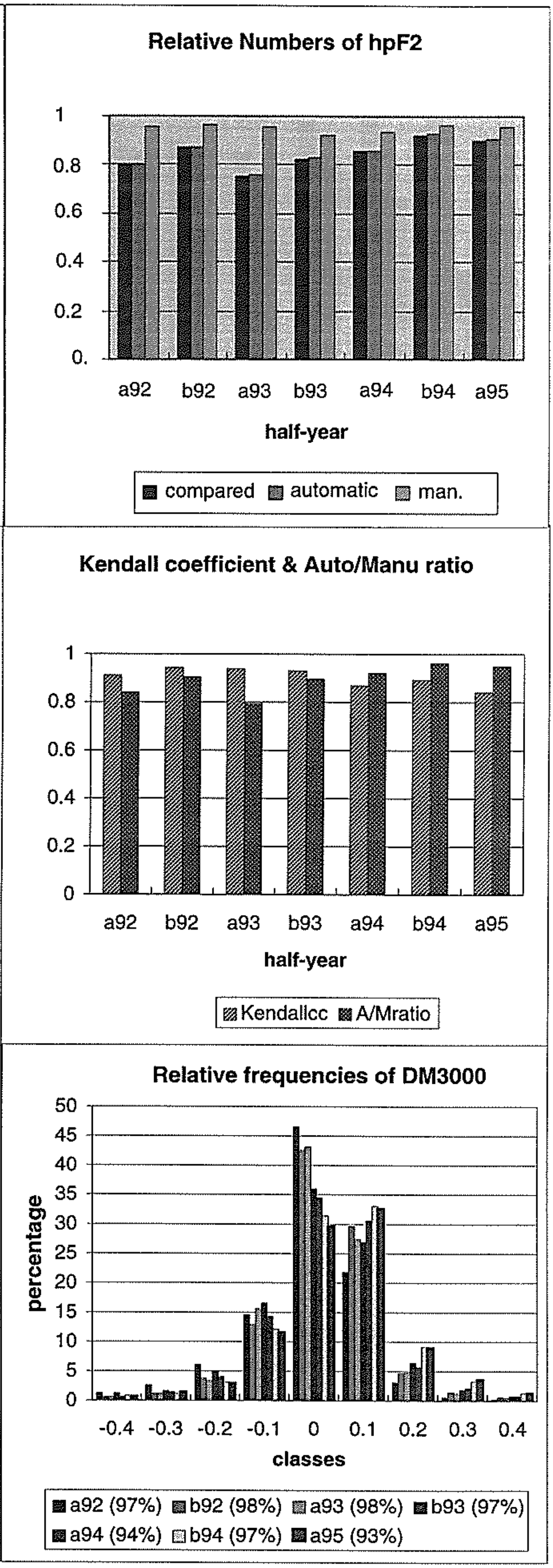
Relative Numbers of hpF2

Kendall coefficient & Auto/Manu ratio

Relative frequencies of DM3000

Fig.1b M3000 data

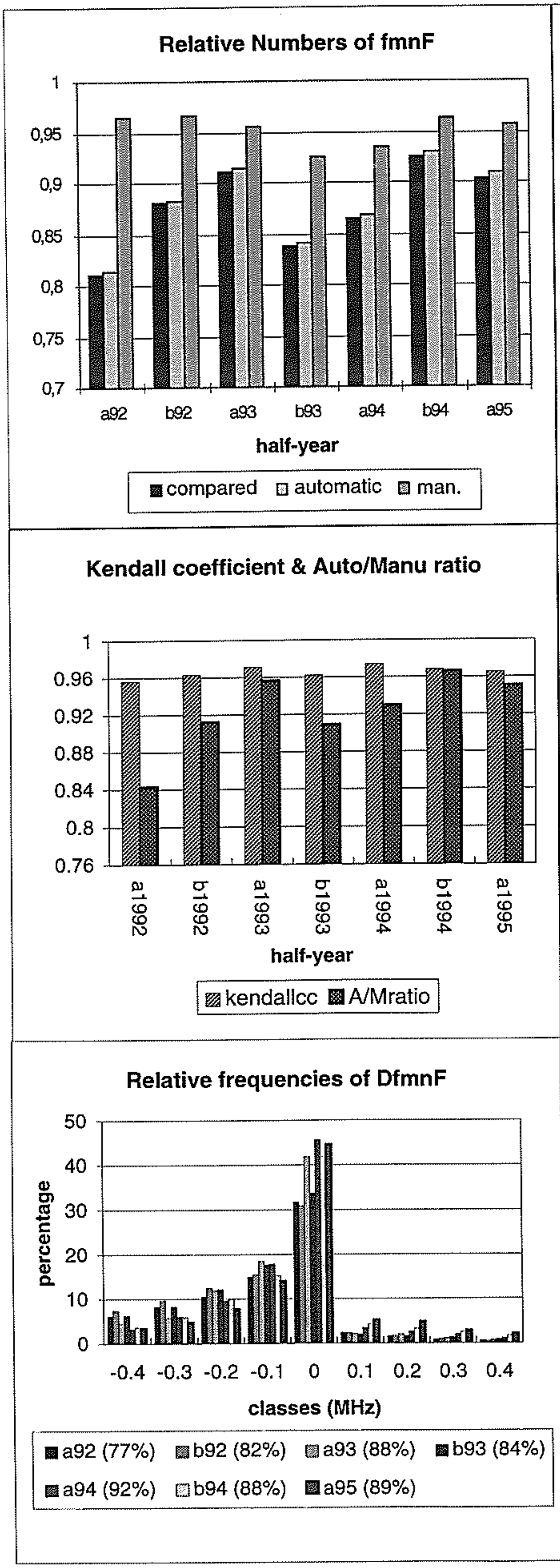
Relative Numbers of fmnF

Kendall coefficient & Auto/Manu ratio

Relative frequencies of DfmnF

Fig.2a fmnF data

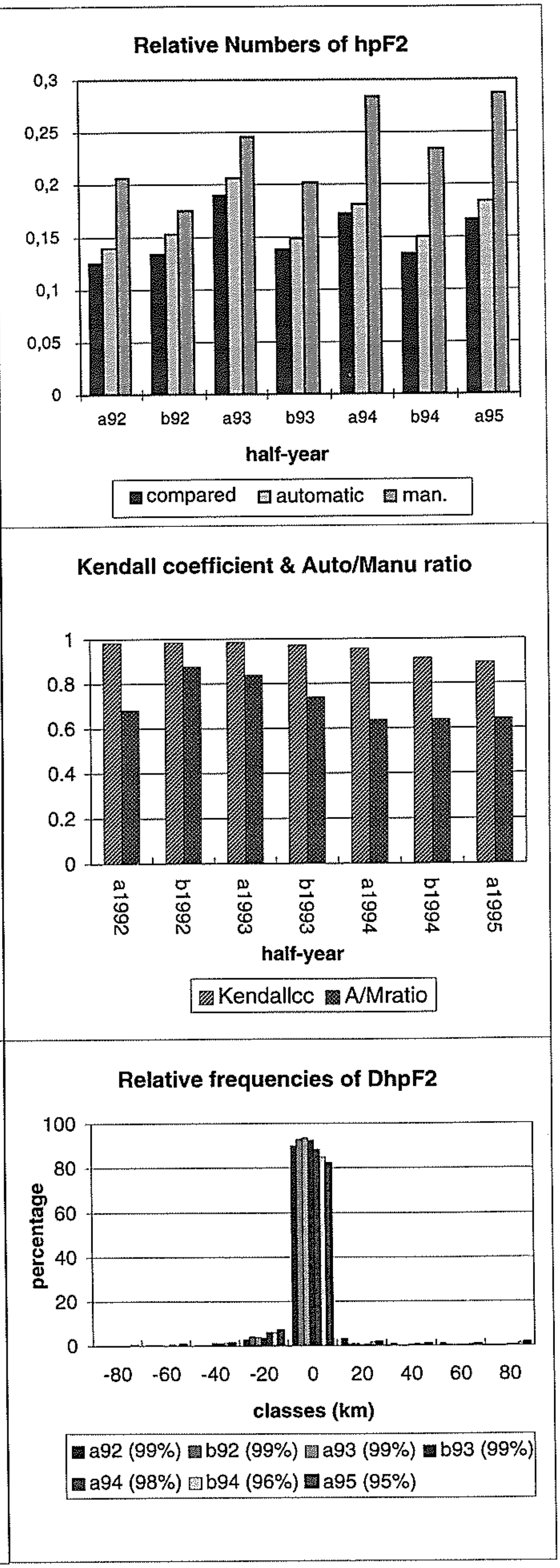
Relative Numbers of hpF2

Kendall coefficient & Auto/Manu ratio

Relative frequencies of DhpF2

Fig.2b hpF2 data

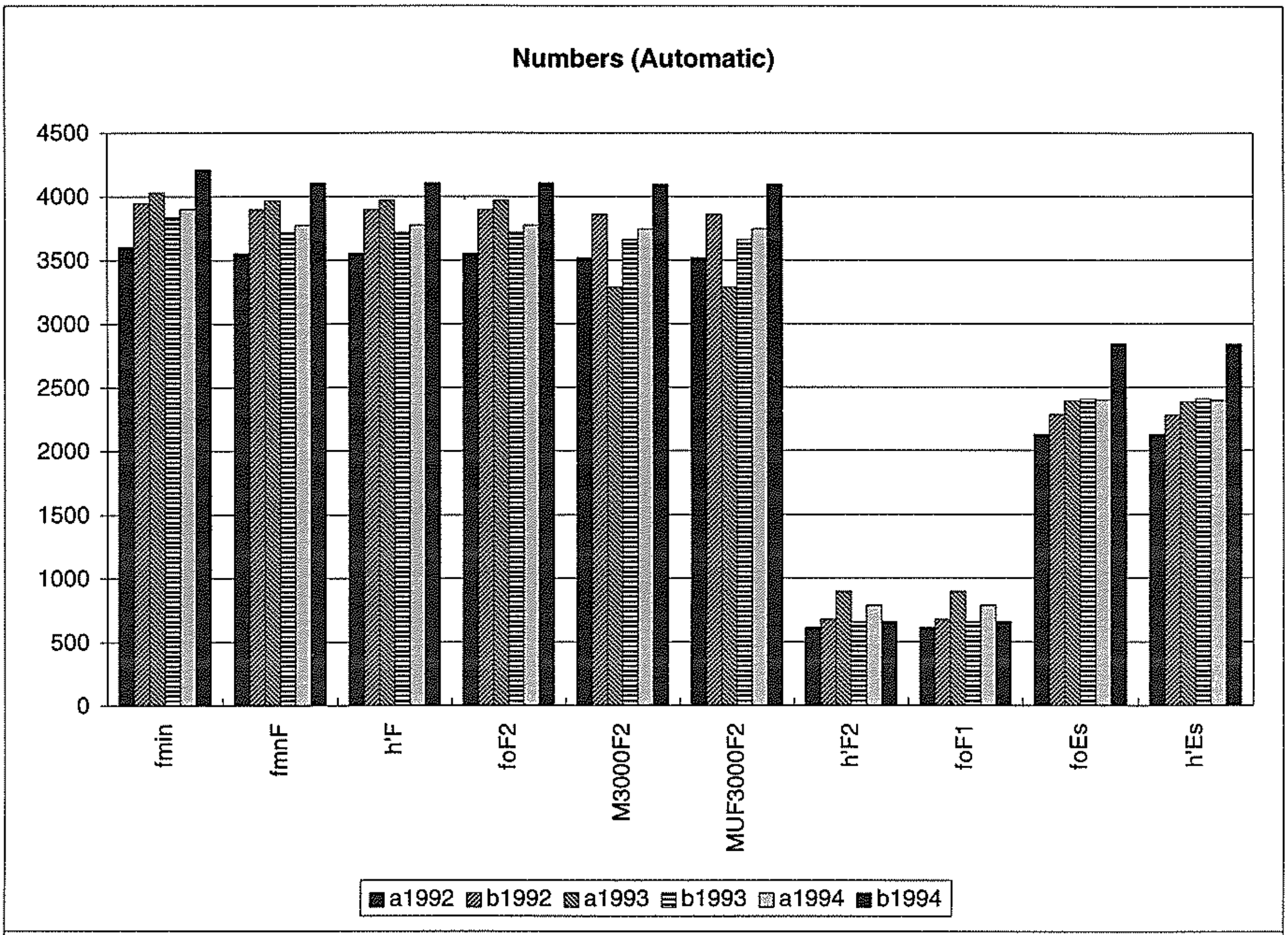

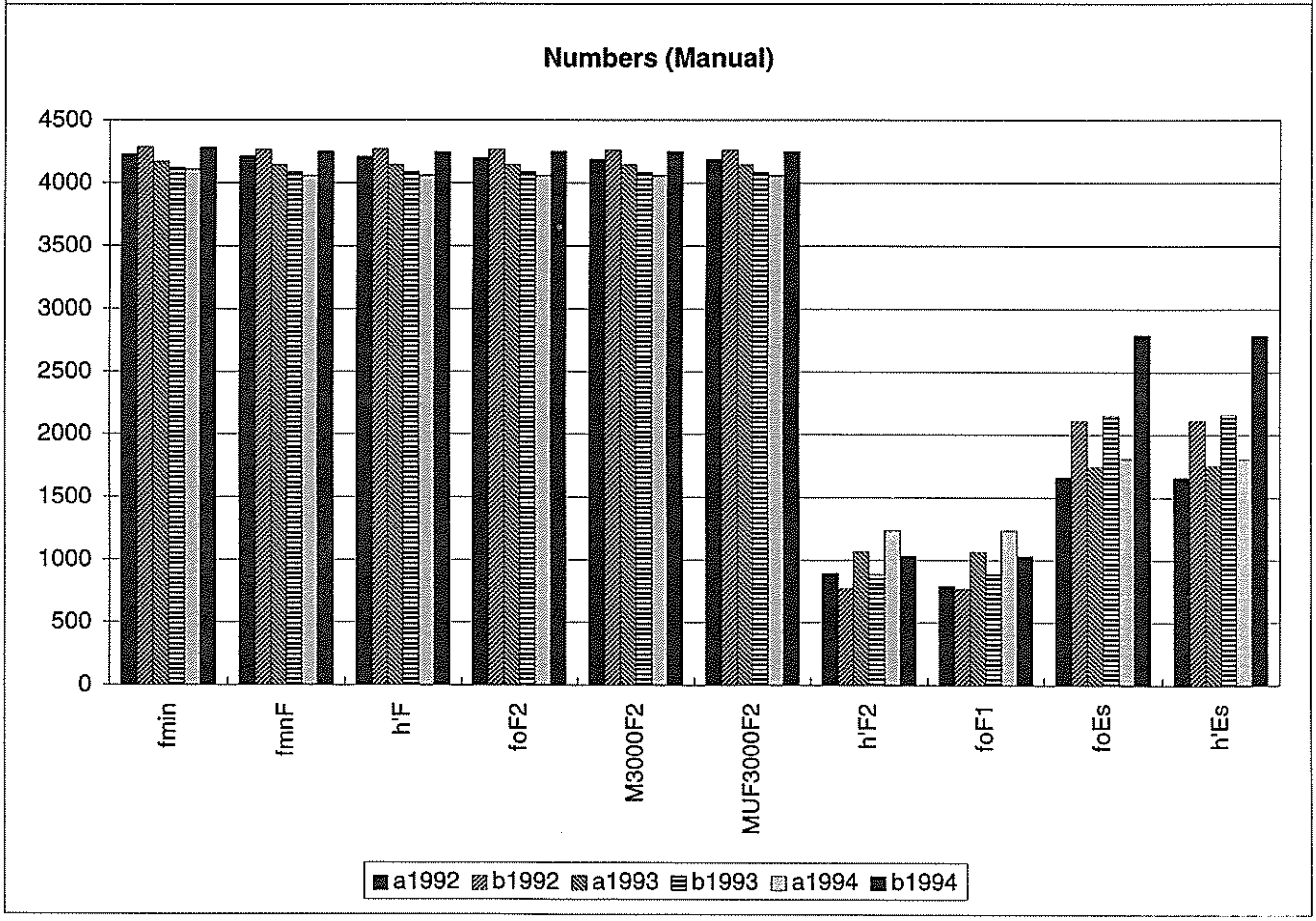

Fig.3 Numbers of automatic (top) and manual (bottom) determinations for 3 years

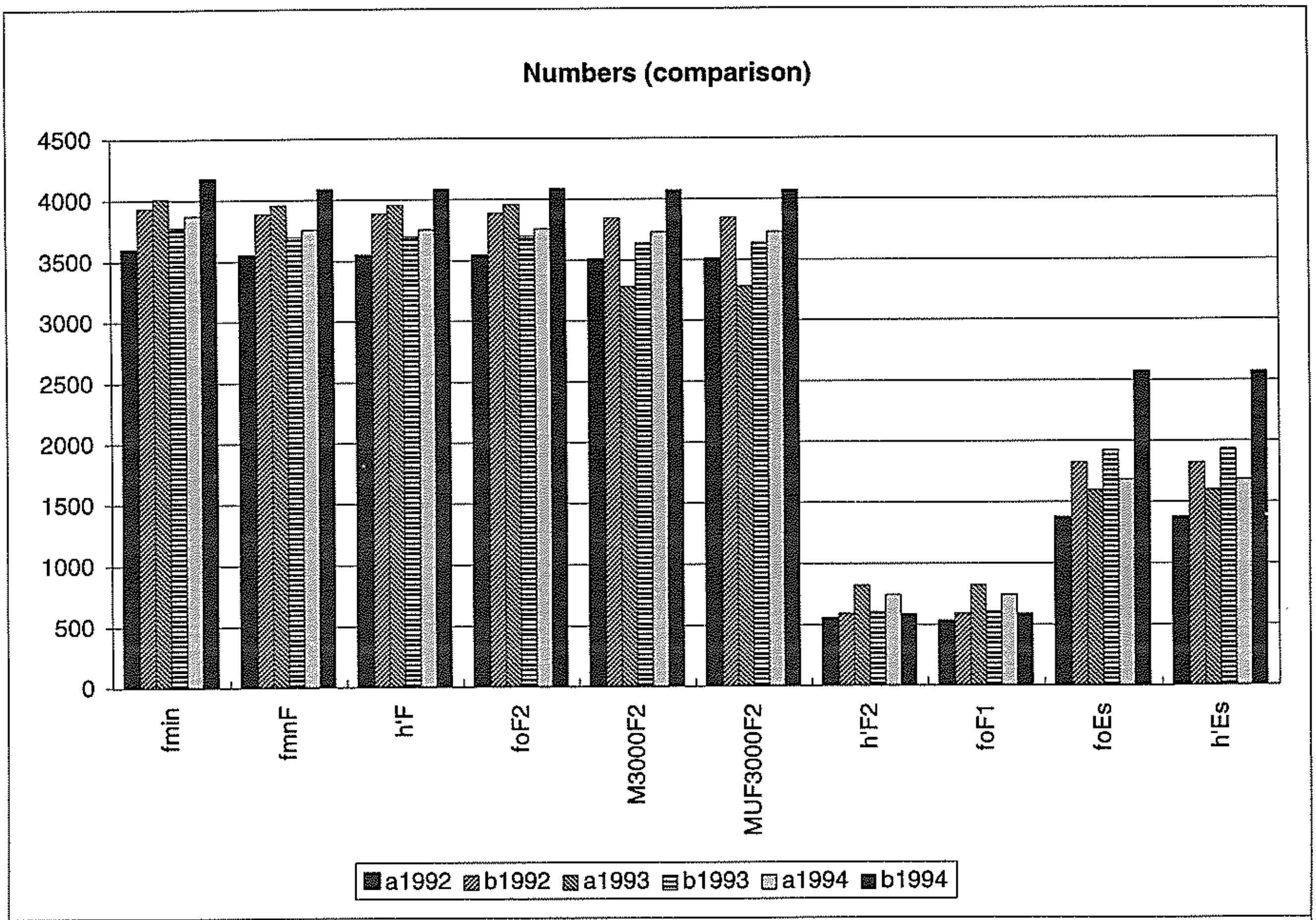

Numbers (comparison)

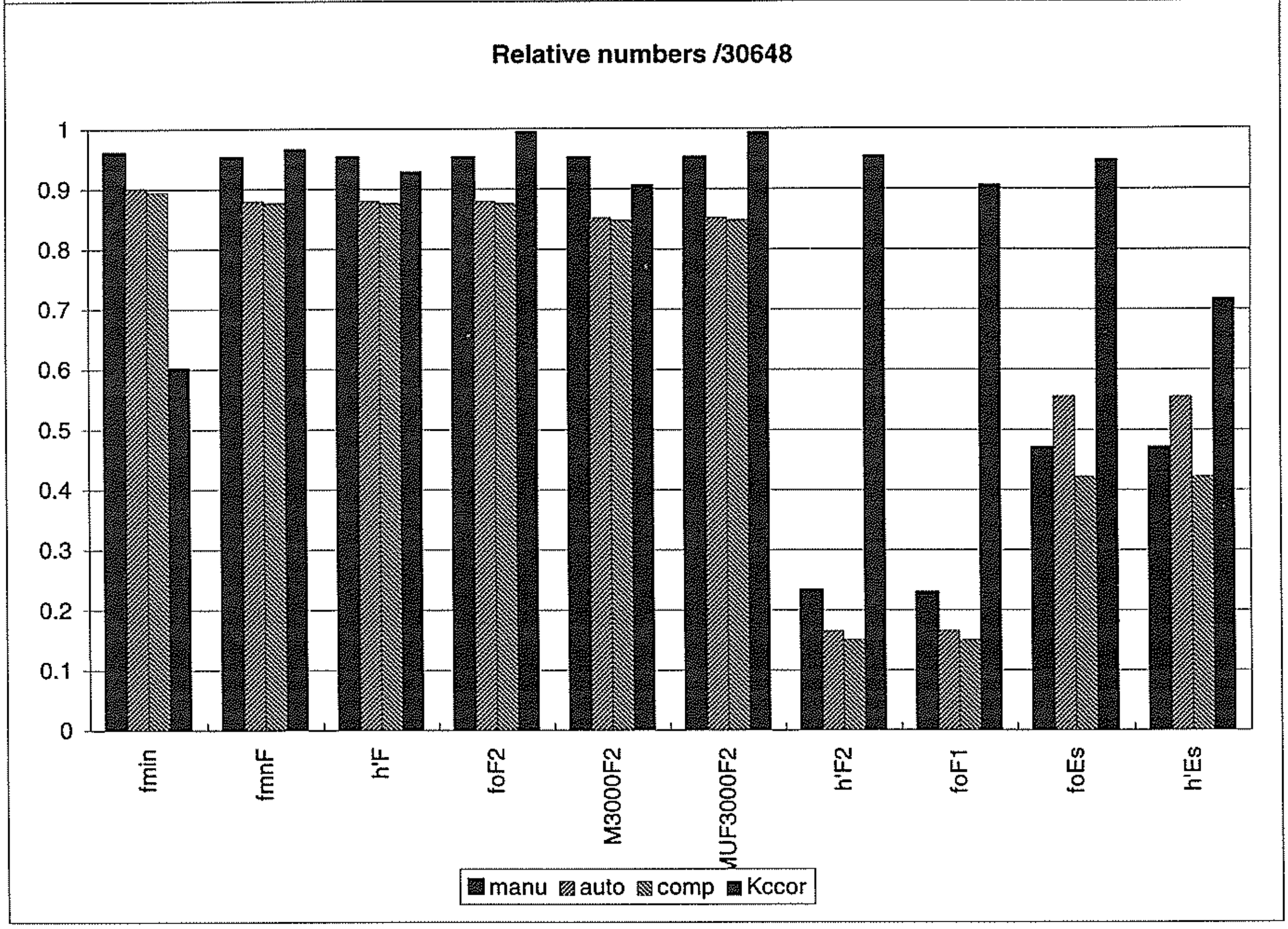

Relative numbers /30648

Fig.4 Numbers of comparisons (top) and relative numbers for all the data (bottom)

Power failure, ionospheric situation, breakdown or loss of data reduce the number of data especially for the 1st half-year of the year 1992. The main features are reviewed hereafter for some of the parameters.

3.1 foF2 : (fig.1a)

The top graph shows the relative numbers of simultaneous (rnberc), automatic (rnbera) and manual (rnberm) determinations. During the first half of 1992 there were some automatic data losses. Let us point out that the old version of ARTIST needs a 2 MHz range (20 points) to work and that noise could suppress the trace for several successive frequencies so that some automatic determinations are missing.

The middle graph displays the Kendall coefficient, **w**, for the automatic versus manual ratio and is excellent (over 0.99).

The bottom graph reveals that the differences (in MHz) of the values (manual minus automatic) are small. These differences are ranked in 9 classes for each half-year. Almost 50% of them are within ±0.05 MHz. The accumulative sum of percentages for the classes have a half-year label (a94(97%) means that 97% of all the differences for this half-year, for 1994, fell within ±0.45).

3.2 M3000 : (fig.1b)

The same type of graphs are displayed with a change of the left scale (from 0 to 1). Note the slightly higher values of the dispersion of the differences (in units) which still lies within ±0.45.

3.3 fminF : (fig.2a)

The results are very good, with the appearance of a more asymetrical dispersion. This could be due to the fact that ARTIST may sometimes use the double Es echoes.

3.4 hpF2 : (fig.2b)

This is an example of virtual height data. There is a low dispersion of the differences but the routine resolution is 5 km for one bin.

3.5 All parameters analysed : (fig 3a,3b,4a and 4b)

The first three figures (Figs. 3a, 3b, and 4a) are plotted for the years 1992, 1993 and 1994. The last figure (Fig. 4b) also includes the first half of the year of 1995. One sees some seasonal behavior although it is less prononced for manual data.

4. CONCLUSIONS

(i) For foF2, foF1, foEs, h'F, h'F2, fminF, M3000F and MUf3000F there is no statistical difference between manual and automatic ARTIST scaling for the Dourbes data. The Kcc is over 0.99 for foF2 and MUf3000F during the 7 half-years analysed. This also means profile determination in the F region starts on good basis.

(ii) For fmin and h'Es one must be circumspect. The contribution of fminE in fmin is not the same for automatic and manual determination. Noise may confuse the determination of h'Es.

(iii) For the analysis of special ionospheric situations, it is always worthwhile to look at the ionograms.

(iv) More time should be devoted to employ other statistical procedures to compare the data, but when looking at the details one may raise the question: is the machine or the human be right?

Acknowledgement

The author would like to thank Dr. F. Demeyer for discussions on statistics and for running the statistical software with the data.

References

[1] Reinisch, B. W. and Huang X. (1983), 'Automatic calculation of electron density profiles from digital ionograms. 3. Processing of bottomside ionograms', Radio Sci.,18,3,477.

[2] Siegel S., (1956), Nonparametric statistics for the behavioral sciences,McGraw-Hill, Int. Student Edition.

Autoscale Software For Computerised Processing Of Digital Ionograms

Yogesh Tripathi
IPS Radio and Space Services
P. O. Box 5606, West Chatswood, NSW 2057, Australia
Phone: +61 2 9414 8382, Fax: +61 2 94148340, e.mail: yogesh@ips.gov.au

ABSTRACT

Computerised processing of digital ionograms has become an area of growing interest in recent years. The Autoscale software, developed at IPS Radio and Space Services, has been designed to clean and scale vertical incidence mid-latitude ionograms. In the present paper, techniques used in the modified version of the IPS Autoscale software have been discussed.

1.0 INTRODUCTION

An important function of IPS Radio and Space Services is the continuous monitoring of the ionosphere. The main aim is to obtain the best working description of the ionospheric conditions, thereby providing superior services to the HF community.

The data obtained from a sounding are viewed in the form of a virtual height versus frequency plot called an ionogram. An ionogram is then scaled to get various parameters of the ionosphere and radio wave propagation. In the past, the ionogram signals were recorded on photographic films and the interpretation of the critical ionospheric parameters was performed by manual scalers.

In recent years, the increased need for more timely access to sounding stations has posed a serious problem which has added to that of training manual scalers. These problems call for the development of a computerised ionogram scaling software. However, the implementation of such a system is not trivial because of the variable nature of the physical properties of the ionosphere, mainly due to disturbances of internal and external origin.

In the present paper, a basic philosophy of the new version of the Autoscale software is presented. Although, the system has been primarily designed to clean and scale the ionograms produced by the IPS 5A series ionosondes , it has been used to scale ionograms produced by other ionosondes such as DPS (Digisonde Portable Sounder), Digisonde, and AIS (Advanced Ionospheric Sounder). The 5A ionograms have usually been 'mid-latitude' ionograms with a 40 kHz frequency interval and 1.2 km height resolution in the ionogram image.

2.0 AUTOSCALE SOFTWARE

The Autoscale software is designed to scale typical mid-latitude ordinary (O) wave and extraordinary (X) wave ionograms. At IPS the separation is done using a hardware phase shift network placed on the antenna signals. The software has also been designed to cope with minor leakage between the two ionograms.

The software is based on a simple general approach of trace recognition and curve fitting. The procedures used in the system are very close to those adopted in manual scaling. The software has five main steps:

(1) Ionogram Cleaning
(2) Slice Formation
(3) Pseudo-Trace Formation and Extrapolation
(4)Trace Identification, and
(5) Ionogram Scaling.

These steps are discussed in the following sections.

2.1 Ionogram Cleaning

Cleaning is the first stage of the software. Raw ionogram data contain ionospheric returns accompanied by noise and interfering signals that should be filtered out. Therefore a suitable cleaning method is required to remove the unwanted noise and interference from the raw ionogram data.

The task is carried out in two parts. First, an amplitude threshold is determined to enable some distinction to be made between signal and noise. The question is: what, in the context of this ionogram, is an amplitude threshold below which an echo is considered to be noise? Second, cleaning involves a step that is performed reasonably easily by the human eye - i.e. identifying which channels suffer from interference.

The previous algorithm employed by the autoscaling system[1] was based on the assumption that a pixel at a particular frequency containing a real signal, i.e. not noise or interference, has an amplitude that is significantly greater than the average amplitude for all the pixels of that channel. Such pixels, that exceed the amplitude threshold are called "occupied".

A feature of using a comparison with the average amplitude is that some assumption on the overall distribution of amplitudes needs to be made, so some degree of normality is assumed, and we require that ionospheric trace echoes have amplitudes that distinguish them from the background noise level. The most appropriate amplitude threshold in any channel for the 5A has been determined as 2.0 times the average channel amplitude.

The assumption of constancy of the noise in a channel as employed in the previous method, does not hold good in a significant number of cases. For instance, sometimes the noise is very spiky which gives much too low a value for the threshold, while in the case of flat (weak amplitude) noise, the threshold value comes out to be too high. Thus, the observations of a variety of amplitude distributions imply that no formula approach would be able to cope with all of these cases.

In the new cleaning method, the maximum noise level is set to the top of the three pulses that are of roughly the same height and are 'close' together. It is assumed that the noise amplitudes are fairly uniform, while signal amplitudes are much more varied. Thus the highest three pulses of roughly the same height are assumed to be the top of the noise. For each sounded frequency in an ionogram, the highest amplitude primary pulses can be detected by looking into a sorted list of the amplitude vs virtual height data. Then, in the unsorted list of amplitudes, the greater of the two values of lower amplitude on either side of the primary maximum amplitude is considered to be a secondary maxima.

An assumption about the constancy of noise is necessary for any cleaning method. In the case of a single layer, signal pulses are obviously varied since the primary echo is stronger than the multiples. In fact, for the method to fail completely, by treating all the returns as noise, there would have to be three primary pulses of different origin (e.g. O trace, X trace, F trace, Sporadic E (Es) trace), all of roughly the same amplitude. This is unlikely, especially near critical frequencies.

Three pulses are defined as being 'close' together in amplitude (and thus noise) if the secondary maximum of each pulse is less than the smallest of the three pulse amplitudes, allowing for some variation. The allowable variation is the noise variation truncated to between 2 and 10 amplitude units, plus .05th of the difference between the maximum amplitude in the channel and the smallest value of the amplitudes of the three pulses are significantly lower than the largest pulses, i.e., if one large pulse has already been found then three smaller pulses are more likely to be noise. An example of three 'close' pulses, which are called noise, is shown in Figure 1.

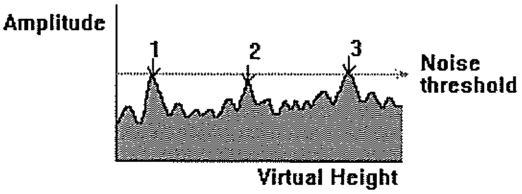

Figure 1: The noise threshold is set at the top of three 'close' pulses (labeled 1, 2, and 3) which have roughly the same amplitude.

The lower limit on the noise is the median channel amplitude plus the average of the amplitude variation below the median. This limit is necessary for determining the extent of a pulse. The average amplitude variation below the median is used as an estimate of the noise variation. That is, only points below the median are used, to avoid any influence of the large signal amplitudes. For a signal pulse to be detected, the noise threshold level must be less than the secondary maximum of the signal pulse, as shown in Figure 2. The second highest amplitude in a pulse is of significance since amplitude values below the noise threshold are rejected.

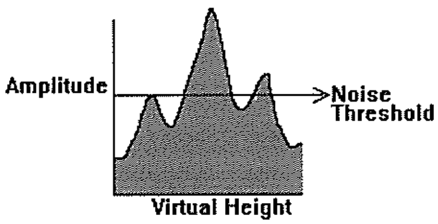

Figure 2: The secondary maximum of a signal pulse should be above the noise threshold.

Once three noise pulses have been found in a channel, the noise threshold can be determined using the following procedure. If the three noise pulses are the highest pulses, then there is no signal (and the threshold is the maximum channel amplitude). If there are no amplitudes more than half the noise variation above the three noise pulses, then it is again considered that there is no signal present. If there are pulses higher than the three noise pulses, the noise threshold is set to the lowest amplitude that excludes any smaller pulses that may have higher secondary maximum. This threshold is the lowest possible amplitude that excludes all noise.

Final checks on signal pulses are performed to filter out the flat, broad, smooth pulses and pulses having a slow rise time.

2.2 Slice Formation

After an ionogram is cleaned, it is reduced to its 'skeleton' by forming 'slices'. Slices are formed by grouping consecutive echo samples (represented by pixels in the ionogram) for all heights at each frequency, as shown in Figure 3. When a gap of at least one height step occurs, a new slice is started. A slice is thus defined to have top and bottom pixels and also a pixel corresponding to maximum amplitude. Ideally each trace on the ionogram would give one slice at each frequency. However, particularly with spread F, there can be a gap of two or more pixels in the trace. This gives more than one slice for the same trace and frequency, which will have to be merged in a later step.

At the end of this step, the ionogram has been reduced to its 'skeleton', since instead of several pixels representing a trace at each frequency, there is now just a single slice.

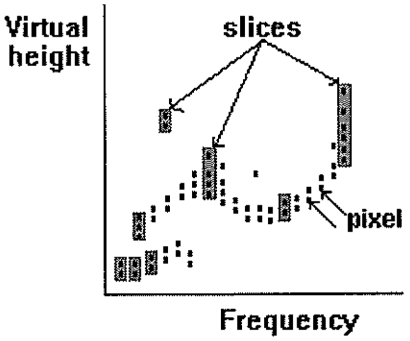

Figure 3: Forming slices of echoes.

2.3 Pseudo-Trace Formation and Extrapolation

The skeleton of slices is further analysed to form traces by examining slices intersecting a particular height range, starting at the lowest frequency and height. The first unexamined slice becomes the start of a new pseudo-trace. A range of allowed heights is determined from this slice, and the next channel is examined for any slices that intersect this range of heights, subject to certain rules. Gaps of one frequency channel are allowed when connecting slices to form a pseudo-trace. After the first slice, subsequent slices determine the gradient of the trace. This is used to extrapolate the expected height range and so improve trace following where the trace is steep. Very small traces are removed from the ionogram.

The process of forming pseudo-traces has been described in the previous section. It has the sole purpose of organising the occupied pixels into a sensible order; in particular; the order in which the pixels in a trace would be read by a manual scaler while following a trace by eye.

However, simply joining the pixels does not necessarily form sensible ionospheric traces (such as the case of continuous data across a cusp). For example, there may be a jump between adjacent pixels in the pseudo trace which is not considered physically reasonable for a real ionospheric trace.

The extrapolation follows pseudo-traces with gaps wider than a single channel. Each pseudo-trace is linearly extrapolated forward and backward. For the linear extrapolation, a regression line is fitted for slices calculated from 0.31/(channel width) or 3 slices, whichever gives the most slices. If the extrapolated line intersects a slice belonging to another pseudo-trace, the two pseudo-traces are joined. If the slice does not belong to any sub-trace, it is joined and the extrapolation is repeated.

2.4 Trace Identification

Traces arriving at this stage are assumed to be either real traces or pieces of real traces. One should be cautious while extrapolating traces because pseudo-traces which have been merged wrongly to form a well defined trace will result in wrong identification and scaling. The two purposes of identifying the traces are: to name the traces and to describe their nature. Trace identification is performed by comparing the locations of traces in an ionogram with those of E, Es and F traces appearing in a typical day-time or night-time ionogram. The extraordinary component of the F trace is then sought and, if detected, is removed, whereas the traces appearing to be a part of a single F traces are joined. Thus, it is possible for any number of traces to be identified as any of the E, Es, and F primary traces or joined E & F or E & Es. A single F trace is identified at this stage and F1 and/or F2 traces are identified at a later stage.

The tentative identification described above is further consolidated as listed below:

- If multiple F traces are present, then each combination of their pairs is checked for being O or X traces. If two traces have corresponding heights for at least 90% of their length or the "split" from the fitted lines at their ends is less than 1.5 MHz and greater than 0.2 MHz, then the higher frequency trace is an X-trace. If an X-trace is found, it is removed from the count of F-traces and not processed further. Autoscale uses only the O component of the trace for scaling.
- If there is still more than one F trace, pairs are re-checked for being part of the same trace, since there might be a possibility that a single F trace has gaps in it and therefore its parts have been identified as F-layer traces. Therefore these F trace types are tested for the possibility of joining. In a daytime ionogram, traces separated by a gap in frequency caused by attenuation are detected and joined. A gap caused by attenuation is one in which the gap width is less than 0.5 MHz; the number of slices in each trace on either side of the gap is greater than 3 and the total in both is greater than 10; and the height at which an echo of minimum amplitude ('minrow') occurs for the first trace is less than 'minrow' for the second trace. F-traces separated by interference gaps are also detected and joined, provided the gap is less than half the total number of channels, the slope increases with frequency and that the heights correspond.
- All non-primary traces are checked for being multiples of a primary trace and the order of the multiple trace is also determined. Examples of 'multiple' identification are shown in Figures 4 and 5, where the multiples of the Es layer (and F layer) have been identified and removed.
- If there is an Es layer, then any remaining unidentified traces are identified. These are not primary traces, but they may be first order echoes from the F layer observed through non-blanketing Es.

- In each trace, a search for possible cusps is performed by fitting a series of lines. To find a cusp in a trace, several tests for the downturn in the slopes of each fitted line are performed.

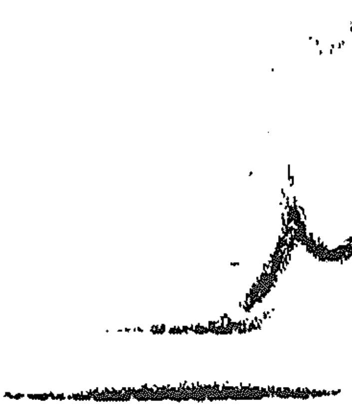

Figure 4a

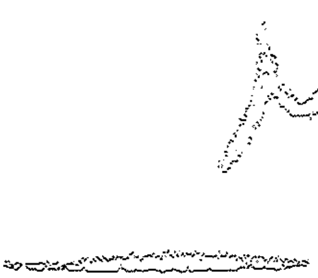

Figure 4b

Figures 4a and 4b: A cleaned night-time ionogram ready for scaling as shown in Figure 4a. Figure 4b shows the skeleton of the ionogram after the ionogram has been processed through the Autoscale software. The multiples of the F and Es traces, as shown in Figure 4a, have been identified and removed in Figure 4b. Note that only the top and bottom echoes, and echoes of the maximum amplitude are shown in Figure 4b.

During the tentative identification of the primary traces, a trace may be identified as both E and Es, or E and F traces. This happens because the traces are sometimes joined. Therefore it is necessary to sort and distinguish the E and Es traces. A brief description of the sorting procedure is given in the following paragraph.

In a trace which is either E or Es, or joined E and Es, a search is performed for a slight cusp. If an F trace is also present in the ionogram, the value of the critical frequency of the E trace (foE) is the frequency where F race starts. In other cases the last frequency of the trace is considered to be foE. It is assumed that there is only Es trace in the night time ionogram. A trace in the day time ionogram which begins after the starting frequency of the F trace or is without cusp (i.e. flat trace) and either is very thin or has a negative slope, is identified as an Es trace. If the trace has its last frequency above the minimum frequency of the F trace or has its end close to it and is not very steep, it may be identified as an Es trace possibly with E trace. The presence of E trace is confirmed by the presence of a cusp in the trace.

A trace having steep slope increasing with height, is identified as E. Presence of more than one cusp implies a mix of E and Es layers. The highest cusp is taken as foE in this case.

If none of the above conditions are satisfied in a day time ionogram, the start frequency of the trace is less than the start frequency of the F trace, the trace is not steep and has no cusp, such a trace is then identified as an E trace.

If an E trace is found in the ionogram, a search for its first multiple is performed. If the start frequency of the multiple is significantly more than the start frequency of the primary E trace, then the trace is probably joined E and Es traces with Es multiple(s). In this case the value of foE is scaled from the minimum frequency of the first multiple.

2.5 Ionogram Scaling

In the final stage of scaling, the scaled parameters are estimated in a particular order. Special tests are carried out for spread F traces. Except for spread F, all traces are scaled from the bottom edge. Spread F is scaled from the 'true heights' of slices, which are calculated by subtracting the average width of the non spread slices from the top of each spread slice[2]. Slices of more than 30 km height width are considered to be spread slices in the current version of Autoscale. Descriptive letter 'F' is used with critical frequencies measured from the spread F traces.

Figure 5a

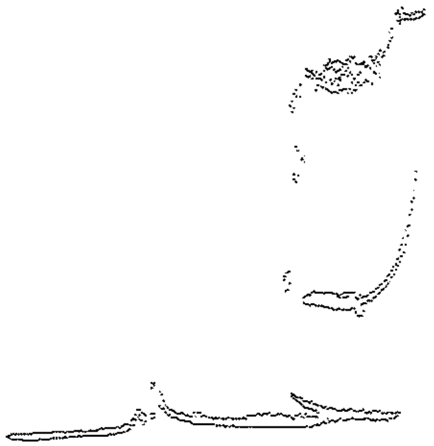

Figure 5b

Figures 5a and 5b: A cleaned daytime ionogram ready for scaling is shown in Figure 5a. The multiples of the Es-trace, as shown in Figure 5a, have been identified and removed in Figure 5b. Note that only the top and bottom echoes, and echoes of the maximum amplitude have been shown in Figure 5b.

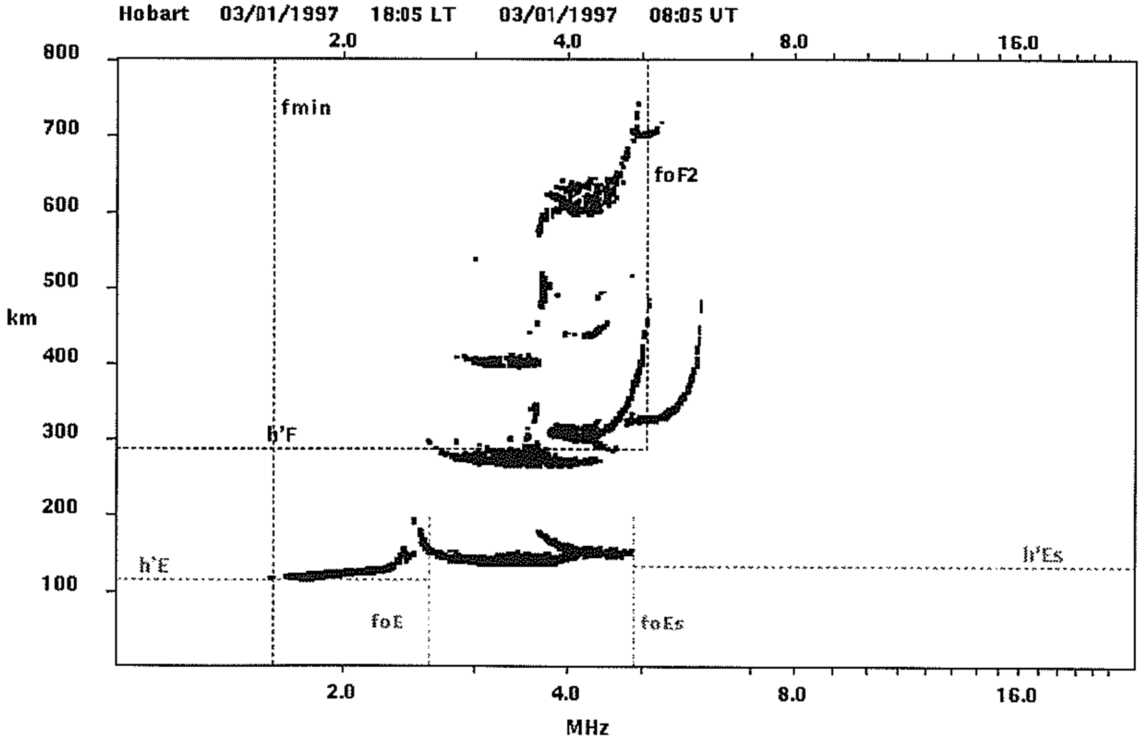

Figure 6: The same ionogram as in Figure 5a after scaling by the Autoscale software. The scaled critical frequencies and heights are shown.

To measure frequency-height pairs for a trace, a median filter (running average) of width 5 is applied. The median filter is faster than fitting a spline, which was originally used, and has better performance with isolated noise 'bumps' on the trace. The appropriate qualifying and descriptive letters are added following URSI conventions[2]. The parameters currently scaled are fmin, foF1, foF2, foE, foEs, h'F, h'F2, h'E, h'Es, foI, fbEs and MUF(3000). The values of foE, foF1 and foF2 are computed through a real height analysis[3].

The scaled ionogram of Figure 5a is shown in Figure 6. It is clear that the Autoscale software has been able to detect the O component trace and scale the critical frequency of the F2 layer. The height of the O component F2 trace is slightly underscaled because of the overlap of the multiple of the X component of the Es trace on the O component F2 trace which could not be completely filtered out. The value of foE is scaled from the first multiple of the O-component of the Es trace, while foEs is slightly overscaled due to either failure to filter out the X component of Es trace or lack of proper extrapolation of the O component of the Es trace.

3.0 COMPARISON WITH MANUAL SCALER

Recently, a comparison between the ionospheric characteristics scaled by a manual scalar and Autoscale software was performed[4]. The two most important ionospheric parameters, namely, foF2 and M(3000)F2, were chosen for statistical investigation and the effect of the presence of spread F on scaling errors were also investigated. Ionograms of the winter months May and June, 1995, from the Digisonde at Learmonth, Western Australia, were chosen for the comparison study. These ionograms have 100 kHz frequency and 5 Km height steps, and have separated O and X traces

For comparison, each ionogram was scaled manually using standard URSI[2] procedure. The distribution of the differences (Manual - Autoscale) for foF2 and M(3000)F2 was calculated and the effect on scaled values due to the presence of spread F has also been investigated. Limits of acceptability were adopted as 0.5 MHz for foF2 and ±0.40 for M(3000)F2, roughly in line with the URSI limits of ±5Δ (Δ is the reading accuracy) or ±20%, whichever is greater. An accurate value is considered to lie within ±0.05 of the true value for M(3000)F2 and ±0.1 MHz for foF2.

Table 1

foF2 *[Manual - Autoscale]*	May		June	
	% of ionograms with foF2 within ±0.2 MHz	% of ionograms with foF2 within ±0.5 MHz	% of ionograms with foF2 within ±0.2 MHz	% of ionograms with foF2 within ±0.5 MHz
All ionograms	63.5	96.4	54.2	92.2
Ionograms without spread F	66.1	96.4	67.4	94.0
Ionograms with spread F	55.3	96.4.	27.9	88.9

Table 2

M(3000)F2 *[Manual - Autoscale]*	May		June	
	% of ionograms with M(3000)F2 within ±0.1	% of ionograms with M(3000)F2 within ±0.4	% of ionograms with M(3000)F2 within ±0.1	% of ionograms with M(3000)F2 within ±0.4
All ionograms	41.9	92.5	45.9	91.7
Ionograms without spread F	49.0	96.3	54.6	93.3
Ionograms with spread F	19.4	80.6	28.2	88.5

Some of the results of this investigation are summarized in Tables 1 and 2. The distribution of differences for foF2 and M(3000)F2 values indicate that, within the limits of acceptability, Autoscale is capable of scaling M(3000)F2 and foF2 characteristics quite close to manual scalers. The presence of spread F affects the values scaled by Autoscale. The potential cause of the difference in the scaled parameters are: (i) the 100 kHz frequency steps of the Digisonde ionograms did not favor Autoscale which is trained for frequency steps 40 kHz, and (ii) the Autoscale cleaning method was basically designed to clean ionograms produced by IPS 5a series ionosondes.

4.0 CONCLUSION

The IPS automatic scaling system, Autoscale, in its current form is a reliable method for scaling simple mid-latitude ionograms. In addition, a number of more complex ionograms have been successfully scaled. The existing ionograms should form a reliable base for future work in automatic scaling and real time ionospheric analysis. Critical parameters and layer identifications are expected to be correct in a large majority of cases.

Incorrect estimates will arise for complex or noisy ionograms, or cases where the estimates of foE or foF1 are inappropriate. These are regarded as limitations of the existing system.

Further comparison study based on other ionospheric characteristics and the effect of other known conditions that compromise scaling, besides spread F (e.g. sporadic E multiples) need closer investigation. The results presented in Section 3.0 are likely to be typical of winter, but summer is different because of the greater influence of sporadic E on scaling. A full analysis of scaling errors will be undertaken in due course. This will involve not only the magnitude of the derived critical parameters, but tests on the correctness of trace identifications and of the detection of other ionospheric conditions.

5.0 REFERENCES

[1] M. W. Fox and Craig Blundell, Automatic scaling using digital ionograms, Radio Science, 24(6), 747 (1987).

[2] W. R. Piggot and K. Rawer, Report UAG-23A, World Data Center A for S. T. P., 1978.

[3] J. R. Titheridge, Report UAG-93, World Data Center A for S. T. P., 1985.

[4] Yogesh Tripathi and Miro Dubovinsky, Comparison of ionospheric characteristics using Autoscale software, Presented in '1996 Western Pacific Geophysics Meeting", Brisbane, 23-27 July, 1996.

Acknowledgments: I thank Dr Phil Wilkinson and Dr John Caruana for valuable suggestions, and Dr David Cole for continuous support and encouragement during the Autoscale software project. Referees' suggestions are gratefully acknowledged.

ARTIFICIAL NEURAL NETWORKS FOR COMPUTER-AIDED IONOGRAM ANALYSIS

V.P.Grozov and V.E.Nosov, Institute of Solar-Terristrial Physics,P.O.Box 4026, Irkutsk,33, 664033, Russia e-mail: rp@istp.irk.ru

G.A.Ososkov, Joint Institute for Nuclear Research, Dubna, Moskow region, 141980,Russia, e-mail: : ososkov@cv.jinr.dubna.su

E.G.Zaznobina, Ivanovo State University, Ermaka St. 37/7, Ivanovo 153377, Russia. e-mail: root@ivgu.ivanovo.su

ABSTRACT.

Ionospheric radio channel diagnosis is based on the analysis of vertical-incidence, oblique-incidence and backscatter sounding ionograms. Hopfield artificial neural network (ANN) complemented by Mean Field Theory (MFT) was proposed for processing ionograms. Because of the complicated character of ionospheric traces with their specific and heavy background, a modified rotor model of ANN was used. An initial configuration ANN was successfully constructed by applying an angular histogram in the area with the size determined by the average local trace curvature. This results in a fast convergence of the network evolution. The model was tested on ionograms obtained on the chirp-ionosonde (ISTP, Irkutsk, 1987-1996). Results show the efficiency of our approach for solving the problem of ionogram processing.

1. INTRODUCTION.

Ionospheric radio channel diagnosis is important for both fundamental ionospheric research and radio wave propagation as well as for a wide range of applied problems. The latter problems cannot be successfully solved without automatically controlled data processing and an interpretation system for information about the radio channel conditions. By analogy with high energy physics patterns, ionogram data can be considered as traces of a complicated structure with a considerable background. There are two basic problems encountered in processing: (i) to recognize traces with a minimum of computer time without using additional information (angles of arrival, polarization characteristics, etc.); and (ii) to approximate traces according to characteristic points (CP) of the amplitude pattern. Nonlinearity, discreteness, and other complications of this problem were the reason for the application of the artificial neural networks (ANN) methods for its solution. The ANN approach has been used to solve many difficult optimization and recognition problems in recent years *[Hopfield,1985; Ososkov,1995]*. It was also successfully applied in high-energy physics for automatic tracing of charged particles *[Denby,1988; Peterson,1990; Glasov et al,1992]*. A similarity of tracing problems in both fields: high energy physics and ionogram processing allowed for the first time the ANN technique to be applied to trace recognition on vertical-incidence sounding ionograms [*Zaznobina, 1993]*.

The ionograms received on chirp-ionosonde [Brynko, 1988] have a complicated structure formed by various sounding modes, including various kinds of reflections from regular and irregular ionospheric layers and from the terrestrial surface. A complicating factor is the absence of additional information (angles of arrival, polarization characteristics, etc.). Human intervention makes it possible to analyze ionograms, i.e. to identify all traces and to coordinate them with corresponding propagation modes. However a computer implementation of the human perception and recognition skills with visual information is not yet sufficiently reliable feasible. Therefore in this work an attempt is made to develop an algorithm for a functional modelling of this process.

2. ARTIFICIAL NEURAL NETWORKS.

In quite general terms, the ANN is a structure of computing elements, which are referred to as neurons by an analogy with the human brain due to their identical features of close mutual interconnections and interdependence [*Rosenblat,1962; Hopfield,1982*]. The ANN method is advantageous and fast in solving a wide range of problems of a serious combinatorial complexity. This is explained by an ability of the neural network to evolve to some equilibrium states corresponding either to certain patterns (in recognition problems) or to optimal values (the optimization problem). In terms of a formal mathematical description, ANN equilibrium states correspond to minima of the so-called network energy function.

The Hopfield ANNs are chosen to solve our problem because of their capacity to find the optimum decision without preliminary training as feed-forward networks (multilayer perceptrons). The Hopfield ANN (HNN) is a feed-back network with full-connected neurons. The response of such networks to outer input information is dynamic: neuron outputs being transmitted via feedbacks are then modified by inputs; then the output is iteratively calculated and whole process is repeated in the HNN evolution. A steady network evolution results in the convergence to one of network equilibrium states.

As was shown [*Hopfield, 1982*], such an HNN convergence means that the HNN energy function reaches one of its local minima. However, in the case of trace recognition, one needs to find a global minimum of the HNN energy function, since a local minimum corresponds to an erroneous solution when a trace is incorrectly identified as a combination of pieces of other traces. Therefore, it is necessary to use methods which would force a network to avoid local minima. In two HNN models where neurons were defined as segments *(Denby, 1988; Peterson, 1986)* or rotors *(Peterson, 1990)* , it was realized on the basis of the Mean Field Theory (MFT) and the simulated annealing scheme. Peterson's rotor model was then considerably modified to improve the HNN robustness for recognizing circular traces in high energy physics (see Fig.1) [*Glasov, 1992*].

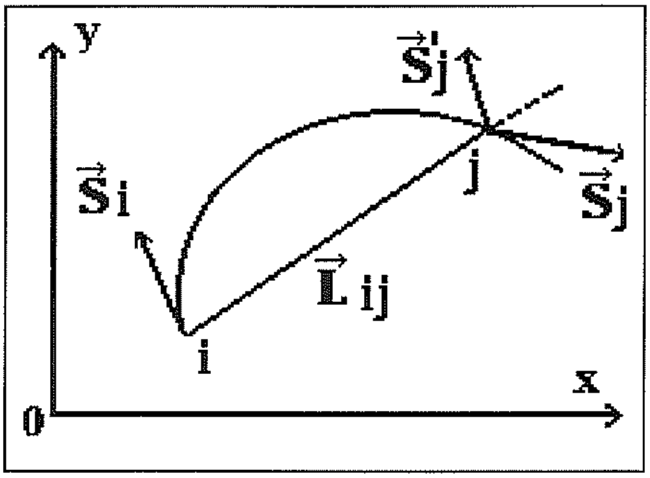

Fig. 1. HNN modified rotor model .

However, none of these methods could be applied directly to process ionogram measurements. The analysis of their 2D-images (Fig.2a to 5a) clearly demonstrate that it is impossible to approximate ionospheric traces having a specific alternative curvature either by a straight line or by a circle. However, a local circular approximation, when a trace is approximated piecewise by arches of different length and curvature, looks quite adequate. Besides this, due to indications of too high noise sensitivity of segment and rotor HNN models *[Kisel,1993]* they are inapplicable for ionograms characterized by a considerable background.

Therefore it was reasonable to choose the circle-oriented, robust modified rotor HNN model and to develop this version with a local circular approximation for processing vertical-incidence ionograms *(Zaznobina, 1993).* In this work we extend the approach to processing oblique-incidence and backscatter sounding ionograms. It should be noted that the approach proposed in this paper makes it possible to solve a more general problem of identifying ionogram traces. No additional information (such as polarization signal characteristics , etc.) is required, and the approach is suitable for ionograms of any type.

Recently, on simplifying conditions that polarization signal characteristics are known, the ANN technique *(Zaznobina, 1993)* was used for other ionogram types [*Galkin, 1996*].

3. TRACE IDENTIFYING ALGORITHM

Experience of HNN applications in high energy physics *(Denby1988, Ososkov, 1992)* showed some difficulties specific to that type of network with fully connected neurons: (i) "a dimensionality damnation", i.e. allowing gross increases in the HNN degrees of freedom caused the appearance of extra neurons. (ii) too long HNN evolution before attaining the global minimum of the HNN energy function. So, two important preliminary procedures are needed to overcome these difficulties. The first is a raw data compression. The second is the HNN initialization in such a way that an initial configuration of HNN rotors should lie in close vicinity to the energy function global minimum.

Hence the trace recognition algorithm can be carried out in three main stages*[Zaznobina, 1993]:*

(1) preliminary data compression,
(2) determination of the initial configuration of neurons close to the global minimum of the HNN energy function,
(3) HNN trace identification.

Data compression is accomplished by a sequential selection of frequencies, reconstructing missing points, eliminating background points and extracting points with the maximum amplitude. In cases of traces intersecting each other (Fig.3a) or strong diffusion (Fig.5a,6a) it is a difficult procedure. However, it can be efficiently realized by an algorithm based on a special cellular automaton *[see, for example, Kisel, 1993],* which results in reducing the amount of data by a factor of 5 to 10.

After that, data are already suitable for analysing them by HNN. For a modified rotor HNN model every neuron is represented as a rotor [Fig. 1], i.e. a vector, whose dynamic parameters are coordinates, modulus and angle. HNN evolution rules must direct this so that all neurons related to a trace will align themselves tangentially to a circle approximating locally a given part of this trace. Their moduli will grow, although moduli of all neurons that lie apart from the given trace will effectively diminish.

Let two points **i** and **j** lie on a local approximating circle (see fig.1). Using the field terminology we introduce the quantity $\mathbf{h}_{ij}$ as the field produced at the point **i** by neuron $\mathbf{s}_j$ as given below

$$\mathbf{h}ij = Tij\ sj \qquad (1)$$

Then the total field $\mathbf{H}_j$ at point **i** will be defined as the vector sum of fields from all neurons:

$$\mathrm{H}_i = \sum_j \mathrm{h}_{ij} = \sum_j T_{ij} \mathrm{s}_j \qquad (2)$$

Keeping in mind the locality concept we can assume that rotors $\mathbf{s}_i$ of a given local part of the trace must be oriented as close as possible to the direction of the field vector $\mathbf{H}_i$.

The scalar product of these two vectors can be taken as a suitable measure of the closeness. It gives the following expression for the energy function of the neuron system:

$$E = -\tfrac{1}{2}\sum_i \mathrm{H}_i \mathrm{s}_i = -\tfrac{1}{2}\sum_{i,j} \mathrm{s}_i \mathrm{T}_{ij} \mathrm{s}_j \qquad (3)$$

With an appropriate choice of the weight function, its global minimum corresponds to an optimum rotor configuration in the neural network equilibrium state, when all rotors with large absolute values are originated from points of corresponding traces and are oriented along those traces.

To realize the locality concept determining the weight function we introduce a sliding window with a size limited by the demand that within it a local circle approximation of any trace is satisfactorily accurate. We determine the weight function from the following geometrical considerations: if two points **i** and **j** inside the chosen window belong to the same local circle, then the vector $\mathbf{S}_j'$ [Fig.1] obtained as the mirror reflection of the vector $\mathbf{S}_j$ with respect to the chord $\mathbf{L}_{ij}$ should coincide with the vector $\mathbf{S}_i$. Therefore, the weight function may be written as *[Zaznobina, 1993],*

$$\mathrm{T}_{ij} = |s_i|\ |s_j| * \delta_{ij}\, Cos(\Theta), \quad \text{where} \quad \delta_{ij} = \begin{cases} 1, & |L_{ij}| \langle\ \boldsymbol{R_c} \\ 0, & |L_{ij}| \rangle\ \boldsymbol{R_c} \end{cases}. \qquad (4)$$

Here Θ is the angle between vectors $\mathbf{S}_i$ and $\mathbf{S}_j'$, and R_c is equal to the diagonal of the sliding window.

Now, according to the stages listed above, we determine the HNN initialization procedure. To obtain an initial rotor configuration sufficiently close to the global minimum of the energy function we use the angular histogram method recommended in [*Baginyan, 1994*], but restrict the number of neurons histogrammed to the square inside the sliding window. That speeds up and simplifies the HNN initialization. The initialization algorithm is as follows. Each preprocessed point is placed in the middle of the left edge of the sliding window, which is then split into 1° angle sectors. Then the number of points falling into each of these angle bins is counted. The center of gravity of three adjacent bins surrounding the peak of this histogram is taken as the initial direction of a rotor looking from this point. Its modulus is calculated as the mean value number of points in these three bins.

At the final stage of the trace identification the network owes converges to the state corresponding to the minimum of the energy function. The MFT is obtained by an iterative procedure. At every step, consecutive calculations of the field at points corresponding to neurons, and a determination of the neuron's state and of the new value of the vector for the next iteration are made. Its modulus is determined from the known formula (see, for example, [*Kisel, 1993*]),

$$|\mathbf{s}_i| = \tanh(|\mathbf{H}_i|/T), \quad \text{where } T = 1.5\,. \tag{5}$$

Its new direction is taken according to the field direction at this point. This new vector is then used to determine all other neurons . On the next iteration these calculations are repeated until the energy function does not vary .

The final trace identification is made by clustering based on the following neighborhood definition: two points are considered to be close (lying on the same trace), if their contribution to the energy function $\mathbf{S}_i \mathbf{T}_{ij} \mathbf{S}_j$ is minimal. The main difficulties at this stage are: (1) formulating of conditions how to end one trace and begin a new one, when traces are close to each other; (2) a rule for joining together left and right halves of two crossing traces. The reliability of ionogram interpretation depends crucially on the correct solution of these two problems since they cause most of the errors.

4. RESULTS OF APPLICATIONS

The neuron network, constructed in such a manner, was used to process vertical-incidence, oblique-incidence and backscatter ionospheric sounding ionograms obtained at the ISTP with a chirp-ionosonde [*Brynko,1988*]. (Figs. 2-5 for three types of ionograms.) Typical ionograms were selected, for different seasons (during 1987-1996), at different times of the day and on different paths (Irkutsk-Magadan, Irkutsk-Alice-Springs, etc.). Totally 196 vertical-incidence, 187 oblique-incidence and 223 backscatter ionograms were chosen. Processing one ionogram took 15-20 seconds on an IBM PC 486(DX2) depending on the type of ionograms.

In the case of vertical-incidence ionogram processing in the absence of spread F and ionospheric traveling disturbances, traces are reconstructed with sufficiently high quality (Fig. 2). The region of the O and X component intersection is described quite well. In the region of critical frequencies, although local points are formed correctly, but the trace is reconstructed with errors (Fig. 2b) (some points are too far for the given trace curvature). An inaccurate description of a trace gives errors in determining critical frequencies ranging up to several tens of kHz. In cases of very noisy ionograms, diffuse signal traces are reconstructed with large errors.

Oblique incidence ionograms of the classical type (Fig. 3) are processed without any errors. For summer time ionograms, when the F1 and F2 modes are superimposed errors in ionogram reconstruction occur. In cases of diffuse (e.g. spread-F) and distorted returns (traveling disturbances), there will be errors in the reconstructed traces. Whenever the 1F2 mode and the diffuse 2F2 mode (Fig.4) are observed, the 1F2 mode is processed correctly in the majority of cases, although the MUF region in this case is described with some errors.

When processing backscatter ionograms in the absence of the superposition of signals from the back direction, the trace reconstruction is mainly correct(Fig. 5). However, when some points on a trace are missing, a "spurious" trace can be formed in this region. Our algorithm does not always work reliably in cases of the superposition of backscattered signals and in the presence of additional reflections from F1.

5. CONCLUSION

Our research shows the efficiency of ANN applications for the interpretation of data from complex ionograms. Evidently, it is possible to improve our results significantly. It can be achieved by improving the frequency resolution (in our case a frequency step is 90 kHz), as well as by imposing certain constraints on the behavior of elementary vectors and by invoking some *a priori* data on the basis of the results of a long term prognosis. Currently our algorithm is being updated according to the remarks made above in order to have at least 80% of ionograms successfully processed.

References

Brynko I.G., Galkin I.A., Grozov V.P. et al., An automatically controlled data gathering and processing system using an FMCW ionosonde. Adv. Space Res., 1988, 8, No.4, pp. 121-124.

Baginyan S., Ososkov G. A. et al., Tracing by a modified rotor model of neural network. Comput. Phys. Commun., No. 79, 1994, 165-178.

Denby B. Comp. Phys.Commun., 49 (1988), 429

Galkin I.A, Reinish B.W., Ososkov G.A.,Zaznobina E.G., Neshyba S.P., Feedback neural network for ARTIST ionogram processing. Radio Science,V.31,N.5,p.1119.,1996.

Glasov A.A.,Kisel I.V., Ososkov G.A. et al., Trace reconsruction in discrete detectors by neural networks. Comm. of the Joint Institute for Nuclear Research. E10-92-352, Dubna, 1992.

Kisel I.V., Nescoromnyi V.N., Ososkov G.A., Neural network applications in experimental physics. , Particles and Nucleu, 1993, Volume 24, N.6,1551-1595 .

Hopfield J.J., Neural networks and physical system with emergent collective computational abilities, Proc. Natl. Acad. Sci. USA, 79(1982),2254-2258

Hopfield J.J. and Tank D.W., *Biological Cybernetics*, 52(1985),141.

Ososkov G.A., Robust tracing by cellular automata and neural network with nonlocal weights, in Applications and Science of Artificial Neural Networks, S.K.Rogers, D.W. Ruck, Editors, Proc. SPIE 2492,(1995), 1180-91.

Peterson C., Nucl.Instr. and Meth.,1986, vol. A279, p.537

Peterson C., Neural networks and high energy physics, LUND preprint LU TP 90-6

Rosenblatt F., Principles of Neurodynamics. Washington, D.C.:Spartan, 1962

Zaznobina E.G., Ososkov G.A., Neural Network Application for Data Analysis of Vertical Ionosphere Locating.Comm. of the Joint Institute for Nuclear Research. P10-93-404, Dubna, 1993.

QUESTIONS OF IONOGRAM PROCESSING

Victor. P. Grozov and V.E. Nosov Institute of Solar-Terrestrial Physics, 664033
Irkutsk 33, P. O. Box 4026, Russia e-mail: rp@istp.irk.ru

ABSTACT.

Statistical techniques are considered for image processing applied to automatic processing of vertical-incidence, oblique-incidence and backscatter sounding ionograms. The results derived from a practical implementation of such an approach are presented.

1. INTRODUCTION

The central theme in ionospheric informatics is to reduce the time required to obtain current information about ionospheric conditions. Prompt data availability has become of crucial importance for the reasons that

(i) it facilitates greatly the organization of geophysical and radio experiments for ionospheric research making the recording of difficult data sets easier,
(ii) it is needed for a great variety of practical purposes, especially the rapid distribution of working frequencies for HF communications and radar.

Operational processing of large data flows are feasible only in the case of automatic ionogram analysis, provided there are different ionospheric sounding regimes.

In general terms, an ionogram is a raster image of the distance-frequency characteristic recorded by an ionosonde [1]. Each pixel (of the ionogram) is determined by three parameters: coordinates (frequency and delay) and brightness (i.e., amplitude) [Figures 1a - 3a]. Thus, the image of interest is represented as a matrix, $\mathbf{A[F_i,D_j]}$, of the size N*M. As a result of processing, it is possible to separate the coupled lines formed by points (determined by some rule) marking signal arrival, i.e., to construct a trace for a particular propagation mode.

Within the framework of such a problem, one may identify the following phases of ionogram processing:

- **correct the image** filter interference pulses; correct amplitude characteristics; noise suppression; etc.;
- **improve the image** improve contrast, separation of areas characterized by the coupling property;
- **determine signal arrival times** corresponding to physically meaningful characteristics of the image;
- **construct traces** and tie them to a particular propagation mode.

These problems are intimately interrelated with the methods for solving them. They are based on the presence of noise, whose properties are associated with the effect of the medium, the nature of the reflection process, the performance of receive-transmit equipment, interfering signals etc. Noise is virtually always present as the ionogram is being formed, so the image can be interpreted as a random process of two variables, i.e., as random fields and consequently image processing can use statistical data methods. There are different methods for image correction and improvement [2-6]. While relying on estimates of distribution laws, these methods permit ionogram processing to be carried out reasonably efficiently and with high accuracy. Proficiency of the method is set by the statistical properties of noise. A noise model includes a statistical description of a set of elements that form the image, as well as the noise-signal interaction.

2. ALGORITHM FOR PROCESSING THE IMAGE.

A standard Rayleigh distribution model is used for the image model, and a multiplicative model is used as an analytic description of the noise-signal interaction. The model makes it possible to use local methods of smoothing that feature high computational efficiency in updating the image. Image valuation is achieved by the analysis of image fragments. The method uses a multiplicate model and assumes that the mean noise value is equal to unity and the variance does not depend on signal changes. A 5*5 matrix $\{\mathbf{A}\}$ is used as an ionogram fragment. Choosing such a size is determined by the following conditions:
(i) the band where the signal has virtually not changed;
(ii) the ionosonde resolution;
(iii) to ensure sufficient data are selected and computations are minimized.

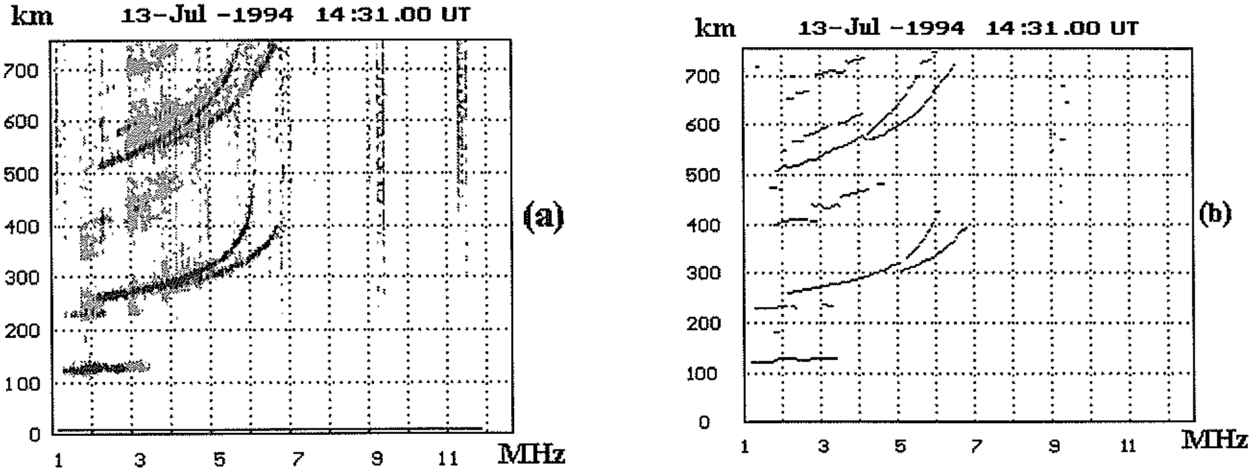

Figure 1 A vertical-incidence ionogram.

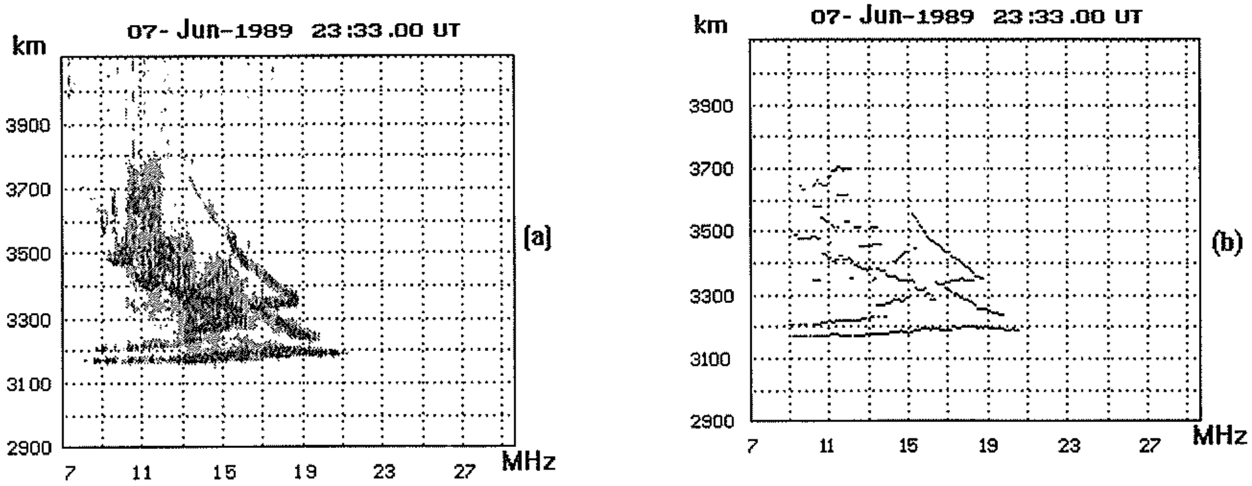

Figure 2 An oblique-incidence ionogram.

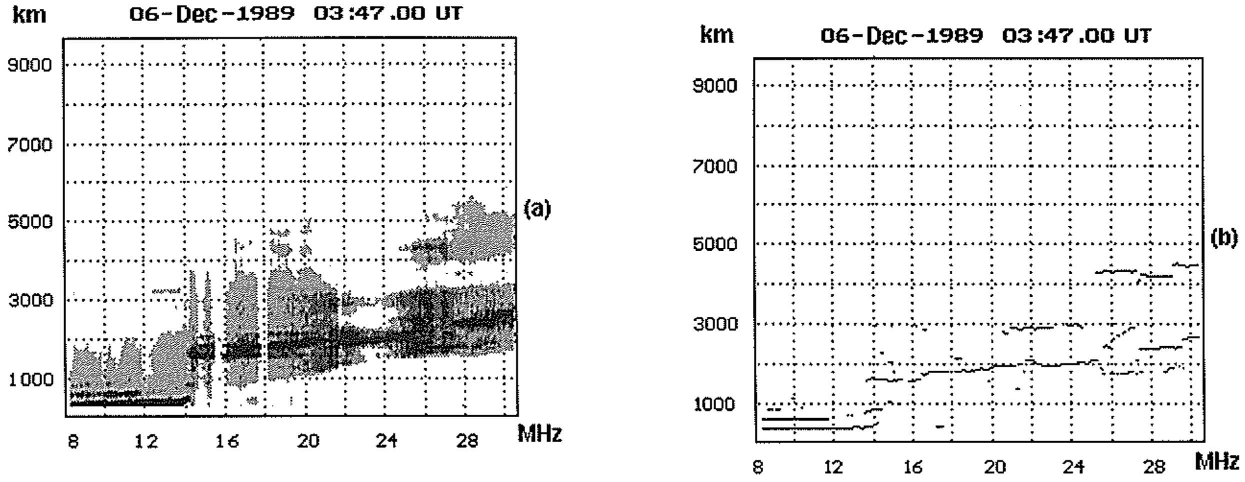

Figure 3 A backscatter ionogram.

2.1 The initial phase

This involves rejecting interference in vertical bands at different frequencies on ionograms. These bands may be present both at individual frequencies and occupy a significant portion of the ionogram and, usually, cover the entire range of delays. The presence of interference greatly affects the determination of physical parameters, such the critical frequencies of vertical incidence ionograms. Therefore, when handling such data, it is necessary to solve the following two problems:

(i) determine, automatically, the frequencies affected by interference and
(ii) carry out an analysis in order to decide whether data at these frequencies are to be rejected or corrected.

Since the data corresponding to "vertical" bands, have a uniform distribution close to a "white noise" type, the notion of the entropy [7] is the most useful measure to characterize its law of distribution. Initial inspection of the ionogram involves determining entropy values for the entire frequency range of the ionogram. This is followed by a calculation of the mean and root mean square (rms) entropy value, and the frequency entropy is examined over a three sigma interval. Data at frequencies where the entropy exceeds these limits, are rejected. Data at frequencies whose entropy is within a two to three sigma range are corrected. Correction is extremely important for oblique and backscatter ionograms, because in different conditions the signal width plus noise becomes comparable with the ionogram itself.

Corrections can be carried out using linear prediction methods where the updated value is determined as the sum of values, taken with certain weights, of neighboring elements [Figure 4]. In this work the following formula was chosen [5]

$$B_{i,j} = 0.3 * (A_{i,j-1} + A_{i-1,j}) + 0.2 * (A_{i-1,j-1} + A_{i+1,j-1})$$

For the removal of pulsing interference a median filter is used. These methods are correct from a distribution law conservation the point of view of and are computationally efficient.

2.2 Noise smoothing

Operations that minimize the noise level without blurring brightness (amplitude) differences are of greatest interest here and methods based on local order statistics are most powerful. Thus, to remove noise, techniques based on eliminating contributions to an average value of counts that do not satisfy a certain irregularity model are used. Essentially, the problem is as follows: within a large fragment window (5*5, for example), fragments of a smaller size (3*3) are chosen. In each of them a mean value and the variance are calculated. A mean brightness value of the vicinity with minimum variance is assigned to the central element of the fragment [8]. To increase the speed, instead of the variance, the index of inhomogeneity may be represented by the expression (for a 5*5 fragment):

$$S(k) = \sum_{l=1}^{9} Abs(A_{i,j} - A_l(k)), k = 1,2,3,.....9$$

Here $A_{i,j}$ is the brightness of the central point of the large fragment; and $A_l(k)$ is the brightness of the 1st point of the k^{th} small fragment. In this case $A_{i,j}$ is replaced with a mean brightness level within the fragment with a minimum value of A(k). This approach does not require any *a priori* knowledge and is fully adapted by the nature of the scene.

2.3 The next phase

This includes contrasting image details using nonlinear adaptive amplitude conversion constructed by measuring and analyzing a distribution histogram of signal values. Essentially, the signal conversion is chosen so that the converted signal has the required distribution histogram. In the problems of interest, good results were obtained when a uniform probability density is used as the output distribution. The transfer function in this case has the form:

$$D = (D_{max} - D_{min}) * P_A(A) + D_{min}$$

where $P_A(A)$ is a probability distribution function of the source image, and D_{max} and D_{min} are the maximum and minimum levels of the transformed signal. Such a conversion results in an increase in image contrast in areas with the most common signal values. If, for example, the image histogram has a single-mode, then details that were close together are expanded, giving greater contrast with respect to the background. This conversion is carried out in an overlapping, fragment-by-fragment fashion. In this case the distribution histogram is constructed throughout the entire fragment, and only its central part is converted, with the size equal to that of the superimposing areas.

Results derived by carrying out image contrasting (areas with increased and decreased brightness) make it possible to initiate a segmentation using threshold processing methods. Since threshold values may be thought of as constant for the problems at hand, in the vicinity of an image point, depending on local image signatures (properties), as well as on its coordinates, then it is possible to use processing techniques with a variable threshold (spatially-dependent). Essentially, the processing implies that there is always nonuniform image brightness. Also, the object brightness ratio is taken into consideration and the background is conserved, so the objects and background turn out to be significantly brighter in one part of the image than in another. Therefore, by a suitable threshold choice, regions with meaningful information may be separated from the background region. Since the nonuniform brightness is difficult to describe by a function, estimates of the threshold are made within a limited fragment. If the fragment contains both the object and the background, then, ideally, its brightness histogram should be (at least) bimodal. A minimum histogram value in the area between the regions gives a local threshold for separating the object and the background in a given image fragment. When the fragment contains only the object or only the background, then the histogram is unimodal, and the local threshold for the fragment cannot be determined. In this case it is determined by interpolating local thresholds determined for the nearest bimodal fragments. The outcome of this stage implies separation, on the ionogram, of quasi-homogeneous regions with increased amplitude corresponding to the signal modes. Separation of regions permits the determination of points corresponding to signal arrival times. Local maxima for each of the separated regions are chosen as such points.

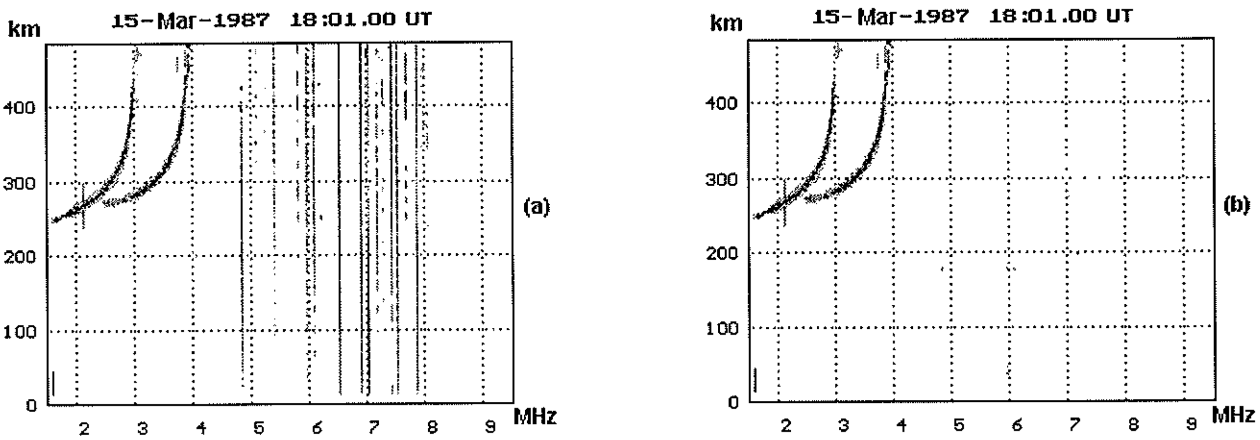

Figure 4. Correction for interference channels.

3. SUMMARY.

The algorithm under consideration was implemented in the form of a software package and was tested on ionograms obtained with the Radio Wave Propagation Division [1] chirp-sonde (Figure 1a - 3a). As a result of the algorithm it is possible to remove interference, smooth out the noise and compress the data by leaving only maximum amplitude (Figure 1b - 3b) points. These data are now ready for analysis and trace construction.

Two approaches have been implemented to date. One used in high-energy physics when carrying out an automated processing of images obtained on bubble and spark chambers is the method of rotating histograms [11,12]. The idea of the rotating histograms method implies dividing the entire image area being analyzed into narrow parallel bands and counting the number of points corresponding to each of the bands. The set of numbers obtained forms a peculiar kind of histogram. Subsequently, various variants of the angle of inclination of the bands are exhausted. Once the band falls within a trace, a maximum arises in a corresponding digit position of the histogram. Once all rotating histograms are formed, an algorithm is used to seek significant maxima corresponding to traces. The second approach involves using the method of artificial neural networks and is being successfully employed in high-energy physics [9,10]. The effectiveness of the neural network method is evident in its ability of form equilibrium states to which there corresponds a minimum of energy functions. With a suitable choice of the weighting functions, a minimum of energy function corresponds to an optimum distribution of points in traces. By virtue of the similarity of the problem, the neural networks method was implemented for trace recognition on vertical-incidence sounding ionograms [10] under conditions of no *a priori* data available. Research on the efficiency of the artificial neural networks method is currently being carried out in processing ionograms.

References

[1] Brynko I.G. et al., An automatically controlled data gathering and processing system using an FMCW ionosonde. Adv. Space Res., 1988, 8, No.4, pp. (4)121-(4)124.

[2] Pratt W.K., Digital Image Processing. New York, 1978, v.1, 368 p.; v.2, 368 p.

[3] Duda R. and Hart P., Pattern Recognition and Analysis of Scenes. Moscow: Mir, 1976.

[4] Ramm A.G., Random Estimation Theory. Harlow-Longman, 1990, 271 p.

[5] Yaroslavsky L.P., Introduction to Digital Image Processing. Moscow: Sov. Radio, 1979, 312 p.

[6] Fukunaga K., Introduction to Statistical Pattern Recognition. Academic Press, New York and London, 1972, 360.

[7] Shannon C.E., A mathematical theory of communication, Bell System Tech., J., 27(11948), No. 3, 379-423; 27(1948), No.4, 623-656.

[8] de Albuquerque Araujo A., Electronics Letters, 1985, v.21, No.25-26, pp. 1219-1221.

[9] Baginyan S., Ososkov G. et al., Tracking by a modified rotor model of neural network. Comput. Phys. Commun., No. 79, 1994, 165-178.

[10] Zaznobina E.G ,Ososkov G.A.,. Neural Network Application for Data Analysis of Vertical Ionosphere Locating. Preprint Communication of the Joint Institute for Nuclear Research,Dubna, 1993, 12 p.

[11] Automated Data Processing From Bubble and Spark Chambers. Trans. from English, ed. by V.S. Rozov. Moscow: Atomizdat, 1971.

[12] Nergui V. A, fast algorithm for determining trace elements: Communication of the Joint Institute for Nuclear Research, P10-80-302, Dubna, 1980, 8 p.

EXTENDING THE DIAGNOSTIC POTENTIAL OF VERTICAL-INCIDENCE SOUNDING

N.V.Ilyin, A.V.Medvedev, A.I.Orlov, K.G.Ratovsky, and B.G.Shpynev
Institute of Solar-Terrestrial Physics
P.O. Box 4026, Irkutsk, 664033 RUSSIA
Tel: (395)246-0265, Fax: (395)246-2557, E-mail: root@sitmis.irkutsk.su

ABSTRACT

New opportunities for extending the diagnostic potential of digital ionosondes, based on full echo shape analysis, are proposed. This analysis allows us to extend the accuracy of the usual radiochannel parameter (amplitude, phase and delay) measurements and introduce new parameters (radiochannel amplitude and frequency characteristic slope) in ionospheric investigations. The first results of simultaneous observations of these four parameters are presented and discussed.

1. INTRODUCTION

One of the possible ways for extending the diagnostic potential of the vertical-incidence sounding technique is a fuller analysis of the signal waveform. Usually it is assumed that the ionogram signal is reflected from the ionosphere without significant distortion and may be described by its amplitude, phase and delay. Is this assumption correct?

The full shape of an arbitrary narrowband signal, $f(t)$, may be defined by its quadrature (cosine and sine) components $a(t)$ and $b(t)$

$$f(t) = a(t) \cdot \cos(\omega_0 t) + b(t) \cdot \sin(\omega_0 t), \qquad (1)$$

where ω_0 is the carrier frequency. A convenient tool for visualization of the full signal shape is the phase diagram (PD); a curve in rectangular coordinates with axes that are the quadrature components $a(t)$ and $b(t)$. We have observed an interesting phenomenon. The PD of the undistorted signal is a segment of a straight line. But usually we observe a widening PD of the reflected signal to an loop (Fig.1). This kind of distortion is hardly visible on the signal envelope

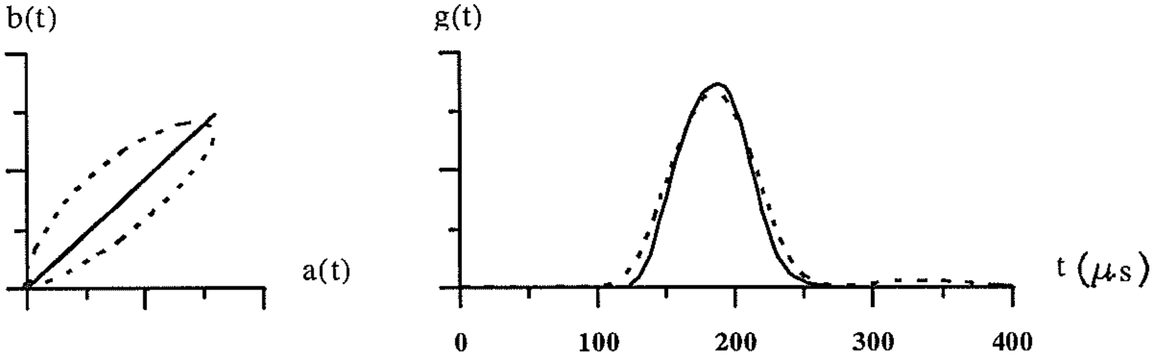

Figure 1. Phase diagram (first quadrant) and envelope of the emitted (solid line) and received (dashed line) signals.

$$g(t) = \sqrt{a^2(t) + b^2(t)}\,.$$

The same phenomenon was observed by *From and Whitehead* [1981], who explained the effect as multipathing. Of course, interference between the O and X modes can widen the PD, but when the time separation of the modes is certain, and when such phenomenon are observed for both O and X modes, we need to look for another explanation.

Ionospheric radiochannels may be imagined as a linear system with its own amplitude - frequency characteristic (AFC). Theoretical studies [*Zasenko et al.*, 1991] have shown that the distortion of a narrowband signal waveform is determined primarily by the slope of the AFC (modules of the reflection coefficient). Let the AFC of the ionospheric radiochannel be characterized not only by a smooth component, defined by the regular ionization, but also by some instantaneous structure. A possible structure of the ionospheric radiochannel amplitude - frequency characteristic, $\alpha(\omega)$, is shown schematically in Fig. 2.

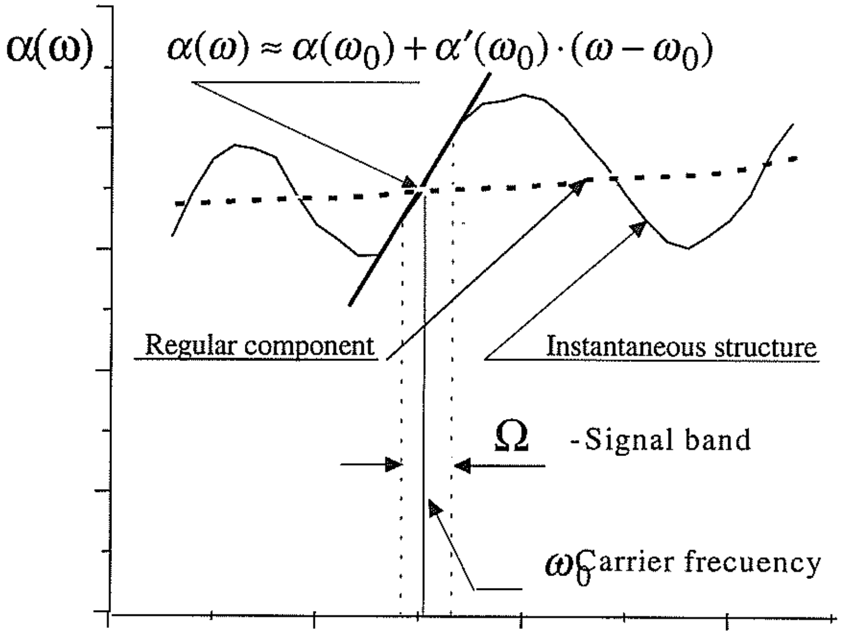

Figure 2. Amplitude-frequency characteristic of the ionospheric radiochannel

2. RADIOCHANNEL MODEL AND METHOD OF MEASUREMENT.

From Fig.2, the AFC has a good linear approximation in terms of Taylor series inside signal band:

$$\alpha(\omega) \approx \alpha(\omega_0) + \alpha'(\omega_0)\cdot(\omega-\omega_0) = \alpha(1-\gamma(\omega-\omega_0)), \qquad (2)$$

where the slope of AFC, $\gamma = -\alpha'(\omega_0)/\alpha(\omega_0)$.

The same expansion for the phase-frequency characteristics

$$\varphi(\omega) \approx \varphi(\omega_0) + \varphi'(\omega_0)\cdot(\omega-\omega_0) = \varphi + \tau(\omega-\omega_0), \qquad (3)$$

gives an expression for the quadrature components $a_r(t)$ and $b_r(t)$ of the reflected signal:

$$\left.\begin{aligned} a_r(t) &= \alpha\cdot(\cos\varphi\cdot g_0(t-\tau)+\gamma\cdot\sin\varphi\cdot g_0'(t-\tau)) \\ b_r(t) &= \alpha\cdot(\sin\varphi\cdot g_0(t-\tau)-\gamma\cdot\cos\varphi\cdot g_0'(t-\tau)) \end{aligned}\right\}, \qquad (4)$$

where $g_0(t)$ is the envelope of emitted signal. The PD of a signal of this type is a loop. So far, the signal undergoes distortion when reflected from the ionosphere and is described not only by its amplitude α, phase φ and delay τ, but also by a parameter γ (slope of the AFC) as well. The parameter γ defines the extent of the distortion. Referring to Figure.3, we can see that the loop rotation angle is the phase, the loop length is the amplitude, and the width-to-length ratio is the product of the AFC slope and signal band. Thus, the possibility exists to measure the AFC slope by analyzing the PD.

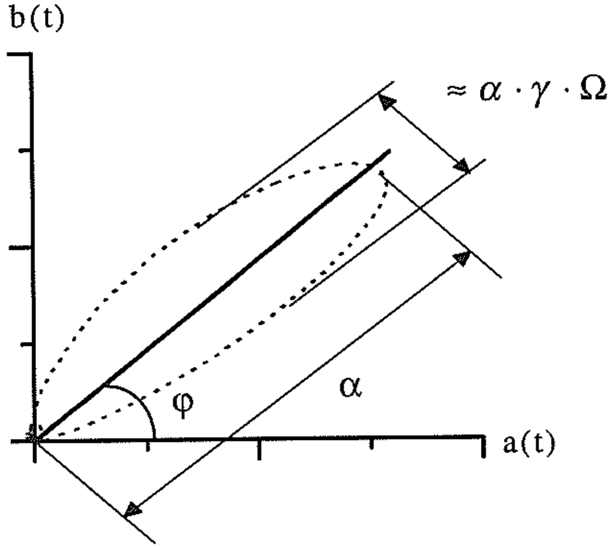

Figure 3. Interpretation of the phase diagram

To determine the radiochannel parameters, a technique [*Ratovsky et al.*, 1996] was developed and a program implemented following stages:

(1) make a digital recording of quadrature components of the received signal,

(2) construct the correlation functions, $R_a(t)$, $R_b(t)$, of the quadrature components with the envelope and the correlation functions, $D_a(t)$, $D_b(t)$, of the quadrature components with the derivative of the emitted signal envelope,

(3) determine the AFC slope, along with the amplitude, phase and delay for each echo using the next expressions:

$$R_g(\tau) = \max\big(R_g(t)\big)\ , \tag{5}$$

$$\alpha = R_g(\tau)\ /\ E_0\ , \tag{6}$$

$$\varphi = arctg(R_b(\tau)\ /\ R_a(\tau))\ , \tag{7}$$

$$\gamma = \frac{R_b(\tau)D_a(\tau) - R_a(\tau)D_b(\tau)}{R_g^2(\tau)} \cdot \frac{E_0}{E_1}\ , \tag{8}$$

where

$$R_g(t) = \sqrt{R_a^2(t) + R_b^2(t)}\ , \qquad E_0 = \int_0^T g_0^2(t)\,dt\ , \qquad E_1 = \int_0^T (g_0'(t))^2\,dt\ ,$$

where T is the duration of the emitted signal.

In the case of a single echo, or several echoes separated in time, it is possible to automate the technique for real-time data processing and plotting .

Thus the full signal shape analysis allows us:

(1) to determine traditional ionospheric parameters (amplitude, phase and delay) more correctly;

(2) to carry out quantitative measurements of the new parameter, γ (the AFC slope).

A set of vertical-incidence ionospheric sounding data was collected near Irkutsk (52°N, 104°E). Transmission and reception were done with a polarized vertical-rhombic antenna. Sounding operations were carried out with Gaussian-shaped pulses of ~150 microsecond duration, with 10 Hz repetition rate. The full signal shape was recorded and radiochannel parameters (amplitude, phase, delay and AFC slope) were determined. Figure 4 shows a representative sample of the parameter's time variations during a 10-minute interval. Phase variations with respect to an initial value are converted to the phase path variations (Pf) and delay variations are converted to the group path variations (Pg). O and X modes were separated in delay with confidence during this interval. Figure 4 shows parameters for O mode only.

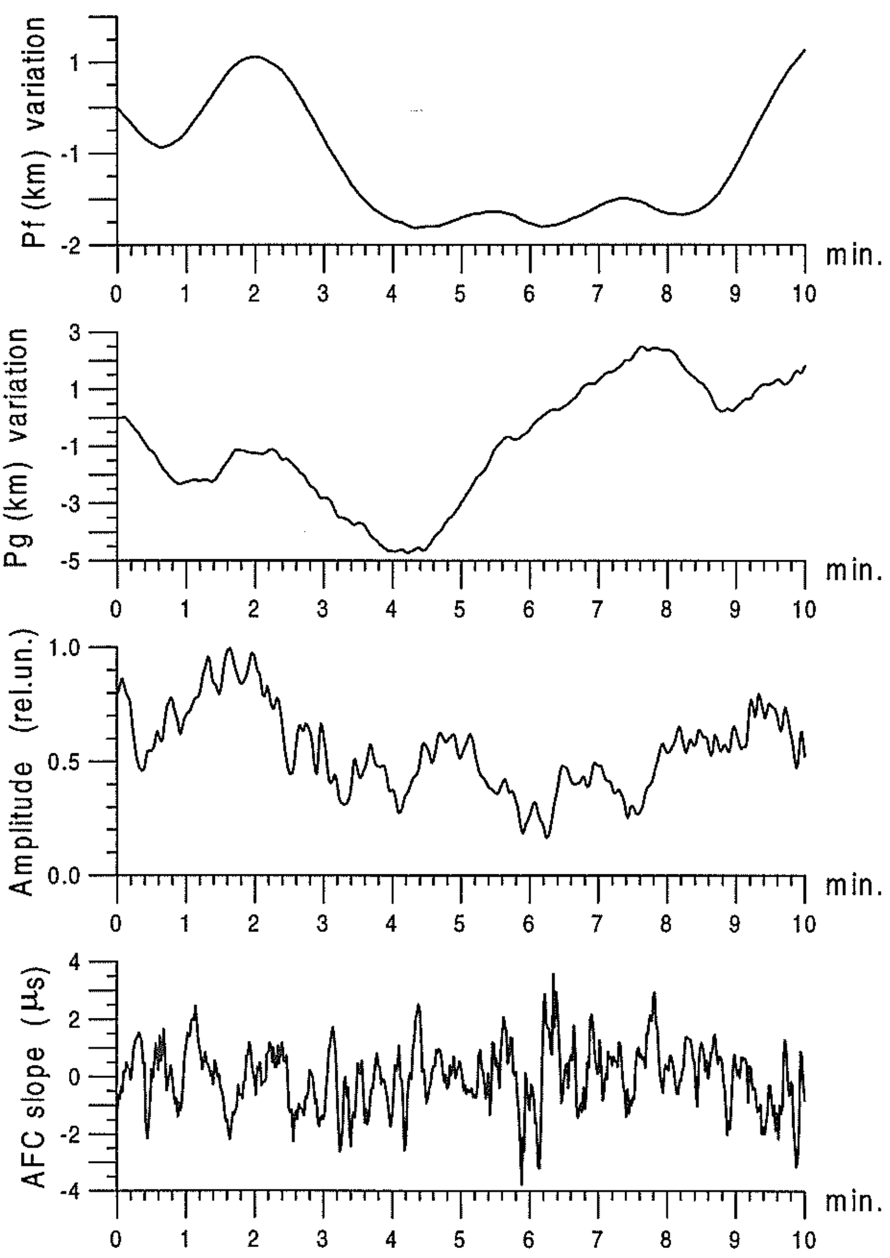

Figure 4. Time variations of the radiochannel parameters.
17 March 1995 LT 00:36 frequency 2.1 MHz

According to the model suggested by *Medvedev and Ratovsky* [1995], the accuracy of the parameter's determination, for particular signal/noise ratio in this experiment, is estimated to be: 0.5m for phase path variations; 2% for amplitude and 0.7 μs for AFC slope.

The group path accuracy, limited by noise, was estimated as - 150 m, as the data sampling step (4 μs) gives the group path uncertainty ± 300 m. Notice that group path accuracy with mono-frequency measurements in our technique is comparable to the most advanced ionosondes [*Reinisch*, 1986], [*Wright and Pitteway*, 1979].

The parameter determination accuracy can be improved by applying special signals [Medvedev and Ratovsky, 1995]. According to the results of this work, using a distortion-sensitive signal permits a three to six-fold reduction of the AFC slope error compared with the Gaussian-shaped pulse.

One can see in the figures a substantial difference in time scale variation of the various parameters of the channel; phase and group path variations are characterized by scales of several minutes, the AFC slope is typified by several seconds, while in amplitude one can see a variety of time scales. Processes that cause fast fluctuations in amplitude and AFC slope certainly impact on the variations in phase and group path, but they are virtually imperceptible on the scale of the figures. In the simplest stratified ionospheric model, the parameter, γ, has a clear physical meaning, representing a frequency derivative of the absorption coefficient. It is evident from Fig. 4 that the time dynamics of γ do not agree with this model. It is most likely that the AFC slope of the radiochannel is sensitive to fast processes localized near the reflection region. Returning to Fig. 2, we can conclude that in the absence of interference, observed variations of this parameter can only be explained by irregular structure. In our opinion, the irregular structure results from scattering off small-scaled irregularities.

The AFC slope is an independent parameter carrying additional information on ionospheric features. This parameter characterizes, by definition, the amplitude fluctuations of different frequencies inside the signal band. Its dynamics provide a way of estimating the frequency correlation range of the fast amplitude fluctuations, which are connected with small-scale irregularity behavior, in the context of some models. The determination of small-scale structure parameters using only amplitude fluctuations is a difficult task due to the problem of separating different scale components caused by variously scaled irregularities. Whereas the AFC slope variations are the product of small-scale structure dynamics in the uncombined state.

3. SUMMARY

The full shape analyzing method proposed extends the diagnostic capabilities of vertical-incidence soundings without the cost of additional facilities. Its sensitivity to fast processes will undoubtedly be useful for monitoring the ionosphere, especially studying its small-scale structure. Certainly the method goes beyond the simplest case of the slightly distorted single-path channel. The full signal shape analysis can be applied to the:

- problem of separation of the unresolved signal in time,
- case of strong delay-frequency distortion,
- studies of spread-F phenomenon.

References

From W.R. and Whitehead J.D. (1981), The use of phasor display in studying ionospheric radio echoes, *J. Atmos. Terr. Phys.*, v.43, ¹.12, 1265-1266.

Medvedev A.V. and Ratovsky K.G. Using composite signals to diagnose distortions at vertical-incidence ionospheric sounding. in *Issledovaniya po geomagnetizmu, aeronomii i fizike Solntsa.* Novosibirsk: Nauka, 1995, v.105 (in press).

Ratovsky K.G., Medvedev A.V., Zasenko V.E., Orlov A.I. and Shpynev B.G. (1996), A technique for determination of the four independent parameters of ionospheric radiochannel on the base of full shape signal analysis, in *Issledovaniya po geomagnetizmu, aeronomii i fizike Solntsa.* Novosibirsk: Nauka, v.107 (in press).

Reinisch B. (1986), The digisonde 256 system and ionospheric research, in *INAG Ionospheric Station Inf. Bull.* edited by R.Haggard, 48.

Wright J.W and Pitteway M.L.V. (1979), Real-time data acquisition and interpretation capabilities of the Dynasonde, *Radio Sci.*, 14, 815-835.

Zasenko V.E., Ilyin N.V. and Orlov I.I. (1991), Signal distortion in vertical-incidence ionospheric sounding, in *Issledovaniya po geomagnetizmu, aeronomii i fizike Solntsa.* Moscow: Nauka, v.96, pp.128-136.

AUTOMATIC IONOGRAM TRACE IDENTIFICATION USING FUZZY CLASSIFICATION TECHNIQUES

L.-C. Tsai[1,2] (lctsai@csrsr.ncu.edu.tw), F. T. Berkey[3,4]
(berkey@psi.sci.sdl.usu.edu), and J. Y. Liu[2,1] (jyliu@jupiter.ss.ncu.edu.tw)
[1] Center for Space and Remote Sensing Research, National Central University, Chung-Li, Taiwan 32054
[2] Graduate Institute of Space Science, National Central University, Chung-Li, Taiwan 32054
[3] Rome Laboratory/OCSA, Rome, NY 13441-4514
[4] Space Dynamic Laboratory, Utah State University, Logan, Utah 84322-4145

ABSTRACT

In this report, a method for the automatic identification of ionogram traces using fuzzy classification techniques will be discussed. A measure of the continuity or discontinuity between ionospherically reflected echoes can be obtained using a fuzzy relation that describes a set of rules for echo connectedness. Based on such measures, segmentation processing of ionograms can be defined and their properties obtained. Segments representing the ordinary and extraordinary reflections from the E- and F-layers can easily be differentiated from multiple hop echoes. By choice, the major segment to be derived is usually the F-layer trace, although the daytime E-layer trace can also be obtained. This autoscaling program has been successfully applied to data from a Digisonde operated by National Central University (24.6° N, 121.0° E) as well as to ionograms obtained with Utah State University Dynasonde (41.9° N, 111.4° W).

1. INTRODUCTION

Radiowave sounding of the Earth's ionosphere, which began nearly six decades ago, was the first application of what today is commonly termed remote sensing. Although more sophisticated techniques of *in-situ* measurement of ionospheric parameters are available, the ionospheric sounding radar (ionosonde) still remains an inexpensive and viable environmental monitor at nearly every national geophysical observatory. Synoptic ionospheric measurements in the form of ionograms have provided valuable information both for the HF communications and for studies related to the physics of the ionosphere. However, since deployment of the first automatic ionosonde in 1933, it is conservatively estimated that over 200 million ionograms have been recorded at several hundred observations world-wide, of which less than 25% have been reduced to quantitative data following internationally agreed criteria (Wright, unpublished note, 1991). An even smaller fraction of these data has been reduced to basic ionization profiles, which can be obtained from ionograms by a mathematically complex inversion process. For the reasons cited above, the scaling of ionospheric parameters can be a laborious task because of the complex structures that frequently characterize ionograms.

During the past decade, interest in fuzzy subset theory has led to the development of a well-organized theory pioneered by Zadeh [1965]. This theory has been applied to a broad spectrum of studies, including various branches of pure and applied mathematics, as well as topology, graph theory, mapping, automata and pattern recognition. Fuzzy set approaches have also been applied for image processing by some researchers and encouraging results have been achieved in these applications. One of the most promising approaches was proposed by Rosenfeld [1979, 1983, and 1984]. In his work, Rosenfeld regarded a gray scale image as a fuzzy subset of two-dimension discrete space. Thus, image understanding became a problem in fuzzy geometry. For example, the problem of image segmentation is to find all fuzzy connected subsets; this method will be used to segment echoes on ionograms. The chosen segments will be linked to become the main trace of ionospheric reflection. This information can be provided either to a scaling process or an inversion, which can derive either the standard set of ionospheric parameters or the electron density distribution in the overhead ionosphere. Previous applications of fuzzy theory to the problem of ionogram reduction can be found in Chen and Berkey [1995].

2. AUTOMATIC SCALING PROCEDURES

In developing the principles for automatic scaling, the input information for the processing algorithms needs to be taken into consideration. The autoscaling algorithm described here has been designed for digital modern ionosondes of the digisonde [Bibl and Reinisch, 1978; Reinisch 1986] and the NOAA HF radar [Grubb, 1979; Argo and Hindman, 1986] class. The digisonde measures the following parameters: (1) group travel time of h', (2) echo amplitude, (3) phase, (4) Doppler frequency, (5) angle of arrival, (6) wave polarization (separation of ordinary and extraordinary modes), and (6) wave-front curvature. The virtual height (to 2.5 or 5 km resolution) and amplitude (to 1.5 dB) are measured over a selected frequency range between 0.4 and 40 MHz. The information on angles of arrival and Doppler shift is limited but the wave polarization is identified for all frequency-range bins. The NOAA HF radar (dynasonde) measures the complex vector amplitude of echoes as a function of range and frequency (0.1-30 MHz), to enable the derivation of echo amplitude, phase, pulse group delay (to 0.75 km resolution), stationary phase ($d\phi/df$) group delay, the direction of arrival, wave polarization, Doppler spectra, irregular structures in the wave front, and the temporal variation of the above characteristics. In the algorithm described here, we use the two-dimensional frequency-time delay measurement as input parameters. We also include the amplitude of the reflected signal into the processing procedure, using it as the reference to choose the threshold value of the echo signal, separating the normal E layer and the sporadic E (E_s) layer (if both are connected in a segment), and distinguishing the overlapped multi-hop E_s echoes and F-region echoes. The final input parameter is the echo polarization, which separates the ordinary and extraordinary and simplifies the process of ionogram scaling. The primary input for fuzzy processing is then a two dimensional (frequency-virtual height) image with amplitude and polarization information. The main processing steps are as follows:

(1) to identify and remove interference from the ionograms,

(2) to segment the ionograms using a fuzzy continuity technique,

(3) to identify the main segment as the F-region segment,

(4) to discriminate between normal E and E_s in the E-region segment,

(5) to delete multiple-hop E_s echoes overlapping F-region signals (the determination of E_s type),

(6) smoothing, extrapolating, and interpolating processing for F-region trace, and

(7) to derive ionospheric parameters in URSI IUWG format.

2.1 Removing Interference Signals in Ionograms

An analysis of interference signals and ionospheric echoes identifies one feature that differentiates between them. This feature is that interference signals have a strong and more-or-less uniform signal strength distribution that is independent of range, since the HF transmitter (i.e. interference source) nominally transmits a constant power level during the time of an ionosonde sweep interval. On the other hand, for an ionosonde signal, the amplitude of reflected pulse is not constant, even if spread-F exists. Koschmieder [1994] developed a neural network method to be used to identify stray signals within ionograms. The algorithm correctly identifies 85% of the stray HF signals recorded by the CIT measurement (model IPS-71 by KEL Aerospace Pty.). In this paper, we incorporate a simple technique that uses a threshold amplitude corresponding to entire range bins to remove interference. The resulting gap in the frequency domain can be recovered by subsequent interpolation or extrapolation (at clusters of the ionospheric regions) procedures. For weak signals, the removal procedure can be addressed by segmentation and smoothing processes.

2.2 Ionogram Segmentation

In the following, we discuss fuzzy connectedness on fuzzy subfibers [Chen *et al.*, 1994a] and their application to determine ionogram segmentation. Let Σ_2 be a two-dimensional discrete space corresponding to frequency-virtual height information. We require that $g_a : \Sigma_2 \times \Sigma_2 \rightarrow [0,1]$ is a mapping of two adjacent points from a two-dimensional frequency-virtual height regime to single-valued fuzzy subfiber corresponding to echo amplitude connectedness; g_f (g_r) : $\Sigma_2 \times \Sigma_2 \rightarrow [0,1]$ represents another mapping function between two adjacent points in Σ_2 corresponding to frequency (echo range) connectedness. We further define the degree of adjacency, which is the degree of connectedness (connectivity) between two adjacent points, as

$$C_a(p_1, p_2) = \begin{cases} g(p_1, p_2) & p_1 \textit{ and } p_2 \textit{ are adjacent} \\ 0 & \textit{otherwise} \end{cases}$$

Here $0 \leq g(p_1, p_2) \leq 1$, and $g(p_1, p_2)$ is defined to be the minimum of amplitude connectedness g_a, frequency connectedness g_f, and range connectedness g_r as

$$g(p_1, p_2) = \min\left\{ g_a(p_1, p_2), g_f(p_1, p_2), g_r(p_1, p_2) \right\},$$

and

$$g_a(p_1, p_2) = 1 - \frac{\min(\,\Delta Amp, \Delta Amp_{\max}\,)}{\Delta Amp_{\max}}$$

$$g_f(p_1, p_2) = \frac{\Delta f_{\max} - \max(\,\Delta f, \Delta f_{\min}\,)}{\Delta f_{\max} - \Delta f_{\min}}$$

$$g_r(p_1, p_2) = \frac{\Delta r_{\max} - \max(\,\Delta r, \Delta r_{\min}\,)}{\Delta r_{\max} - \Delta r_{\min}}$$

where ΔAmp, Δf, and Δr are the incremental changes of echo amplitude, frequency, and range, respectively, between two adjacent points. Some basic topological properties of the adjacent point and connectedness in image application have been discussed in Rosenfeld [1979, 1983, and 1984]. However, in this paper, we require that the adjacent region of a special point is defined as shown in Figure 1, and all points in such region are its corresponding adjacent points. Let $\Pi = p_0, \ldots, p_n$ is a path in Σ_2 (frequency-virtual height); the quantity of connectedness of Π is denoted by

$$C_p\,(\,\Pi(p_0, p_n)\,) = \min\left\{ C_a(p_i, p_{i+1}) \,\middle|\, i = 0, \cdots, n-1 \right\}.$$

And, the degree of connectedness of any two points p_1 and p_2 as

$$C(p_1, p_2) = \max\left\{ C_p(\Pi(p_1, p_2)) \,\middle|\, \Pi(p_1, p_2) \textit{ is a path in } \Sigma_2 \right\}.$$

For a $\lambda \in [0, 1]$, we say p_1 and p_2 in Σ_2 is λ-connected if $C(p1, p2) \geq \lambda$. Furthermore, let $\lambda_1 > \lambda_2$; if p_1 and p_2 are in a λ_1-connected class [Chen, 1991; Chen *et al.*, 1994b], then p_1 and p_2 must be in a λ_2-connected class. Thus, if $\lambda_1 > \lambda_2$, then λ_1-connected segmentation is a refinement of λ_2-connected segmentation. In fact, λ-connectedness is a fuzzy connectedness, which is one kind of fuzzy relations.

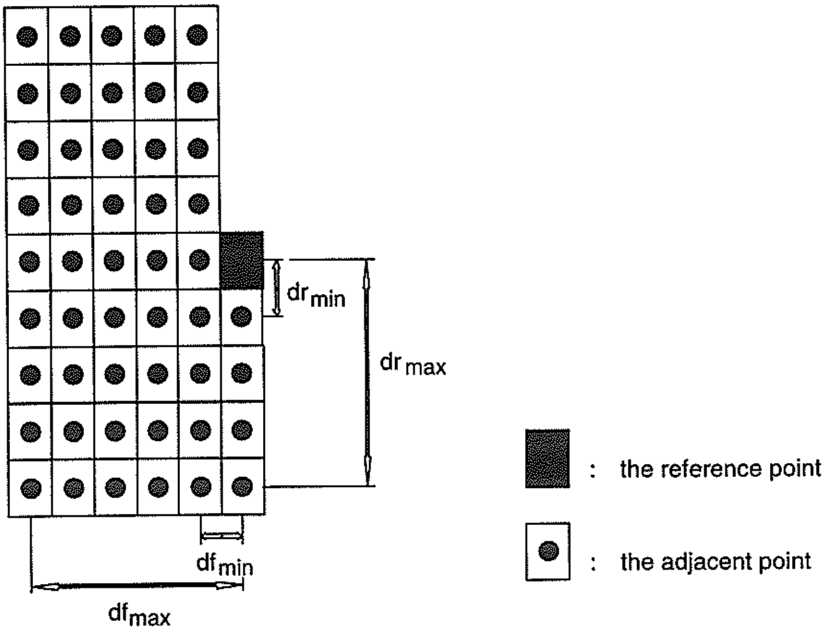

Figure 1. A reference point and its corresponding adjacent points in frequency-virtual height information.

We already introduced the concepts of fuzzy subfiber and λ-connectedness. Now, we start to discuss the algorithms for λ-connected-segmentation. Let g_a, g_f, g_r : $\Sigma_2 \times \Sigma_2 \rightarrow [0, 1]$ be a fuzzy subfiber, and the function of adjacency, $g(p_1, p_2)$ and $C_a(p_1, p_2)$ were given. For arbitrary $\lambda \in [0, 1]$; the algorithm, which can find all λ-connected parts in Σ_2, is shown by the following procedure.

Algorithm : Ionogram segmentation using fuzzy λ-connectedness technique.

1. Let p_0 be a point in Σ_2. Set $L(p_0) \leftarrow *$.
2. For all adjacent points p_a corresponding to p_0, if there exist a point p, and $C(p, p_0) \geq max(\lambda, g(p_a, p))$, then $L(p_0) \leftarrow p$, $SEGMENT \leftarrow SEGMENT \cup p_0$, and go to step 1 (looking for another point in Σ_2), i.e. labeling p_0 and p_0 is sent a stack *SEGMENT*; otherwise, go to step 3.
3. $L(p_0) \leftarrow 0$, and create a new stack *SEGMENT*.

Using data from the Chung-Li digisonde, Figures 2 and 3 show the corresponding segmentation results in different gray scales applied to the ordinary mode echoes from ionograms acquired in day and night time, respectively. Segments can easily be differentiated from the E- and F-layer traces, multi-hop echoes, noise, and spurious signals. Even for spread ionograms, the results retain a significant amount of information which can be utilized for scaling or true-height reduction.

2.3 E-E$_s$-F Interpretation

After applying segmentation processing to the ionograms, an identification of the F-region segment is carried out by a search of the largest segment. As noted previously, it is often observed that the pulse reflected from the F2-layer has a much longer duration than the transmitted pulse; this phenomenon is called spread F. Fortunately, spread F echoes can be "fuzzy" connected to the main segment by an adequate choice of the value of λ. The next step is the construction of the E segment between f_{min} and the minimum frequency of the F-region segment. Adding further complexity to the identification process is the presence of the sporadic E-layer (E$_s$-layer).

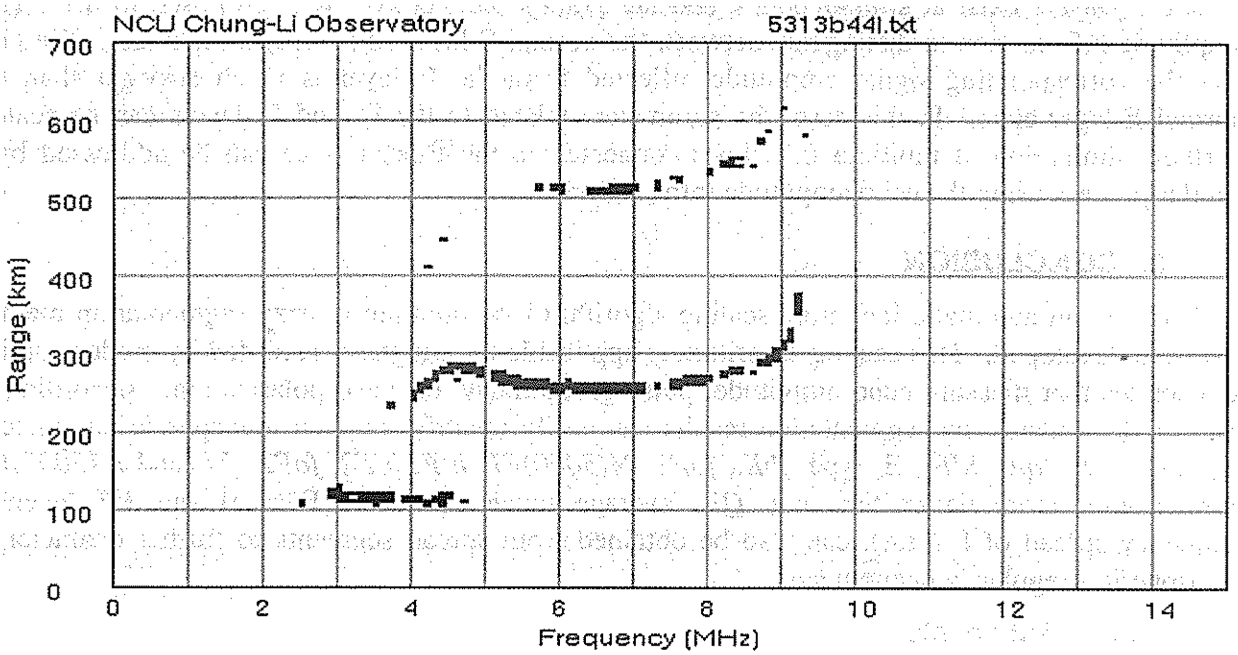

Figure 2. An example of segmentation processing applied to the ordinary mode echoes from a daytime Chung-Li ionogram.

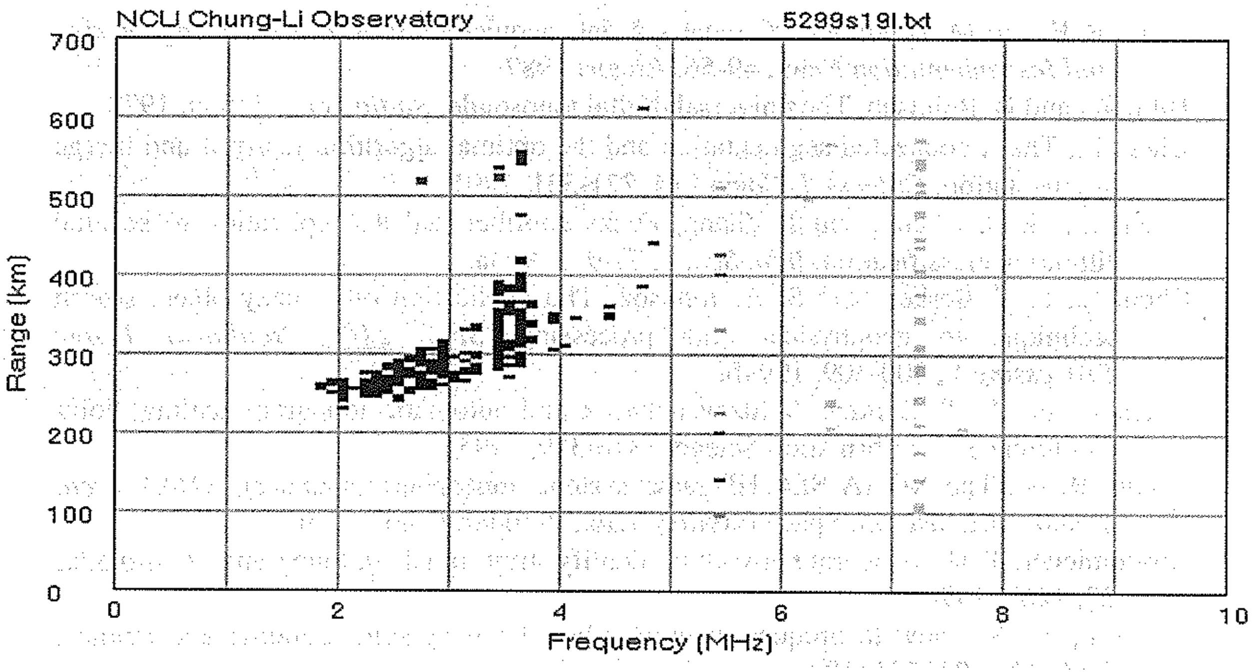

Figure 3. An example of segmentation processing applied to the ordinary mode echoes from a nighttime Chung-Li ionogram.

Recognizing whether or not the F-layer echoes are absorbed or blanketed by the E_s-layer is a critical step. A process becomes important to detect the presence of the E_s-layer. As a result, the echo traces observed in the E regions exhibit very complex structures on an ionogram when both

E- and E_s-layers exist at similar height and are "fuzzy" connected. It is proposed to use signal amplitude information to distinguish between the normal E-layer and the E_s-layer traces. We note that the corresponding signal amplitude reflected from the E_s-layer is much stronger than the normal E-layer echo. In this case, the parameters related to the E- and E_s-layers can be scaled. Further elimination of multiple E_s echoes connected to the F-layer trace can be addressed by a similar process using the echo amplitude information.

3. CONCLUSION

In this note, an automatic ionogram scaling algorithm incorporating a fuzzy segmentation method has been developed. This scaling algorithm is applicable to ionograms recorded by modern digital ionosondes that measure echo amplitude, pulse group delay, or wave polarization. According to the URSI standard, the segmentation results can easily identify fourteen ionospheric parameters: f_{min}, *foE*, *h'E*, foE_s, $h'E_s$, E_s type, fbE_s, *foF1*, *M(3000)F1*, *h'F*, *h'F2*, *foF2*, *fxI*, and *M(3000)F2*. Furthermore, more parameters, e.g. *QF* (average range spread of F-trace) and *FF* (average frequency spread of F-trace), can also be obtained from spread segments to further characterize ionospheric irregularity phenomena.

Acknowledgments

This work at the National Central University is supported by the NSC86-2111-M-008-005 and NSC86-2111-M-008-012. One of the authors (FTB) was partially supported by the AFOSR University Resident Research Program and NSF Grant ATM-9525818.

References

Argo, P. E. and M. Hindman, PC radar - A data acquisition tool, *Personal Engineering and Instrumentation News*, 49-56, August 1987.

Bibl, K., and B. Reinisch, The universal digital ionosonde, *Radio Sci.*, 13, 519, 1978.

Chen, L., The λ-connected segmentation and the optimal algorithm for split-and-merge segmentation, *Chinese J. Comp.*, 14, 321-331, 1991.

Chen, L., H.-D. Cheng, and J. Zhang, Fuzzy subfiber and its application to seismic lithology classification, *Info. Sci.*, 1, 77-95, 1994a.

Chen, L., F. T. Berkey, and S. A. Johnson, The application of a fuzzy object search technique to geophysical data processing, *SPIE 2180*, *Nonlinear Image Processing V*, 300-309, 1994b.

Chen, L. and F. T. Berkey, A fuzzy network and automatic ionogram scaling, Joint Conference on Information Science, 316-319, 1995.

Grubb, R. N., The NOAA SEL HF radar system (ionospheric sounder), *NOAA Tech. Memo. ERL SEL-55*, Space Environ. Lab., Boulder, Colo., 1979.

Koschmieder, T. H., A neural network to identify stray signals in ionograms, *Radio Sci.*, 29, 1467, 1994.

Reinisch, B. W., New techniques in ground-based ionospheric sounding and studies, *Radio Sci.*, 21, 331, 1986.

Rosenfeld A., Fuzzy digital topology, *Inform. and Control*, 40, 76-87, 1979.

Rosenfeld A., On connectivity properties of grayscale pictures, *Pattern Recognition*, 16, 47-50, 1983.

Rosenfeld A., Fuzzy geometry of image subsets, *Pattern Recognition Lett.*, 2, 311-317, 1984.

Wright, J. W., personal communication, 1991.

Zadeh, L. A., Fuzzy sets, *Inform. Cont.*, 8, 338-353, 1965.

AN OVERVIEW OF A SYSTEM FOR AUTOSCALING OBLIQUE-INCIDENCE IONOGRAMS

Nicholas J. Redding
Defence Science and Technology Organisation, Salisbury, South Australia, 5108.
Nick.Redding@dsto.defence.gov.au ph. +61 8 259 7058, fax 5200

ABSTRACT

This paper presents ongoing work on an autoscaling system for oblique ionograms involving three stages. Firstly, the ionogram is filtered by estimating the noise in each pixel of the image by fitting orthogonal second-order multinomials to its 3×3 neighbourhood. Secondly, feature vectors for each trace of the filtered ionogram are extracted using a process of thinning, trimming, model fitting, and a final merging stage that accounts for broken traces. The model used for ionogram traces is an implicit quartic equation, and is fitted to the cleaned-up skeleton of the trace using orthogonal distance regression. A third stage of the overall system uses the feature vectors to identify the prominent modes and other important features of the ionograms, and to track these modes and features as they evolve across sequences of ionograms. This work will automate the task of identifying and tracking ionospheric propagation modes in oblique ionograms.

1. INTRODUCTION

This paper describes ongoing work for an autoscaling system for oblique ionograms (figure 1) collected in the Low-Latitude Ionospheric Sounding Program (LLISP) [12]. This autoscaling system involves taking a raw ionogram, identifying its major features, reducing these to a vector that usefully summarizes them, and using these to identify the components of the ionogram that correspond to each propagation mode (figure 1). The system that is described here to do this has been developed in three overall stages. The first stage filters the raw ionograms to remove noise and enhance features.

The idea behind feature extraction, the second overall stage, is to find a simple description of the traces in a symbolic form. This is achieved by finding a suitable model such that for some value of the model parameters there is a good correspondence between the shape of the trace and the shape of the model. This highlights a number of problems. Firstly, we need to choose a suitable model for the traces. Secondly, we have to find a measure of the goodness of fit and a fitting routine to determine a value of the model parameter that minimizes the measure. Lastly, we need to separate the pixels that correspond to particular traces and reduce them in number somehow because this will have a serious impact upon the overall speed of the autoscaling system (*i.e.*, the optimization involved in fitting is the rate determining step for speed in the autoscaling system). Incorporated into the feature extraction process is a stage designed to account for broken or missing features in an ionogram. Merging is the process of reconnecting trace fragments, which clearly belong to the same propagation mode, that have become disconnected for some reason (noise, attenuation, *etc.*) and so have been fitted separately. Thus merging is one more step designed to move towards the ideal where one trace corresponds to one propagation mode and vice versa. Merging will only be briefly mentioned in here (see [7]).

The final overall stage of the autoscaling system includes, firstly, a tracking stage that is designed to assist mode identification in circumstances where one or more of the simple modes are missing from the ionogram because of various ionospheric effects; secondly, a mode identification stage which makes use of an ionospheric model to identify the propagation modes of each trace; and lastly a measurement stage to output the desired measurements from the ionogram. Figure 3 depicts the result of each processing step on an example ionogram.

2. FILTERING

The filter found to perform well against all others tested on the ionograms (see [6] for the comparison) is the unpublished filter, developed by Whatmough [11], which fits a second order multinomial in two variables to

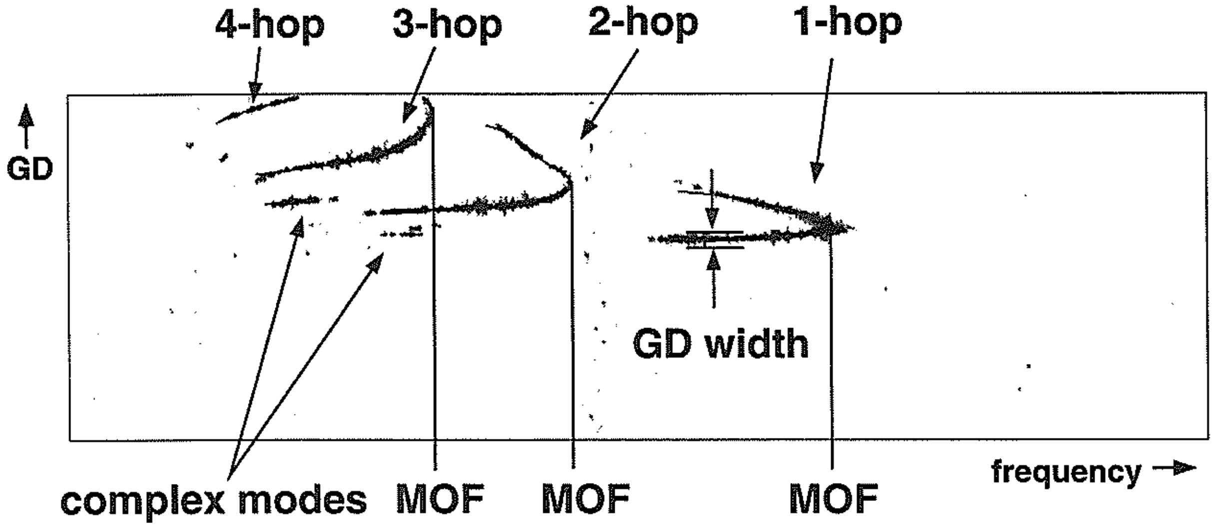

Figure 1: A typical LLISP oblique-ionogram with the information determined by an autoscaling system annotated. The scope of measurements that could be determined using the autoscaling system include the propagation mode of each trace, the maximum observable frequency (MOF) which occurs at the nose of each of each simple propagation modes, and the group delay (GD) width of each of the traces. The complex modes are those modes left over after identifying the simple propagation modes and are due to combinations of bounces off the sporadic-E layer. (Note that with LLISP oblique incidence ionograms, the lengths of paths precludes E-layer propagation. Sometimes a simple sporadic-E layer may be present as a horizontal trace, but it is easily identified because it occurs at a known GD.)

each 3 × 3 window in the image. It assumes that the highest order coefficients of the multinomial are only influenced by noise in the image and therefore these coefficients can be used to estimate the noise at each window position. The filtered value is given by a mean of the raw centre value and the window mean, weighted according to the signal and total power. This filter can thus be considered to be an adaptive mean filter.

Note that all ionograms were normalized to have a peak signal strength of 255 before filtering was carried out. The polynomial-fit cleaning filter was applied to the ionogram for 10 iterations and the background cleaned by clipping all values below 20.

3. FEATURE EXTRACTION

The most prominent features in an ionogram are the *traces*. These are connected segments in the ionogram and reflect discrete structures and associated modes of signal propagation in the ionosphere: they are clearly visible in figure 1. (Connectivity is defined here to be 8-connectivity, *i.e.*, a pixel may be connected to any of its 8 nearest neighbours including the diagonals). This figure also shows, however, that the traces and associated modes can be obscured by noise or other effects, that they can be broken with several distinct traces being obviously associated with the one underlying structure, and that they can take quite complicated forms. No two ionograms are precisely the same, and the variation between two ionograms can be enormous (see [6] for more examples), making it sometimes difficult even for an expert to interpret them. The shape of traces and the types present can vary tremendously from ionogram to ionogram. Thus the primary aim of the first part of the feature extraction stage for autoscaling is to separate the significant trace shapes. These will then be used to compute feature vectors that summarize trace location and extent for each important propagation mode.

There are two assumptions implied here when dealing with an ionogram as a collection of distinct traces which are defined to be a contiguous area of connected pixels. The first assumption is that a trace will be the product of a single ionospheric propagation mode. Secondly it is assumed that for each possible propagation mode, there is at most one trace that corresponds to it. Of course, these simplistic assumptions are commonly violated in ionograms, and a number of steps have been incorporated into the autoscaling system to try and cope with these eventualities. The first assumption can be violated when traces are erroneously connected, and the branch selection process that is briefly discussed later tries to address this problem. The merging stage,

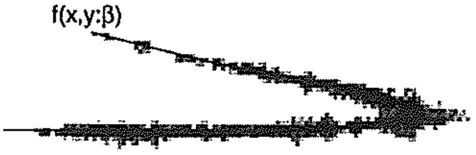

Figure 2: The principles of feature extraction. A model f with model parameter β is determined such that for a particular value of β there is a good correspondence between the model and the trace. Feature extraction is the process of choosing a suitable model and determining the best value of β.

the details of which can be found in [7], is designed to deal with those situations where a trace is cut into disconnected segments, breaking the second assumption. In this way we will approach the ideal where all the signal that corresponds to a single propagation mode and no other has been isolated into a single trace of the ionogram. Note that I will refer to a trace as a trace *structure* when I want to emphasize that the trace contains signal that was received by more than one ionospheric propagation mode, and as a trace *fragment* or trace *segment* when I want to emphasize that it is only a small part of the signal received by a single propagation mode.

The idea behind feature extraction is to find a simple description of the traces in a symbolic form. This is achieved by finding a suitable model such that for some value of the model parameters there is a good correspondence between the shape of the trace and the shape of the model. This is represented in figure 2. This highlights a number of problems. Firstly, we need to choose a suitable model for the traces. Secondly, we have to find a measure of the goodness of fit and a fitting routine to determine a value of the model parameter that minimizes the measure. Lastly, we need to separate the pixels that correspond to particular traces and reduce them in number somehow because this will have a serious impact upon the overall speed of the autoscaling system (*i.e.*, the optimization involved in fitting is the rate determining step for speed in the autoscaling system).

The first step in feature extraction takes the grey-valued filtered image and, using grey-scale thinning, produces a skeleton that captures the shape of the traces in a single pixel wide line. The next stage, trimming, removes artifacts left by the thinning process. These stages are to reduce the amount of data under consideration. Lastly, the thinned and trimmed traces are fitted with parameterized curves. The final feature vectors consist of the parameters describing the best fitting curve along with entries giving the start and finish of the trace.

3.1. Thinning

A method to generalize binary-thinning algorithms to give grey-scale thinning is presented in [9], which it achieves by performing repeated binary thinnings between different thresholds. This technique was used to generalize the algorithm for binary-thinning due to Zhang and Suen [13]. It was used in conjunction with 16 thresholds which were chosen automatically using an automatic threshold selection algorithm [10]. Qualitatively, it was found that 16 levels produced a noticeable improvement over a smaller number of levels, whilst more than this number did not seem to have appreciable effect.

3.2. Trimming

After thinning, the thinned ionograms traces still contain two particular types of unwanted rubbish. First, there are a number of small isolated lines that are due to noise that was not removed by filtering. Second, a lot of small "spines" occur along the major thinned lines. Obviously, the removal of these artifacts would greatly improve the quality of the thinned ionograms. This can be done by the process of trimming. Along with the problem of trimming, there is also the need to segment the branch structure when trace fragments from differing propagation modes are erroneously connected. A sophisticated algorithm developed to deal with these problems is presented in [4].

3.3. Branch Selection

The result of thinning and trimming the traces of a filtered ionogram by the processes we have just considered is a branching structure that can still be rather complicated. It will contain a principal set of branches that correspond to the important shape of the ionogram trace, plus other branches that are not relevant to the important shape but have not been removed by the trimming stage. Thus branch selection is the process of choosing those branches of the thinned-trimmed traces that are deemed to be important to the shape of the trace. These components will be used in the next stage of feature extraction described in the following section. A simple branch selection is achieved using by choosing those branches in the structure that correspond to the longest pathway. However, this does fail is certain circumstances. Visually, an ionogram trace corresponding to a single propagation mode is recognizable because it is a smooth curve. Thus a more sophisticated approach is to select the longest smoothly bending pathway through the branch structure, and this can be efficiently determined from the piece-wise linear approximation to the trace already computed by the improved trimming algorithm [4].

3.4. Fitting

The next stage of the feature extraction process after thinning, trimming and branch selection centres on finding a small number of parameters that efficiently describe the shape of the selected branches in the thinned ionograms. This will be done by fitting a model shape to the thinned-trimmed traces, *i.e.*, by determining the best parameters such that a model's shape is closest to the given trace. The resulting feature vector is then passed on to subsequent processing stages which will identify disjoint pieces of the same underlying trace and merge them, and track their evolution over sequences of ionograms. The results can then be used to identify ionogram traces with propagation modes.

It may be possible to perform feature extraction by fitting directly to the filtered ionogram traces (without first thinning and trimming them) using an optimization procedure similar to the one presented in this section. In some circumstances (where there are no confusing branches present) this could achieve a better fit for each trace, but this would be at a cost of greatly increased computation. This increase would be very significant, because the optimization procedure used for fitting is the most computationally intensive algorithm employed in the whole autoscaling system.

There are two key aspects to fitting after the principal branches have been selected according to the methods presented above (see also [4,6]). They are: selecting a suitable model and finding a method of determining the best model parameters. The full details of this can be found in [6,8].

The final model was chosen to be the curve defined by[1]

$$C_\beta \equiv \{(x,y) : f(\mathbf{x} : \beta) = 1 + \sum_{i=1}^{4} \beta_i y^i + \beta_5 x = 0\}, \tag{1}$$

where $\mathbf{x} = (x, y)$, and for numerical stability, the fitting of the model to the trace data is performed in scaled local coordinates such that

$$[x_{\min}, x_{\max}] \times [y_{\min}, y_{\max}] \qquad \to \qquad [-z, z] \times [0, 1],$$

where

$$z = \frac{x_{\max} - x_{\min}}{2(y_{\max} - y_{\min})}. \tag{2}$$

The parameters for the best fit is obtained by solving

$$\begin{array}{l} \min\limits_{\beta} \ \sum\limits_{i=1}^{n} \|w_i \gamma_i\|^2 \\ \text{subject to} \quad f(\mathbf{x}_i + \gamma_i : \beta) = 0 \end{array}$$

---

[1] This model has been replaced by a more sophisticated one based on an implicit bivariate quartic equation in the ongoing work. This new approach requires a more robust fitting procedure than the one used for this paper [1].

using orthogonal distance regression [1], where w_i are a set of weights that are proportional to the intensity of the i-th pixel in the thinned-trimmed trace, and

$$\|\gamma_i\|^2 = \min_{\mathbf{x}\in\mathcal{C}_\beta} \|\mathbf{x}_n - \mathbf{x}\|^2$$

is the minimum distance of the trace point $\mathbf{x}_n$ from the curve $\mathcal{C}_\beta$.

3.5. Feature Extraction: Merging

The next stage of the feature extraction process is designed to account for broken or missing features in an ionogram. Merging is the process of reconnecting trace fragments, which clearly belong to the same propagation mode, that have become disconnected for some reason (noise, attenuation, *etc.*) and so have been fitted separately, and consequently, each has a different collection of parameters that describes its shape. Thus merging is one more step designed to move towards the ideal where each trace has a single, different and distinct propagation mode associated with it.

There are many candidates for merging. Any group of two (or more) trace fits could possibly be due to the one propagation mode and consequently are candidates. Furthermore, merging is a difficult task, and it has been found that no single test for merging works in all cases. Therefore a battery of tests is required to solve this problem. The merging problem is too lengthy to be considered here but the details can be found in [6,7].

4. MODE IDENTIFICATION AND MEASUREMENT

In this section the final stages of the autoscaling system are presented. These are, firstly, a tracking stage that is designed to assist mode identification in circumstances where one or more of the simple modes are missing from the ionogram because of various ionospheric effects. Secondly, a mode identification stage which makes use of an ionospheric model to identify the propagation modes of each trace. Lastly, possible further measurements are outlined.

4.1. Time-Series Tracking

The motivation for the time-series tracking stage is that ionograms are collected at regular intervals during which they usually do not change a great deal. Therefore, information gleaned from one ionogram can be used to make the task of identifying the modes of successive ionograms much easier.

In some ionograms in a sequence, the 1-hop is almost completely missing, and what remains is unlikely to survive filtering. This absence could present difficulties to a mode identification scheme that did not realize when this has occurred. However, it is rather obvious when the modes are tracked across successive ionograms.

The time-series tracking could be achieved by a simple matching of the feature vectors in successive ionograms. Usually there is an excellent correspondence between the shape of merged fits of successive ionograms in time that are due to the same propagation mode, even though they may move around in group-delay and frequency. Therefore, the feature vectors determined from the previous processing stages is ideal as an input to the tracking stage. This approach has beneficiary side effects in that it could assist in merging.

The first step in matching features across successive ionograms is to transform β from each of the fits into the same coordinate system so that the fits being compared are at the same scale. The best match can be found using an optimization procedure [6] or by computing invariants of the polynomial coefficients [3].

After finding the best match between each pair of trace fits, a search is performed to find the best possible set of these matches between the features subject to the condition that the translation of a particular propagation mode's trace from one ionogram to the next should be similar to that of other traces. As a possible extension to this approach, a Kalman filter could be used to predict the location of each trace of a particular propagation mode in the next ionogram to narrow down the number of possible comparisons between trace fits.

4.2. Mode Identification

The purpose of mode identification is to determine the hop number of traces that are due to simple propagation modes through the ionosphere. This is the second last stage in the overall autoscaling system, and the first

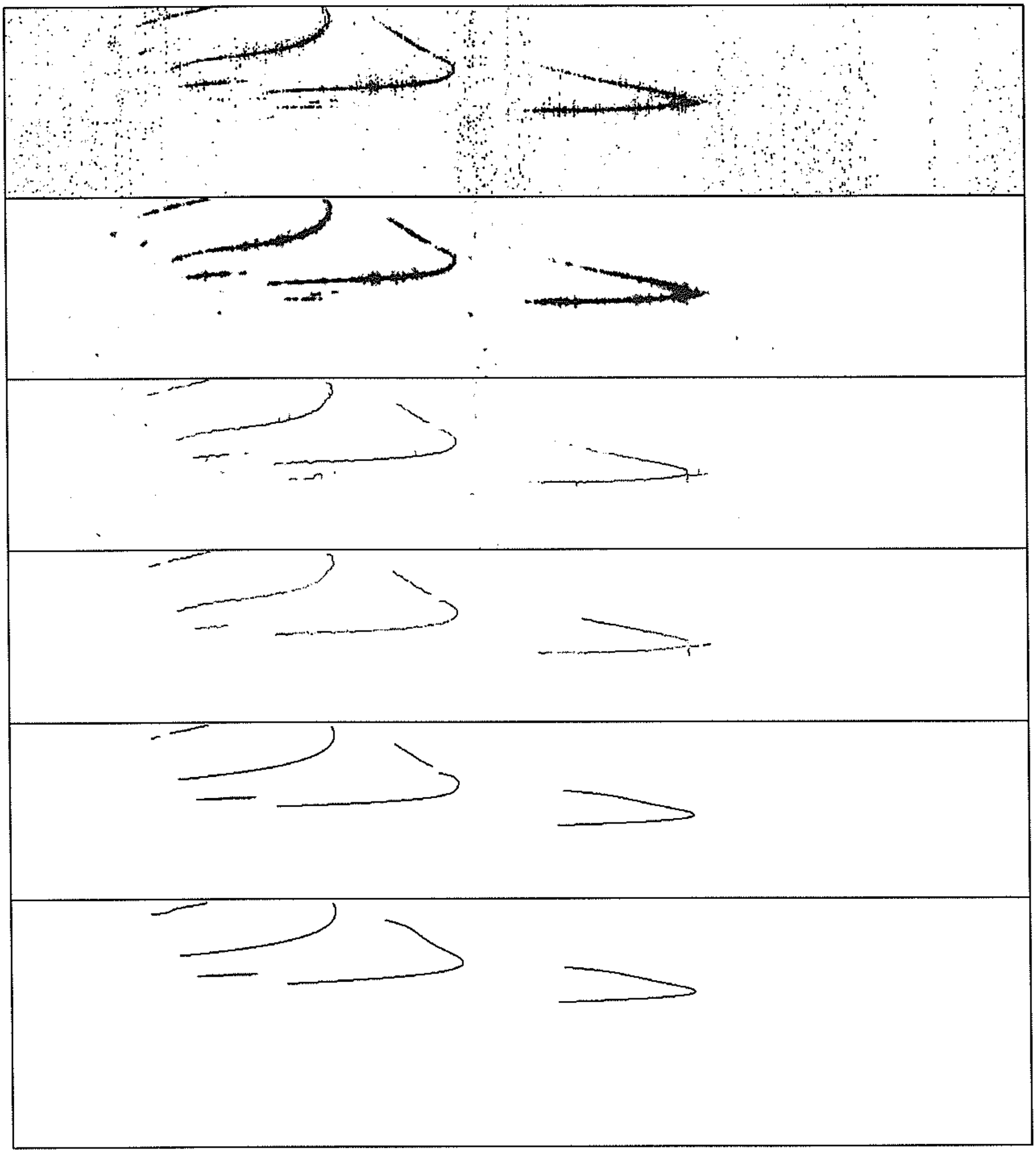

Figure 3: An example ionogram at each step in the image understanding problem. From the top is the original image, then the result of filtering, thinning, trimming, fitting, and merging.

one that will produce quantitative results for the user. This last stage departs from strict image processing and feature extraction domains to incorporate simple ionospheric physics (problem-specific knowledge) to complete the solution of the image understanding problem.

The mode identification stage is broken up into a number of smaller steps. The first of these determines which trace in the fitted ionogram is the 1-hop trace. Mostly this will be the right-most trace except mainly in two special circumstances. Sometimes when the ionosphere contains a strong phenomenon called a sporadic-E layer and the path length from transmitter to receiver is short a trace that bounces off this layer may extend in frequency out past the 1-hop trace. However, it is possible to identify traces due to sporadic-E layers in group-delay and thereby eliminate them. Secondly, the 1-hop trace may be missing from the ionogram, but the tracking stage of the previous section has been designed to recognize when this occurs. If the 1-hop trace is missing, then we continue the processing using the 2-hop trace instead and we must make some corresponding changes later on. Thus, after eliminating the two special cases, determining the 1-hop trace fit (or substituting the 2-hop) should be quite straight forward.

The next step assumes that we have a reasonable ionospheric model for oblique ionogram traces that can be used to predict the higher hops from knowledge of the 1-hop. Given then that we have a fit for the 1-hop trace (ignoring for a moment the complication of substituting a 2-hop for a non-existent 1-hop), we now have to find the parameters for this simplified ionospheric model so that there is a good correspondence between the 1-hop trace of the model and the 1-hop fit. This is not a trivial procedure because of the complexity of even a simplified ionospheric trace model as we will see.

Once a good fit of the ionospheric model's 1-hop (or 2-hop) to the appropriate trace of the ionogram has been obtained, the next step is to determine where this model predicts the higher order hops will occur. Then, lastly, these trace predictions are cross-matched against the other fitted traces in the ionogram — the correspondences that occur will indicate the propagation mode of the important ionogram trace fits. Any traces that are not identified by this procedure will be due to complex propagation modes and are of lesser interest.

4.2.1. Ionospheric Model

Let us now consider the ionospheric model. The model is due to Lynn [5] (derived from [2]) and was produced by range converting a vertical incidence ionogram, based on a single parabolic layer, to an oblique incidence one. The model firstly defines the equation for a trace of a vertical ionogram derived from a parabolic electron density as

$$h_1 = h_0 + \frac{b}{2} f_1 \ln \left[\frac{1+f_1}{1-f_1} \right] \tag{3}$$

where h_0 is the height of base of ionosphere (200–300 km), h_1 is the vertical reflection height, b is the distance from base to peak electron density heights (10–150 km), and f_1 is a parameter of the model with range $0 < f_1 < 1$. Using conversion formulae for sky range [5], the equivalent oblique ionogram's time-delay t (in milliseconds) is given by

$$t = \frac{1}{150} \left[a^2 + (a+h_1)^2 - 2a(a+h_1) \cos\left(\frac{d}{2a}\right) \right]^{1/2} \tag{4}$$

and its frequency f by

$$f = \frac{f_s f_1}{\left[1 - \left\{ \frac{a}{150t} \sin\left(\frac{d}{2a}\right) \right\}^2 \right]^{1/2}} \tag{5}$$

where a is the radius of the earth (6371 km), d is the path length (distance of transmitter to receiver (300–6500 km)), and f_s a frequency scaling parameter. Higher hops can be calculated by dividing path length by the hop number and multiplying the resulting time-delay by the same factor.

Substituting (3) into (4) and (5) and including the hop number denoted by n, results in a model for an oblique ionogram trace that is given by two parametric equations with parameter $0 < f_1 < 1$ and variables h_0, b and f_s.

4.2.2. Range Conversion Fit

We now have a suitable ionospheric model with which to predict the location of higher hops given a good fit to the 1-hop (or 2-hop) just by varying n in the parametric model. The problem that has to be solved is how to find a set of values for h_0, b, and f_s, given the feature vector for this one trace. This can be achieved by an optimization procedure, the details of which are ommitted here [6].

4.2.3. Cross-Matching the Traces

The process of cross-matching the predicted higher hops of the ionospheric model against the fitted traces of the ionogram will be straight forward. All that is required is to determine if there is a trace that lies under the predicted higher hops for much of its length. Note that the predicted traces are least accurate around the nose region, so emphasis should be placed on the lower ray when determining a match. The complex modes are identified as the remaining traces.

4.3. Measurements

The full scope of the measurement has yet to be resolved, and will need to be more fully determined by user's requirements. None the less, the sort of measurements that could be determined by this system are illustrated in figure 1.

5. CONCLUSION

In conclusion, I have presented all the stages necessary to implement an image understanding system for oblique ionograms. These stages include a clean-up stage, feature extraction, and a final measurement stage.

Acknowledgements

I wish to thank Garry Newsam for his valuable suggestions and comments, and David Kettler and Bob Whatmough for their contribution to the algorithms.

References

[1] P. T. Boggs, R. H. Byrd, J. E. Rogers and R. B. Schnabel, "User's reference guide for ODRPACK version 2.01 software for weighted orthogonal distance regression," Applied and Computational Mathematics Division, National Institute of Standards and Technology, U.S. Department of Commerce, NISTIR 92-4834, 1992.

[2] K. Davies, Ionospheric Radio. Peter Peregrinus Ltd, 1990.

[3] D. Keren, "Using symbolic computation to find algebraic invariants," IEEE Transactions on Pattern Analysis and Machine Intelligence, **16**, no. 11, pp. 1143–1149, 1994.

[4] D. I. Kettler and N. J. Redding, "A trimming algorithm to clean thinned features for feature extraction in image understanding," presented at Proceedings of Fourth Australian and New Zealand Conference on Intelligent Information Systems, Adelaide, South Australia, Nov., 1996.

[5] K. J. W. Lynn, "Ionogram range conversion," unpublished note, 21 May 1992.

[6] N. Redding, "The autoscaling of oblique ionograms," DSTO Electronics and Surveillance Research Laboratory, Salisbury, South Australia, Australia, DSTO-RR-0074, 1996.

[7] N. J. Redding and G. N. Newsam, "A merging procedure for connecting fitted implicit polynomials for features," presented at Proceedings of Fourth Australian and New Zealand Conference on Intelligent Information Systems, Adelaide, South Australia, Nov., 1996.

[8] N. J. Redding, "Fitting implicit polynomials to use as features in image understanding," presented at Proceedings of Fourth Australian and New Zealand Conference on Intelligent Information Systems, Adelaide, South Australia, Nov., 1996.

[9] M. Roughan, "A method for generalising binary skeletonisation algorithms to grey-scale images," Cooperative Research Centre for Sensor Signal and Information Processing, draft report, June 27, 1995.

[10] R. J. Whatmough, "Automatic threshold selection from a histogram using the "exponential hull"," CVGIP: Graphical Models and Image Processing, **53**, no. 6, pp. 592–600, 1991.

[11] R. J. Whatmough, personal communication, 1993.

[12] C. S. Wright, D. I. Kettler, P. L. Trudinger, W. P. Malcolm, B. Sprey, D. Taylor and R. H. Clarke, "The LLISP data base of low-latitude oblique-incidence ionograms," presented at Proceedings of the Trans-Equatorial and Near Equatorial Radio Propagation Conference, Monterey, California, June, 1993.

[13] T. Y. Zhang and C. Y. Suen, "A fast parallel algorithm for thinning digital patterns," Communications of the ACM, **27**, no. 3, pp. 236–239, 1984.

AUTOMATIC OBLIQUE-INCIDENCE IONOGRAM INTERPRETATION

V. I. Kurkin, V. E. Nosov, and S. N. Ponomarchuk
Institute of Solar-Terrestrial Physics, P.O.Box 4026,
Irkutsk 33, 664033, Russia e-mail: rp@istp.irk.ru

ABSTRACT

A technique for the automatic interpretation of oblique-incidence ionograms, obtained from a continuous chirp-signal ionosonde is presented in this paper. The algorithm for identifying modes of propagation involves determining a maximum of the histogram of the experimental point number distribution that falls within the mask. The mask is constructed using the results of a computer ionogram modelling and adiabatic relationships for previously established signal characteristics. Points inside the mask are tallied up as the mask is displaced through a parallel translation until the cusp of the lower and upper rays is coincident with selected signal arrival time points. Results of computer-aided oblique-incidence sounding ionogram interpretation on the Magadan-Irkutsk path are presented.

1. INTRODUCTION

Modern frequency management technology for HF communications using ionosondes needs processing and interpretation of the received ionograms Because the radio waves propagate in a complex and dynamic medium, the amplitude envelope of observed signals has a complicated shape. When statistical processing the observed images, it is possible to find a group of points corresponding to times of signal arrival with a significant amplitude. For the determination of HF bands it is necessary to separate tracks and to interpret their meaning.

One possible way to interpret oblique-incidence sounding (OIS) ionograms, with the subsequent construction of tracks, is artificial neural networks [1]. Another approach is to use a mask that is constructed by computer simulation. The mask is moved over an ionogram and the arrival times for points falling in the mask are tallied up. Determination of the histogram maximum for the experimental point number distribution makes it possible to calculate the values of the maximum usable frequency (MUF) and group path at this frequency. Constructing a track, using points falling in band mask, is then possible.

This paper presents results of the computer-aided interpretation of OIS ionograms obtained from an ionosonde with a continuous chirp-signal [2], modified for oblique-incidence and backscatter sounding. It is anticipated that pre-treatment of experimental data has been carried out to give an image in the form of "clouds" of points with a significant amplitude on the coordinates: group path and operating frequency, i.e., there exists a matrix of experimental points, P_{ij}, corresponding to a two-dimensional set of values of group path P_i on the frequency grid f_j [1].

2. IONOGRAM INTERPRETATION TECHNIQUE

The technique for interpreting oblique-incidence ionograms from sounding by chirp-signals is based upon using results derived by modelling OIS ionograms on a given path using long-term prediction models and adiabatic relationships between frequency and group-path signal characteristics for different propagation modes. Model OIS chirp-signals ionograms are simulated using an operational algorithm for modelling chirp-signals characteristics using a normal mode approach[3].

By analyzing the OIS signal's group characteristic frequency dependencies under different geophysical conditions, it was possible to show the following relationships which were slowly vary with a change of ionospheric parameters [4]:

- the ratio of the group path P_m , corresponding to the signal delay received at the maximum usable frequency, to the range to the illuminated zone boundary D_m;
- the ratio of MUF modes of different radio paths.

The above ratios are confirmed by oblique-incidence sounding signal characteristic model calculations for the case of a 20% change in the ionospheric parameters. In addition, this is also confirmed by the analysis of experimental OIS data obtained from a chirp-sonde.

In doing model calculations of OIS ionograms and analyzing experimental ionograms, it was also noted that the group path of the OIS signal depends weakly on a change of ionospheric parameters on the relative frequency grid $\beta = f/f_m$; f_m being the maximum usable frequency for the mode of a chosen range [5]. Especially, this property is strongly manifested for signals that propagate by the low ray.

For interpreting oblique-incidence ionograms, it is possible to make the following assumptions. In the case of ionospheric parameter variations within long-term prediction errors, there remain:

- the ratio of the group path P_m at the junction point of the lower and upper rays of any one of the modes to the path length;
- the ratio of the MUF modes (χ) of different multiples that propagate in one of the waveguide channels (their lower wall is the terrestrial surface, and the upper layer is the *E*, *F1* or *F2* region);
- the group path of one mode, of multiple l, on the relative frequency grid $\beta = f/f_m$, l, where f_m, l is the MUF mode for the range under consideration.

An algorithm for interpreting oblique-incidence ionograms under automatic conditions is constructed in the following manner. Model OIS ionograms are calculated for a given path under long-term prediction conditions. Results of calculations are used to choose the reference propagation mode, l_o, on the path being analyzed for a given run. Usually, it is represented by the mode with the minimum number of reflections (l_{min}) from the *F2*-layer, whose maximum frequency does not exceed a limiting sounding frequency. The distinctive feature of this mode is a reasonably good coincidence of the dependence of the group path on the frequency of the modelled and observed ionograms in the vicinity of the mode MUF (on the relative frequency grid) for both the low and high rays. Based on this, a model mask is then constructed for the mode of multiples, l_o, including two bands with a width of ΔP km (vertically) and a frequency range from $0.7 f_{mp}$ to f_{mp}, where f_{mp} is the predicted MUF of the reference mode, for the low ray and of an extent from $0.8 f_{mp}$ to f_{mp}, for the high ray. The bandwidth, ΔP, can be varied within 50 km.

Fig. 1a shows an observed ionogram, for a 3000 km path reflected from a single layer winter ionosphere. Results of signal pretreatment are shown by dark squares. The figure also gives the results of a numerical simulation of the OIS ionogram for the same path under long-term prediction conditions. For the mode with minimum multiples, the MUF prediction error is about 18%.. Fig. 1b illustrates the method for constructing the mask on a relative frequency grid β.

The algorithm for identifying the reference trace on the ionogram implies counting the number of arrival time points in the matrix of P_{ij} signals as the model mask moves over the ionogram. Methods for displacing the mask on the ionogram and counting the number of arrival time points, depend substantially on whether there is absolute referencing of the group path scale in the experiment. When there is absolute referencing of the group path then one may take advantage of one of adiabatic invariants: the ratio of the group path P_m, corresponding to the MUF mode, to the range. Hence, a rectangle on the ionograms is selected in which the model mask will be displaced, centered on a point corresponding to the frequency f_{mp} and the predicted group path value on this frequency P_{mp}. The size of the rectangle is $[f_{mp} - \gamma f_{mp}, f_{mp} + \gamma f_{mp}]$ horizontally and $[P_{mp} - \alpha\Delta P, P_{mp} + \alpha\Delta P]$ vertically, where α and γ are numerical parameters. P_{ks} points of the entire point set P_{ij} fall inside the chosen rectangle. By displacing the mask through a parallel transfer until the junction points of the lower and upper rays match with P_{ks} points, the number of P_{ij} matrix elements inside the mask is calculated. In this case the mask starts its displacement from the right-hand side of the rectangle, and at every step the mask bands are scaled by the factor f_s/f_{mp} along the horizontal axis. The maximum on the histogram of the distribution of the number of experimental points depending on the position of the mask makes it possible to determine the value of the MUF, f_{mr}, and the group path at this frequency, P_{mr}, for the propagation mode of multiple *lo*. If the maximum number of points corresponding to the mask is less than some number (say four, for example), it is presumed that the mode of multiple *lo* is not identified, and the procedure is repeated for the mode of multiple *lo+1*. The mode of multiple *lo+1* is also used when the reference mode leaves the right-hand edge of the ionogram. Therefore, prior to identifying the reference mode, it is necessary to 'scan' the right-hand edge of the ionogram with a rectangular mask, with a size of

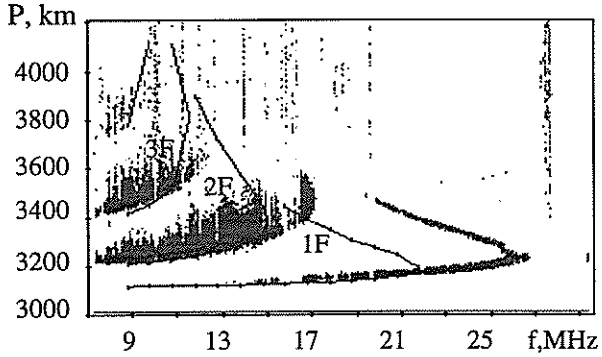

Fig.1a.Experimental OIS ionogram, and longterm prediction results for February,15,1989.

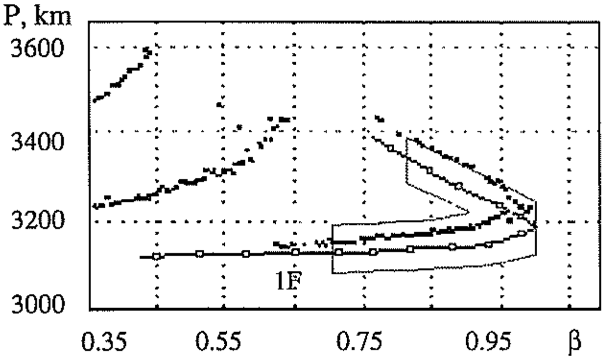

Fig.1b.Experimental OIS ionogram, and longterm prediction on the relative frequency grid.

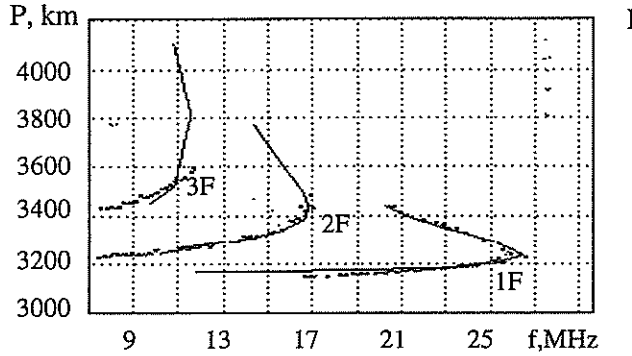

Fig.1c.Processing and identification results on the OIS ionogram for February,15,1989.

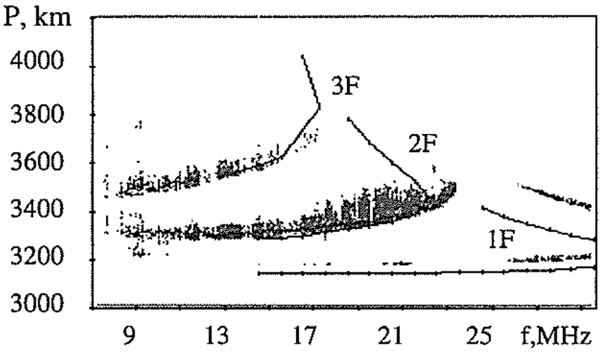

Fig.2a.Experimental OIS ionogram, and longterm prediction results for October,25,1989.

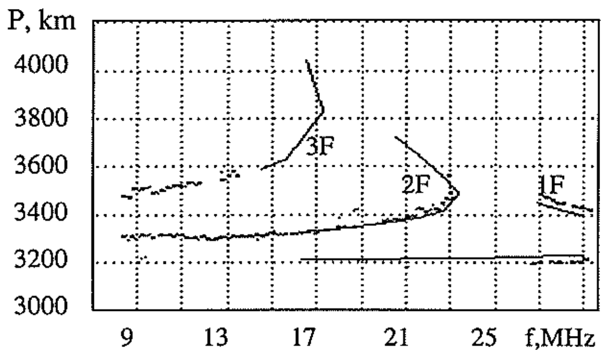

Fig.2b.Processing and identification results on the OIS ionogram for October,25,1989.

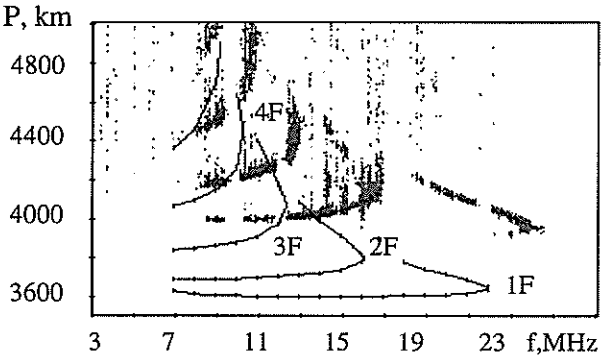

Fig.3a.Experimental OIS ionogram, and longterm prediction results for October, 9,1992.

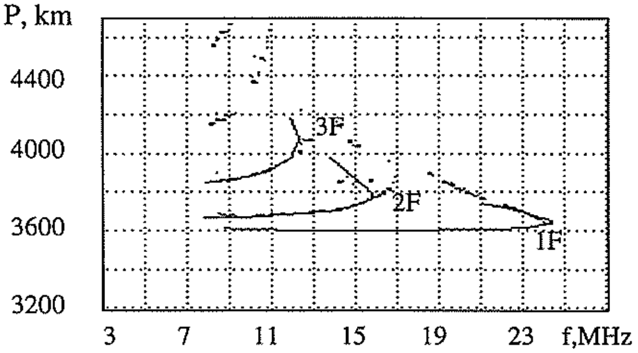

Fig.3b.Processing and identification results on the OIS ionogram for October, 9,1992.

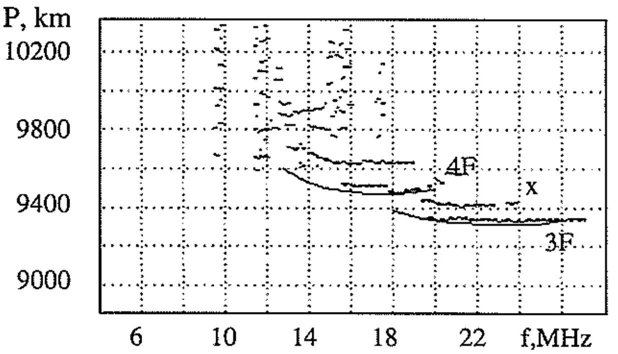

Fig.4.Processing and identification results on the OIS ionogram for March, 9,1996.

1000 kHz horizontally and ΔP vertically. When determining f_{mr} and P_{mr}, the remaining observed points, corresponding to the mode of multiple lo, are identified by extending the mask bands into the low frequency region along a model OIS ionogram, scaled by the factor f_{mr}/f_{mp}, and by looking for P_{ij} elements corresponding to these bands.

The adiabatic character of the MUF ratio of modes of different multiples $\chi_k=f_{m,k}/f_{m,s}$, $k=s\pm 1$ is used to calculate the tentative MUF values of other modes of multiple l: $f_{m,l}=f_{mr}\,\chi_l$, $l=lo\pm 1$. Values of the group path P_{m},l can be assumed equal to predicted values. The values determined in this way serve as the center of the rectangle inside which the real values of f_{mr},l and P_{mr},l are found following the above procedure of constructing a histogram of the number of points corresponding to the mask as it is displaced. Subsequently, a sequence of experimental points is formed that correspond to the neighbourhood of the scaled model ionogram with modes of multiple l. Modes of multiple $lo+2$ etc. are identified in a similar manner.

If there is no absolute referencing of the group path scale, the junction point of the upper and lower rays must be found by scanning a model mask throughout the entire ionogram. In this case, two displacement variants of the model mask exist: one is when the mask moves from the right-hand lower corner upward in group path at steps ΔP and to the left in frequency at steps Δf (of about 500 kHz); the other variant is when the mask moves through the points of the matrix P_{ij} by making the 'nose' match with the point $P_i(f_j)$. In the former method of displacing the mask, for each current frequency f_k we construct a histogram of distribution of points P_{ij} which fall within the mask during its parallel transfer along the vertical axis at steps ΔP. The maximum value of the number of observed points n_k, and also the corresponding (for this mask position) value of the group path for the junction point of the high and low rays $P(f_k)$ are memorized. After passage of the entire operating frequency range, we construct a histogram of distribution of n_k -values in frequencies f_k. An absolute maximum of this distribution makes it possible to determine the center of the rectangle, i.e. the frequency f_m and the group path P_m, inside which more accurate values of f_{mr} and P_{mr} are sought in the same manner as done in the presence of referencing to the common timing system. If the number of experimental points in the distribution maximum is larger than four, then the mask for the mode of multiple $lo+1$ is used, and the whole procedure is repeated.

The second method of displacing the reference mode mask is used to count the number of points corresponding to the mask from the points P_{ij} and a maximum of the histogram of the distribution in these points corresponds to values of f_{mr} and P_{mr}. By determining f_{mr} and P_{mr} for the reference mode, taking into account the adiabatic group path on the relative frequency grid, it becomes possible to accomplish referencing the group path scale of the ionogram by shifting the origin by an amount equal to the difference between the predicted value of P_{mp} and P_{mr}. Subsequently, the sequences of experimental points corresponding to the neighborhood of the scaled model ionograms of other modes are identified and formed in much the same way as in the case described previously when signal delays are recorded.

In some cases the algorithm for automatic identification of oblique-incidence ionograms does not reliably identify the arrival time points of signals for the observed ionogram. This is associated with the presence of severe geophysical conditions on the sounding path (disturbances, interference, ionospheric stratification) and with errors inherent in long-term predictions. In such a case it is possible to employ the semi-automatic ionogram identification approach. Identified arrival time points of signals are also the input ones. Ionogram traces are interpreted based on a long-term prediction and experience in interpreting oblique-incidence sounding ionograms.

3. RESULTS OF IONOGRAM INTERPRETATION

Our algorithms developed for processing and interpreting OIS ionograms were tested on observed ionograms obtained on the 3000 km long path between Magadan and Irkutsk. Fig. 1c illustrates the implementation of the algorithms for the case of a single layer, winter ionosphere. Differences in group path in the presence of referencing to the common timing system are insignificant. Thus the junction point of the high and low rays on the ionogram falls within the search rectangle centered on the junction point of the rays on the predicted ionogram. In accordance with the search algorithm for the real MUF f_{mr} and the group path P_{mr}, corresponding to this frequency, the mask was displaced until the best match of the predicted and observed ionograms was achieved. For the ionogram concerned, the result of matching automatically is shown in Fig. 1c. The mode with minimum multiples is identified as 1F. In addition, the 2F and 3F modes are identified on the ionogram.

This case refers to the simplest kind of ionogram. The identification procedure for observed points is more complicated if the real MUF of the mode of minimum multiple *lo* exceeds the upper boundary of the operating frequency range of the chirp-sonde. In such a case the mode of multiple *lo+1* is taken to be the reference mode, and upon reaching f_{mr} and P_{mr} the mask for identifying experimental points belonging to the mode *lo* is constructed allowing the junction point of the high and low rays of this mode to lie outside the operating frequency range limits. Figures 2a and 2b illustrate the operation of a program for automatic interpretation of the oblique-incidence sounding ionogram in this case.

A further complication is associated with the absence of a common time system reference. It is evident from Fig. 3a that in this case experimental points and the predicted ionogram can differ greatly in group path. This does not permit us to indicate the approximate position of the junction point of the high and low rays of the reference mode. The approximate position is determined by scanning the mask throughout the entire ionogram at uniform steps in frequency and group path. Results of automatically referencing the observed ionogram vertical scale and the interpretation of the ionogram to observed points of the 1F mode is shown in Fig. 3b. According to the technique developed, the reference mode mask is built out of two bands in the neighborhood of the predicted ionogram corresponding to the high and low rays of the 1F mode, although the low ray is not present on the experimental ionogram. Nevertheless, sequences of experimental points are automatically identified satisfactorily in the example.

By testing the identification algorithm, we have demonstrated its suitability for winter and night-time summer conditions on one hop paths. In these cases, the speed and accuracy of ionogram interpretation depends critically on referencing the diagnostic system to the common timing system. Summer daytime ionograms present the greatest problems for accomplishing of automatic ionogram interpretations. Automatic ionogram interpretation is also difficult on long paths when, in addition to standard modes, combined propagation modes are present. As an illustration, Fig. 4 shows results derived for a 9000 km path OIS ionogram. The symbol "x" marks the combined mode which was not interpreted by the algorithm.

4. CONCLUSIONS

Our software package is useful for the pretreatment of ionograms, detection of traces and identification of modes. It can be used as a component part of a system for automatically selecting radio frequencies for a radio-communication link based on results of ionospheric channel sounding by the chirp-signal.

References

[1] V.P.Grozov, N.V.Nosov et al. XXVth General Assembly of URSI, Abstracts, Lille, France, p.395, 1996,.

[2] I.G.Brynko, I.A.Galkin et al. Adv. Space Res., , v.8, No.4, pp.(4)121-(4)124, 1989.

[3] N.V.Ilyin, V.I.Kurkin, et al. Researches on Geomagnetism, Aeronomy and Solar Physics, Moscow: Nauka, v. 104, pp.149-157, 1995.

[4] V.I.Kurkin, V.E.Nosov et al. Proceedings of International Symposium on Antennas and Propagation. Sapporo, Japan, pp.1189-1192, 1992.

[5] V.I.Altyntseva, I.G.Brynko, et al. Researches on Geomagnetism, Aeronomy and Solar Physics, Moscow: Nauka, v.96, pp.92-103, 1991.

OBLIQUE-INCIDENCE-SOUNDING AS AN AID TO ANALYSIS OF HF COMMUNICATION SCENARIOS: SUMMARY OF A MULTI-STATION EXPERIMENTAL CAMPAIGN[1]

John M. Goodman[2], John W. Ballard, Eugene D. Sharp, and Trung Luong

TCI/BR Communications, Sunnyvale CA 94089

1. INTRODUCTION

A comprehensive HF channel data collection campaign was initiated in December 1994 and has continued well into calendar 1996. We call this the Northern Experiment. A major consideration in station selection for the Northern Experiment was a need to mimic as closely as possible the climatological conditions to be experienced by HF Data Link communication (HFDL) over a generic set of aircraft flight paths across the North Atlantic. To do this we recognized that ionospheric conditions in the F region are best organized by geomagnetic field considerations rather than geographic coordinates. Since the magnetic pole lies somewhat equatorward in the American sector, Chirpsounder® (T and R) deployments in Canada and CONUS, which serve as proxies for the aircraft platforms and the aggregate of service provider stations, map from greater geographic latitudes. In short we map the source to a candidate proxy environment which has similar magnetic field conditions. We refer to this process, if done successfully, as climatological invariance.

Using selected Chirpsounder® systems deployed throughout the northern hemisphere, concentrating on the North American sector, over 28 paths have been evaluated. These paths have been grouped to ascertain the relative correlation properties, and the resultant data are being used to validate emerging real-time ionospheric and HF performance prediction models. Transmitters are located at Jan Mayen, Reykjavik, Stockholm, Madrid, Tors Cove (Newfoundland), Puerto Rico, Edmonton (Canada), Vancouver (Canada), and San Francisco. Receivers are located in Stockholm, Reykjavik, Tors Cove, Iqaluit, Fairbanks, Churchill (Canada), Winnipeg (Canada), Austin (Texas), Henrico (North Carolina), and San Francisco. Oblique-incidence ionograms are recovered remotely and downloaded to a data collection center at TCI/BR headquarters in Sunnyvale, California. Figure 1 is a map showing the communication paths which were monitored during the Northern Experiment. The transmitters and receivers are indicated by TX and RX respectively. Path distances between nodes are shown.

Preliminary results of the Northern Experiment have been presented at the 1996 Ionospheric Effects Symposium [1], and additional information about the use of Oblique-Incidence Sounders for communication assessment may be found in [2].

2. DATA COLLECTION AND MEASUREMENT PROCEDURES

Each Chirpsounder® receiver site was programmed to recover ionograms from up to four transmitters at a rate of twice per hour. The receiver passed the digital ionograms to a storage device which was controlled by a collocated PC. The site were equipped with an upload feature which could initiated through a dial-up capability. All data sets were uploaded to a central processing facility located at Sunnyvale California.

---

[1] based upon full paper submitted to Session G5: Computer-Aided Processing of Ionograms and Ionogram Records; URSI

25th General Assembly in Lille, France on 28 August - 5 September, 1996.

[2] TCI/BR Communications, STE 200, 601 Madison Street, Alexandria VA 22314; Email: QJYQ48A@prodigy.com

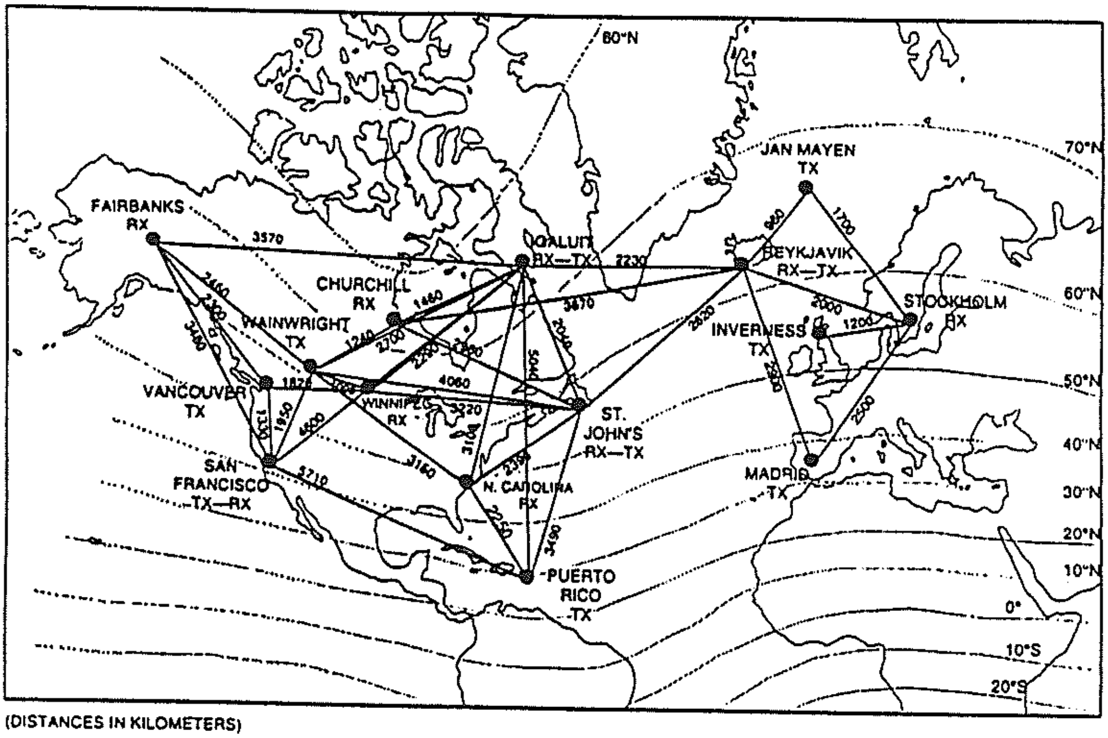

(DISTANCES IN KILOMETERS)

Figure 1. Geometry of the Northern Experiment

While a considerable amount of scientific information is contained in the data base which has been archived, our analysis has been principally conducted with the view directed toward the elucidation of HFDL performance for specified service areas (determined by a given group of sounder nodes) for various groups of frequencies. The Chirpsounder® system provides data for the entire HF band excluding a limited number of blocked channels. We extracted data from the sounder records at specified Aeronautical-Mobile (AM) bands which were also covered by the sounder scan. We also obtained estimates of the noise level for each AM band, and we computed the Signal-to-Noise ratio (SNR) for each band. These data were compared with the minimum values of SNR required to pass traffic at bit rates from 300 to 1800 bps.

The sounder receivers used in the experiments measure the Signal plus Noise (S+N) and Noise (N) in a 500 Hz bandwidth in 100 kHz steps throughout the 2-30 MHz HF spectrum. Specifically, the S+N and N are sampled and averaged over the upper 50 kHz of each 100 kHz slice of spectrum. As the sounder transmitter is sweeping through each 100 kHz, which takes 1 second, the sounder receiver is performing two different measurements in time sequence. All the measurements are divided into one second time frames that correspond to 100 kHz of frequency sweep. During the first 0.5 second that it takes to sweep 50 kHz, the sounder receiver is offset tuned to sweep the upper half of the 100 kHz frequency spectrum while the sounder transmitter is sweeping the lower half of this 100 kHz spectral region; thus the receiver does not receive signals from the sounder transmitter during this first 0.5 second. Rather, during this time the receiver is measuring HF noise as well as interference from unwanted stations. During the second 0.5 second of each frame, the receiver is synchronized with the remote transmitter and a measurement of S+N is made. In the analysis of S+N and N, four independent samples are taken, spaced 0.1 second or 10 kHz apart. The sample amplitudes thus represent averages over the 500 Hz bandwidth, and these values are stored for subsequent analysis. Ultimately the measurements are related to a bandwidth of 3 kHz.

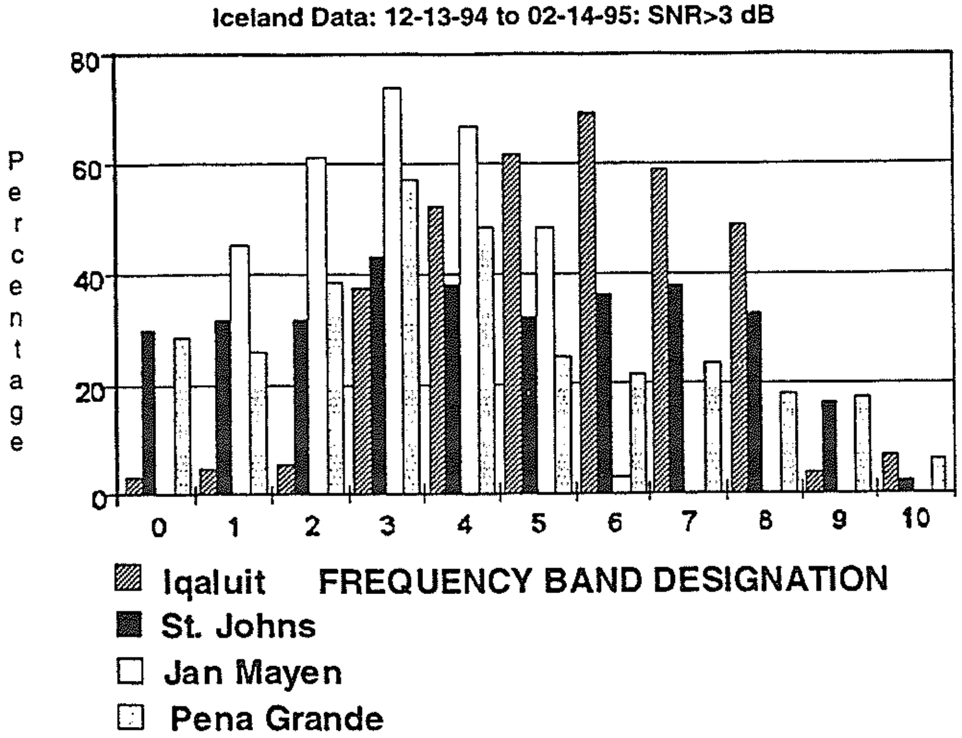

Figure 2 (a). Percentage availability of signals in the Aeronautical-Mobile bands received at Iceland and transmitted from Iqaluit, St. Johns, Jan Mayen, and Pene Grande (Madrid, Spain) over a 2-month period (12-13-94 to 02-14-95).

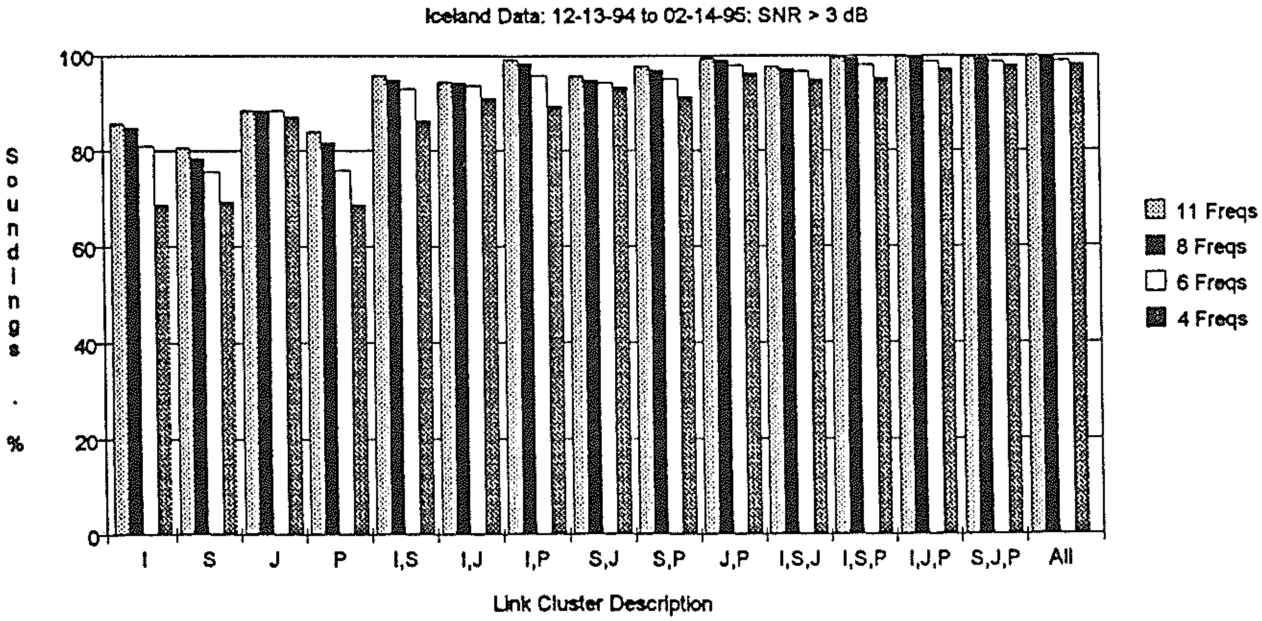

Figure 2(b). Percentage availability of signals at Iceland for selected frequency groups and transmitter station combinations. (For each group of four, the ordering from left to right is 11, 8, 6, and 4 frequencies respectively.)

Figure 2 contains analyzed data obtained at Iceland from transmitters at Iqaluit, St.Johns, Jan Mayen, and Pena Grande. These plots address the issues of space and frequency diversity. Figure 2a gives the percentage of successful threshold crossings as a function of frequency band designation, for each path. involved and for the period 12-13-94 to 02-14-95. (In this instance the threshold corresponds to the SNR requirement for successful modem operation at a data rate of 300 bps). Figure 2b exhibits the percentage availability of HFDL service for each path and for frequency groups of 11, 8, 6, and 4 frequencies respectively. The advantage of combining paths is obvious. It is of some interest to note that if all stations are used, then 4 frequencies will suffice in this particular example. Obviously it is essential that we have a good selection of frequencies, and the more we have the better. However they must be the correct frequencies. In any case there should be no dispute that station diversity is an important mitigation tool.

Correlation of variability relates directly to the issue of network diversity. From the point of view of nowcasting, in which we wish to use a control path as an update source for a remote communication path, high spatial correlation is good. But from a network engineering point of view, rapid decorrelation of disturbance amplitude with distance only assists in the successful application of diversity solutions in netted communications. We have observed a distinction in correlation for benign and disturbed conditions. We see that the correlation is greater as the magnetic activity is enhanced, a fact which has been observed by other workers. This suggests that link impairments are larger in amplitude and larger in scale as the magnetic activity level becomes enhanced. In practical terms, this means that we must select widely separated paths under stormy conditions, or accept lower diversity gain.

3. SYNOPSIS OF RESULTS

A practical system design includes a specification of the number of ground station transmitters, hereafter termed GSs, and frequencies to provide HFDL communication on a worldwide basis. As HF practitioners are well aware, a variation in network topology or a change in the frequency list will lead to differing levels of link and network performance. This situation is also quite region-specific.

There are a number of conclusions which have been reached based upon the data collected during the Northern Experiment, and the analyses which have been carried out. The major conclusions are given below. Some flow directly from axiomatic principles of HF propagation and the ionospheric interaction.

1. Studies have shown that connectivities approaching 100% may be achieved provided one has access to four widely-separated GSs, and can select from among a pool of frequencies residing in the eleven aeronautical-mobile bands (3.0, 3.5, 4.6, 5.6, 6.6, 9.0, 10.1. 11.4, 13.3, 18.0, 22.0 MHz), wherein the selections are dynamic, based upon full-band sounding.
2. Based upon the principle of space diversity, we find that HF connectivity between a central node (i.e., aircraft) and a cluster of GSs is improved substantially if the cluster population is increased. Conditions dictate the size of the cluster of GSs, but it has been shown that four stations are fairly optimum if the geometry is specified properly.
3. The cluster (i.e., network) connectivity is enhanced if the correlation between the paths linking the clusterhead (i.e., aircraft) and the GSs is low.
4. The overall network consists of an assembly of subnets or clusters, with the primary distinction between them being the respective clusterheads (i.e., aircraft designation) although not all clusters will have the same GSs. By definition, these clusterheads are evolving, first because the aircraft is moving, and secondly, because the ionosphere is changing. Frequencies which were once optimum will not remain so for very long. It also points to the importance of dynamic management of network resources, including the swapping of frequencies between ground stations.
5. System availability is seen to decrease with increasing magnetic activity. (See Figure 3)
6. Dynamic frequency management is superior to a method of frequency management using static predictions. (See Figure 4)

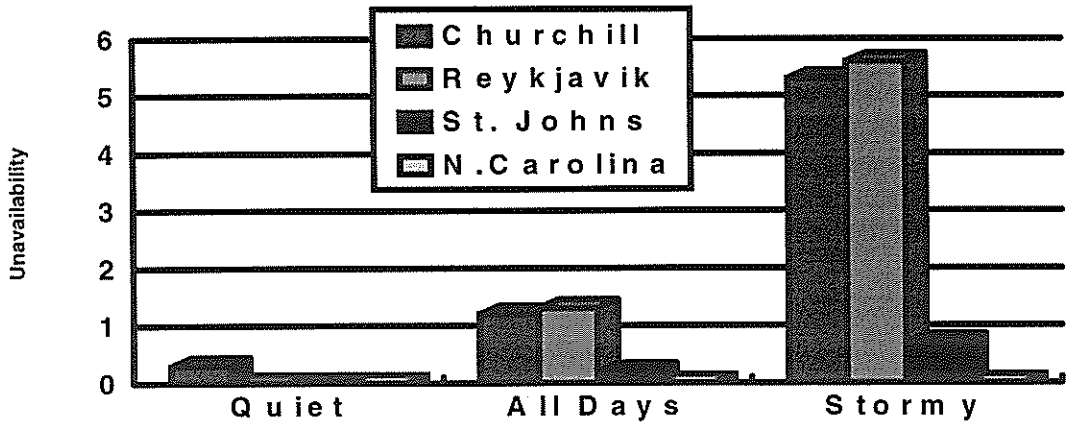

Figure 3. The unavailability of communication, in percent, as a function of magnetic activity conditions for four star-net clusters during April of 1995, a month a wide-ranging variation in the magnetic activity parameter Ap. The clusterheads are located at Churchill, Reykjavik, St. Johns, and North Carolina, and each cluster consists of four paths terminating at the clusterhead. In this sample calculation, each star-net has access to one frequency in each of the eleven aeronautical-mobile bands, and these frequencies are shared between the four links in each cluster. The "stormy" period corresponds to the period 7-12 April during which time: 22>Ap>100. For the remainder of the period, the Ap was less than 8, and is termed "quiet".

The long-term availability is an important consideration for system planning. We have determined this parameter for a period of time between December 1994 through October 1995. The average availability is deduced under the following condition. We assert that connectivity is established if any one of the eleven aeronautical-mobile bands will pass the SNR test reckoned at the clusterhead for passage of 300 bps messages over any one of the four paths in the star-net or cluster. We are really determining service availability. Figure 5 is a chart showing the monthly-average availabilities and composite service availability for each of the selected clusters of paths. We see that the least reliable cluster is Churchill (polar) with gradually improving availability arising for Iceland (auroral), Tors Cove (trough), and North Carolina (midlatitude). There are also certain months with low availabilities for selected sites. For example, the lowest value for Churchill is in December 1994, the lowest for Iceland is in May, the lowest value for Tors Cove is in October, and the lowest value for North Carolina is in June. Thus we see little seasonal consistency in the data base.

We observe that the Churchill cluster never exhibits a month in which the service availability is 100%. Iceland exhibits 3 months out of the 11 analyzed for which the availability is 100%. Tors Cove exhibits 4 months having 100% availability out of 9 analyzed, and North Carolina exhibits 5 months with 100% availability out of 10 analyzed. It is noteworthy that August provided the highest composite availability: 100% for North Carolina, Tors Cove and Iceland, and the highest computed monthly value for Churchill: 0.9993. The overall composite availability for August for all four sites was 0.9998.

We have also examined the impact of the diurnal cycle. We have determined that the availability in the 16-hour period 1300 to 0500 is approximately 0.99993 based upon the number of possibilities for failure during this temporal epoch. On the other hand, the composite average availability for the 8-hour period from 0500-1300 LMT is reduced to about 0.988. Clearly this will have important implications for frequency management for the ultimate HFDL system.

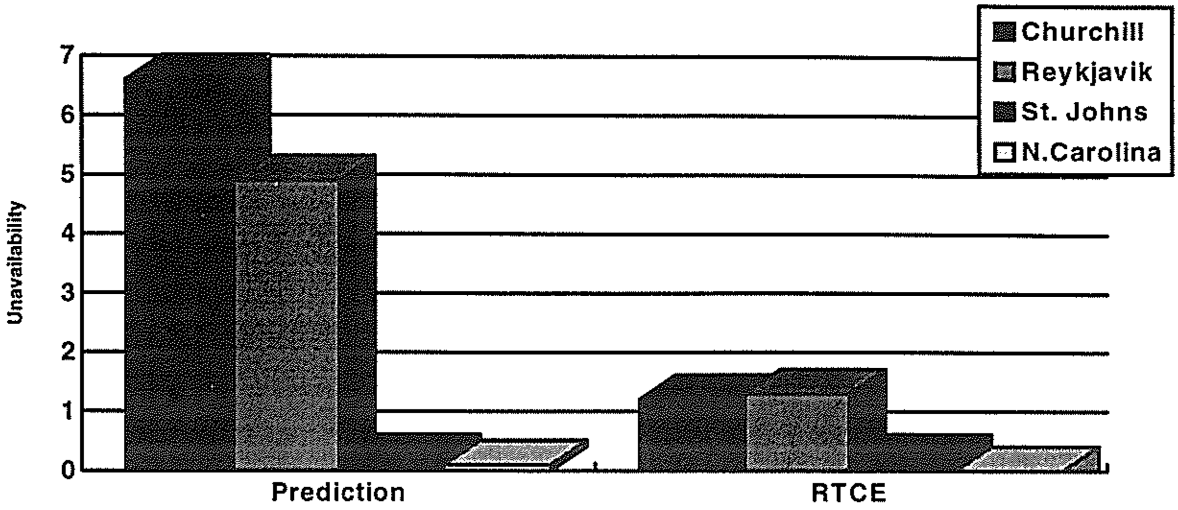

Figure 4. The unavailability, in percent, under two frequency management schemes. The scheme labeled "prediction" corresponds to the condition whereby IONCAP is utilized to preselect the three most likely frequencies for consideration. The second scheme labeled "RTCE" (viz., real-time channel evaluation) corresponds to the best frequency derived from real-time sounder measurement.

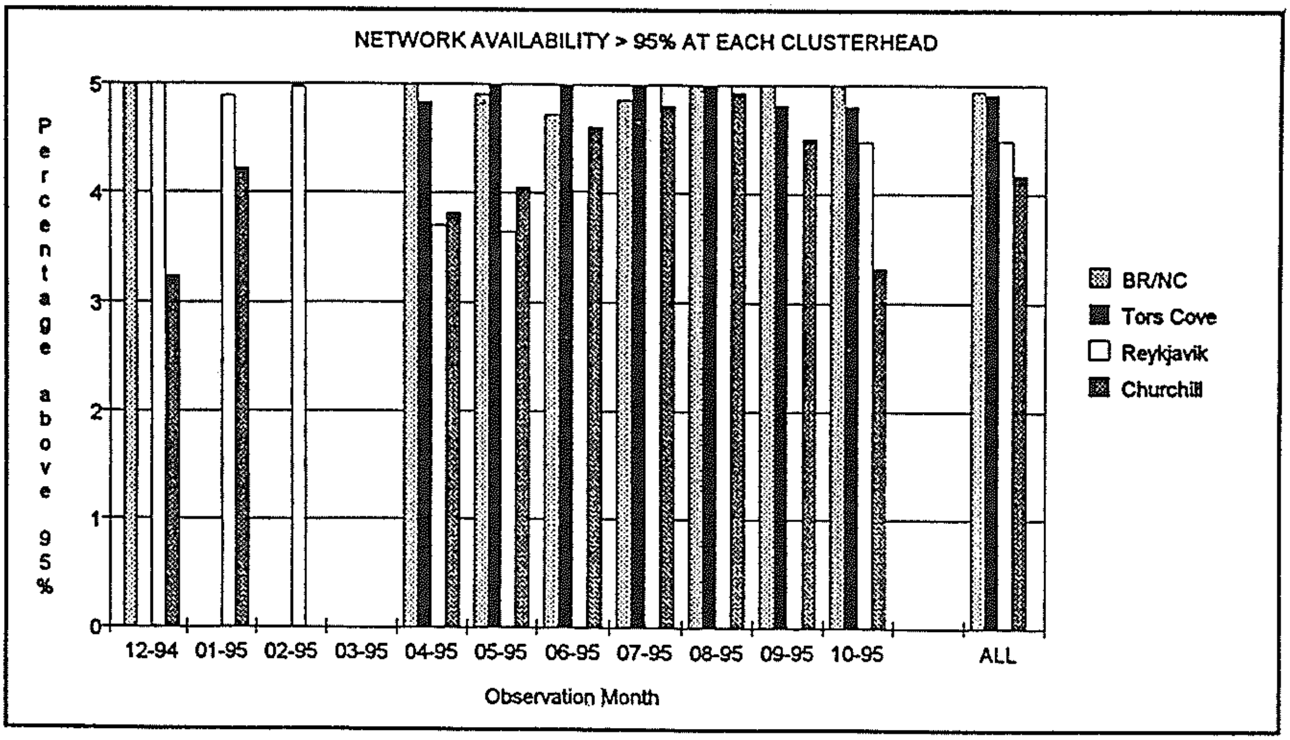

Figure 5. Graphs of the link cluster availabilities for the Northern Experiment. The clusterheads represent aircraft positions, but in fact are locations of Chirpsounder® receivers. At these locations, we obtain data from four paths representing air-to-ground links. The clusterheads we have considered in this study are: (1) a site in northeastern North Carolina (BR/NC), (2) a site near St. Johns, Newfoundland (Tors Cove), (3) a site at Reykjavik, Iceland, and (4) a site located at Churchill, Canada. The links to each clusterhead may be determined from Figure 1. The "ALL" corresponds to a composite average availability for the entire period of observation for each cluster of links. The reader should note that the plotted availability must be added to 95% to get the total value. Thus a plotted value of 4% corresponds to 95 + 4 or 99%.

4. CONCLUSIONS

A study of link and network availability has been carried out based upon oblique sounder observations over an extensive region in the Northern hemisphere for approximately a year. We have applied the measured propagation conditions in an analysis of HFDL performance based upon a specific system design specification. Nevertheless the general conclusions will not change. We have concluded that space and frequency diversity will enable the normally unsatisfactory ensemble of HF channels to be be utilized effectively to provide an HFDL service with long-term average availabilities approaching 100%. We observe that average availabilities decrease as the network clusters migrate to higher geomagnetic latitudes. Daily, and monthly variations are observed as well. There is also a striking diurnal influence on average availability, with very little limit on the performance for netted HFDL service between 1400-0400 LMT at the clusterhead (i.e., aircraft) position.

It is emphasized that this result represents the very best that may be achieved under conditions for which full-band sounding is available to drive a dynamic nowcasting and forecasting subsystem for resource management. Frequency sharing and dynamic reallocation is a requisite condition, but it may not be sufficient. A full suite of frequencies populating all of the Aeronautical-Mobile bands is needed to exploit the dynamic forecasting capability. The reader is also reminded that these data sets were obtained during a period of low solar activity, with only a few episodes of enhanced magnetic substorms. The resource management challenges will become more daunting as the period of solar activity increases in the next few years, and this will surely necessitate some greater consideration of real-time failure mode assessment and mitigation.

References:

[1] "A long-term investigation of the HF communication channel over middle and high latitude paths", by J.M. Goodman, J.W. Ballard, and Eugene Sharp; Proceedings of 1996 Ionospheric Effects Symposium (Alexandria VA); available through NTIA, Springfield VA; Order No. PB97-100101; paper to appear in Special Issue of Radio Science in 1997.

[2] "HF Communication: Science & Technology", John M. Goodman, Van Nostrand Reinhold, New York, 1992.

Acknowledgments

The authors would like to acknowledge a number of personnel TCI/BR who have been involved in the Northern Experiment effort including Roy Sasselli, Trung Luong, Clint Gilliland and Bud Erickson. We are also indebted to a number of organizations for assistance in data acquisition from remote sites: the Iqaluit Weather Service, the University of Alaska, Telia Mobitel AB of Sweden, and PTT Iceland, to name a few. Additionally, we express our appreciation to members of the FAA, the AEEC, the RTCA and other agencies who have taken an interest in our work.

IONOSPHERIC HF PROPAGATION PREDICTION UNDER DISTURBED CONDITIONS USING DATA FROM OBLIQUE-INCIDENCE SOUNDING BY CHIRP-SIGNALS

G. A. Zherebtsov, V. I. Kurkin, V. E. Nosov, O. M. Pirog, N. M. Polekh, and
L. V. Chistyakova Institute of Solar-Terrestrial Physics, P. O. Box 4026,
Irkutsk, 664033, Russia E-mail: root@sitmis.irkutsk.su

ABSTRACT

The opportunity to improve long-term HF-propagation predictions on a test path using real-time data from oblique-incidence sounding is investigated. Experimental data for a 3000km path for 1993-1995 are analyzed. A FMCW ionosonde, designed and built in the Institute of Solar-Terrestrial Physics, was used. The main idea of the technique for temporal extrapolation of the maximum usable frequency (MUF) on a path is to use *a priori* information about the diurnal variation of MUFs from models. It is shown that the error in predictions, especially under disturbed conditions, can be reduced by using linear extrapolation.

1. INTRODUCTION

Determining the best working frequencies for HF radio communications on a real-time basis, especially during ionospheric disturbances, remains one of the "hottest" areas in current applied research. The ionosphere is characterized by large day-to-day fluctuations (about 10 - 15 % under quiet conditions and more than 50 % under disturbed conditions). Ionospheric disturbances depend on many factors and are locally specific. Therefore, it is necessary to use real-time data for HF propagation predictions.

Many approaches have been developed to solve this problem [1-8]. Updating magnetic and solar indices was described in [1]. Another approach converts vertical incidence ionograms to equivalent oblique ionograms in real-time for HF communication frequency management [2-4]. This approach is useful for short HF communication forecasting (up to 1000 km in length). A mixed network of vertical and oblique ionosondes provides significant reductions in the prediction errors for circuits of arbitrary one-hop length with reflection points within the area covered by the ionosonde network [4-8] but short-term forecasting for multihop HF propagation has not been adequately investigated.

The present paper describes a technique for the forward time extrapolation of the maximum usable frequency (MUF) scaled from oblique-incidence sounding ionograms. It may be used as a forecasting subsystem for multihop real-time frequency management of HF communications.

2. TECHNIQUE

Newton's formula [9] for the interpolation polynomial, $P(t)$, for equally spaced values of an independent variable t was used to extrapolate the MUF forward in time, as below.

$$P(t) = f(t_0) + \sum_{k=1}^{n} \frac{\Delta^k f(t_0)}{k!\,h^k}(t-t_0)(t-(t_0+h))\ldots(t-(t_0-(k-1)h)) \qquad (1)$$

Here h is a step in the variable t, t_0 is the value of t for the last scaled MUF, and $\Delta^k f(t)$ represents consecutive differences of the function $f(t)$, given for discrete values for the variable t, calculated by the formulae, as given below

$$\begin{aligned} &\Delta f(t) = f(t) - f(t-h) \\ &\Delta^2 f(t) = \Delta f(t) - \Delta f(t-h) = f(t) - 2f(t-h) + f(t-2h) \\ &\cdots\cdots\cdots\cdots\cdots\cdots\cdots\cdots\cdots\cdots \qquad (2) \\ &\Delta^n f(t) = \Delta^{n-1} f(t) - \Delta^{n-1} f(t-h) \end{aligned}$$

At time, $t = t_0 + h$, the short-term forecast is made possible by extrapolating the past observations according to (1), being limited to various degrees of the polynomial, $P(t)$.

As a zeroth approximation,

$$f(t) = f(t_0) \tag{3}$$

as a first approximation,

$$f(t) = f(t_0) + [f(t_0) - f(t_0 - h)] \tag{4}$$

and as a second approximation we obtain

$$f(t) = f(t_0) + [2f(t_0) - 3f(t_0 - h) + f(t_0 - 2h)] \tag{5}$$

The higher order approximations can be obtained in a similar manner. According to the equations (2) values t are further from $(t_0 - nh)$ as n increases. Therefore the extrapolation error increases with increasing n.

Short-period variations, caused by both small-scale irregularities and various wave processes, are superposed on the background of a diurnally varying MUF. The short period variations can change sign from measurement to measurement, even within 15 minutes. The extrapolation of experimental data, without preliminary smoothing, consequently results in large errors. Therefore, it is worthwhile to single out the most meaningful MUF variations and smooth out fluctuations caused by small-scale inhomogeneous structures in the ionosphere, retaining the most meaningful period of an hour or longer. Various ways of smoothing experimental data were tested: linear smoothing of three and five points and smoothing by a third order polynomial over seven points [10]. Table 1 presents standard deviation (SD) smoothed values for different days.

Table 1. Standard deviations for various variants of smoothing (in %)

Standard deviation (SD) %			
DATES	linear 3 point	linear 5 point	3rd order 7 point
02.11.93	0.99	2.06	0.74
08.11.93	1.23	2.11	0.78
10.11.93	1.30	2.65	1.00
13.11.93	1.38	2.98	0.99
14.11.93	0.99	1.98	0.59
18.11.93	1.39	2.7	0.86
19.11.93	1.50	3.11	1.14
24.11.93	1.22	2.68	1.06

From Table 1, it is clear that the five points linear smoothing gives rise to an error about twice that of the three point smoothing. The seven point nonlinear smoothing error is less than the three point smoothing, but the seven point nonlinear smoothing is more difficult for likely experimental data passes.

Thus, the three points linear smoothing of the data is better for short-term forecasts. It reduces errors due to an inexact MUF determination, especially at night because of spread-F, and takes account of the general tendency for temporal MUF changes whilst preserving meaningful MUF variations. Conversely, *a priori* errors in the forecast, caused by neglecting the influence of small-scale irregularities occur.

Formulae (1-5) can be used for short-term forecasts using experimental data. However, extrapolation errors will decrease if *a priori* information about the diurnal variations of the MUF is used. In reference [11] it was shown that the ratio of MUF's for various paths show an adiabatic dependence on ionospheric parameter deviations. Assuming that it is applied to the same path for various moments of time, we bring *a priori* information from the numerical simulation.

Then formulae (4-5) will look like:

$$f(t) = f(t_0) + f^m(t_0 + h) - f^m(t_0)\ , \tag{6}$$

$$f(t) = f(t_0) + 2f^m(t_0 + h) - 3f^m(t_0) + f^m(t_0 - h)\ \ , \tag{7}$$

The value $f(t_0)$ in formulas (3-7) is taken from experimental data and consecutive differences are calculated from experimental data and from an ionospheric model. Index *m* indicates that this value is obtained from model. By so doing, this takes account of the main geophysical factors determining the MUF variation with time.

3. EXPERIMENT

These techniques were tested using observational data from paths in north-eastern Russia. From November 1993 to November 1995 regular experimental HF propagation observations were made on the 3000 km long Magadan-Irkutsk path. Oblique-incidence ionograms and amplitude characteristics were recorded every month on Regular World Days (see the International Geophysical Calendar). The measurements were made with a chirp-sounder (FWCM) designed and built at the Institute of Solar-Terrestrial Physics [12]. This system was developed to make oblique-incidence and backscatter soundings. An artificial neural network method has been applied in computer-aided ionogram analysis to extract the ionospheric traces [13]. Ionograms were digitized, interpreted [14] and accumulated in a computer database. With this database we extracted data subsets for disturbed conditions and quiet conditions when long-term MUF predictions had large errors. During the selected observing intervals round the clock one-hop and two-hops propagation modes were observed. Reflections from mixed (E + F) modes, as well as reflections from the regular E layer during daytime and Es layers, were observed.

All these data were collected at solar minimum. Between November 2-25, 1993 the monthly average solar radiation level, $F_{10.7}$, was 93.8. During this time there were two magnetic storms, which caused ionospheric disturbances on November 3-6 and on November 18-19. On subsequent days, after the storm, traveling ionospheric disturbances (TID) were observed on the oblique and vertical incidence ionograms, for appreciable daytime hours. In February and April 1994, when the experiments were carried out, the conditions were disturbed while September was quiet. On October 17-20, 1995, the beginning and development of a magnetic storm was accompanied by a sharp decrease in the electron density of the ionosphere.

4. RESULTS

Errors predicting MUFs were estimated with the objective of finding the best procedure for predicting MUFs compared with those from oblique-incidence ionograms. To accomplish this, MUFs for regular propagation modes, obtained from oblique-incidence soundings at 15-min intervals were used. 1F and 2F MUF's on this path, with forward prediction times ($\Delta\tau$) of 15, 30, 45 and 60 minutes, were forecast to compare the various extrapolation methods. The standard deviations were calculated for the relative errors between the predicted MUFs and the observed ones. Fig.1 shows the dependence of the standard deviations of relative errors in predicted MUFs for forward prediction times calculated by different extrapolation methods by averaging about 2000 ionograms over November, 1993 (In Figure 1 the labels 1 and 2. indicate extrapolation using experimental data only for zeroth and first approximations respecti9vely and label 3 indicates linear extrapolation using numerical simulation). It is clear, that the linear extrapolation using a long-term prediction model is best. The forecast, based only on experimental data (lines 1, 2) , gives a sharp increase in forecast errors with increasing forward prediction time. Extrapolation polynomials of higher degrees (i.e., quadratic is indicated by label 4)

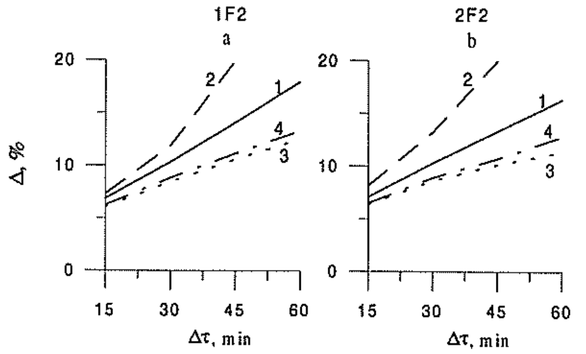

Fig.1 The dependence standard deviations of relative errors of predictand of forward prediction time for different ways of interpolation.

using numerical simulations do not give appreciable increases in prediction accuracy.

Table 2 presents standard deviations of relative errors for separate dates typical of different geophysical conditions. It is clear that forecast errors obtained for quiet conditions *are about 1-2 % less* than those obtained for disturbed conditions. Similar behavior is also observed for the 2F2 mode.

Fig. 2 illustrates the observed diurnal variations (line 1) and predicted variations (line 2) of the MUFs with forward prediction times equal to 15 and 30 minutes for two disturbed days calculated using a linear extrapolation of experimental data with a long-term prediction model. Line 3 shows diurnal MUF variation from the long-term predictions.

Table 2. Standard deviations of relative errors (in %) of the predictand for quiet and disturbed conditions

Conditions	Day	$\sum K_p$	SD (%) Long-term prediction	SD (%) Forward prediction time (min)		
				$\Delta t = 15$	$\Delta t = 30$	$\Delta t = 45$
Quiet conditions	14.09.94	14	15.5	4.3	6.23	8.25
	2.11.93	4	12.5	4.7	6.6	8.3
	17.10.95	24	19.9	5.3	7.7	10.4
Disturbed conditions	15.02.94	34	23.0	7.8	10.2	12.9
	15.03.94	36	16.0	5.7	8.8	10.6
	13.04.94	35	16.9	4.9	7.2	9.5
	19.11.93	31	20.8	7.0	9.7	11.4
	19.10.95	36	35.0	6.4	10.2	14.1

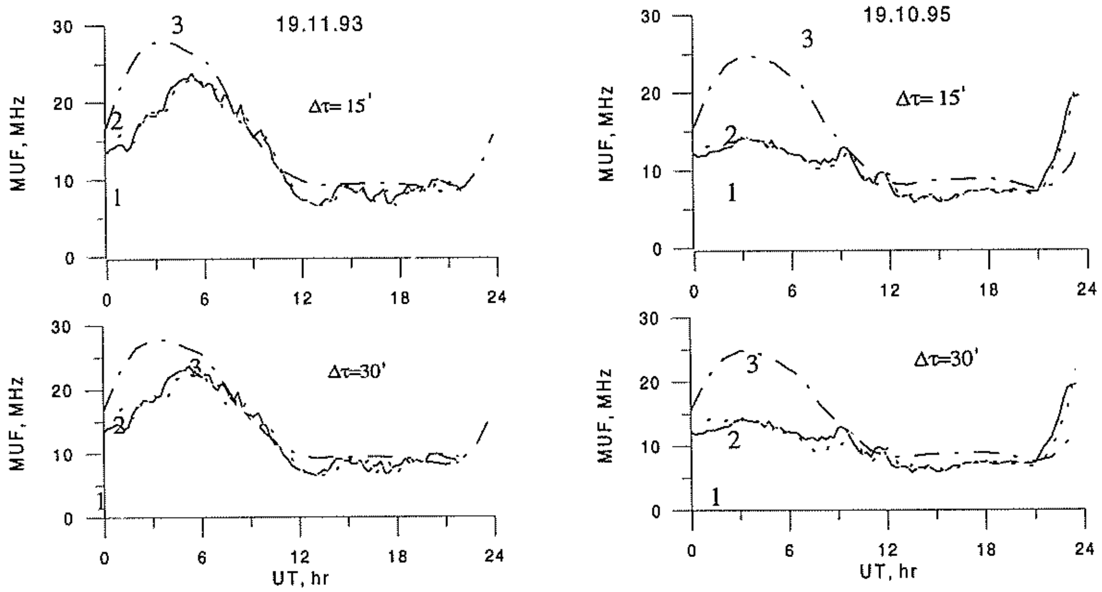

Fig. 2 Diurnal variations observable (line 1) and predicted (line 2) MUF for two disturbed days. Line 3 is the long-term forecast of the MUF.

The analysis of diurnal variations in the relative errors for different dates has shown that under quiet conditions the largest errors are during sunrise and sunset hours and at night. It appears that it is caused by the generation of waves at the passage of the solar terminator through an average point on the path [15]. Similar waves result in significant ionization and density gradients in the atmosphere and ionosphere, introducing additional contributions to the sizes of observed MUFs. These variations are not taken into account in the long-term prediction models. During disturbances, additional electrical fields can arise in the ionosphereand may possibly enhance atmospheric dynamics.

5. SUMMARY

A technique has been developed to forecast the MUF of regular propagation modes by using real time observed MUFs for a given path and numerical simulations with an ionospheric model. Results of applying the technique to a test path indicate significant reductions in predicted MUF errors, especially under disturbed conditions. Under disturbed conditions the largest errors are during the night. The reason is that wave processes and intense spread F may be responsible for the sharp variations in the observed MUF's.

References

[1] D.V.Blagoveshchenskiy and T.D.Borisova (1989), About correction of model HF radio-channel with taking account of variations of solar and magnetic activity Geomagn. and Aerom., V. 29, 4, 696-698.

[2] J.Chen, J.A.Bennet, P.L.Dyson (1992), Synthesis of Oblique from Vertical Ionograms Using Quasi-Parabolic Segments Models of the Ionosphere J. Atmos. And Terr. Phys., V.54, 1, 23-33.

[3] J.A.Bennet and P.L.Dyson (1996), Automatic fitting of quasi-parabolic segments to true height profiles for the prediction of oblique ionospheric radio propagation XXVth General Assembly of the International Union of Radio Science. Abstracts. Lille, France, 389.

[4] K.J.Lynn (1993), The Application of Ionosondes to HF Real-time Frequency Management in Northern Australia. Ionosonde networks and stations. Proc. Of Session Gb at XXIV General Assembly of URSI, Kyoto, Japan, August, 59-64.

[5] R.I.Beckwith, N.Narayana (1975), Real-Time of Maximum Usable Frequency Prediction for HF Radio Communication IREE Transaction on Communications, February, 286-288.

[6] M.Reilly, M. Daehler (1986), Sounder updates for statistical model predictions of maximum usable frequencies on HF sky wave paths Proceeding of IREE, V.74, 120-136.

[7] J.M.Goodman, J.W.Ballard, E.D.Sharp, and T. Luong (1996), Oblique-Incidence Sounding as an Aid to Analysis of HF Communication Scenarios: Summary of Multi-Staton Experimental Campaign XXVth General Assembly of the International Union of Radio Science. Abstracts. Lille, France, 388.

[8] B.M.Lunborg, M.Broms, and H.Derblom (1995), Oblique sounding of an Auroral Ionospheric F Channel J.Atmos.and Terr.Phys., V. 57, 1, 53 - 58.

[9] A.I.Gelfond (1967), Calculation of finite differences, Moscow. Nauka, 375.(in Rus.)

[10] D.Z.. Rumshinskiy (1971), Mathematical processing of results of experiments, Moscow, Nauka, 193. (in Rus.)

[11] V.I.Kurkin,V.E.Nosov, et.al. (1992), A technique for current diagnostics on the high-frequency radio channel Proceedings of International Symposium on Antennas, and Propagation - Sapporo, Japan, 1189-1192.

[12] I.G.Brynko et al. (1988), An automatically controlled data and processing system using an FMCW ionosonde Adv. Space Res., V.8, 4, 121-124 .

[13] V.P.Grozov, V.E.Nosov, G.A.Ososkov., E.G.Zaznobina (1996), Research result on the artificial network method in computer-aided ionogram analysis XXVth General Assembly of the International Union of Radio Science. Abstracts. Lille, France, 395.

[14] V.I.Kurkin, V.E.Nosov, S.N.Ponomarchuk (1996), Automatic Oblique Incidence Ionogram Interpretation XXVth General Assembly of the International Union of Radio Science, Abstracts, Lille, France, August, 387.

[15] I.M. Somsikov (1991), Wave in atmosphere caused by the solar terminator Geomag. and Aerom., V. 31, 1, 1-12.

ERRORS IN PARAMETERS DEDUCED FROM IONOSPHERIC SOUNDINGS

Denisenko, P.F., E.V. Kuznetsov, N.V. Nastasyina and V.I. Vodolazkin
Institute of Physics, Rostov State University, 194,Stachky Ave., 344104 Rostov-on-Don,
RUSSIA. phone: +7 8632 280985, fax: +7 8632 285044,
e-mail: denis@riphys.rnd.su and denis@iphys.rnd.runnet.ru

ABSTRACT

Estimating errors in ionospheric parameters scaled from ionosondes is an important problem. It is shown here that this problem may be solved in an invariant form under the condition that the required parameters are connected with radio physical measurements by Volterra's first kind integral equations. Expressions connecting the dispersion of the estimated parameters with correlation functions of the measured values were obtained. A sample solution for topside ionospheric sounding is proposed.

1.INTRODUCTION

Error estimation for ionospheric parameters deduced from radio sounding data should be a compulsory stage of inverse problems solution. This problem is readily solved when the height profile model parameter vector, $\vec{\xi}$, for one characteristics is linearly connected to the observation vector, $\vec{\vartheta}$,

$$\vec{\vartheta} = \hat{A}\vec{\xi},$$

where $\hat{A}$ is a matrix. In the simplest case, when the dispersion, σ^2, of the measured values does not depend on the frequency, the covariation matrix, $\hat{D}(\vec{\xi})$, is

$$\hat{D}(\vec{\xi}) = \sigma^2(\hat{A}^T\hat{A})^{-1}.$$

This method for estimating the dispersion, $\sigma^2(\xi_i) = D_{ii}(\vec{\xi})$, of vector $\vec{\xi}$ components has the following considerable short coming. The results depend on the assumed height profile model of some ionospheric characteristics. At the same time, for several problems, the possibility of obtaining direct connections between the estimated ionospheric parameter errors and the physical radio measurement errors exists.

Some inverse problems of vertical ionospheric sounding require the Volterra linear integral equations of the first kind (Danilkin et al., 1988) to be inverted

$$\psi(x) = \int_a^x \frac{H(x,t)}{\sqrt{x-t}}\eta(t)dt, \qquad (1)$$

where $\psi(x)$ is a function obtained experimentally, $\eta(t)$ is the required function, $x = f^2$, for the ordinary wave, $x = f^2 - ff_H$ for the extraordinary wave, f is the working frequency, f_H - the electron gyrofrequency, $t = f_N^2, f_N$ is the electron plasma frequency, $a = f_0^2$, f_0 is the electron plasma frequency at the layer start; $H(x,t)$ is an equation kernel, $a \le x \le b$, $a \le t \le x$, $b = f_m^2$, f_m is the maximum working frequency. These equations are geometrical optics approximations and arise when determining a monotonic electron density height profile from virtual height measurements; effective electron collision frequency height profile from radio wave absorption measurements; and plasma motion velocity height dependencies from Doppler frequency shift measurements (Danilkin et al., 1988).

The linearity of Eq.(1) allows the connection between the correlation functions to be obtained

$$B_\psi(x_1,x_2) = \langle \delta\psi(x_1), \delta\psi(x_2) \rangle,$$
$$B_\eta(t_1,t_2) = \langle \delta\eta(t_1), \delta\eta(t_2) \rangle$$

for fluctuating observed values, $\delta\psi(x)$, and deduced values, $\delta\eta(x)$. Symbol $\langle ... \rangle$ means statistical average.

The present paper is aimed at obtaining relations connecting the accuracy of experimental and deduced values, and to demonstrate their application to inverse problems of monotonic $n_e(z)$-profile reconstruction.

2.THEORY

Using the standard method (Volterra, 1959), Eq.(1) transforms to Volterra's integral equation of the second kind

$$\eta(y) = F(y) + \int_a^y V(y,t)\eta(t)dt, \tag{2}$$

where

$$F(y) = \frac{1}{\pi H(y,y)} \int_a^y \frac{\psi'(t)}{\sqrt{y-t}} dt, \tag{3}$$

and

$$V(y,t) = -\frac{1}{\pi H(y,y)} \int_0^\pi \frac{\partial}{\partial y} H\left(\frac{y+t}{2} + \frac{y-t}{2}\cos\alpha, t\right) d\alpha . \tag{4}$$

Via resolvent $R(x,t)$ satisfying the equation

$$R(x,t) = V(x,t) + \int_t^x V(x,u)R(u,t)du, \tag{5}$$

the solution of Eq.(2) is presented in the form

$$\eta(x) = F(x) + \int_a^x R(x,t)F(t)dt. \tag{6}$$

Hence, for fluctuations $\delta\eta$ and $\delta\psi$ we obtain the following relation

$$\delta\eta(x) = \delta F(x) + \int_a^x R(x,t)\delta F(x)dt.$$

Substituting the last expression for the correlation function, B_η, we obtain

$$B_\eta(x_1,x_2) = B_F(x_1,x_2) + \int_a^{x_1} R(x_1,t_1)B_F(x_2,t_1)dt_1 + \int_a^{x_2} R(x_2,t_2)B_F(x_1,t_2)dt_2 + \int_a^{x_1}\int_a^{x_2} R(x_1,t_1)R(x_2,t_2)B_F(t_1,t_2)dt_1 dt_2 \ , \tag{7}$$

where

$$B_F(x_1,x_2) = \frac{1}{\pi^2 H(x_1,x_1)H(x_2,x_2)} \int_a^{x_1}\int_a^{x_2} \frac{B(t_1,t_2)dt_1 dt_2}{\sqrt{x_1-t_1}\sqrt{x_2-t_2}}, \tag{8}$$

and

$$B(t_1,t_2) = \frac{\partial^2}{\partial t_1 \partial t_2} B_\psi(t_1,t_2). \tag{9}$$

From the expressions for dispersion, $\sigma_\eta^2(x) = B_\eta(x,x)$, we obtain

$$\sigma_\eta^2(x) = \sigma_F^2(x) + 2\int_a^x R(x,t)B_F(x,t)dt + \int_a^x\int_a^x R(x,t_1)R(x,t_2)B_F(t_1,t_2)dt_1dt_2. \qquad (10)$$

Thus, formulae (7) to (10) solve the problem of determining the errors in deduced ionospheric parameters when measurement errors are correlated, arising from fluctuations in the observing equipment as well as in the propagation media. The expressions show that provided the equipment is the same, the ionospheric parameter errors depend on the geographical observation location as well as the sounding signal polarisation. This is connected with dependence of the kernel, $V(x,t)$, and consequently, of resolvent $R(x,t)$, on the magnetic dip and electron gyrofrequency.

3. ERRORS IN DEDUCED $n_e(z)$ -PROFILES FOR TOPSIDE IONOSPHERIC SOUNDING

As an example, the dispersion, σ_z^2, of real heights for the inversion of the electron density $n_e(z)$-profile for ordinary (o) wave, topside ionospheric sounding data is determined. Starting with Eq.(1), the following concepts are used.

The Z-axis is directed down from the satellite to the Earth's centre, the co-ordinates beginning at the satellite, the plasma frequency in the neighbourhood of the satellite is equal to f_0, i.e. $a = f_0^2$.

An auxiliary value is introduced

$$S(f) = \int_{f_0}^{f} P_g(f)df = P(f)f \ , \qquad (11)$$

where P_g is the virtual height, and P is the phase height of the sounding signal.

The phase height is written in the form

$$P(f) = \int_{f_0^2}^{f^2} \mu \frac{dz}{df_N^2} df_N^2 \ , \qquad (12)$$

where μ is the phase index of refraction

$$\mu = m\sqrt{1-X}, \qquad m = \left[\frac{R + Y_T^2 + 2Y_L^2}{R + Y_T^2 + 2Y_L^2(1-X)}\right]^{1/2}, \qquad R = \sqrt{Y_T^2 + 4Y_L^2(1-X)^2}$$

$$X = \frac{f_N^2}{f^2}, \qquad Y = \frac{f_H}{f}, \qquad Y_L = Y\cos\Theta, \qquad Y_T = Y\sin\Theta,$$

f_H is the electron gyrofrequency, Θ is the angle between the zenith and direction of the electromagnetic field intensity vector.

Integrating formula (12) by parts gives

$$P(f) = -\int_{f_0}^{f} \frac{d\mu}{df_N^2} z(f_N^2) df_N^2 \ . \qquad (13)$$

Taking into account that μ = 0 at the upper integration limit and z = 0 at the lower one. The expression for $d\mu/df_N^2$ has the form:

$$\frac{d\mu}{df_N^2} = -\frac{1}{f^2}\frac{H}{\sqrt{1-X}}, \qquad H = \frac{m}{2} - (1-X)\frac{\partial m}{\partial X}. \qquad (14)$$

Combining the formulas (11), (13) and (14), finally gives

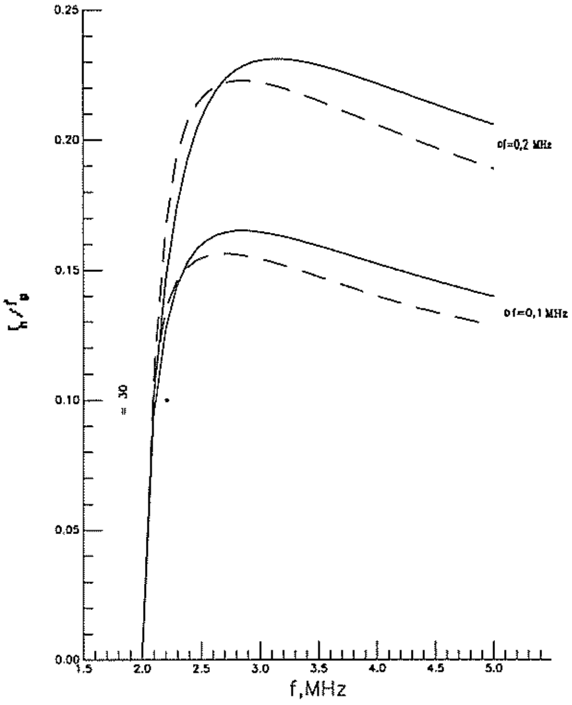

Figure 1: see text for details

$$\psi(x) = \int_a^x \frac{H(x,t)}{\sqrt{x-t)}} z(t)dt \ , \tag{15}$$

where $\psi(x) = S(\sqrt{x})$, $x = f^2$, $t = f_N^2$.

In accordance with the general Exp.(6), the solution of Eq.(15) is

$$z(x) = F(x) + \int_a^x R(x,t)F(t)dt \ ,$$

where

$$F(x) = \frac{1}{2\pi H(x,x)} \int_a^x \frac{P_g(\sqrt{t})dt}{\sqrt{t}\sqrt{x-t}} \ .$$

Thus, it is possible to express the real heights, **Z**, by virtual heights. P_g. In particular, $\boldsymbol{H} = 1/2$, $\boldsymbol{V} = 0$, $\boldsymbol{R} = 0$ without magnetic field and from Eq.(16) the known result follows:

$$z(f_N^2) = \frac{2}{\pi} \int_{f_0}^{f_N} \frac{P_g(f)df}{\sqrt{f_N^2 - f^2}} \ .$$

Further, it is convenient to take the squares in f and f_N in terms of x and t and express them as linear values $y = \sqrt{x} = f$ and $u = \sqrt{t} = f_N$. Then the previous expressions has the form:

$$h(y) = G(y) + 2\int_\alpha^y R(y^2,u^2)G(u)udu \ , \tag{16}$$

where $\alpha = \sqrt{a} = f_0$, $h(y) = z(y^2)$, $G(y) = F(y^2) = \frac{1}{\pi H(y^2,y^2)} \int_\alpha^y \frac{P_g(u)du}{\sqrt{y^2 - u^2}}$, (17)

Accordingly, for dispersion of real height $\sigma_h^2(y)$, expressed as a function of the plasma frequency, we finally obtain

$$\sigma_h^2(y) = B_g(y,y) + 4\int_\alpha^y R(y^2,u)B_G(y,u)udu +$$

$$+4\int_\alpha^y\int_\alpha^y R(y^2,u_1^2)R(y^2,u_2^2)B_G(u_1,u_2)u_1u_2du_1du_2 \ , \tag{18}$$

where

$$B_G(u_1,u_2) = \frac{4\sin^2\Theta}{\pi^2} \int_\alpha^{u_1}\int_\alpha^{u_2} \frac{B(t_1,t_2)dt_1dt_2}{\sqrt{u_1^2 - t_1^2}\sqrt{u_2^2 - t_2^2}} \ . \tag{19}$$

Here it is taken into account that $H(y^2,y^2) = 1/(2\sin\Theta)$ and assume $B(t_1,t_2) = \left\langle \delta P_g(t_1)\delta P_g(t_2) \right\rangle$.

In the absence of a magnetic field, or in the case of sounding on the magnetic equator, ($\Theta = \pi/2$), $H \equiv 1$, $V \equiv 0$, $R \equiv 0$, and , from formula (16) we get the known result (Wright *et al.*, 1957)

$$h(f_N) = \frac{2}{\pi} \int_{f_0}^{f_N} \frac{P_g(f)df}{\sqrt{f_N^2 - f^2}} \quad .$$

The dispersion of real height for this case is

$$\sigma_h^2(y) = \sigma_G^2(y) = \frac{4}{\pi^2} \int_\alpha^y \int_\alpha^y \frac{B(t_1, t_2)dt_1dt_2}{\sqrt{y^2 - t_1^2}\sqrt{y^2 - t_2^2}} \qquad (20)$$

This example, firstly, demonstrates the application of the general scheme of dispersion determination of deduced values, and secondly, shows that in for each individual case more suitable modifications of this problem are possible.

4. THE RESULTS OF COMPUTED MODELLING

The calculations were aimed at investigating the dependencies of real height errors, σ_h, at the working frequencies, the geomagnetic latitude of the sounding (i.e. angle Θ) and the kind of correlation function. For computer modelling, statistical radio physics correlation functions were very often used, as given below

$$B_1(f_1, f_2) = \sigma_g^2 \exp\left(-\frac{|f_1 - f_2|}{\Delta f}\right), \qquad B_2(f_1, f_2) = \sigma_g^2 \exp\left(-\left[\frac{|f_1 - f_2|}{\Delta f}\right]^2\right)$$

Here σ_g^2 is a dispersion constant on the whole frequency interval of measurements, beginning from frequency f_0=2 MHz. To investigate the influence of the frequency correlation radius, Δf, on the computed results, two values of the frequency correlation radius: Δf_1=0.1 MHz and Δf_2=0.2 MHz were used. The results of the calculations are shown on the Figures 1 to 3.

In Figure 1, the results of the frequency dependence calculations for the ratio $\Delta(f) = \sigma_h / \sigma_g$ for middle latitude conditions under $\Theta = 30°$ are shown. Solid lines for the correlation function B_1, dashed lines for B_2. The dependence of $\Delta(f)$ begins at zero values (height $z(f_0)$ is assumed to be known accurately), then it reaches a maximum and after that smoothly decreases as the frequency increases. The ratio, σ_h / σ_g, depends weakly on the correlation function. It is determined mainly by the frequency correlation radius: with increasing Δf the mean square errors ,σ_h, increases. In all cases $\sigma_h < \sigma_g$.

In Figure 2, the dependence of function Δf from angle Θ for the correlation function B_1 with Δf_2=0.2 MHz, is shown. It is clear that as Θ decreases the errors in deduced real heights decrease. Formula (18) shows that the dispersion, $\sigma_h^2(f)$, is a sum of three terms. Their contributions are different for different angles Θ. In the equatorial ionosphere the main role is played by the first term. Moving from the equator to the pole the second and third terms begin to dominate. This is shown in Figure 3 for the correlation function B_1 and Δf_2=0.2 MHz. The lines on Figure 3 show the relative contributions for each of the three dispersion terms, $\sigma_h^2(f)$, in formula (18). Solid lines show Θ=30°, dashed lines for Θ=15°, and digits near the curves show the number of the term.

The calculations show that under the same statistical real height characteristics measured from ordinary polarisation signals, the accuracy of the monotonic $n_e(z)$-profile reconstruction increases going from the equator to the pole.

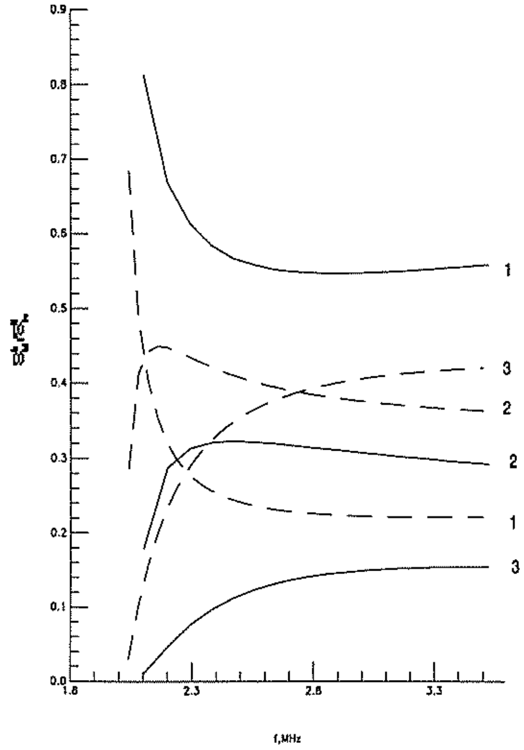

Figure 2: see text for details

5. CONCLUSIONS

Errors estimation of ionospheric parameters deduced from radio sounding data should be a compulsory stage in inverse problems solution. In the present paper, a case is considered and then the inverse vertical sounding problem is reduced to an inversion of Volterra integral equation. Analytical expressions are obtained connecting the accuracy characteristics for deduced and observed values. As an example, the problem of reconstructing the $n_e(z)$-profile from ordinary-wave topside sounding ionograms was considered. Using the same virtual height errors, the real height error determination depends on the geomagnetic latitude of observation point: they are a maximum at the equator and after that they decrease to the pole. The calculation technique and the results are useful for solving topside ionosphere sounding methods.

References

Danilkin, N. P., P. F. Denisenko and V. V. Sotsky, Peculiarities of the inverse problems of vertical radio sounding of the ionosphere, *Adv. Space Res.*, 8(4), 91-94, 1988.

Volterra, V., Theory of functionals and of integral and integro-differential equations, *Dover publications Inc.*, New York., 1959.

Wright, J. W., R. W. Knecht and K. Davies, *Annals of IGY, Vol.III, Part I, Oxford, Pergamon Press, 1957.*

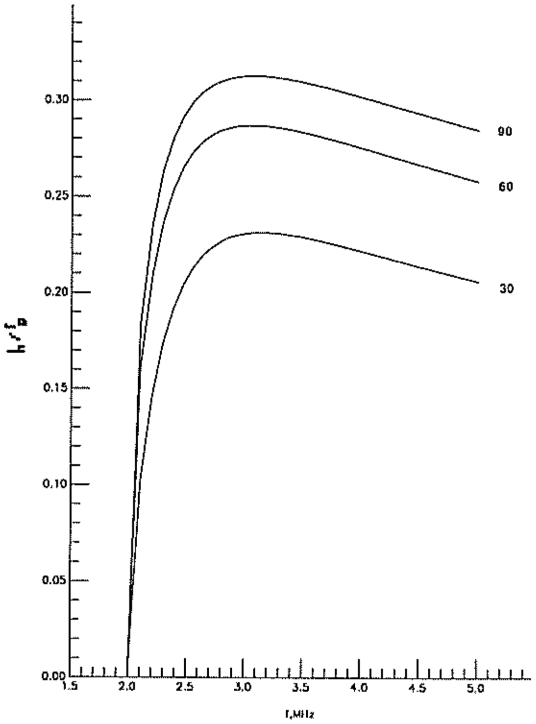

Figure 3: see text for details

USING THE REGULARIZATION METHOD FOR ELECTRON DENSITY HEIGHT PROFILE RECONSTRUCTION

P.F. Denisenko, N.V. Nastasyina and V.V. Sotsky
Institute of Physics, Rostov State University, 194,Stachky Ave., 344104 Rostov-on-Don, RUSSIA
phone: +7 8632 280985, fax: +7 8632 285044,
e-mail: denis@riphys.rnd.su and denis@iphys.rnd.runnet.ru

ABSTRACT

A comparison of the least-squares method and the regularization method was carried out for the problem of electron density height profile reconstruction using topside and trans-ionospheric sounding data. It is shown that the regularization method is effective when simultaneously using ordinary and extra-ordinary wave ionogram traces The real height root mean square errors are a tenth of those obtained using the least-squares method (LSM).

1. INTRODUCTION

Satellite ionospheric radio sounding data contains information for reconstructing the electron density height profile, $N(h)$, below the satellite height. Information is contained in the topside ionogram traces for signals reflected from the topside ionosphere as well as the Earth's surface. The $N(h)$ is found for the F-region above the maximum and then below it.

The problem of full $N(h)$-profile reconstruction is an improperly posed problem (Danilkin *et al.*, 1988) Indeterminacy of the results below the F-region maximum essentially depends on the determination of errors in the critical frequency, f_m, (Kovalev *et al.*, 1991). The errors in calculations of f_m arise because of gaps in the ionogram traces caused by radio wave absorption near the F-layer maximum. Usually, it is possible to find an interval where the required value, f_m, is contained such that $f_{\min} \le f_m \le f_{\max}$.

The present paper is aimed at demonstrating, with the help of calculations, that the regularization method for the bottomside $N(h)$-profile reconstruction problem gives an accuracy improvement compared with LSM. The efficiency of the regularization method has been demonstrated for the problem of reconstructing the effective electron collision frequency dependencies using radio wave absorption measurements (Denisenko *et al.*, 1995; Denisenko *et al.*, 1996).

2. THEORY

To solve the direct and inverse problems, the following model of the $N(h)$-profile was taken. The F-layer maximum is assumed to be situated at a height h_m. Below the maximum, $N(h)$ is assumed to have a parabolic distribution and consequently the same distribution is assumed for the squared plasma frequency $f_N^2(h)$ given below

$$f_N^2(h) = f_m^2\left[1-\left(\frac{h_m - h}{H_2}\right)^2\right], \quad h_0 \le h \le h_m , \tag{1}$$

where H_2 is a half-thickness of the lower parabola and $h_0 = h_m - H_2$ is the base height of the ionosphere. The topside satellite sounder is situated at a height, h_s, with a known plasma frequency f_{Ns}. It is assumed that above the maximum, h_m, the $N(h)$-profile may have an approximately parabolic dependence:

$$f_N^2(h) = f_m^2\left[1-\left(\frac{h - h_m}{H_1}\right)^2\right], \quad h_m \le h \le h_s , \tag{2}$$

where H_1 is a semi-thickness of the upper parabolic layer.

The following expressions hold for the group paths:

$$P_g(f) = \begin{cases} \int_{h_s}^{h_r(f)} \mu'(f, f_N)dh, f < f_m \\ h_0 + \int_{h_0}^{h_s} \mu'(f, f_N)dh, f > f_m \end{cases} \tag{3}$$

where μ' is the group refraction index, $h_r(f)$ is a topside ionospheric reflection height. Using Exp.(1), (2) and (3) this can be presented in the form:

$$P_g(f) = M_1(f, f_m)H_1, \qquad f < f_m, \tag{4}$$

$$P_g(f) = M_1(f, f_m)H_1 + M_2(f, f_m)H_2 + h_0, \qquad f > f_m, \tag{5}$$

where $M_{1,2}(f, f_m)$ are expressions depended only on the working and critical frequencies f and f_m. Since

$$h_0 - h_m = H_1^* = H_1\sqrt{1 - \frac{f_{Ns}^2}{f_m^2}},$$

then $h_0 = h_s - H_1^* - H_2$. Substituting h_0 into (5) gives

$$\Delta P_g(f) = \left[M_1(f, f_m) - \sqrt{1 - \frac{f_{Ns}^2}{f_m^2}} \right] H_1 + \left[M_2(f, f_m) - 1 \right] H_2, \tag{6}$$

where $\Delta P_g(f) = P_g(f) - z_s$ is the group retardation of signals reflected from the Earth's surface.

If we have n_1 virtual height measurements for signals reflected by the topside ionosphere, and n_2 group retardation measurements for signals reflected by Earth's surface, then using (4) and (6) gives a system of linear equations $(n = n_1 + n_2 > 3)$

$$\hat{A}\vec{x} = \vec{y}, \tag{7}$$

where vectors $\vec{x}^T = (H_1, H_2)$ and $\vec{y} = (P_g(f_1), \dots, P_g(f_{n_1}), \Delta P_g(f_{n_1+1}), \dots, \Delta P_g(f_n))$ are the matrix elements for $\hat{A}$.

The problem is linear in the vector components x_1 and x_2 and non-linear in f_m.

In real conditions, the measurement vector, $\vec{y}$, has a random error $\vec{\varepsilon}$, therefore in the solution of the inverse problem, the right hand side of (7) should be replaced by $\vec{y}_\varepsilon = \vec{y} + \vec{\varepsilon}$. Thus, instead of (7) we have:

$$\hat{A}\vec{x} = \vec{y}_\varepsilon. \tag{8}$$

From calculations, the error vector was generated so that the average value of its components was equal to the null vector, i.e. $\langle \varepsilon_i \rangle = 0$, and the covariant matrix (matrix of errors), $D(\vec{y}_\varepsilon) = \langle \vec{\varepsilon}\vec{\varepsilon}^T \rangle$, has a constant multiplier, σ^2, with a dispersion of measurements, $D(\varepsilon_i) = \sigma^2$, which coincides with the unitary matrix $\hat{E}$, thus $\hat{D}(\vec{y}_\varepsilon) = \sigma^2 \hat{E}$.

The regularizing solution is determined in two stages. First stage the LSM-estimates, $\vec{x}_R$ for vector $\vec{x}$ and f_{mR} for parameter f_m, are obtained by computing the minimisation of the function

$$\Phi(f_m) = (\hat{A}\vec{x}_R - \vec{y}_\varepsilon)^2 \tag{9}$$

where $\vec{x}_R$ is for each value of f_m from the interval $(f_{\min}, f_{\max})$ and is calculated by

$$\vec{x}_R = \hat{B}^{-1}\hat{A}^T\vec{y}_\varepsilon , \qquad \hat{B} = \hat{A}^T\hat{A} . \tag{10}$$

With the help of the values $\vec{x}_R$ and f_{mR}, the dispersion is estimated to be

$$\sigma^2 \approx \Phi_{\min}/(n-p) , \tag{11}$$

where p=3 is the number of parameters, $\Phi_{\min} = \Phi(f_{mR}, \vec{x}_R)$ is the minimum value of the remainder square residue sum for the vector $\vec{y}_\varepsilon$.

Second, the exact regularizing solutions, $\vec{x}_\alpha$ and $f_{m\alpha}$, are determined. The critical frequency, $f_{m\alpha}$, is obtained as a result of functional minimisation

$$G(f_m) = (\hat{A}\vec{x}_\alpha - \vec{y}_\varepsilon)^2 + \alpha\vec{x}_\alpha^T\hat{U}\vec{x}_\alpha , \tag{12}$$

where the vector $\vec{x}_\alpha$ is a function of unknowns for which the problem is linear, and α is a regularization parameter. Then

$$\hat{U} = \begin{pmatrix} \lambda_{\min}^2 & 0 \\ 0 & \lambda_{\max}^2 \end{pmatrix} , \tag{13}$$

where $\lambda_{\min}$ and $\lambda_{\max}$ are the minimum and maximum eigenvalues of the matrix $\hat{B}$. From a numerical search, the minimum of equation (12) for each value of f_m from interval $(f_{\min}, f_{\max})$ is found and the regularizing solution, $\vec{x}_\alpha$, is obtained from

$$\vec{x}_\alpha = \hat{C}^{-1}\hat{A}^T\vec{y}_\varepsilon , \qquad \hat{C} = \hat{B} + \alpha\hat{U} . \tag{14}$$

The regularization parameter, α, for each value of f_m is determined from the following function minimum condition:

$$F(\alpha) = \frac{1}{2}\left[\frac{(\hat{A}\vec{x}_\alpha - \vec{y}_\varepsilon)^2}{(\hat{A}_R\vec{x}_R - \vec{y}_\varepsilon)^2} + \frac{\langle\delta\vec{x}_\alpha^2\rangle}{\langle\delta\vec{x}_R^2\rangle}\right] , \tag{15}$$

where $\hat{A}_R = \hat{A}(f_{mR})$, and vectors

$$\delta\vec{x}_R = \hat{B}_R^{-1}\hat{A}_R^T\vec{\varepsilon} , \qquad \text{with} \qquad \hat{B}_R = \hat{A}_R^T\hat{A}_R , \tag{16}$$

$$\delta\vec{x}_\alpha = \hat{C}_\alpha^{-1}\hat{A}_\alpha^T\vec{\varepsilon} \tag{17}$$

are random errors as a consequence of the LSM-solution with $f_m = f_{mR}$ and of the regularizing solution for the current value of f_m.

Moreover, in determining the solutions, the important problem is the determination of the error matrices. For that, it is necessary to obtain the preliminary linearization of equation (4) and equation (6) for parameter f_m (Hudson, 1964). This linearization leads to the appearance of an additional (third) column in matrix $\hat{A}$, from equation (8)

$$y_i = A_{i,1}x_1 + A_{i,2}x_2 + A_{i,3}x_3 , \qquad i = 1,2,\ldots,n ,$$

where $x_3 = \Delta f_m$ is an increment of the critical frequency. For the LSM, the linearization is carried out near the LSM-solution whereas for the regularization method the linearization is carried out near the regularizing solution.

Denoting the expanded matrix by $\hat{A}_e$, the LSM-solution is $\vec{x}_{eR}^T = (x_{1R}, x_{2R}, x_{3R})$, and the regularizing solution is $\vec{x}_{e\alpha}^T = (x_{1\alpha}, x_{2\alpha}, x_{3\alpha})$. Then the matrix $\hat{B}$ becomes $\hat{B}_e = \hat{A}_e^T \hat{A}_e$, and matrix $\hat{C}$ becomes matrix $\hat{C}_e = \hat{B}_e + \alpha \hat{U}_e$, where

$$\hat{U}_e = \begin{pmatrix} \lambda_{\min}^2 & 0 & 0 \\ 0 & \lambda_{\max}^2 & 0 \\ 0 & 0 & 0 \end{pmatrix}.$$

After linearization, according to the definition (Hudson,1964) of the covariation matrices for LSM and regularizing solutions we have

$$\hat{D}(\delta\vec{x}_{eR}) = \left\langle \delta\vec{x}_{eR} \delta\vec{x}_{eR}^T \right\rangle, \qquad \text{and} \qquad \hat{D}(\delta\vec{x}_{e\alpha}) = \left\langle \delta\vec{x}_{e\alpha} \delta\vec{x}_{e\alpha}^T \right\rangle,$$

where $\delta\vec{x}_{eR}$ and $\delta\vec{x}_{e\alpha}$ are determined by equations (16) and (17) replacing the corresponding matrices by their expanded analogies. Finally, the previous expressions take the form

$$\hat{D}(\delta\vec{x}_{eR}) = \sigma^2 \hat{B}_{eR}^{-1}, \tag{18}$$

$$\hat{D}(\delta\vec{x}_{e\alpha}) = \sigma^2 \hat{C}_{e\alpha}^{-1} C \hat{A}_{e\alpha}^T \hat{A}_{e\alpha} \hat{C}_{e\alpha}^{-1}. \tag{19}$$

It is clear that when $\alpha \to 0$, equation (19) transforms into (18), since $\hat{A}_{e\alpha} \to \hat{A}_{eR}$ and $\hat{C}_{e\alpha}^{-1} \to \hat{B}_{eR}^{-1}$.

The inverse solution is aimed at determining the real heights and their errors. Therefore, at the beginning, consider that for bottomside ionosphere

$$h(f_N) = h_s - H_1 F_1(f_m) - H_2 F_2(f_N, f_m), \qquad f_0 \le f_N \le f_m,$$

$$F_1 = \sqrt{1 - \frac{f_{Ns}^2}{f_m^2}}, \qquad F_2 = \sqrt{1 - \frac{f_N^2}{f_m^2}},$$

and for the topside ionosphere

$$h(f_N) = h_s - H_1 F_3(f_N, f_m), \qquad f_{Ns} \le f_N \le f_m.$$

According to previous expressions, the real height errors for the bottomside ionosphere are

$$\delta h = -F_1 \delta H_1 - F_2 \delta H_2 - \left(H_1 \frac{\partial F_1}{\partial f_m} + H_2 \frac{\partial F_2}{\partial f_m} \right) \delta f_m, \tag{20}$$

and for the topside ionosphere

$$\delta h = -F_3 \delta H_1 - H_1 \frac{\partial F_3}{\partial f_m} \delta f_m. \tag{21}$$

Taking into account that $\delta\vec{x}_e^T = (\delta H_1, \delta H_2, \delta f_m)$ for the dispersion of real height errors according to $D[h(f_N)] = \hat{P}(f_N) \hat{D}(\vec{x}_e) \hat{P}^T(f_N)$. According to the structure of equation (20), the transfer matrix, $\hat{P}$, for the bottomside ionosphere has the following form

$$\hat{P} = \left(-F_1, -F_2, -H_1 \frac{\partial F_1}{\partial f_m} - H_2 \frac{\partial F_2}{\partial f_m} \right).$$

Analogously, according to equation (21), we have for the topside ionosphere

$$\hat{P} = \left(-F_3, 0, -H_1 \frac{\partial F_3}{\partial f_m} \right).$$

3. THE RESULTS OF COMPUTED MODELLING

A computed simulation of the inverse problem was carried out for two values of the critical frequency, $f_m$equal to 6 MHz and 10 MHz. In both cases, h_m=350 km, H_1=100 km, H_2=75 km, $f_{\max} - f_{\min}$= 0.2MHz, root mean square deviate, σ, for the group paths, $P_g(f)$, and group retardation, $\Delta P_g(f)$, was assumed to be equal to 10 km. The height, z_s, corresponds to the plasma frequency, $f_{Ns} = f_m - 0.5$ MHz, for the group retardation corresponding to n_2=5. The signals reflected from the Earth's surface were taken from the interval $(f_m, f_m + 0.5MHz)$. A number of working frequencies, n_1=5, so n=10, were used for the topside ionospheric sounding. The calculations were carried out for different angles, Θ, between the vertical and the geomagnetic field intensity vector. It turned out that the results for two values of f_m agree with each other in quality and also closely in quantity. Therefore, the results below for modelling the inverse problem for f_m=6 MHz are described. The calculations show that the LMS and the regularizing solutions are close to each other. However, random errors in the diagnosing parameters differ. This is demonstrated in the Figure.

It is clear, from the graphs, that for calculations of the ordinary wave trace, $\sigma(h)$ increases from the pole to the equator. However, for the extra-ordinary wave trace, $\sigma(h)$ doesn't depend on the angle Θ. Roughly the same result is found for simultaneous calculations of the ordinary and extra-ordinary wave traces of an ionogram. It is easy to see that in all cases the regularizing solution has a $\sigma(h)$ that is smaller than the LSM solution. For simultaneous use of the ordinary and extra-ordinary wave traces, the divergence between root-mean-square deviations for real heights reach a factor of 20.

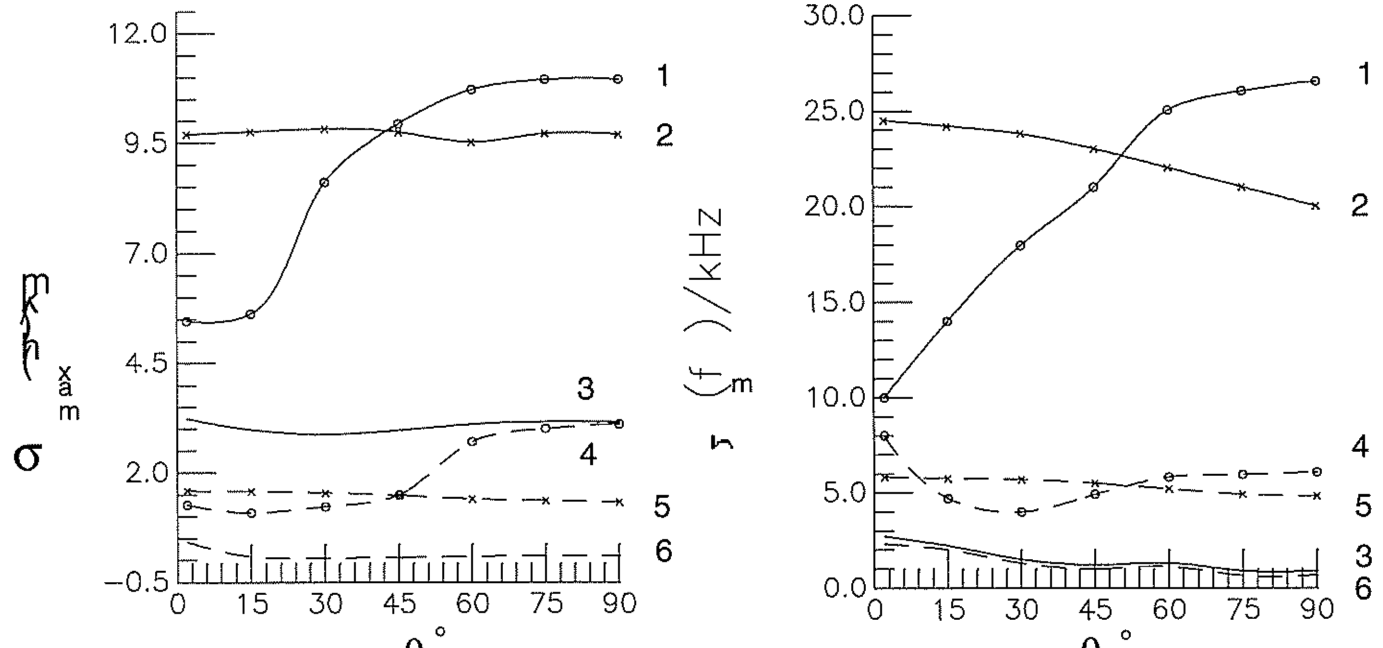

Figure. Θ-dependencies of the maximum values of $\sigma(h)$ for a layer beginning in the lower ionosphere (on the left) and for values of $\sigma(f_m)$ (on the right) under different cases of ordinary and extra-ordinary wave traces use. For the LSM solution: curve (1) describes the ordinary wave trace, (2) the extra-ordinary wave trace, and (3) is for simultaneous ordinary and extra-ordinary sounding, and for the regularizing solution: curves (4) describe ordinary wave trace, (5) is extra-ordinary wave trace, and (6) is for simultaneous ordinary and extra-ordinary sounding.

In the Figure, it is clear that from the simulation, the $N(h)$-profiles separate for each trace and the regularizing solution has a smaller random error for f_m than the LSM-solution. With the simultaneous use of both ordinary and extra-ordinary traces, the regularization method, on the whole, improves the f_m determination compared with the LSM-method.

4. CONCLUSIONS

Modelling inverse problems for vertical, transionospheric sounding shows that using regularization decreases the random real height errors for $N(h)$-profiles compared with the least-squares method. The regularization method is especially effective when simultaneous ordinary and extra-ordinary ionogram traces are used: root-mean-square deviates for the real height $\sigma(h)$ decrease by approximately 20 times.

References

Danilkin, N.P., P.F. Denisenko and V.V. Sotsky, Peculiarities of the inverse problems of vertical radio sounding of the ionosphere, *Adv. Space Res., Vol.8, N 4, pp.(4)91-(4)94, 1988.*

Denisenko, P.F., N.V. Nastasyina and V.I. Vodolazkin, Possibility of using ionosondes for regular observation of irregularities of electron density, *Report UAG-104, World Data Centre A for Solar-Terr.Phys., Ionosonde network and stations, Jan.1995, pp.94-99.*

Denisenko, P.F., N.V. Nastasyina and V.I. Vodolazkin, Usage of regularization techniques for effective electron collision frequency determination from oblique ionospheric sounding, *Ann. Geophisicae 14, pp.811-815, EGS - Springer-Verlag, 1996.*

Kovalev, V.A., V.V. Sotsky and M.D. Fligel, The increase accuracy of determination of full $N(h)$-profile from satellite vertical sounding data, *Geomagn. Aeron., Vol.31, N 4, pp. 738-740, 1991*

Hudson, D.J., Statistics, lectures on elementary statistics and probability, *Geneva, 1964.*

THE EFFECT OF THE D-REGION AND E/F VALLEY ON N(H)-PROFILE CALCULATIONS AND RADIO WAVE PROPAGATION CHARACTERISTICS

G.I.Gordienko,
Institute of Ionosphere, Akademy of Sciences, 480068, Almaty, Kazakstan
E-mail: gord@ionos.alma-ata.su

1. INTRODUCTION

Organisation of computer aided processing of ionograms, causes problems such as: which computer method to use for scaling ionograms, what information should be scaled, which requirements and tasks for particular users are needed and which tasks should be assumed? On the other hand, computer analysis of ionosonde records makes it possible to obtain a large quantity of ionospheric data. As a result another problem arises - how can the ionospheric station operation be optimised as a whole. This paper discusses an aspect of this - how much advantage could be gained by separating ordinary and extraordinary modes? This point is considered in two parts: first, the calculation of N(h) - profiles from the ionograms, and second, how N(h) - profiles are used to estimate radio wave propagation characteristics.

It is well known that N(h) profile calculations need to overcome specific difficulties with ionograms as the D-region and the E/F valley are unobserved by the vertical sounding method. Calculations of N(h) profiles take account of this by assuming some electron density distribution in the unseen regions and by using extraordinary mode information to correct the results. Several methods exist for making these calculations. We use the computer program [2] for calculating the electron density profiles from ground - based vertical - incidence ionograms to investigate the effects of uncertainties in the electron density distribution in the D-region and the E/F valley on calculations of N(h)-profiles.

We investigate the effectiveness of using the extraordinary mode information as a correction parameter in N(h) profiles calculations. Simulations of different unobserved regions are made by inverting h'(f) into N(h) profiles and then recalculate theoretical h'(f) curves from the resulting N(h) profile. The results are compared with the tests [1]. The tests are accurate numerical ionograms corresponding to known electron density profiles N(h) and were made with the aim of testing methods for the analysis of ground-based vertical incidence ionograms. Typical day and night conditions are considered. Virtual heights h'(f), simulating the vertical sounding method, and radio wave trajectories are computed by the method of characteristics [16, 17]. Frequencies in the range 0.1MHz to foF2 are analysed for h'(f). Oblique trajectories are calculated for the frequency range 2-15 MHz using different takeoff angles so that the day-time refraction heights are 95-270 km and 122-260 km at night. The oblique range (L) changes from 250 to 1500 km by day and from 500 to 3000 km by night. A dipole geomagnetic field is used. Radio wave trajectories are considered in the magnetic meridian plane and the electron concentration distribution is assumed to be spherical stratified.

2. THE D-REGION AND VALLEY IN N(H) PROFILE CALCULATIONS

At night, reflections on real ionograms are observed only from the F-region and the underlying ionisation in the D, E-region and valley is unknown. The influence of different underlying ionisation distributions on the F-region ionogram form is investigated. A series of h'(f) calculations are made when the underlying N(h) - profile is given by [1] above 200 km while below 200 km it is varied within the observed bounds [3-6], Figure 1. The h'-values for practically all versions don't change by more than 5 km in virtual height even if the electron density profiles of the E-region have large differences

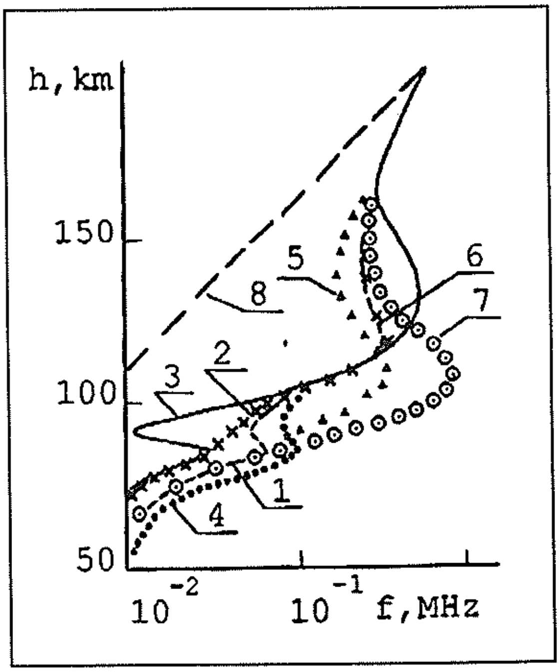

(version 7). For the versions 1-4, the difference between the calculated and test heights, h', is not more than 1 km. By night, the details of the underlying ionisation height distribution does not have an important effect on the ionogram F-region trace shape. Thus, the real N(h)-profile in the unobserved regions of the ionogram is problematic. Further, using an algorithm [2], test ionograms have been made and inverted giving N(h)-profiles. If the height distribution of the electron concentration in the underlying ionospheric region is known, then method [2] makes it possible to calculate the N(h)-profile exactly. If the electron concentration distribution below fmin is unknown, then the best result was achieved by correcting the calculation of N(h) - profile using the data for the extraordinary component (fx). But it is extremely important to know that the value fx is close to fmin.

Using the free lower part entails distorting the N(h)-profile as a whole and, evidently, is unreasonable. (If the height distribution of the electron concentration in the underlying ionospheric region is as a certain section of the N(h)-profile, which is set arbitrarily, the final N(h)-profile is incorrect).

If the information about the underlying electron concentration distribution is not available then method [2] makes it possible to calculate the nighttime N(h)-profile with an accuracy of 5-15 km at the base of F-layer.

Above 200 km profiles from [1] are used in tests. Below 200 km tests using E-region N(h)-profiles together with N(h) for the D - region taken from [3]; and rocket N(h) - profiles from [5, 6, 4] are used.

For day-time conditions, the uncertainties (inaccuracies) of the N(h)-profiles in the ionospheric D-region and valley are considered separately. The day-time D-region was set by the test (in [1]; Fig. 9, p.89; Table 11, p. 59; with DIP = 70 ; fH = 1.5) with variations chosen to conform with the scatter interval of the experimental observations and model output [3, 7-14]. The D-region day-time variations lead to a change in the N(h) results of up to 5 km in the E-region while the F-region h'(f) results were unchanged.

Next the E-region is set by the test [1], and the E/F valley is varied. Calculations for the corresponding h'(f)-curves show that the differences in the N(h)-profile for the valley only have an influence on the results near fminF2. For frequencies f > 1.2 foE, the h' heights are nearly equal. Calculations of the N(h)-profiles for the test ionogram show that the best approach to the test N(h)-profile is achieved when correction parameters such as the extraordinary component for the F - region or the valley depth are used.

So, algorithms like [2] make it possible to calculate reasonably accurate N(h)-profiles in the region of the ionosphere observed by an ionosonde both by day and by night. However, the N(h)-profile in the "unobserved" regions is not determined.

3. PROFILES AND RADIO WAVE PROPAGATION CALCULATIONS.

We showed that order of magnitude variations in the nighttime D-region electron concentration do not lead to important differences in propagation ranges, L. However, if the N(h)-profile varies in the E-region, then the propagation range changes to a greater extent, sometimes more than 50 per cent. In all the N(h) models, foE < 1 MHz; i.e., the ionograms only had F-region reflections. When calculating propagation ranges it is necessary to know the real N(h)-profile, especially in the E-region, to avoid significant errors. However, as the reflection region recedes from the unobserved underlying regions, the errors drop below 1 per cent.

During day-time everything indicates that radio waves reflected beneath the valley may have errors of about five per cent in L Therefore, to improve the calculation of L it is necessary to set the D-region N(h)-profiles more precisely than "on average". Calculations of L, with N(h)-profile variations in the valley, show that errors decrease as the reflection region moves away from the valley.

Errors in L are greatest if the valley is not taken into consideration but is replaced by a monotonic profile with Nv = NmE.

Ionograms calculated for all N(h) models, for frequencies greater than 1.2foE, do not differ from one another and it is consequently impossible to say anything about the valley depth. But it follows that the existence of a valley affects calculations of L and therefore it must be taken into account. Even if an average valley is used, and the average Nv differs from the real Nv by up to 35%, the errors will decrease by an order of magnitude. As a result, on the one hand algorithms like [2] make it possible to calculate useful N(h)-profiles from ionograms for their observed sections and on the other hand, for the oblique path it is extremely important to know the actual height distribution of electron concentration in the ionosphere, especially in the D-region and the valley. It is essential to use the best ionospheric models for these regions when reducing ionograms to electron density profiles. For example, for night-time ionograms, known N(h) models of the whole underlying unobserved ionosphere can be used and for day-time the existing N(h) D-region models can be used while it will be better to set the valley functionally with heights of the E layer maxima h(foE) and beginning of F-layer h(fmin).

Available models of N(h) can be used also, for example IRI [18]. Using model experiments, the effects on N(h)-profiles and range propagation calculations caused by uncertainties in the height distribution of the electron density profile were investigated. Aided by this experiment, some features appeared in real situations connected with reducing ionograms to true height profiles. These were applied to N(h)-profiles from ionograms compared with those received during rocket experiment electron density determinations. The N(h)-calculations were carried out by the algorithm [2] using all possibilities of this method together with suitable models such as the IRI [18] and [15] to verify their potential for correcting results. The N(h)-profiles calculated with the IRI true height sections for the D- and E-regions included differed from the rocket N(h)-profiles by 10 to 30 km. while the calculations corrected by the model [15] give N(h)-profiles differing from the rocket profiles by 10 to 20 km. However, N(h) calculation errors caused by manually scaling ionograms and other problems (spread F, sporadic E, great fmin and other) cause errors in the calculated true heights of up to 40 km.

4. CONCLUSION.

Using model insertions is probably the best and most effective way to calculate N(h)-profiles compared with another methods. That is why uncertainties in the ionograms arising in real situations require some algorithms. Currently, it is difficult to gain greater accuracy for N(h)-profile calculations than that obtained with the good N(h)-profile models of the unobserved regions. The latter determines the best accuracy of calculated radio wave propagation characteristics.

References

[1] McNamara L.F. and J. E. Titheridge. Numerical ionograms for comparing methods of N(h)-analysis. IPS-X5, 1977, 91 p..

[2] Gulyaeva T.L. FORTRAN-program ITERAN for rapid iterative N(h) analysis of ionograms. Moscow, No. 1460-78 Dep., VINITI, 39 p.,1978.

[3] Kozin I.D., G.I.Gerasimov, B.T.Zumabaev et al. Dynamic models of the lower ionosphere for predictions of disturbances of the outer sources of the ionization. In: Modulation and Geophysical effects in cosmic rays. Alma-Ata, p.20-31, (in Russian), 1985.

[4] Knight P.F. Classification of night-time electron density profiles. J. Atmos. Terr. Physics,\1972, v. 34, p. 401.

[5] Smith L.G. A sequence of rocket observations of night-time sporadic E. J. Atmos. Terr. Phys., 1970, v. 32, pp.1247-1257.

[6] Smith L.G. Roc ket observation of sporadic E and related features of the E-region. Radio Sci., 1966, v.1, # 2, pp. 178-186.

[7] Mechtly E.A., J.S. Shirke. Rocket electron concentration measurements on winter day of normal and anomalous absorption. J. Geophys. Res., 1968, v. 73, # 19, pp.6243-6247.

[8] Thomas L. The lower ionosphere. J. Atmos. and Terr. Phys., 1971, v. 33, p.157.

[9] Seddon J. C. Propagation measurements in the ionosphere with the aid rockets. J. Geophys. Res., 1969, v. 74, # 5, p. 1184.

[10] Lee H. S., A. J. Ferraro. Winter D-region electron concentration and collision frequency features obtained with high-power interaction measurement. J. Geophys. Res., 1969, v. 74, # 5, p.

[11]

[12] Belrose J. S. Radio wave probing of the ionosphere by the partial reflection of radio waves (from heights below 100 km). J. Atmos. and Terr. Phys., 1970, v. 32, p. 567.

[13] Belikovich V.V., E.A.Benedictov, V.D.Vjakhirev et al. Catalogue of the electron density profiles of the D-region of the mid-latitude ionosphere. Development of empirical model. Preprint No. 171, NIRFI, Gorky, 51 p., (in Russian), 1983.

[14] Pakhomov S.V. Simultaneous rocket measurements of electron concentration of the ionospheric D region at polar, middle and equatorial latitudes. Geomagn. and Aeronomy, v. 20, No.5, 934- 936, 1980.

[15] Kidijarova V.G., Yu.A.Rjabov, A.A.Yastrebov. Atmospheric processes and the lower ionosphere structure in winter. Geomagn. and Aeronomy, v.20, No.5, 937-940, 1980.

[16] Zelenova T.N. Regularities of variations of the E-F valley parameters. Preprint No. 19(285), IZMIRAN, Moscow, 29 p., (in Russian), 1980.

[17] D.S.Lukin, V.A.Shkolnikov. Kosmicheskie Issledovanija, v.6, No.3, 389-394, 1968.

[18] Troitsky B.V. Response of sygnal of radio sounding on the ionospheric inhomogeneties. Nauka, Alma-Ata, (in Russian), 1983.

[19] Bilitza D. International Reference Ionosphere IRI-1990. NSSDC/WDC-A-R&S Rept. 90-22, GSFC, Greenbelt, Maryland 20706, 1990.

AN ALTERNATIVE DISTRIBUTION FOR STUDIES OF AMPLITUDE FLUCTUATIONS OF HF-SIGNALS REFLECTED VERTICALLY FROM THE IONOSPHERE

P. F. Denisenko, N. E. Sheidakov, V. V. Sotsky and Yu. N. Faer
Institute of Physics, Rostov State University, 194, Stachky ave, 344104, Rostov-on-Don, RUSSIA
Phone: +7 8632 280985, fax: +7 8632 285044, e-mail: denis@riphys.rnd.su and denisen@phys.runnet.ru

ABSTRACT

It is acceptable to describe the amplitude fluctuations of signals reflected from the ionosphere by Rice's law. The experimental data for parameter β^2 (the ratio of the signal to noise) obtained from this distribution tells us about the predominance of a mirror component of radiation in a signal (β^2>1). However, calculations carried out for an exponential spectrum of electron density irregularities in the F-region, on the contrary, indicate that a noise component (β^2<1) is prevalent. An amplitude distributi0on model different from the Rice model is offered in this work. It was used to determine β^2 for night F-region vertical sounding data at the Rostov-on-Don ionospheric station. The model describes the observed amplitude distribution well, giving values of β^2 that do not contradict the theoretical estimates.

1. INTRODUCTION

In radio physics, $\beta^2 = E_0^2 / < E_s^2 >$ is equal to the ratio of the middle intensities of the coherent (mirror) and noncoherent (noise) components of radiation passing through a medium and is used to describe the statistically irregular structure of the ionosphere [1]. For plane waves, β^2 is connected by a simple relation, $\beta^2 = [\exp(L) - 1]^{-1}$, to the attenuation (optical thickness) of a coherent vertical sounding signal

$$L = 2\int_{h_0}^{h_r} \alpha_0 dh,$$

where α_0 is the extinction coefficient [2]; h_0 is the height of the lowest layer; and h_r is the reflection height.

If the characteristics of electron density irregularities are known, it is possible to obtain α_0 and determine β^2. Theoretical estimates for the E-layer give values of β^2>1 [3], and for the F-region, β^2<1 [4]. However, an overwhelming number of experiments show β^2>1 [1,5]. In the E-layer, theory and observation agree, while for the F-region, they disagree. It follows, from theoretical calculations, that the noncoherent radiation component should dominate the reflected signal, but experimental data, interpreted using Rice's model [1], indicate mirror (coherent) signal components dominate. This report examines this contradiction.

2. ALTERNATIVE DISTRIBUTION OF THE AMPLITUDES

We will use the following treatment to describe the statistical characteristics of radiation. We suppose that the resulting field formed at the Earth's surface, after the signal is reflected from the ionosphere, arises from interference between two waves, one, a coherent component having a constant phase, φ_0, and amplitude, E_0, and the other, a noncoherent, noise component having random phase, φ_s, and amplitude, E_s. The envelope for the superposition of these waves is given by the following solution

$$R = \left[\left(E_0 \cos\varphi_0 + E_s \cos\varphi_s \right)^2 + \left(E_0 \sin\varphi_0 + E_s \sin\varphi_s \right)^2 \right]^{1/2} . \qquad (1)$$

In the standard (basic) model, the phase, φ_S, changes evenly in the interval from 0 to 2π, and the amplitude, E_S, has a Rayleigh's law distribution

$$w_1(E_s) = \frac{E_s}{\alpha_1^2} \exp\left(-\frac{E_s^2}{2\alpha_1^2} \right), \qquad (2)$$

where $2\alpha_1^2 = \left\langle E_s^2 \right\rangle$. This description is a consequence of the supposition of quadrature components

$$E_S \cos\varphi_S = \sum_i E_i \cos\varphi_i, \qquad E_S \sin\varphi_S = \sum_i E_i \sin\varphi_i,$$

that are the sum of a great number of random vectors each having a Gaussian probability density [1].

In our alternative model the log-normal law is taken instead of distribution (2)

$$w_2(E_s) = \frac{1}{\sqrt{2\pi}} \frac{1}{E_s} \exp\left[-\frac{(\ln E_s - m)^2}{2\alpha_2^2} \right], \quad E_s > 0, \qquad (3)$$

where α_2 and m are the distribution parameters. The choice of probability density (3) is based on the following considerations.

Under the interference field assumption, it is necessary to take into account the spherical nature of the sounding. Coherent and noncoherent components are formed by rays incident on the ionosphere with different angles. Waves reflected vertically, and attenuated by scatter from electron density irregularities, form the coherent component. The noncoherent component arises as a result of multi-fold small-angle scattering of signals incident on the ionosphere with angles close to vertical. The small angle scattering for vertical sounding is a well-known experimental fact [1]. The multi-fold scatter follows from the condition that the optical thickness $L_S > 1$ for the F-region [4]. Since the fluctuation field component is formed inside of small body angle, the sphericity of the waves in this part of space may be neglected. For plane waves under multi-fold scatter, the level of fluctuations is proportional to $\ln E_S$ and is described by the normal law [5]. Therefore, E_s changes according to equation (3).

The argument above is heuristic. Nevertheless, it is confirmed by the experimental data offered below.

Using the transformation rules for probability densities of random quantities that are functions of one random quantity, R, expressed by formula (1), we get Rice's law [1] for the basic model (2):

$$W_1(R) = \frac{R}{\alpha_1^2} \exp\left(-\frac{E_0^2 + R^2}{2\alpha_1^2} \right) I_0\left(\frac{E_0 R}{\alpha_1^2} \right), \qquad (4)$$

where $0 \le R \le \infty$, I_0 is the modified Bessel's function of zero-degree. Analogously, for the alternative model, we have

$$W_2(R) = \frac{1}{(2\pi)^{3/2}} \frac{2R}{\alpha_2} J(R, \mathrm{E}_0, \alpha_2, \mathrm{m}), \qquad (5)$$

where

$$J(R, \mathrm{E}_0, \alpha_2, \mathrm{m}) = \int_0^\pi \frac{d\varphi}{R^2 + 2E_0 R\cos\varphi + E_0^2} \exp\left\{ -\frac{1}{8\alpha_2^2} \left[\ln\{ \frac{R^2 + 2E_0 R\cos\varphi + E_0^2}{\mu} \} \right]^2 \right\},$$

$\mu = \exp(2m)$. The shape of curve (5) depends on E_0. For small values of E_0 $\left(\beta^2 << 1\right)$ the distribution is single-peaked and close to log-normal law. As E_S increases, an additional maximum appears to the right of the primary maximum. Thus, the alternative distribution, (5), differs from the basic one, (4); the former having a two-peak amplitude distribution.

3. β^2 Parameter determination

To obtain β^2, the initial moments, $\langle R^k \rangle$, of the random quantity R (given by equation (1)) are used. Since the basic distribution depends on the parameters E_0 and α_1, it is sufficient to calculate the first two moments [1]:

$$\langle R^1 \rangle = \sqrt{\frac{\pi}{2}}\alpha_1 \exp\left(-\frac{\beta^2}{2}\right)\left[(1+\beta^2)I_0\left(\frac{\beta^2}{2}\right)+\beta^2 I_1\left(\frac{\beta^2}{2}\right)\right], \qquad (6)$$

$$\langle R^2 \rangle = 2\alpha_1^2(1+\beta^2),$$

where I_1 is a modified Bessel's function of the first-degree. The system of equations (6) has an unambiguous solution.

The alternative distribution (5) depends on three parameters: E_0, m, and α_2, and requires a corresponding number of equations. Because formula (5) is awkward, we cannot obtain analytic expressions for the odd moments, $\langle R^k \rangle$. The first three even moments are

$$\langle R^2 \rangle = \langle E_0^2 \rangle + \langle E_s^2 \rangle,$$

$$\langle R^4 \rangle = \langle E_0^4 \rangle + 4\langle E_0^2 \rangle\langle E_s^2 \rangle + \langle \mathrm{E}_s^4 \rangle,$$

$$\langle R^6 \rangle = \langle E_0^6 \rangle + 9\langle E_0^4 \rangle\langle E_s^2 \rangle + 9\langle \mathrm{E}_0^2 \rangle\langle \mathrm{E}_s^4 \rangle + \langle \mathrm{E}_s^6 \rangle,$$

and taking into account that $\langle R_s^k \rangle = \exp\left(\frac{1}{2}k^2\alpha_2^2 + km\right)$, the previous expressions can be reduced to the following system of nonlinear equations

$$\langle R^2 \rangle = (\beta^2+1)\mathrm{u},$$

$$\langle R^4 \rangle = (\beta^4+4\beta^2+w)\mathrm{u}^2, \qquad (7)$$

$$\langle R^6 \rangle = (\beta^6+9\beta^4+9\beta^2 w+w^3)\mathrm{u}^3,$$

for auxiliary variables $u = \langle E_s^2 \rangle = \exp(2\alpha_2^2+2m)$, $w = \exp(4\alpha_2^2)$. System (7) has three solutions. The selection of solutions is made using a χ^2 criterion [6] giving the best correspondence between the theoretical distribution and the experimental data.

4. EXPERIMENTAL RESULTS

These arguments were tested at the Rostov-on-Don ionospheric station using amplitude measurements of vertical ionospheric sounding signals reflected from the F-region. The measurements were made on March 1, 1990, prior to sunset and at night, from 16:40 till 19:40 LMT. Polarization reception (separating ordinary and extraordinary components) was used at the frequencies: 2.0, 3.5, 4.0, 4.5, 5.5 MHz, for the ordinary component, and at the frequencies: 2.7, 4.2, 4.7, 5.2, 6.2 MHz for the extraordinary component. One pulse per each second was transmitted sequentially at each frequency. The amplitude of the reflected signals were recorded on magnetic tape and were later converted, using an analog-to-digital converter, and stored on PC disks.

The data were divided into 300 five-minutes intervals (samples), containing 300 amplitude measurements in each sample. The radius of correlation between amplitude measurements was controlled by constructing histograms of experimental distributions for each sample. More than 10 independent measurements were made in each histogram interval. The current average amplitude, from the first to the last sample, was also controlled. This allowed the degree of stationarity for the time series to be determined. When these conditions failed, the sample was either rejected or was added, together with new measurements, to the next 5-minutes amplitude record.

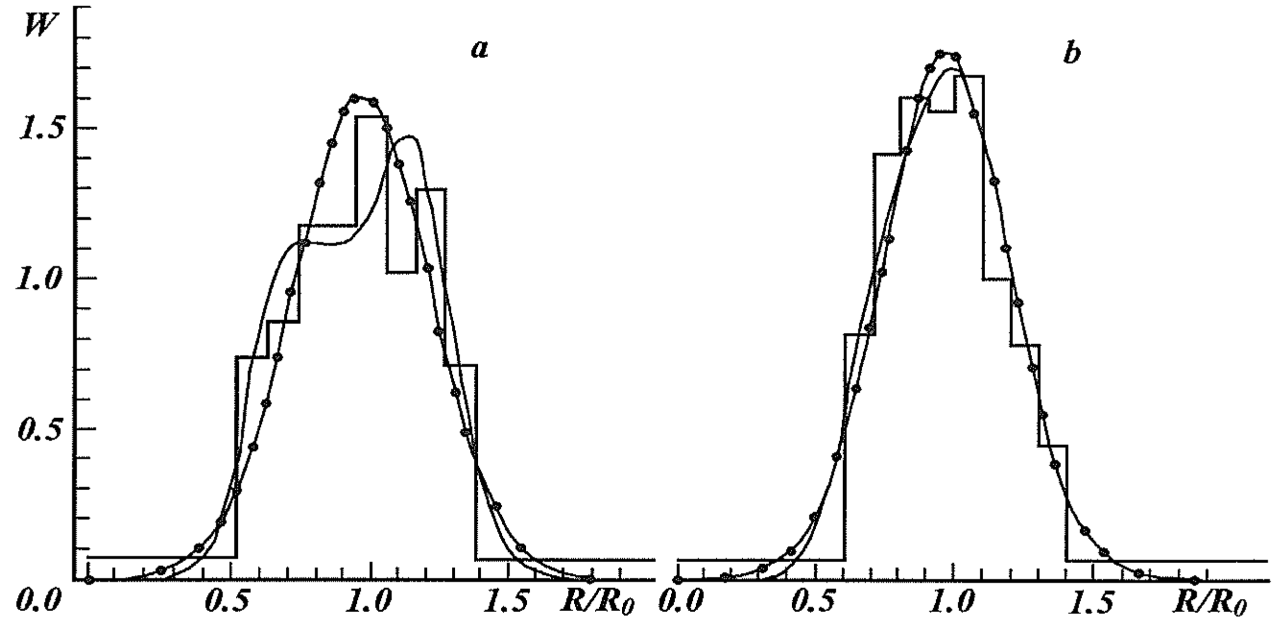

Figure: The experimental and theoretical amplitude probability densities for decametric signals reflected vertically from the ionosphere, observed at Rostov-on-Don, March 1, 1990, 17:40-17:45 LMT. The continuous curves are the alternative distributions, curves with dots are the Rice distributions. $R_0 = \sqrt{\langle R^2 \rangle}$; (a) 4.0 MHz, ordinary component, β_2^2=0.11, β_1^2=6.9; (b) 5.2 MHz, extraordinary component, β_2^2=0.05, β_1^2=8.4.

For each sample, using the χ^2 criterion, the hypothesis that the experimental data are described by distributions (4) and (5) was tested. As a result of selection (at the 5%-level of importance), in 77 cases it turned out that it was possible to use distribution (5) and, at the same time, distribution (4) could be used in 51 cases. In 8 cases out of the 51, the values of β^2>1 were close to each other for both distributions. In another 43 cases, for distribution (5), values of β^2<<1 were obtained and at the same time for distribution (4) the values of β^2 were more than 1. In the figure, frame (a) shows the experimental histogram for the ordinary component amplitudes measured for frequency 4 MHz between 17:40-17:45 LMT, together with the alternative distribution (5) and the Rice distribution (4). The alternative distribution has two maxima and β_2^2=0.11 for χ^2 corresponding to the 19%-level of importance. The Rice distribution gives β_1^2=6.9 for χ^2 corresponding to the 2%-level of importance. In the figure, frame (b) similar results are presented for a one-peak alternative distribution (5) for a sample of extraordinary component amplitudes measured for the frequency 5.2 MHz during the same time interval. For the alternative distribution (50%- importance level for the χ^2 criterion) the value of β_2^2=0.05 was obtained with β_1^2=8.4 for the Rice distribution (38%-level of importance for the χ^2 criterion). These examples demonstrate that the curves determined by models (4) and (5) may both to differ and also coincide with each other. The values of β^2 are determined by the choice of model and leads to different conclusions.

5. CONCLUSION

Thus, the results for the β^2 parameter determination by the experimental data essentially depends on using a theoretical law of the amplitude distribution for signals reflected from the ionosphere. For the thin layer (E-region) where scattering near the reflection level plays a basic role (a rough diffusion screen model) Rice's law describes the real situation well. But for a thick layer (the F-region) it is necessary to take into account multi-fold radio wave scattering processes. These processes can be accounted for using the distributions offered in this paper, adjusted to fit the experimental and theoretical estimates of β^2. However, the problem of determining β^2 for the ionosphere cannot be considered finally solved.

References

1. Ya. L. Alpert, Radio waves propagation and the ionosphere. M., Nauka/Science, 1972, 563 pp. (in Russ.)
2. S. M. Rytov, Yu. A. Kravtsov and V. I. Tatarsky, Introduction in statistical radio physics. Random fields. M., Nauka/Science, 1979, 464 pp. (in Russ.)
3. N. G. Denisov, L. M. Yeruchimov, Statistical properties of phase fluctuations under the full wave reflection from the ionospheric layer, Geomagnetizm i aeronomia, 1966, V.6, No 4, p.695 (in Russ.)
4. A. G. Bronin, P. F. Denisenko and N. A. Zabotin, About attenuation of coherent field component of decameter waves under the vertical sounding of the ionosphere because of scatter on the random irregularities, Geomagnetizm i aeronomia, 1993, V.33, No 1, p.169 (in Russ.)
5. I. S. Vsechsvyatskaya, Statistical properties of signals reflected from the ionosphere. M., Nauka/Science, 1972, 153 pp. (in Russ.)
6. D. Hudson, Statistics for physicists. Mir/World, 1970, 296 pp. (in Russ.)

Round-the-clock measurements of absorption and motions in the lower ionosphere at spaced-antenna reception of signals from LF-broadcasting stations

E. L. Afraimovich (email afra@sitmis.irkutsk.su) and K. S. Palamartchouk, Institute of Solar-Terrestrial Physics (ISTP), p. o. box 4026, Irkutsk, 664033 RUSSIA

ABSTRACT

The use of computer Doppler filtering of ground wave method is suggested for treating the data of spaced-antenna reception of signal from LF-broadcasting stations with a high-precision master oscillator signal. This method can be employed in round-the-clock measurements of characteristics of motions, absorption, and angles of arrival of the radio wave. The use of the method is exemplified by a treatment of data from the LF-spaced-antenna receiving facility; first results on D-layer dynamics and absorption are presented.

1. INTRODUCTION

Recent meteorological research has witnessed a clear tendency for the Earth's atmosphere to be regarded as a whole and not to be confined to the tropospheric boundaries alone. Yet there is an obvious shortage of experimental data on atmospheric conditions at stratospheric and thermospheric heights and on the dynamic regime of these regions. The most valuable data of this kind are furnished by MST-radars, but these are too costly in regard to both the construction and operation and are therefore very scarcely distributed over the globe. Furthermore, MST-radars are active instruments and contaminate drastically the cluttered propagation medium.

Traditional incoherent spaced-antenna reception of broadcast LF signals is an alternative crucial method of experimental research into the lower atmosphere dynamics [*Sprenger and Schminder,* 1967; *Afraimovich,* 1982; *Kazimirovsky and Kokourov,* 1995]. Such observations can provide the drift velocity and direction of ionospheric irregularities at the height of reflection (typically 70–100 km for LF-range) provided they are in ordered motion. Such a set of parameters obtained is exceeded by MST-radars, especially as their validity has not yet been rigorously proved (the validity has been confirmed only through a comparison with other observing techniques). On the other hand an installation providing such observations is much cheaper than an MST-radar.

The reliability of these measurements can be ensured only on short radio paths provided that the ground wave is totally suppressed; in this case the ionospheric(A_i) to ground wave amplitude (A_g) ratio $G=A_i/A_g$ does not exceed 30–50 dB, even in the nighttime. A classical approach is to use polarization filtering of the ground wave using magnetic loops, which gives a gain in G of about 30 dB and resolves the problem of nighttime measurements. In the daytime such a method is entirely unacceptable because of a further 20–40 dB decline in A_i, [*Afraimovich,* 1982].

As a consequence, results obtained refer exclusively to the nighttime [*Kazimirovsky and Kokourov,* 1995]. For the same reason, analysis of broadcasting LF signals cannot be used when measuring the diurnal dependence of such an important characteristic as the radio wave absorption.

This work is devoted to a description of an approach to treating spaced-antenna reception data. As a result of this approach we can measure parameters of motions, effective absorption, and angles of arrival on a round-the-clock basis. Upon bringing the technique to the appropriate performance level and defining its validity range, it would become possible to set up an entire network of ionospheric wind monitors because they are relatively inexpensive. Such a network can provide adequate spatial resolution for investigating large-scale processes in the atmosphere, which would qualitatively upgrade the value of geophysical data obtained. This same approach may be useful when constructing spaced-receiver facilities operating in different frequency ranges as well.

2. RAW DATA COLLECTION

The installation was located at the ISTP Research Range, Badary, Republic of Buryatia (51°N, 102°E); it was a modernized facility for D-region drift measurements that has been operational for two decades now

[*Kazimirovsky and Kokourov,* 1995]. Unfortunately, in May 1996 the observatory at Badary was destroyed by a major forest fire. Obtaining of data was discontinued, but we have observations covering about three weeks of November 1995 and February/March 1996. The observatory is currently in the phase of reconstruction at a different location.

We use the radio signal emitted by a broadcasting station located at a distance of 120 km. The signal frequency is 198 kHz, and its relative stability is of the order of 10^{-12}. Height of reflection may be estimated using the data on angles of arrival of radiovave. Angles of arrival may be calculated using phase delays between spaced channels [*Afraimovich,* 1982]. Direct measurements of height of reflection are performed by *Reinisch and Sales,* 1974. Walues of height of reflection for 180 kHz signal lies in 75(night)–95(day) km diapason. The radio station is in operation every day with a 5.5-hour break at night. The facility's location had an additional advantage as the mountain range lying between the facility and the transmitter made a further contribution to ground wave suppression.

A block-diagram of the facility is presented in Fig. 1.

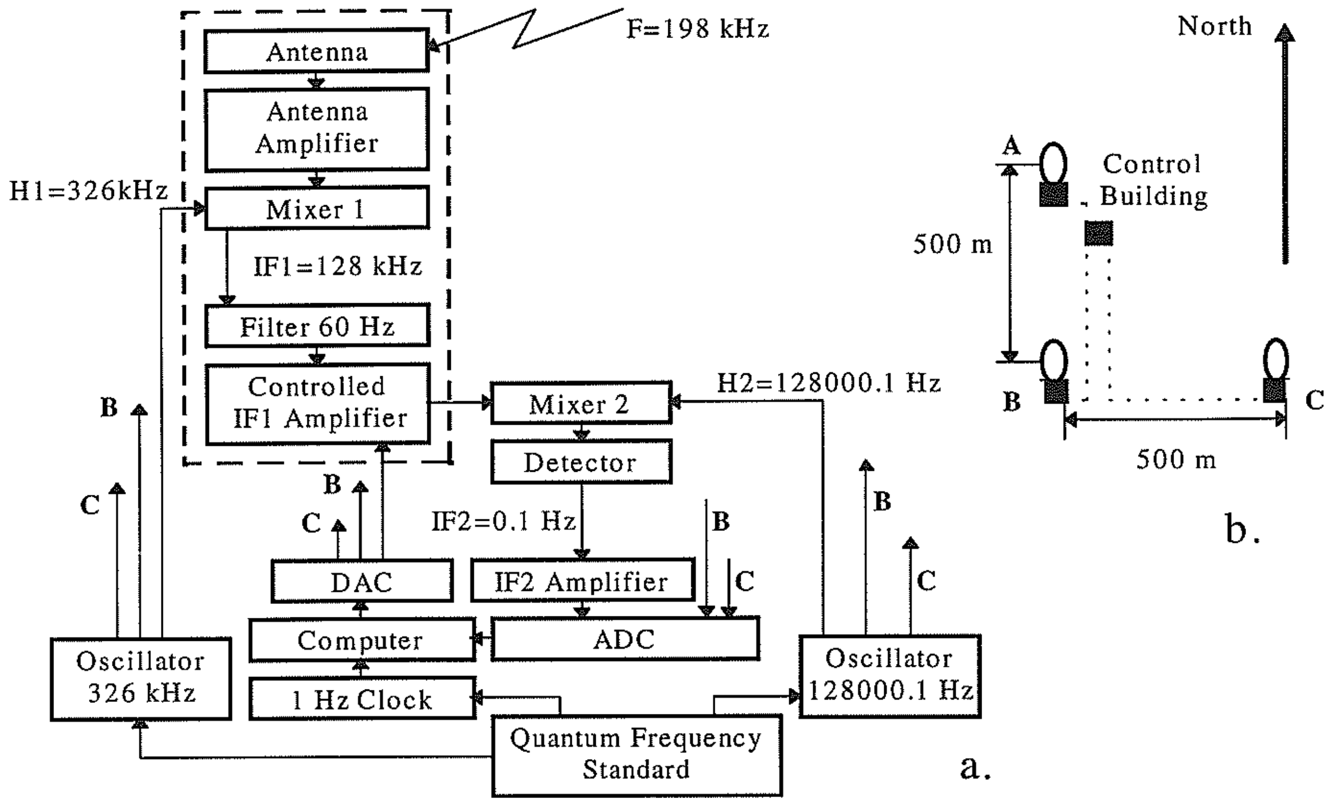

Figure 1a. Block-diagram of recording installation. DAC (Digital-to-Analog Converter), ADC (Analog-to-Digital Converter). F (working frequency of the radio station); H1 and H2 (frequencies of the first and second heterodyne signals); and IF1 and IF2 (first and second intermediate frequencies). The dashed box contains the instrumentation of one of three remote sites; the two others will be the same.

Figure 1b. Schematic map of antenna sites.

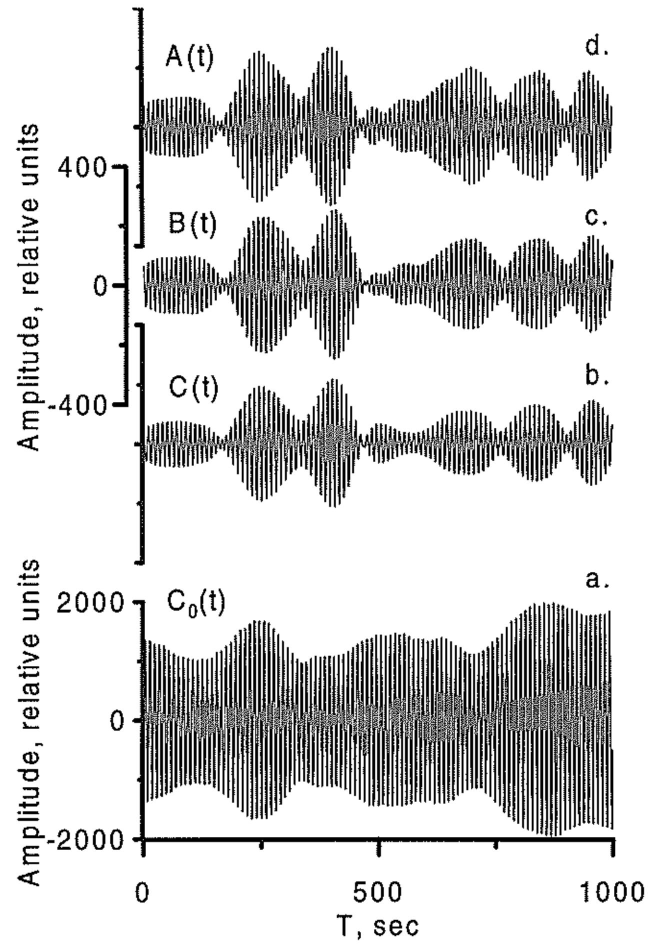

Figure 2. $C_0(t)$ is an example of raw data; $A(t)$, $B(t)$, $C(t)$ are series after Doppler filtering. The record starts on November 19, 1995, 12:48 LT. at Badary.

The facility included three spaced magnetic loops tuned to minimum reception of the ground wave. Antennae were placed at the vertexes of a right triangle with 500-m sides directed from south to north and from west to east. Remote sites were connected to one another via cables.

The signal received by the antenna (F=198 kHz) was amplified, and then mixed with the first heterodyne signal ($H1$=326 kHz), transmitted from the control building by cable converting its frequency, and, filtered by the quartz filter with 60 Hz band. The first intermediate signal ($F1$=128 kHz) was fed to the amplifier with controlled gain. The controlling analog signals were produced for the three antennae separately by a computer using a DAC and were transmitted from the control building by cables. Thanks to computer control of gains and absolute calibration of the receiving system, we can know the real radio wave amplitude round the clock.

The signal from the first intermediate frequency was transmitted by cable to the control building where it was subjected to a second frequency conversion, by mixing with the second heterodyne signal ($H2$=128000.1 Hz). The second intermediate frequency is $IF2$=0.1 Hz. The Detector – $IF2$ Amplifier system was operating as a low frequency filter with the bound of about 1 Hz. And signal IF2 was then fed to the 12-bit ADC and stored by the computer with 1 Hz frequency, specified by a special clock. So the resulting data consist of three rows of 12-digit of numbers (0–4095) sampled with 1-s interval (10 counts for a full cycle of second intermediate frequency)

The computer analyzed the amplitude of the $IF2$ signal and changed gain of the channels if needed.

The System's master oscillator is a quantum frequency standard; it has high relative frequency stability (10^{-12}) and synchronized all the parts of the system both in time and in frequency. So we can store not only the amplitude of the radio wave but also its phase at the three spaced antennae during long periods of time.

Thus raw data are the series $A_0(t)$, $B_0(t)$, $C_0(t)$ of IF2 signal with one second sampling for the three channels. Fig. 2a. gives an example of raw data for one of the channels, $C_0(t)$. This series was recorded in the daytime when $G \ll 1$; so the depth of fading of IF2 is rather small.

3. APPROACH TO DATA TREATMENT

Relatively fast (with periods of tens and hundreds of seconds) amplitude fading of the ionospheric radio signal is caused by interference and diffraction of a multitude of rays reflected from ionospheric regions (traveling with respect to each other and to the receiver) as well as the ground wave. In this case the ground wave remains strictly invariable in frequency because the receiver is fixed with respect to the transmitter and frequencies of rays reflected from travelling reflectors undergo Doppler shifts. Therefore, the spectrum of the received radio signal contains not only the line corresponding to the frequency, emitted by the transmitter, but also components shifted to either side of it.

Fig. 3a. shows the initial amplitude spectrum $C_0(\omega)$ obtained by direct Fourier transform of the $C_0(t)$ record (first 1000 points of $C_0(t)$ are presented in Fig. 2a.). A strong peak at F_g=0.1 Hz is the consequence of the ground wave, and weak serrations at the wings of that strong line are due to ionospheric waves.

Our Doppler filtering technique for the ground wave implies that the received signal is subject to direct digital Fourier transform; subsequently, spectral components corresponding to the ground wave frequency are eliminated and then the inverse Fourier transform is performed. The eliminating procedure involves multiplying the initial spectra by a filter function $R(\omega)$ (see Fig. 3b.), so that spectral components corresponding to the frequency of the ground wave (inside the δF interval) and components that lie too far from the ground wave line (outside the ΔF interval), are replaced by zero. The parameter ΔF is adopted according to the expected width of ionospheric signal spectrum and typically does not exceed 0.02 Hz in LF-band. After filtering the spectra, the inverse Fourier transform is performed.

Hence the resulting series may be regarded as a recording that is completely free of the ground wave. An example of the proposed transformation is shown in Fig. 3c. It should be noted that the ratio of peak values of $C_0(\omega)$ and $C(\omega)$ is about 25 dB, and it is the measure of gain achieved by Doppler filtering. Real gain is smaller and accounts for about 15 dB because the $C(\omega)$ spreads over some frequency range but $C_0(\omega)$ has the form of peak. Fig. 3d. shows the spectrum of the phase difference between IF2 signals of channels C and B. It can be seen that phase difference fluctuations are much stronger at frequencies where the amplitude of $C(\omega)$ is small.

This is additional evidence that $C(\omega)$ is not noise but a spectrum due to the ionosphere within the region where $C(\omega)$ is strong. The final result of filtering is presented in the Fig. 2b. While the initial signal, $C_0(t)$, fades rather weakly, the filtered out signal, $C(t)$, is modulated much more strongly. Curves $A(t)$ and $B(t)$ represent the results of filtering the channels A and B data.

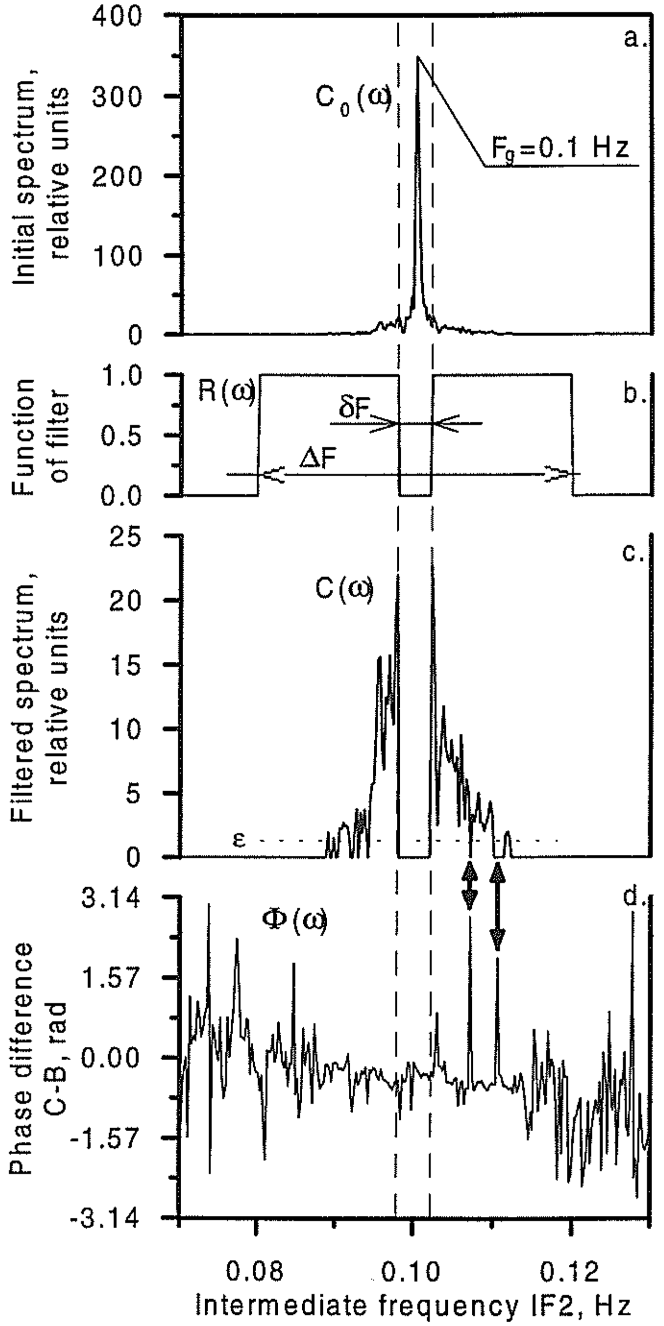

Figure 3. Procedure of Doppler filtering of spectra. (a)—initial spectrum, $C_0(\omega)$; (b)—filter function, $R(w)$; (c)—filtered out spectrum, $C(w)$; (d)—spectrum of phase difference between signals, C and B, $\Phi(\omega)$. F_g — frequency of ground wave; bold arrows point to valleys in the amplitude spectrum, $C(\omega)$, accompanied by spikes in phase difference, $\Phi(\omega)$. The horizontal dashed line on 3c. shows the threshold, ε, used to estimate the ionospheric wave amplitude. Vertical dashed lines mark the boundaries of the ground-wave spectrum. November 19, 1995, 12:48 to 13:56 LT. at Badary.

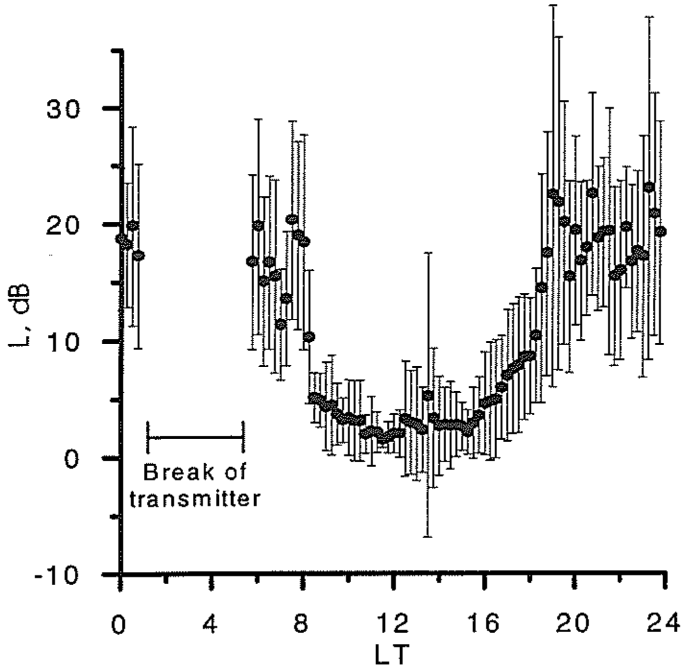

Figure 4. Mean value, L(t) (bullets), and root mean square, RMS (vertical bars), of the relative amplitude of ionospheric wave for 7 days in February/March 1996, Badary.

During the filtering a narrow interval of the ionospheric spectrum is lost within the δF. When the typical width of ionospheric spectrum in the LF band is 0.02 Hz, δF is chosen according to the natural width of the ground wave line. The longer the initial recording, the narrower the spectral interval of ionospheric rays and the smaller the ionospheric spectrum components information loss. To improve the characteristics of the method, it is important to increase the length of continuous registration, provided it is smaller than the characteristic time of phase instability in the transmitter-receiver system. Both our radio station and the master oscillator have relative stability of about 10^{-12} so that the time may be estimated at hundreds of days which is much more than the time of continuous operation of the transmitter. Therefore it is the optimal variant for decreasing the ground-wave width to perform Doppler filtering for each 18.5-hour session. It requires Fourier transform of 66600-point series. In this case the lost part of ionospheric spectrum will not exceed 10^{-4} Hz (or 10^{-2} in relative units).

The strong ground wave line sidelobe influence on the ionospheric part of spectrum can be reduced by employing an appropriate time window [*Harris,* 1978]. When a window with strong (up to 80 dB) sidelobe suppression is used, δF may be doubled but when treating such a long series it is not as important.

After applying the inverse Fourier transform series can be processed by using different methods (based on both coherent and incoherent reception schemes) in order to get ionospheric information with the needed amount of data for desired time resolution.

4. EXAMPLES OF GEOPHYSICAL RESULTS

Data measured using the facility described include recording information on the amplitude and phase of the received radio wave which are then used in computations of ionospheric parameters using different known methods.

A review of methods for analyzing the interference pattern at incoherent spaced-antenna reception is given by *Briggs,* [1968]. When such a method is used in processing the series presented in Fig. 2. the direction of motion (from north through east) and the velocity of ionospheric irregularities are 184.7° and 38.9 m/s, respectively.

Pfister, [1971], gave a description of a method of coherent spaced-antenna reception. When such a method is used, the values of azimuth and velocity are 171.0° and 58.0 m/s respectively.

The measurement of diurnal variations in absorption of the ionospheric wave are possible because of computer controlled gain of channels while the channels are calibrated. The relative amplitude of the ionospheric wave can be estimated as the sum of components of the amplitude spectrum that matched the filter function $R(\omega)$ and greater than the given threshold ε (see Fig. 3c). A diurnal dependence of the mean ionospheric wave amplitude $L(t)$ (in dB) during 7 days in February/March 1996 is shown in Fig. 4. Nighttime to daytime difference of ionospheric wave intensity is due to the daytime enhancement of radio wave absorption and is 17–18 dB. These results are in excellent agreement with the data obtained for the 180 kHz by *Reinisch and Sales,* [1974].

References

[1] Afraimovich E. L., Interference methods of ionosphere radiosounding, Moscow, Nauka, 198 p., 1982.

[2] Briggs B. H., On the analysis of moving patterns in geophysics. J. atmos. terr. Phys., **30**, 1968, pp. 1777–1794.

[3] Harris F. J., On the use of windows for harmonic analysis with the discrete Fourier transform. Proc. IEEE, **66**, 1978, pp. 51–83.

[4] Kazimirovsky E. S., and V. D. Kokourov. Meteorological effects in ionosphere (Rewiew). Geomagnetizm i Aeronomiya, **35**, No.1. pp. 1–23, 1995.

[5] Pfister W., The wave-like inhomogeneities in the E-region. J. atmos. terr. Phys., **33**, 1971, pp. 999–1025.

[6] Reinisch B. W., and G. S. Sales, Multi-frequency long-wave vertical sounding of the lower ionosphere. COSPAR Meth. meas. and results. Lower Ionosphere Strukture. Proc. Symp. Constance, F. R. G., 1974. – Berlin, – 1974. – pp. 139–145.

[7] Sprenger K. and Schminder R. Results of ten years' ionospheric drift measurements in the l. f. Range. J.atmos. terr. Phys., **29**, pp. 183–199, 1967.

STATISTICAL METHOD FOR DETERMINING CHARACTERISTICS OF THE DYNAMICS OF THE RADIO SIGNAL INTERFERENCE PATTERN

E. L. Afraimovich
Institute of Solar-Terrestrial Physics, Siberian Division of Russian Academy of Science
(ISTP SD RAS), P. O. Box 4026, Irkutsk, 664033, Russia; e-mail: afra@iszf.irk.ru

ABSTRACT

A statistical method is proposed for determining the characteristics of the radio signal interference pattern dynamics by measuring variations of phase derivatives with respect to time, and spatial coordinates as a function of time or frequency. These data are used to calculate corresponding values of the velocity vector. Subsequently, velocity and direction distributions are constructed and analyzed to verify the hypothesis of whether there is a predominant displacement. If it exists, then the pattern can be considered to be traveling, and the mean travel velocity can be determined from the velocity distribution. The use of this method is exemplified by an investigation of medium-scale traveling ionospheric disturbances (MSTIDs) and small-scale irregularities (SSI) from simultaneous polarization, angle-of-arrival and scintillation measurements of the ETS-2 radio signal at 136 MHz made in Irkutsk (52° N, 104° E) during December 1989 to December 1990. The method may be useful both in experiments with ionosphere-reflected radio waves and in transionospheric radio sounding operations. The new avenues for remote diagnostics of TIDs are based on exploiting standard measurements of transionosheric radio signal characteristics and coordinate-time measurements using multichannel receivers of the Global Positioning System (GPS).

1. INTRODUCTION

A TransIonospheric Radiointerferometer (TIR) (Afraimovich et al., 1991) is designed for simultaneous measurements of the main parameters of a 136 MHz radio signal from the geostationary satellite, ETS-2, located at 130°E (polarization rotation, angles of arrival, frequency Doppler shift, and amplitude – with a time resolution of 30 s and amplitude scintillations with a time resolution of 0.2 s). The comprehensive nature of our measurements offer a means of investigating the structure and dynamics of ionospheric irregularities simultaneously over a wide range of scales, from a few hundred meters to several hundred kilometers.

Three receiving points A,B,C of the radio interferometer were located at the apexes of a nearly right-angled triangle, with sides about 200 m long. The receiving antennas for channels A, B, and C were single polarization spiral antennas. In addition, the central point, A, incorporated an additional antenna, D, of opposite polarization. The set of antennas at A and D was used to measure the phase difference, $\Delta\phi$, between antennas A and D which is proportional to the total electron content (TEC), $I(t)$, along the line of sight to the satellite.

The set of A, B, and C formed part of the system for measuring time variations of the phase difference $\Delta\phi$ along baselines CB and AB, proportional to values of the gradients I'_x and I'_y, where x and y are directed, respectively, eastward, E, and northward, N. Furthermore, amplitude scintillations with a time constant of 0.2 s were recorded simultaneously from the same antennas.

To implement the method described in Section 2, the continuous series $\Delta\phi_{AB}(t)$, $\Delta\phi_{CB}(t)$ and $\Delta\phi_{AD}(t)$ of at least two-days duration were filtered out in order to eliminate diurnal trends in the measured quantities. An eighth-order Butterworth filter was used in investigating MSTIDs. The period range 30 – 60 min, which lies within the generally accepted range of MSTIDs periods, was used.

Filtered series of $\Delta\phi_{AB}$, $\Delta\phi_{CB}$ and $\Delta\phi_{AD}$ were used to determine TID-induced TEC disturbances $\delta I(t)$ and variations in the phase derivatives, $\phi'_x=\Delta\phi_{CB}/\Delta x$ and $\phi'_y=\Delta\phi_{AB}/\Delta y$, where Δx and Δy are the reduced values of the baseline in the E and N directions. Variations of the phase time derivative $\phi'_t(t)$ were determined by differentiating $I(t)$ (Afraimovich et al., 1991).

2. STATISTICAL MEASUREMENT OF THE RADIO PHASE FRONT VELOCITY VECTOR

Our statistical method developed for determining the velocity, v, and direction, ψ, of the radio signal phase front propagating in the antenna system plane is a generalization of a method proposed by Mercier (1986).

In the simplest form, space-time variations in phase, $\Delta\phi(x,y,t)$, of the transionospheric radio signal are proportional to TEC variations, $\Delta I(x,y,t)$, in the ionosphere, at each time, t, and can be represented in terms of a flat-Earth approximation of a traveling plane phase front

$$\Delta\phi(x,y,t)=k\Delta I(x,y,t)=\phi'_t(t)\Delta t+\phi'_x\Delta x+\phi'_y\Delta y \tag{1}$$

where k is the proportionality factor, and ϕ'_t, ϕ'_x and ϕ'_y are the first phase derivatives with respect to time, t, with respect to the spatial coordinates x and y respectively.

The propagation velocity, $v(t)$, and the direction, $\psi(t)$, of the phase front at each time may be defined as

$$\begin{cases} W_y(t)=\phi'_y(t)/\phi'_t(t)=|W|\cos\psi \\ W_x(t)=\phi'_x(t)/\phi'_t(t)=|W|\sin\psi \\ v(t)=|W|^{-1}=\left(W_x^2(t)+W_y^2(t)\right)^{-1/2} \end{cases} \tag{2}$$

In radio astronomical interferometry, measurements are only made of the spatial derivatives of $\phi'_y(t)$ and $\phi'_x(t)$, which determine the direction ψ modulo 180° (Mercier, 1986). Using the time derivative of the signal phase makes it possible to determine the unambiguous orientation of the wave vector of the phase disturbance in the range 0 – 360° at each particular instant of time.

In practice, we use instantaneous values of v and ψ, determined every 30 s, to construct – on a selected time interval – not only distribution functions of the azimuth $P(\psi)$ (as suggested by Mercier (1986)) but also the velocity $P(v)$.

Ideally, when a "frozen" interference pattern travels in a given direction without changing its shape (specifically, a single plane traveling wave), the phase derivatives $\phi'_t(t)$, $\phi'_y(t)$ and $\phi'_x(t)$ would be either in phase or in anti-phase. Then the transformations (2) give a time-constant value of the azimuth and velocity, while distribution functions show a well-defined maximum at these values.

In real situations, there exist a plethora of factors that leads to more composite distribution functions. Primarily, this can be due to the finite width of the spectrum of directions of TID wave vectors. But the main difference of our proposed method from existing techniques is that its area of application is not limited to some generally accepted model for phase or amplitude

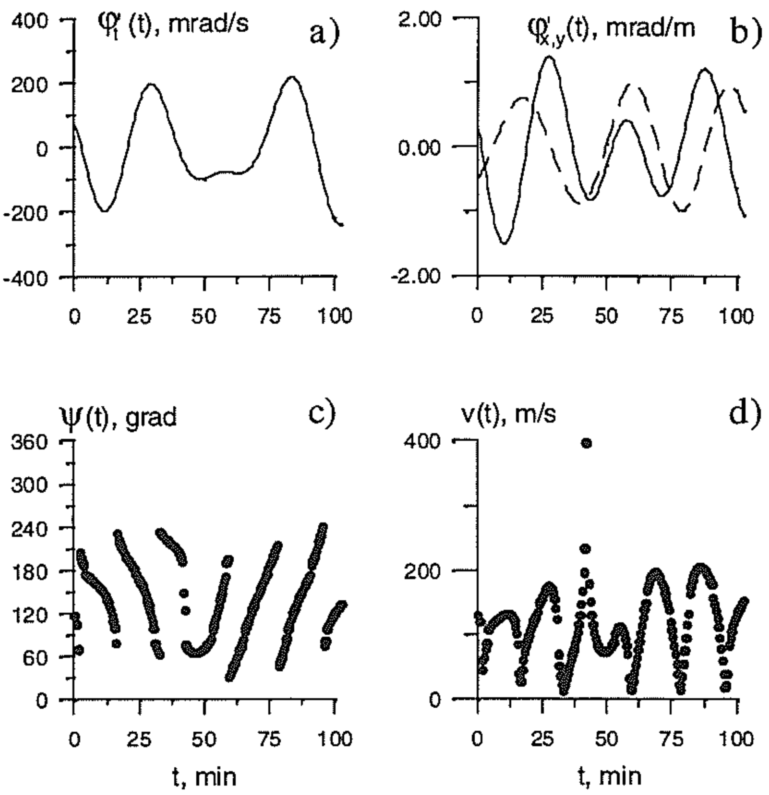

Figure 1. Variations in space-time characteristics of the phase from 10.00 to 12.00 LT on November 10, 1990 (a) $\phi'_t(t)$; b) $\phi'_x(t)$, dashed curve; $\phi'_y(t)$, solid curve; c) $\psi(t)$; d) $v(t)$).

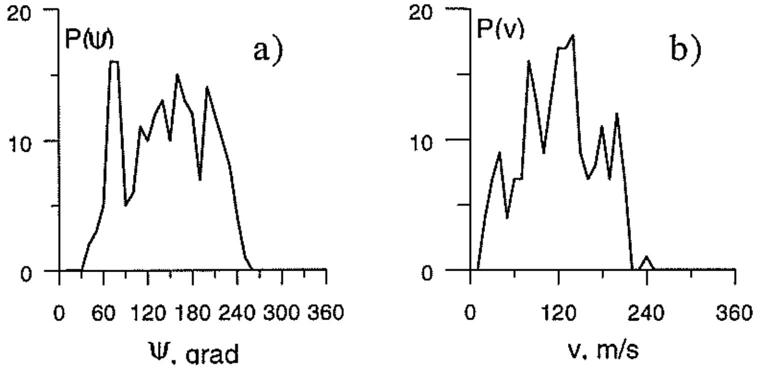

Figure 2. a) Distributions of azimuths $P(\psi)$ and (b) velocities $P(v)$ corresponding to the dependences $\psi(t)$ and $v(t)$ Fig. 1.

perturbation of the interference pattern (for example, a single plane traveling wave). On the contrary, analyzing the distributions facilitates a choice between different models and makes it possible to assess the degree of their validity. Primarily, velocity and direction distributions are constructed and analyzed to verify the hypothesis of whether there is a predominant displacement direction of the interference pattern. If it exists, then the pattern can be considered to be travelling, and the mean travel velocity can be determined from the velocity distribution.

Figure 1 presents typical (of noon) two-hourly variations of the space-time characteristics of the phase, velocity and direction (a) — $\phi'_t(t)$; b) — $\phi'_x(t)$, dashed curve; $\phi'_y(t)$, solid curve; c) — $\psi(t)$; and d) — $v(t)$). Distributions of azimuths $P(\psi)$ and velocities $P(v)$, corresponding to the dependences $\psi(t)$ and $v(t)$ of Figure 1, are shown in Figure 2. The mean value of the velocity, v, for the daytime 2-hour interval is about 120 m/s and the mean value of the azimuth , ψ, is about 150°.

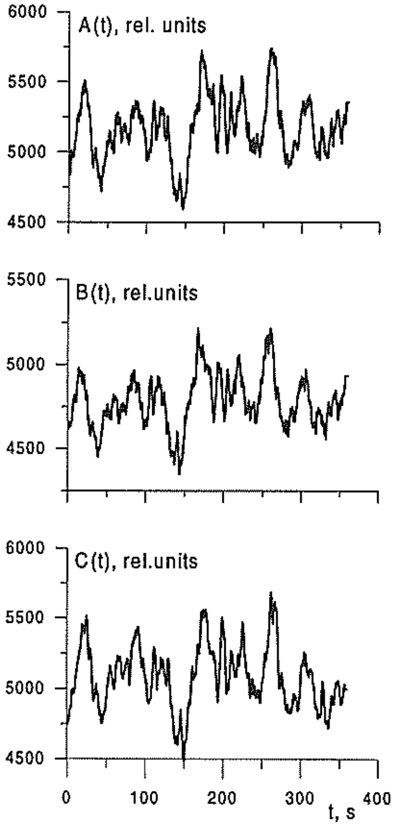

3. DETERMINING THE VELOCITY VECTOR OF THE AMPLITUDE DIFFRACTION PATTERN

An example of a typical 6-minute recording of amplitude scintillations from the outputs of three antennas A, B, and C for the ETS-2 signal is given in Figure 3 (recorded October 6, 1990, beginning at 07.49 LT). The figure illustrates a good likelihood of scintillations at the spaced antennas, with well-defined time shifts caused by the movement of a strongly anisotropic "frozen-in" SSI-induced amplitude diffraction pattern.

A multitude of independent counts of space-time derivatives of the signal phase in terms of the proposed method can be obtained with the spaced-antenna reception method in the frequency region when analyzing a complex spectrum of scintillations for each of the antennas, i.e., the amplitudes $S_A(\omega)$, $S_B(\omega)$ and $S_C(\omega)$ and phase $\Phi_A(\omega)$, $\Phi_B(\omega)$ and $\Phi_C(\omega)$ spectra, where ω is circular frequency.

In this case, the phase derivatives ϕ'_t, ϕ'_x and ϕ'_y are now determined not as functions of time t, as is the case with radio interferometry (Section 2), but as a function of frequency, ω.

Figure 3. An example of a typical 6-minute recording of the ETS-2 signal scintillations from the outputs of three antennas A, B, C (sequentially from top to bottom). The recording of October 6, 1990, beginning at 07.49 LT. Only varying parts of signals are shown. Linear scale; amplitude of variations is about 0.1 of mean value.

$$\begin{cases} \phi_t' = \omega \\ \phi_x' = \left(\Phi_C - \Phi_B\right)/d_x \\ \phi_y' = \left(\Phi_A - \Phi_B\right)/d_y \end{cases} \tag{3}$$

Corresponding values of the velocity *v(ω)* and direction *ψ(ω)* are calculated by formulas (2).

Figure 4 presents frequency dependencies for space-time characteristics of the phase of the ETS-2 radio signal scintillation spectrum, corresponding to the record in Figure 3: a) is the amplitude spectrum, *S(ω)*, of channel A (solid curve) and the phase time derivative, $\phi'_t(\omega)$, is the dashed curve; b) is the spatial phase derivatives $\phi'_x(\omega)$ and $\phi'_y(\omega)$; d) and c) are the azimuth, *ψ(ω)*, and velocity modulus, *v(ω)*, of the phase front propagation. As expected, with a displacement of the "frozen" interference pattern, like Figure 3, $\phi'_x(\omega)$ and $\phi'_y(\omega)$ are almost proportional to the frequency, and all components of the scintillation spectrum travel in the predominant direction with a almost constant phase velocity, *v*. In this case, the results obtained are consistent with data from classical correlation and dispersion analysis (Briggs, 1968).

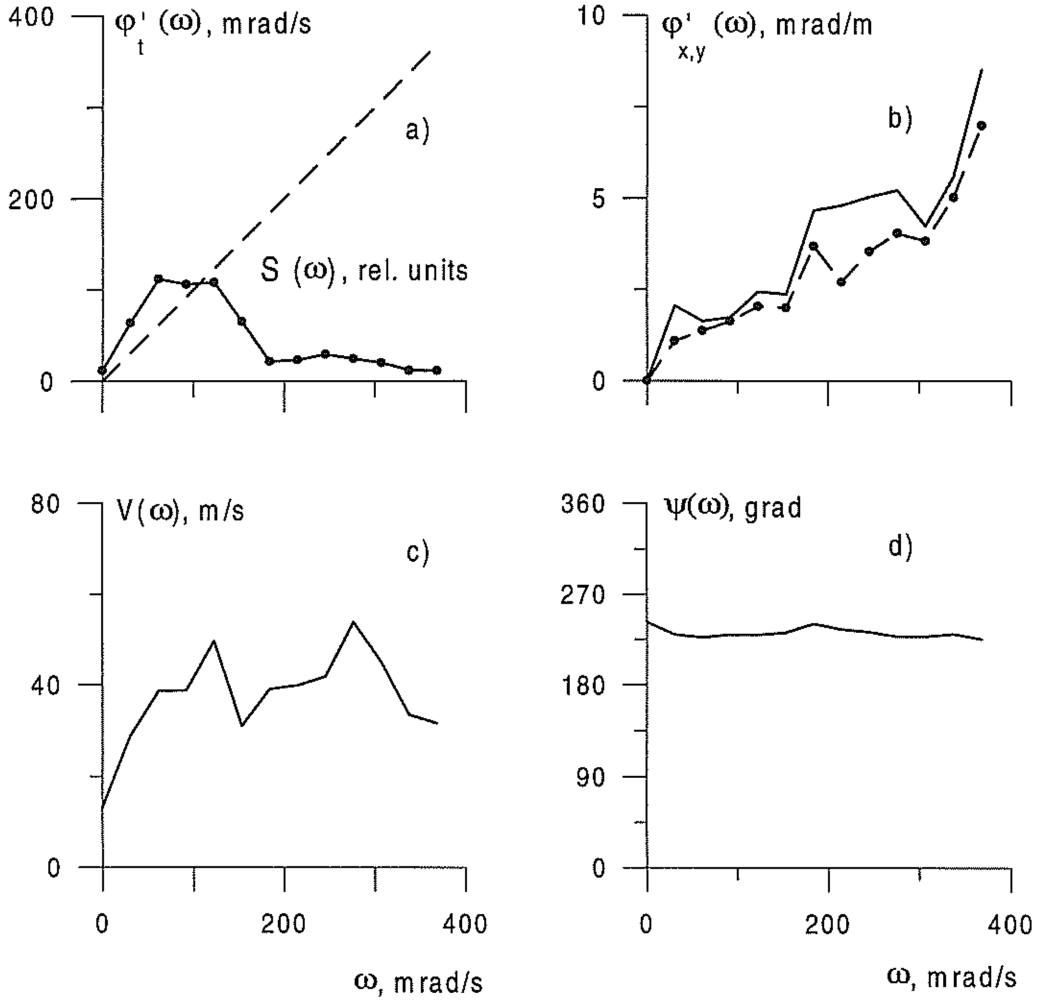

Figure 4. Frequency dependences of space-time phase characteristics of the scintillation spectrum, corresponding to the record in Fig.3: a) is the amplitude spectrum, *S(ω)*, of channel A (solid curve) and the phase time derivative, $\phi'_t(\omega)$, is the dashed curve; b) is the spatial phase derivatives $\phi'_x(\omega)$ solid curve; $\phi'_y(\omega)$ dashed curve; d) and c) are the azimuth, *ψ(ω)*, and velocity modulus, *v(ω)*.

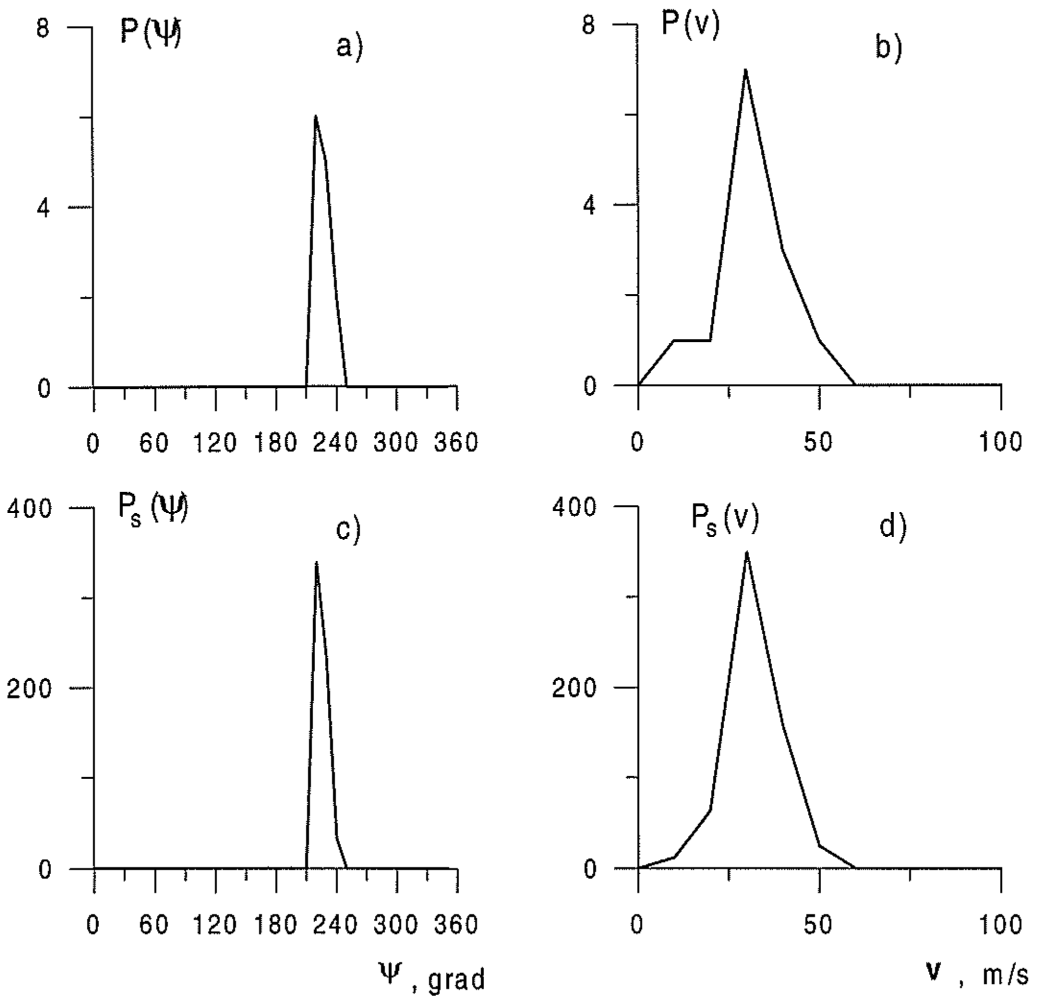

Figure 5. Distributions of azimuths *P(ψ)* — a) and velocities *P(v)* — b); weighted distributions of azimuths $P_s(\psi)$ — c) and velocities $P_s(v)$ — d), corresponding to the dependences *ψ(ω)* and *v(ω)* Fig.4.

Distributions (corresponding to Figure 4) of the azimuths *P(ψ)*, (a), and velocities *P(v)*, (b), are given in Figure 5. *P(ψ)* shows a well-defined maximum at *ψ* of about 220° and *P(v)* shows a maximum at *v* of about 30 m/s. Where necessary, one can construct "weighted" amplitude distributions in directions, $P_s(\psi)$, and velocities, $P_s(v)$, which make it possible not only to take into account the number of cases corresponding to a given interval of distributions, but also the weight of each velocity vector using the amplitude spectrum, *S(ω)*. Relevant distributions are presented in Figure 5 ($P_s(\psi)$, (c), and $P_s(v)$, (d)). As would be expected, the "simple" and "weighted" distributions are almost the same for the "frozen" interference pattern.

4. CONCLUSIONS

1. A statistical method is proposed for determining the characteristics of the dynamics of the radio signal interference pattern in the plane of the receiving antenna system by measuring variations of the phase derivatives with respect to time and spatial coordinates as a function of time or frequency. These data are used to calculate corresponding values of the velocity vector as a function of time or frequency.
2. Subsequently, velocity and direction distributions are constructed and analyzed to verify the hypothesis of whether there is a predominant displacement. If it exists, then the pattern can be considered to be travelling, and the mean travel velocity can be determined from the velocity distribution.When the signal is processed in the time region, this means that a consistent displacement

of the “frozen” interference pattern is proceeding throughout the entire analysis interval; when analyzing in the frequency domain, this means that all components of the signal spectrum travel in the predominant direction. In the latter case, results using this method are in agreement with data from classical correlation and dispersion analysis.

3. Method may be useful both in experiments with ionosphere-reflected radio waves and in transionospheric radio sounding operations. The new avenues for remote diagnostics of TIDs are based on exploiting standard measurements of transionosheric radio signal characteristics and coordinate-time measurements using multichannel receivers of the Global Positioning System (GPS).

Acknowledgments

The author is greatly indebted to V.G. Mikhalkovsky and K. S. Palamartchouck for their assistance in preparing the English version of the manuscript. This work was supported by the Russian Foundation for Fundamental Research under Grants 96-05-64162 and .97-02-96060. We are also indebted to the Illinois University Administration (USA) for support of this work under the Agreement on Scientific Cooperation Between Illinois University and ISTP SD RAS.

References

1. Afraimovich, E. L., V. N. Zvezdin, N. P. Minko, and A. N. Shapovalov, Simultaneous measurements of the polarization, angles of arrival, doppler frequency and amplitude of the VHF radio signal from ETS-2, Radio Sci., 26, 1177–1198, 1991.

2. Briggs B. H., On the analysis of moving patterns in geophysics, J. Atmos. Terr. Phys., 30, 1777–1794, 1968.

3. Mercier, C., Observations of atmospheric gravity waves by radiointerferometry, J. Atmos. Terr. Phys., 48, 605–624, 1986.

SHORT TERM PREDICTION OF foF2 USING NEURAL NETWORKS

[1] Allon W.V. Poole and [2]Lee-Anne McKinnell (nèe Williscroft)
Hermann Ohlthaver Institute for Aeronomy, Physics Department, Rhodes University, Grahamstown, South Africa
e-mail: [1]phap@giraffe.ru.ac.za; [2]phlw@giraffe.ru.ac.za

1. INTRODUCTION

The use of an artificial Neural Network (ANN) to model the noon value of foF2 for Grahamstown (26°E, 33°S), using readily available geophysical parameters, has already been reported (*Williscroft and Poole, [1996]*). The term "model" is used here to emphasize that since the ANN relies on measured values of the geophysical parameters as input, the values of foF2 produced must necessarily be past values and represent either interpolated values or best guess average values for times when foF2 was not measured, but the values of the input parameters were known. In this paper we investigate the ability of the ANN to predict short-term future values of foF2.

2. TRAINING THE NEURAL NET

Williscroft and Poole [1996] give details of the architecture of the ANN used in this investigation. In that paper the ANN was trained with four inputs, representing the sine and cosine components of the day number, a two month running mean of the sunspot number R2, and a two day running mean of the magnetic index which we called A16. These inputs allowed us to model noon foF2 with an rms error of 0.94 MHz, measured over a complete sunspot cycle. The differences between the modeled and measured foF2 appeared to be random, yet it is well known that if foF2 is enhanced or depressed, it tends to stay that way for periods varying from hours to days. This caused us to wonder if using an earlier value of foF2 as additional input would improve the ability of the ANN to model, and indeed to predict short term future values. Our investigation set out to determine two things:

[i] What is the effect, if any, of varying the delay between the input and output foF2 values?

[ii] If an earlier value of foF2 is included as an input parameter, do any of the other inputs become redundant?

Figure 1 shows schematically the input and output configuration for the ANN which we reported in *Williscroft and Poole [1996]*. The inputs are DNC, DNS, R2 and A16. DNC is the cosine component of the day number given by

$$DNC = \cos[2\pi * DN/365]$$

where DN (1 < DN < 365) is the day number, and similarly DNS is

$$DNS = \sin[2\pi * DN/365].$$

The reason for splitting DN into two components is to accommodate the cyclic nature of DN (*Williscroft and Poole, [1996]*). R2 is a two month average of the daily sunspot number, averaged over the two months prior to the data for which the prediction is required. A16 is similarly a 48 hour average of the 3 hourly magnetic index A_k, averaged over the 48 hours prior to the time of the required prediction.

The output (target) values used were the noon foF2 values for Grahamstown for the 11 year period 1973-1983, representing approximately one sunspot cycle, as well as an additional two years, 1989 and 1995. From this data set, 70% was randomly chosen for training while the remaining 30% was used to test the ANN.

For this research, we initially replaced the input set of figure 1 with the 11h00 values of foF2 only, which we call foF2(11h00). The output data remained foF2(12h00) as before. This new ANN was trained and stored. We then sequentially added the inputs of figure 1, retraining the ANN each time and storing the result. The results for the testing set are summarized in table 1, ANNs 1 to 5, which lists the RMS errors between the predicted and measured values in each case.

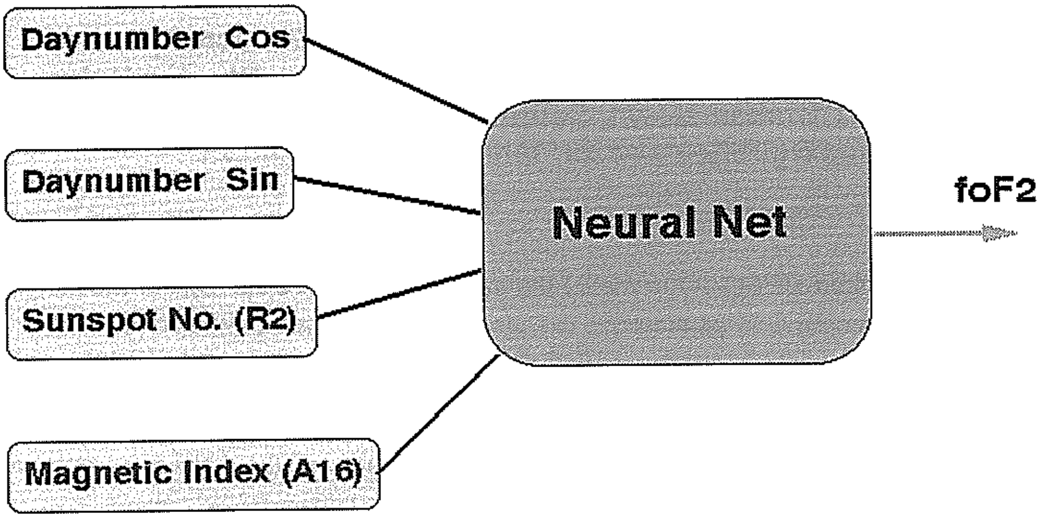

Figure 1. This figure shows a schematic diagram of the input and output configuration of the Artificial neural network, ANN.

Table 1. Results for several ANNs trained with different inputs.

ANN #	INPUT	RMS ERRORS
1	DNS, DNC, R2, A16	0.94
2	foF2(11h00)	0.55
3	foF2(11h00), DNS, DNC	0.53
4	foF2(11h00), DNS, DNC ,R2	0.53
5	foF2(11h00), DNS, DNC, R2, A16	0.52
6	foF2(10h00), DNS, DNC, R2, A16	0.64
7	foF2(09h00), DNS, DNC, R2, A16	0.74

We thus trained several networks, each with different input parameters. Each network was trained on a "best of 10 basis" (see appendix A). ANN 1 represents the results obtained in *Williscroft and Poole (1996)* . ANN 2 was trained with only one input, the 11h00 value of foF2 (i.e, the previous hour). It is noticeable that the rms error improves (decreases) dramatically with the introduction of foF2(11h00), and continues to improve marginally as each additional input is added. ANNs 2-5 thus represent four neural networks trained to predict the noon value of foF2 one hour ahead, but with increasing individual input requirements.

To investigate the effect of increasing the prediction delay, we trained two ANNs using the same input data as ANN 5 but replacing foF2(11h00) with foF2(10h00) and foF2(09h00) in turn. The results are presented in table 1, ANNs 6 to 7.

ANNs 6 and 7 are thus networks trained to predict noon foF2 two and three hours ahead respectively. It is noticeable that the rms errors get worse (increase) as the prediction delay time increases, as one might expect.

3. CONCLUSION

It is emphasized that this investigation only compared ANNs trained to predict the noon value of foF2. There was no particular reason for this choice, just convenience. It is assumed that the results obtained here would be just as applicable to other local times. If this is so, our investigations reveal that a neural net trained with appropriate indicators can be used to predict foF2 up to 3 hours ahead, with a decreasing ability to predict with increasing delay. Our investigation also showed that all the indicators mentioned play a part in improving the prediction, although the role of day number (DNS, DNC), sunspot number (R2) and magnetic index (A16) is less significant than that of the prior value of foF2. We interpret this to mean that short term fluctuations (of the order of 1-3 hours) are well predicted by using the latest available foF2 measurement.

References:

Williscroft L.A., and A.W.V.Poole, Neural Networks, foF2, sunspot number and magnetic activity, *Geophys. Res. Let.*, *23*, 24, 1996.

Appendix A: Best-of-ten training:

At the start of a network training session, the values of the weights within the network are initialized to small arbitrary random values. The training process is chaotic, and very small changes in the initialization values lead to completely different routes to a final configuration, which is different in each case. The predictive ability of each net, trained with identical data, but different intialisation, and measured by comparison of the rms errors, is much the same, but there is a small amount of "noise", with a standard deviation of about 2%. Choosing the one from ten with the smallest rms error (best) gives an rms error value whose standard deviation is reduced by $\sqrt{10}$, and thus improved its level of confidence for comparative purposes. It is worth nothing that "best"' net is only best for that particular exact set of training and target data, and that very small changes in either can lead to another net which is less optimal.

CLASSIFICATION OF THE VERTICAL IONOGRAMS TAKEN IN THE POLAR CAP IONOSPHERE UNDER DIFFERENT GEOPHYSICAL CONDITIONS

A.V. Shirochkov and L.N. Makarova, Arctic and Antarctic Research, Institute 38 Bering Street, Saint-Petersburg, 199397, Russia

Abstract.

A great variety of the vertical ionograms collected in the polar cap area by the ground-based ionosondes cannot be completely interpreted using the standard URSI scaling rules. Therefore, an attempt is made to classify the main types of the polar cap ionograms in accordance with the geophysical situations that are most common in this area. Only winter F2 region cases are considered. It was possible to select six main types of ionogram and tentatively proposed the corresponded geophysical situations for each of them.

1. INTRODUCTION.

The polar cap ionosphere properties attract the attention of many contemporary ionospheric researchers for a number of reasons. First of all, the polar caps are areas of open geomagnetic field lines that are directly connected with the solar wind so the dynamics and features of the polar cap ionosphere must be strongly influenced by solar wind variations and by corresponding magnetospheric phenomena such as plasma convection, electric fields etc. It also means that the polar cap area has none of the intense auroral precipitation fluxes that are an important ionization source in the auroral high-latitude ionosphere. On the other hand, the discovery of ionization patches in the polar cap ionosphere, and their intense study in recent years, has led to the conclusion that these structural forms have their origin in the sunlit part of the subauroral ionosphere. Such a twofold origin of the polar cap ionosphere means great spatial and temporal variability in this part of the Earth's ionosphere. In the early 50's, Russian scientists began regular vertical ionosonde soundings of the polar cap ionosphere and a huge archive of these data are now in the Russian scientific centers.

Standard reduction of the polar cap ionograms using the URSI scaling rules was unproductive in describing all the ionospheric features that were present on the ionograms. Recent progress made studying high-latitude magnetospheric and ionospheric processes allows a re-evaluation of the information contained in the polar cap vertical ionograms. Presumably, the numerous geophysical processes in the polar cap have ionospheric signatures that could provide valuable new information. It seems that ground-based vertical ionosondes, although unfashionable, are still able to contribute significantly to polar cap studies. Recently, Canadian scientists started observations with the newly opened latitudinal chain of vertical ionosondes located in the polar cap area [MacDougall et.al., 1995]. In this paper, we try to classify all typical ionograms taken in the polar cap area in accordance with the main geophysical situations observed in the polar cap. Of course, it is only a preliminary attempt of this kind which must be followed by the more detailed studies. It is hoped that the results of this study could be useful in future explorations of polar cap phenomena. Observations made at Antarctic station Vostok (78,5 S; 106,9 E; invariant latitude 83,3 S) and several ice drifting stations "North Pole" crossing the Arctic polar cap area are used in this study. The ionograms were recorded using the standard analogue Russian sounder AIS (Automatic Ionosphere Station) with a double vertical rhombic antenna. Only the situations in the winter F2 region were consider save the cases

Figure 1. The ionogram with reflection from the regular F - region (Vostok station).

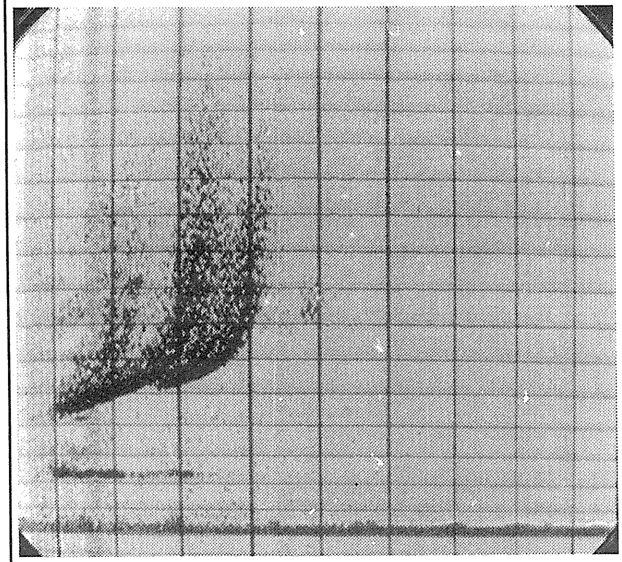

of pure F-spread events.

Figure 2. The ionogram with typical FLIZ - type reflection (Vostok station,)

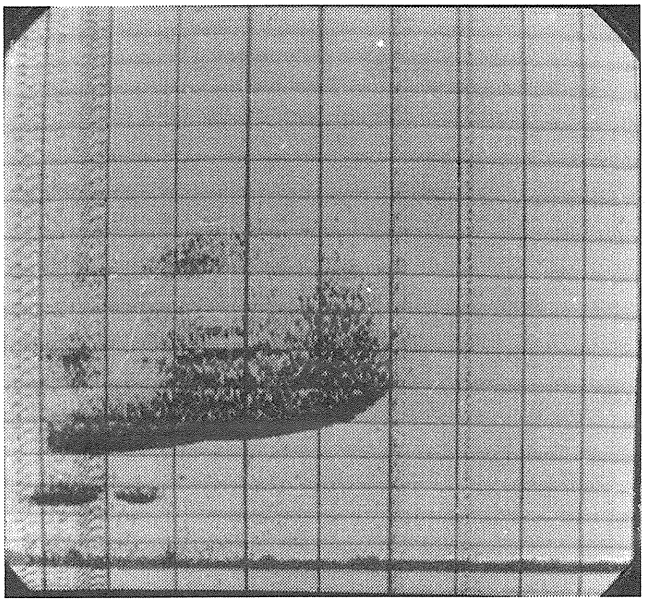

2. DATA ANALYSIS AND DISCUSSION.

After careful examination of the available data, we were able to distinguish the following types of polar cap ionograms (besides the completely diffuse reflections):

1. typical, ordinary, regular layer reflections with signal retardation near the critical frequency;
2. reflections with a very definite bottom part of the track and a diffuse upper part. This track is located at rather low heights (220-250 km) and does not change with increasing frequency. Earlier, this type of reflection was called "FLIZ" (F -layer irregular zone);
3. cloud -like reflections without any definite reflecting layer signature with foF2 about 3 to 5 MHz and hmax between 300 and 400 km;
4. reflections at rather low frequencies, 1.0 to 2.5 MHz with hmax in the vicinity of 250 to 350 km;
5. reflections from a region with an increased foF2, around 6 to 8 MHz, corresponding to a peak electron density of (5 to 8) 10^5 m^{-3} near 400 to 600 km;
6. successive lateral reflections, probably connected with the nightside auroral oval approaching the station.

We are sure that each of these ionogram types corresponds to a definite geophysical situation and does not represent the so -called "signal" effect, i.e. it is not an artefact of the ionosonde recording.

It is well known that the polar cap ionosphere is strongly influenced by convection of the ionospheric plasma, produced by large scale magnetospheric electric fields. It is a very important factor in forming the polar cap ionosphere together with the more common sources of ionization: solar ultraviolet radiation and corpuscular fluxes. Both these latter sources are assumed to be negligible in the polar cap, during winter (polar night conditions). However, in winter the polar cap, ionograms with regular F-layer reflections are frequently observed. They are the same as regular reflections produced by solar ultraviolet radiation at middle latitudes. An example of a such ionogram (type 1 in our classification) is given on Figure 1. The F-layer critical frequency, foF2, is usually about equal to 3 to 5 MHz and hmaxF2 is 250 to 300 km. Most probably this type of reflections is connected with convection carrying ionospheric plasma from middle latitudes to high latitudes. The physical processes of such a phenomenon are discussed in many papers, for example in [Foster,1993]. So the sunlit middle latitude ionosphere becomes the ionization source for the winter polar cap ionosphere. It is worth noting that we have found that the type 1 ionogram appearance does not depend on the IMF vertical component Bz

Figure 3. The ionogram showing reflection from the region of the down - going field - aligned currents (Vostok station)

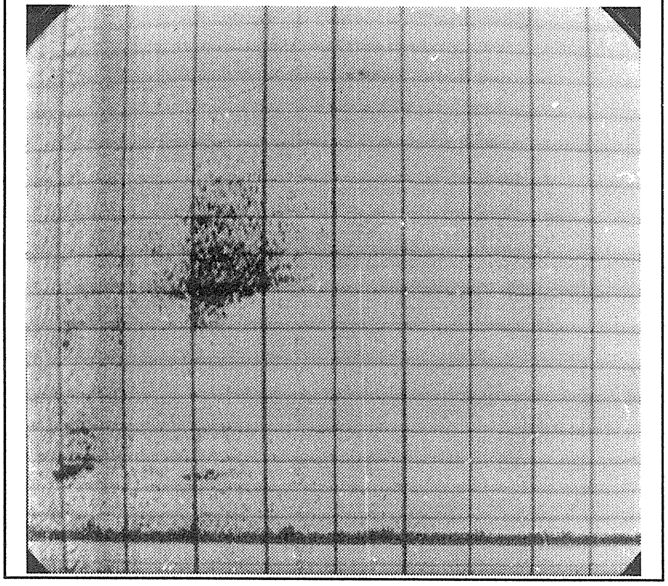

orientation, i.e. the plasma can be brought to the polar cap under both positive and negative Bz. There is reliable evidence that the convecting systems in the polar caps can explain access of ionospheric plasma into the area under different Bz orientations [Kamide and Troshichev,1994].

Figure 4. The ionogram showing reflection from the region close to the ion gyrofrequency (Vostok station)

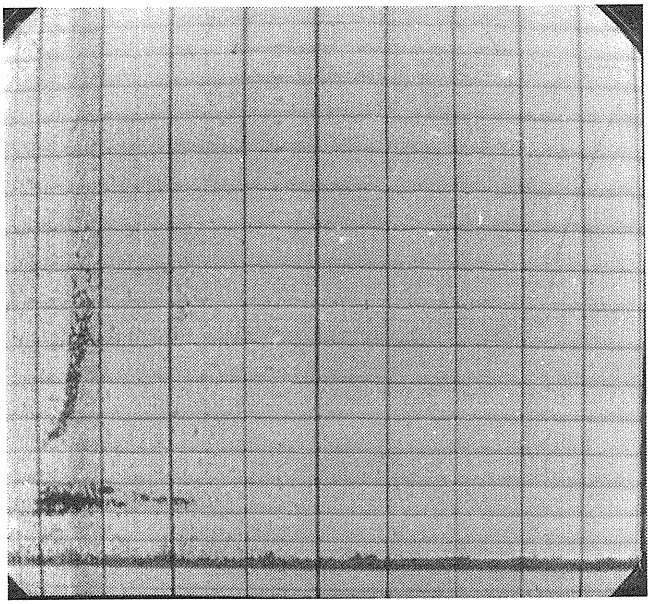

There is a region of intense corpuscular fluxes precipitating into the cusp region which can be considered the equatorial boundary of the dayside polar cap. The so-called third region of the field-aligned currents is thought to terminate here through the ionosphere. It was shown theoretically [Deminov,1979] that in the up-going field-aligned current region an increase in the ionospheric electron density must be seen while in the down-going field-aligned current area a decrease in the electron density is expected. Therefore, we relate the type 2 (Figure 2) reflections with the former phenomena, while the type 3 (Figure 3) reflections with the latter case. The region of the up-going field- aligned currents is formed primarily by the down-going precipitating electron fluxes so a rise in the plasma instabilities is expected in this region and can be seen on ionograms as plasma irregularities (FLIZ or F-spread) [see Pike,1971]. A radiowave reflected from field-aligned plasma irregularities of different scales can produce special tracks on ionograms which do not depend on the frequency.

Besides this, it is possible that a complicated reflection region (layer-irregularity-layer) may form with a big group delay i.e. located at a height greater than the main layer height. If we relate the appearance of types 2 and 3 reflections with the zone 3 of the field-aligned currents, we must expect them to be strongly dependent on the By-orientation. For Vostok Station data, such a dependence is clearly present. The type 2 reflections can be preferentially observed during periods of negative By (80 % of all cases) while type 3 reflections are observed during periods of positive By (67% of all cases). The latter situation corresponds to the ionospheric structure where the up-going ion fluxes, responsible for the down-going field-aligned currents, produce local troughs in the ionospheric plasma.

Figure 5. The ionogram with aurorally associated reflection showing the " spot " of the high electron density at the unusually great altitudes (Vostok Station)

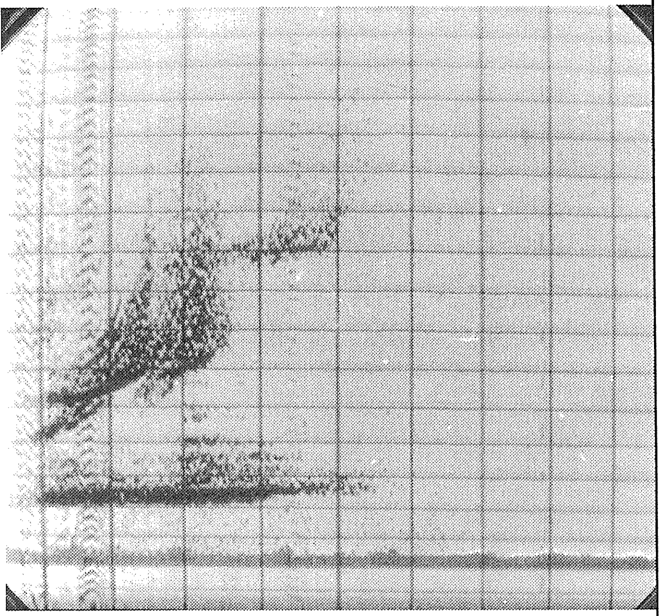

Both type 2 (Figure 2) and 3 (Figure 3) reflections can be observed preferentially at near-noon hours. Such structural forms are moved by convection across the polar cap and can sometimes resemble so called patches of ionization which are widely discussed in the literature [Crowley,1996]. The scale of these ionospheric forms is determined by the spatial scale of field-aligned currents in the polar cap whose fine structure is known not so well. The type 4 (Figure 4) reflection is characterised by very low values of foF2, close to the ion gyrofrequency (about 1.5 MHz at Vostok Station). They are observed mainly in the morning (in magnetic local time, MLT) hours under conditions of a undisturbed sector structure of the IMF. Most probably they are a manifestation of the so called "polar hole" which is formed by the plasma convection peculiarities when the plasma could not be carried out from the dayside and the ionosondes only observe the residual ionization level.

Type 5 reflections look like a faint spot of ionization located at a comparatively great altitudes (Figure 5). It is observed at Vostok Station under positive Bz orientation and is closely connected with the zenith auroral forms observed by the all-sky camera at Vostok. This reflection type appears under specific situation in the IMF when both Bx and By are either positive or negative i.e. under a distorted IMF sector structure. It seems that this polar cap ionospheric structure has not yet been described in the literature.

Figure 6. The ionogram showing a sequence of the reflections from the auroral oval approaching to Vostok Station

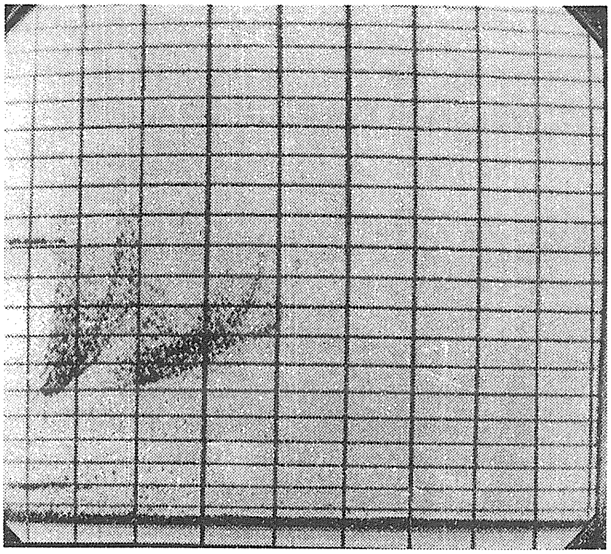

The final classification type is shown in Figure 6. It is characterised by the presence of several successive reflections appearing during nighttime (in MLT) hours. We interpret them to be lateral echoes from the auroral oval approaching the observation point. A favorable situation for their appearance is the simultaneous presence of enhanced solar wind velocity and strongly negative Bz. It was shown (Makarova and Shirochkov,1986) that this situation is a genuine signature of the auroral oval approaching to Vostok Station.

3. CONCLUSION

The results proposed in this paper must be carefully analyzed to get a more detailed interpretation. This is a first attempt to classify the vast variety of the polar cap vertical reflections types and to choose the main ones that can be related to definite geophysical situations. Obviously, it is one of a few possible ways to produce an empirical model of the polar cap ionosphere which is a very complex system. This classification is a result of a careful individual examination of a great number of ionograms accumulated during the last three decades. The standard URSI scaling rules for ionogram reduction proved inadequate for extracting all the information from these ionograms. We hope that the classifications proposed here will be useful for ionospheric researchers who uses other more advanced ionospheric study techniques in the polar cap.

References:

Crowley G. "Critical review of radio science 1993-1996". ed. by W.R. Stone, Oxford University Press, Oxford, UK, 619-648, 1996.

Deminov M.G., Kim V.P. and Khegai V.V. "Influence of the field-aligned currents on the ionosphere structure". Geomagnetism and Aeronomiy, 19, 4, 743-745, 1979.

Foster J.C. "Storm time plasma transport at middle and high latitudes". J.Geophys.Res., 98 (A2), 1675-1689, 1993.

Kamide Y. and Troshichev O.A. "A unified view on convection and field-aligned current patterns in the polar cap".J.Atmos.Terr.Phys., 56(2), 245-263, 1994.

Mac Dougall J.W., Grant I.F. and Shen X. "The Canadian advenced digital ionozonde: design and results". In Ionosonde networks and stations ed. by P Wilkinson, World DAta Center A REport UAG-104, Boulder, CO, USA, 21-27, 1995.

Makarova L.N. and Shirochkov A.V. "Influence of the solar wind on auroral absorption events at very high geomagnetic latitudes". J.Geomag.Geolectr., 38, 11, 1103-1114.

Pike C.P. "A latitudinal survey of the daytime polar F layer". J.Geophys.Res., 76, 7745-7756, 1971.

SPREAD - F OCCURRENCES AT A MIDLATITUDE EUROPEAN STATION

H. Soicher, F. Gorman, U.S. Army CECOM, Fort Monmouth, NJ 07703-5203
(soicher@doim6.Monmouth.army. mil)

E.E. Tsedilina, Space Research Center, Polish Academy of Science, 18A Bartycka, 00-716 Warsaw, Poland,

O.V. Weitsman, RAMOT by Tel Aviv University, Ramat Aviv, P.O. Box 38296, Tel Aviv, 61392, Israel

1. INTRODUCTION

The phenomena of the diffuse broadening of traces in ionospheric vertical ionograms at some specific height (frequency spread) or frequency (range spread) has been studied extensively. The spread of signals strongly influences the propagation of VHF and HF radio waves and the operations of modern sophisticated radio systems. It is known that the main reason of signal spread is scattering of radio waves by ionospheric irregularities or acoustic-gravity waves (Booker, H.G. et al 1986; Bowman, G.G., 1988). The same reason applies to the appearance of amplitude scintillations of radio stars and satellite-emitted radio signals [Aarons, 1982]. The role of acoustic-gravity waves or large and medium-scale structures, and small irregularities of different sizes and elongations in the formation of the spread of traces on the ionograms, or of the rate of amplitude scintillations is still not fully understood.

Spread-F, or scattered signals, at the midlatitude ionospheric sounding station Roquetes, Spain (40.8^0 N; 0.3^0 E) for 1991, a year of high solar activity, has been studied. Spread-F and scintillations appear in this region less frequently in comparison to high and low latitude regions, where they are very actively studied. The extent of measurements, observations and studies of irregularities and associated phenomena such as spread-F and scintillations, in this particular region is limited.

2. SCALING SPREAD-F AND SCATTERED TRACES ON IONOGRAMS

To statistically evaluate the spread characteristics of ionogram traces, index letters and corresponding numerical values were assigned to the different observed frequency spreads. The letter indices were ccc,cc,c,f,ff,fff ranging from no observed spread to significant spread. Associated numerical values ranged from 1 (corresponding to ccc) to 6 (corresponding to fff). In terms of actual frequency spread the indices c,f,ff,fff correspond to trace spreads of F-region echoes of o.5-0.8 MHz, 0.8-1.0 MHz, 1.0-1.5 MHz and 1.5-2.0 MHz, respectively. Nearly 9000 ionograms, representing hourly ionosonde measurements for 1991, have been processed and analyzed for this study (Soicher et al, 1995).

3. DIURNAL, SEASONAL AND ANNUAL VARIABILITY OF SPREAD-F

The averaged hourly index of frequency scattering, S_h, is defined as $\sum Si/_N$, where $\sum Si$ is the sum of all hourly index values and N is the number of ionograms for the considered hour and month. S_h varied from 0.6 to 3.3 during 1991. The variation of S_h for the various months of 1991 is presented in Figure 1. It is seen that S_h normally maximizes at the dawn period and minimizes during the day. A secondary maximum at sunset is only apparent in the spring months. The index variation during winter is irregular (the December/January months are combined in the analysis due to the sparsity of data).

The mean hourly index of frequency scattering for the entire year, S_{hy} is shown in figure 2, again showing the dawn maximum and daytime minimum. The mean monthly index of frequency spread, Sm, defined as the overall sum of spread indices during any one month divided by all processed ionograms during that month, is shown in figure 3. It is seen that Sm maximizes in July with a magnitude of 2.2, and minimizes in March with a magnitude of 1.15.

4. PROBABILITY OF OCCURRENCE OF SPREAD-F

The mean hourly probability, P_s, of spread-F occurrence is defined as $P_s = {}^N c/_N$, where Nc is the sum of significant monthly spread indices c,f,ff,fff (with corresponding numerical values of 3,4,5,6), and N is the

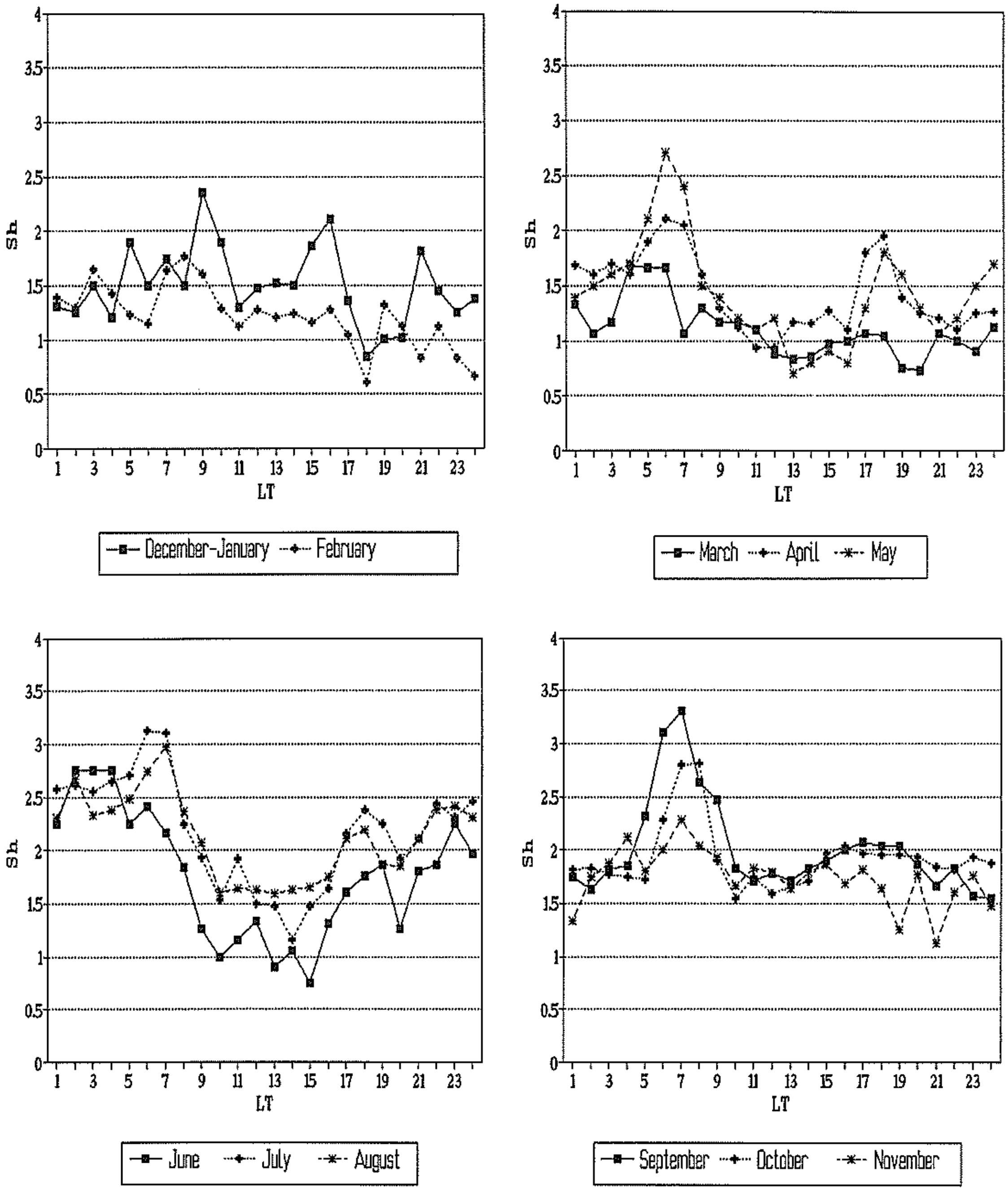

Figure. 1 Mean hour index of scattering Sh for the months of 1991, Roquetes, Spain, 1991.

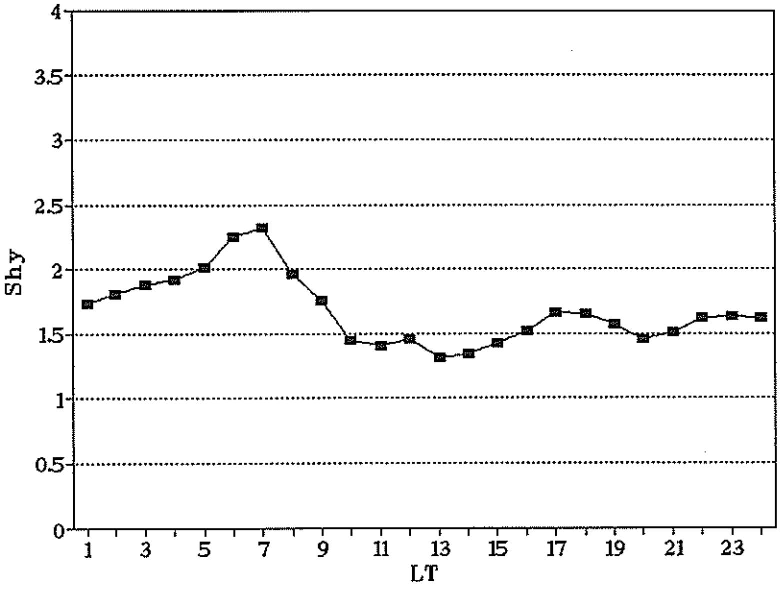

Figure. 2. Mean annual hourly index of scattering, Shy, for 1991, Roquetes, Spain.

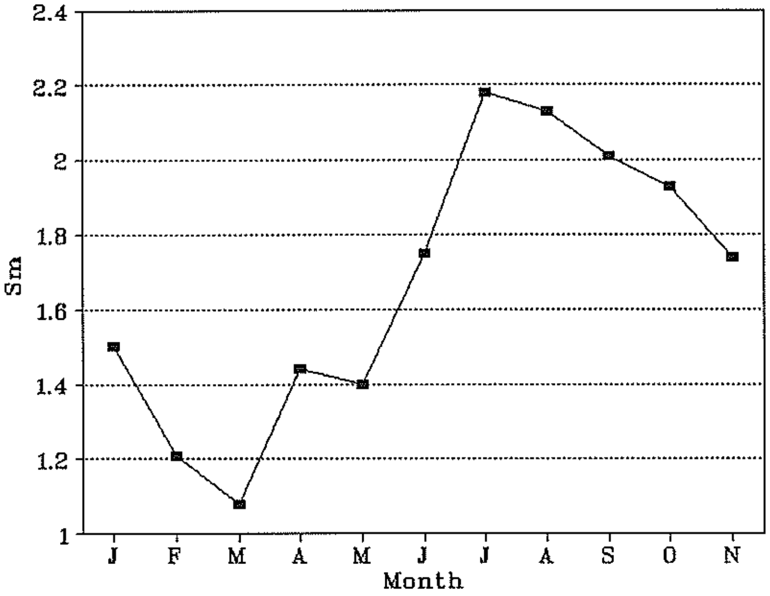

Figure. 3. Mean monthly index of scattering, Sm, Roquetes, Spain, 1991.

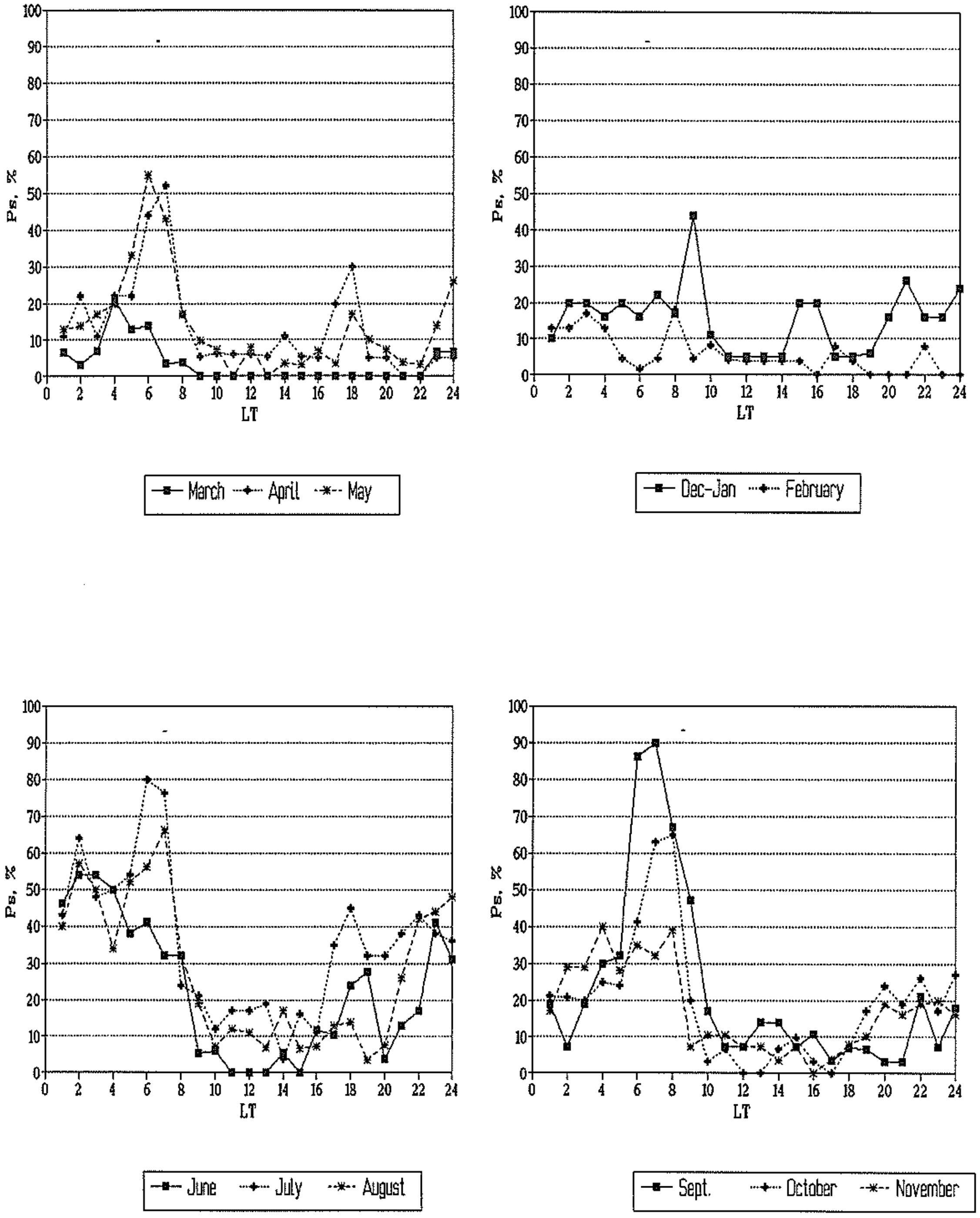

Figure 4. Seasonal probability, Ps, of spread-F occurrence; Roquetes, Spain, 1991.

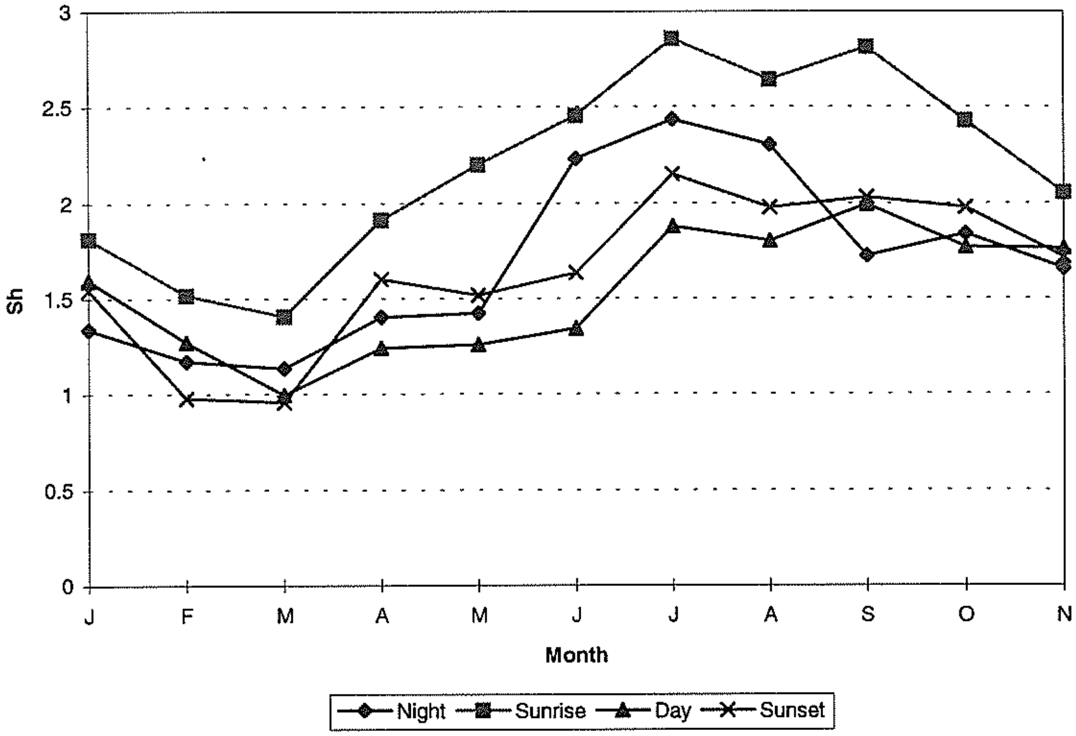

Figure. 5. Mean monthly index of F scattering for night, day and twilight periods; Roquetes, Spain, 1991.

total number of ionograms with detectable F traces for the considered hour and month. The monthly probability curves are shown in Figure 4, and they vary from 0% to 90%. March and April are the quietest whereas June through September are the most disturbed.

5. EFFECT OF THE TERMINATOR

As the obtained data shows (Figs 1,2,3,4), spread-F occurrence reveals a strong diurnal dependence with a large maximum at dawn and a not as large, but noticeable, secondary maximum at dusk. To better demonstrate the effect of the terminator, ionospheric sunrise and sunset times at 200km above the ionospheric sounder at Roquetes were calculated. S_h indices, averaged for the 3 post-sunrise hours, for the 2 pre-sunset hours, and for the daytime and nighttime were determined and are presented in figure 5 for the various months. As may be seen from the figure the index, S_h, is largest for the dawn period throughout the year and maximizes from July to September. For the other diurnal time periods, the index is comparable from September to May, with some more significant differences from June to August. The results indicate that the sunrise terminator generates waves and irregularities in the ionosphere that produce spread-F and scattered signals on the ionograms. The index maximizes for the summer period, the most illuminated, with a probability of 70-80%. The post-sunset period also maximizes during the summer time. The results are consistent with those arrived at by other experiments (Tsedilina, 1994).

6. CONCLUSIONS

The morphology of ionogram Spread-F occurrences at a midlatitude ionospheric station during a year of high solar activity has been described. The Spread-F traces have been looked at in terms of their amplitude and probability of occurrence, and their diurnal and seasonal dependence. The index of frequency spread maximizes in the dawn period for all seasons and normally minimizes during the daytime. In terms of seasonal dependence, the averaged index is highest in summer, maximizes in July and minimizes in March. Monthly probability curves indicate that occurrence rate varies from 0% to 90% with the higher rates prevalent during the summer months.

The dependence of Spread-F on other parameters such as magnetic activity and strong absorption events will be the subject of further investigation.

Acknowledgment

The data at Roquetes, Spain, were taken under the guidance of Luis Alberca of the Ebro Observatory.

References.

Aarons, J., (1982) Global Morphology of Ionospheric Scintillations, Proc. of the IEEE, 70, 360-370

Booker, H. G., P.K. Pasricha, and W.J. Powers, (1986) Use of Scintillation Theory to Explain Frequency-Spread on F-Region Ionograms, J. Atmos. Terr. Phys., 48, 323-354

Bowman, G.G., (1988), Large-Scale Ionospheric Structures Associated with Mid-Latitude Spread F, J of Geoph. Res., 96, No A6, 5955-5958.

Soicher, H., F. J. Gorman, E.E. Tsedilina and O.V. Weitsman (1995), Ionospheric foF2 Values and Their Gradients at European Longititudes, Radio Science, 30, 3, 755-764.

Tsedilina, E.E., (1994), HF Radio Wave Field Strength and Total Propagation Invariants, Radio Science, 29, 1, 127-134.

EXPECTED IONOSPHERIC STATE WITH DIFFERENT IONOSONDE RECORDS

T. L. Gulyaeva and N. R. Makarova, IZMIRAN, 142092, Troitsk, Moscow Region, Russia, Phone: 7 095 334 0284. Fax: 7 095 334 0124, email:tgul@charley.izmiran.rssi.ru

Data from more than 40 ionosondes of the global ionosonde network were analysed to define the quiet or disturbed state of the ionosphere. The geographic coordinates of the stations are given in Table 1. Here three types of data are presented: analogue (A) and digital (D) ionosonde records and quick-look-data (U) exchanged through the International Ursigram Service. Data are used for 3 selected months: June 1993 - summer (winter) in Northern (Southern) Hemisphere; October 1995 (equinox); and February 1997, winter in the Northern Hemisphere and summer in the Southern Hemisphere.

The daily and monthly characteristics were evaluated from the F2 layer critical frequency, foF2. First, the daily mean of foF2 is calculated and gives an integer value for each day:

$$M = (f1 + f2 + \ldots + fn)/n$$

where $n \leq 24$ is the number of hourly values of foF2 recorded during the day. Second, the peak daily value of foF2 represents the maximum hourly electron density at the location:

$$P = \max (fi)\,,\quad i = 1, 2, \ldots, n$$

The third parameter is the first derivative of the hour-to-hour variation of foF2, namely, the mean rate of its change: n

$$R = \Sigma\,(|fi - fj| / (ti - tj)\,) / n,$$

where j= i-1, t - hours, LT.

For all the above parameters, while any number of available numerical records may be available and can be used, the accuracy of each parameter depends on the number of hourly values available.

For each station-day, the values of M, P, and R have been calculated. Their monthly means M*, P*, and R* and standard deviation, are then obtained. The monthly means, M*, P*, and R*, are given in Table 1. For example, Figure 1-a,b,c presents the percentage deviations from the monthly means for each day of February 1997 at 3 selected sites: Magadan, Petropavlovsk, and Tashkent. The daily values of M, P, and R are shown by solid lines and the range of the percentage standard deviation is shown by dotted lines. When a daily value falls outside the one standard deviation range, we consider the day to be disturbed. We see, from Figure 1, an appreciable ionospheric storm with positive phase on 6 February followed by ionization depletion for the next four days at the high latitude station of Magadan. Similar, but less pronounced features, are seen at the mid-latitude station of Petropavlovsk. At the same time, the opposite signature of a positive storm is observed at the lower latitude station of Tashkent.

For comparison, the diurnal variation of foF2 on 11th February at the 3 stations is shown in Figure 2. Here, the observed hourly values (solid line) can be compared with the monthly median (circles). Daily means, M and P, are shown by horizontal lines. The rate, R, of hourly variability is shown in the bottom curves. On the same disturbed day, depletion of ionization occurred at two high and mid-latitude locations but enhancement of the ionization with a greater rate of hour-to-hour change was observed at lower latitudes. With other station data there is wide spectrum of ionospheric states; from quiet to positive and negative disturbances. The above example shows that the ionospheric "space weather" can differ from one global region to another like meteorological weather observations.

The above approach allows us to make daily estimate of quietness, or storminess, in the ionosphere. Ranking the parameters M, P, and R can be carried out the same as for other ionospheric and geomagnetic indices [1,2] to identify ionospherically quiet (Q) and stormy (S) days. This work is in progress using the long-term series of ionosonde observations.

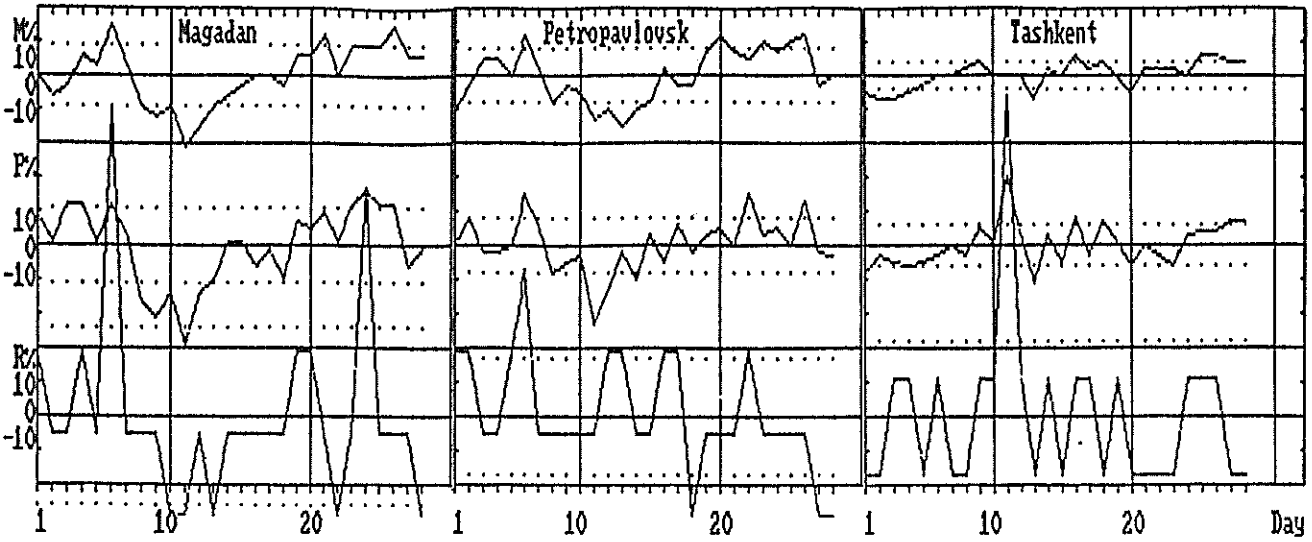

Figure 1. Day-to-day variations of daily mean (M - the upper plots), peak (P - the middle plot) and rate of hourly increments (R - the lower plots) of foF2 (filled lines) for February 1997 at Magadan (left), Petropavlovsk (middle), and Tashkent (right). The range of the standard deviation is plotted as dotted lines in all cases.

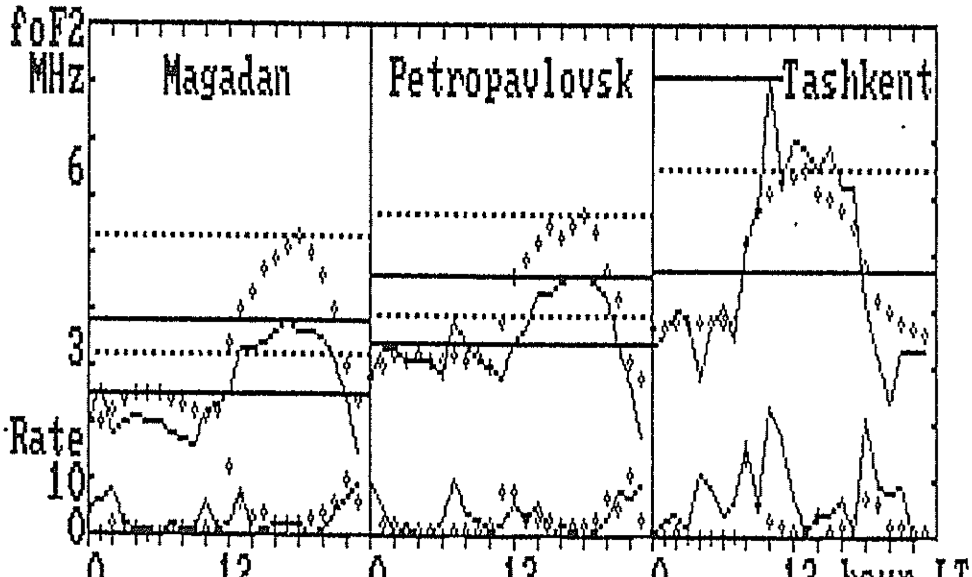

Figure 2. Diurnal variation of foF2 during ionospheric stormy day on 11 February, 1997 (solid lines) and monthly median (circles) at Magadan, petropavlovsk, and Tashkent. Bottom curves - rate of hour-to-hour changes of foF2.

Acknowledgment.

The data used in this study have been provided by WDC-B2, Moscow, Russia; WDC-A for STP and SEC, NOAA, Boulder, Colorado, USA; WDC-C for STP, RAL, Oxford, UK; SRC, Warsaw, Poland.

References.

1. T.L.Gulyaeva. Development of database of the ionospheric disturbance indices. Adv. Space Res., 14, No.12, 149-152, 1994.
2. T.L.Gulyaeva, P.V.Kishcha, N.R.Makarova. AE-storm and sub-storm occurrence: 1957-1990. Proc. of STP Workshop, Hitachi, Japan, Jan. 1996, in press.

Table 1. Monthly mean values of the daily mean (M*10), peak (P*10) and rate (R*100) of hourly variations of foF2 critical frequencies at the ionospheric stations for summer, equinox, and winter months.

A - analogous ionosonde, D - digital ionosonde, U - URSIgram data.

Station	Type	Lat.	Long.	June 1993	October 1995	February 1997
				M* P* R*	M* P* R*	M* P* R*
Preobrazehenija	A	74.7N	113.0E	52 57 17		
Dikson	A	73.5N	80.4E	51 56 19	34 49 26	
Loparskaya	A	68.0N	33.0E	53 59 23		
Kiruna	A	67.8N	20.4E	53 61 25		
Wellen	A	66.6N	190.2E	50 56 22		
Salekhard	A	66.5N	66.5E	53 60 23	32 55 47	31 50 44
Lycksele	D	64.6N	18.8E	54 62 28	34 53 55	
Eielson AFB	U	64.0N	210.0E			35 54 83
Tunguska	A	61.6N	90.0E	55 63 25		
St. Petersburg	A	60.0N	30.7E	55 65 33	34 55 39	31 53 45
Magadan	A	60.0N	151.0E	55 70 31	35 58 43	33 53 42
Uppsala	D	59.8N	17.6E	55 65 33	34 56 55	
Tomsk	D	56.5N	84.9E	58 68 31	38 64 44	35 60 43
Sverdlovsk	A	56.4N	58.6E	60 71 34		
Moscow	D	55.5N	37.3E	63 76 43	39 60 40	36 53 33
Kaliningrad	A	54.7N	20.6E	59 70 36		
Juliusruh/Rugen	D	54.6N	13.4E		37 61 60	36 58 43
Novosibirsk	D	54.6N	83.2E	59 68 30	41 67 44	36 59 44
Goose Bay	D	53.3N	299.2E			46 105 179
Petropavlovsk	A	53.0N	158.7E	59 73 34		40 60 42
Irkutsk	A	52.5N	104.0E	58 70 32		
Warsaw	D	52.2N	21.2E		41 62 63	

Station	Type	Lat.	Long.	June 1993	October 1995	February 1997
				M* P* R*	M* P* R*	M* P* R*
Slough	D	51.5N	359.4E	59 71 40		
Dourbes	D	50.1N	4.6E	58 76 85		
Pruhonice	U	50.0N	14.6E		41 64 65	
Khabarovsk	A	48.5N	135.1E	64 78 36		
Lannion	U	48.5N	356.7E		41 65 69	
Rostov	D	47.2N	39.7E	64 78 47	46 64 40	
Poitiers	U	46.6N	0.3E		43 69 71	41 62 67
Rome	D	41.8N	12.5E	65 85 98		43 66 71
Tashkent	A	41.3N	69.6E	69 89 59	52 81 54	47 67 36
Boulder	A	40.0N	254.7E		40 65 86	
Ashkhabad	D	37.9N	58.3E	70 89 50	53 80 60	
Wallops Island	D	37.8N	284.5E			41 64 75
Kokubunji	D	35.7N	139.5E	67 88 101	51 83 97	
Dyess AFB	D	32.5N	260.3E			43 70 96
Eglin AFB	D	30.4N	273.3E			47 77 100
Chung-Li	D	25.0N	121.2E		63 115 157	55 110 95
Ahmedabad	A	23.0N	72.6E	75 113 121	60 112 122	
Darwin	D	12.4S	130.9E		59 100 133	
Townsville	D	19.3S	146.7E		54 86 115	
Learmonth	D	21.0S	115.0E			50 78 84
Camden	D	34.0S	150.7E		44 62 79	51 76 118
Canberra	D	35.3S	149.0E		41 59 75	
Hobart	D	42.9S	147.2E		36 53 72	
Terre Adelie	U	66.7S	140.0E		34 49 68	

SOLAR CYCLE DIFFERENCES IN THE LONG TERM BEHAVIOUR OF THE F–LAYER OF THE IONOSPHERE

E. Feichter, R. Leitinger
Institut für Meteorologie und Geophysik, Universität Graz
Halbärthgasse 1, A–8010 Graz, Austria
Phone: +43–316–380 5257, Fax: +43–316–380 9825,
e-mail: feichter@bkfug.kfunigraz.ac.at

ABSTRACT

At least in the Northern Hemisphere there are distinct differences from solar cycle to solar cycle in the longterm behaviour of the F layer ionization. Vertical electron content is the best indicator for the differences but they show in peak density too.
The differences are most pronounced in the early afternoon.
Cycle 20 has an enhanced March/April maximum, whereas cycle 21 shows substantially higher October than March/April values. The European data for the following cycle 22 again have the highest early afternoon values of the monthly medians in March/April. The change of the annual variation from October to March/April maxima of the annual variation can be seen both in low solar activity (e.g., $\overline{\mathrm{R}} = 20$) and in high solar activity (e.g., $\overline{\mathrm{R}} = 150$) periods.
For solar cycle 20 no comparable TEC data exist for Europe. However, the change of the annual variation from March/April to October maxima can be seen in peak electron density data when one compares cycle 20 with cycle 21.
One method to demonstrate the odd cycle / even cycle differences more clearly is modelling based on Fourier analysis.
The solar cycle to solar cycle differences nearly disappear when an "ionospheric" index is used instead of $\overline{\mathrm{R}}$ or R_{12}. An alternative is to use two models, one for odd and one for even cycles. The traditional break between solar cycles occurs near the middle of solar minimum. For modelling purposes however, solar minimum is attributed to the new cycle. An appropriate condition must be defined for "solar minimum": e.g., $\mathrm{R}_{12} < 40$.

1. INTRODUCTION

Electron content from the Differential Doppler effect on signals from the US Navy Navigation Satellites (NNSS, formerly TRANSIT, with polar orbits, almost circular with a height around 1100 km) (Leitinger et al., 1975; Leitinger and Putz, 1978) was the main data source for these investigations.

Two European receiving stations have been in continuous coordinated operation since the beginning of 1975: Lindau / Harz in Germany (51.6°N, 10.1°E) and Graz in Austria (47.1°N, 15.5°E). The evaluation results are latitudinal profiles of ionospheric electron content, which means sequences of data equidistant in latitude (data distance 0.5° in geographic latitude of the 400 km ionospheric points). Up to the mid–80s, the observations from Lindau gave more material and were used for the statistical investigation into the interval 1975–1986. The Graz data were applied indirectly, namely to calibrate electron content by means of the "two stations method" (Leitinger et al., 1975). For a high solar activity interval, 1988–92, the observations from Graz were used. For a given latitude there is no significant difference in the monthly medians and quartiles calculated from Graz or Lindau data.

From the latitudinal profiles the data for the geographical latitudes 60°N, 55°N, 50°N and 45°N were selected. The observations from Graz which reach 30°N show that the results are valid down to 35°N where the influence of the equatorial anomaly begins at high sunspot numbers.

The TEC data used are monthly medians for two hours intervals. The data were divided into two classes: "Low Sunspot number" (LS) ($\overline{R} \leq 40$, nominal monthly mean sunspot number for modelling purposes: $\overline{R} = 20$) and "High Sunspot number" (HS) ($130 \leq \overline{R} \leq 170$ [cycle 21], $120 \leq \overline{R} \leq 180$ [cycle 22], resp., nominal value $\overline{R} = 150$). (The widening of the $\overline{R}$ interval for HS/cycle 22 was necessary in order to ensure data from at least two years for each month. Using data for $130 \leq R_{12} \leq 170$ — all months from November 1988 through December 1991 — leads to nearly identical results in statistical investigations.)

These selection criteria meant all data from 1975 and 1976 and data from July 1984 through December 1986 were included in the LS class and selected months from 1978 to 1982 and from 1988 through 1992, resp. in the HS class (see Feichter and Leitinger, 1993).

The first statistical studies (see Feichter et al., 1988, 1990, 1991, Feichter and Leitinger, 1993) were based on two LS intervals (1975–1976 and 1984–1986) and on the cycle 21 HS interval (1978–82). In 1989 data from 1984–86 were compared with two consecutive solar minima (1975–76 and 1984–86) (Feichter et al., 1990). Since 1995 we have enough data to compare the HS period of cycle 22 (selected months from 1988–92) with that of cycle 21 too. Both LS and HS data show a switch from an autumn maximum for cycle 21 to a spring one for cycle 22.

To extend the investigation to a wider range of solar cycles we included the annual variation of N_{max} from ionosonde scalings (hourly values of foF2). For N_{max} linear regressions were applied to find the relation between R_{12} and the peak electron density for each month and for each hour of the day. The regressions were based on different data selections, e.g., all data from one solar cycle, data from the rising part of a cycle and data from the falling part, the interval around the sunspot maximum. Some regressions gave negative slopes or negative $R_{12} = 0$ intercept points. However, no negative coefficients occured during daytime. For HS ($R_{12} = 150$) and intermediate sunspot numbers (e.g., $R_{12} = 85$) solar cycle to solar cycle differences in the vernal–autumnal asymmetry of the seasonal variation is stable and does not depend on the data selection: it appears when all data of one cycle are included and also in partial data (rising part, falling part, etc.).

If not indicated otherwise the following TEC examples are for 50°N. The other latitudes investigated show similar behaviour but the semi–annual component of the annual variation is more pronounced at lower latitudes.

The results are discussed in terms of the Fourier transform of the 12 monthly medians of the annual variation (cosine terms $a_0 \cdots a_6$, sine terms $b_1 \cdots b_5$) and reconstruction to order n:

$$\begin{aligned} F_n(t) &= \sum_{j=0}^{n} a_j \cos(j\,\omega\,t) + \sum_{j=1}^{n} b_j \sin(j\,\omega\,t) = a_0 + a_1 \cos(\omega\,t) + b_1 \sin(\omega\,t) + \\ &+ a_2 \cos(2\omega\,t) + b_2 \sin(2\omega_t) + \cdots = C_0 + C_1 \cos(\omega\,t - \phi_1) + C_2 \cos(2\omega\,t - \phi_2) + \cdots \end{aligned}$$

with $C_j = \sqrt{a_j^2 + b_j^2}$ and $\tan\phi_j = \frac{b_j}{a_j}$, $\omega = \frac{2\,\pi}{12}$ (t in months) or $\omega = \frac{2\,\pi}{365.25}$ (t in days).

For details of data preparation and analysis see Feichter et al., 1990, Feichter and Leitinger, 1993.

The 22 years periodicity aspect of our investigations is dealt with in another publication (Feichter and Leitinger, 1997), here we stress modelling consequences.

2. THE VERNAL–AUTUMNAL ASYMMETRY IN THE F LAYER IONIZATION OVER EUROPE

For simplicity, we include all of the sunspot minimum 1975/76 into cycle 21, all of the sunspot minimum 1984/86 into cycle 22.

2.1 Examples

Figure 1 is an example for latitude 50°N. It contains the annual variation for 12 LT reconstructed from the first 3 Fourier components (mean, annual, semi–annual) for cycle 21 (top) and cycle 22 (bottom), LS (left) and HS (right). Figure 2 contains the diurnal variation of the first 3 Fourier components (amplitudes and phases) for HS of cycle 21 (top half) and cycle 22 (bottom half) and the latitudes 45°N (left), 50°N (middle), 55°N (right).

2.2 Explanation by means of the Fourier phases

Annual component: LS cycle 21: from 1500-0900 LT the maximum of the annual component occurs during the second half of June, for the other LT intervals between the first half of July and the first half of August. Cycle 22: from 1500–0900 LT the maximum of the annual component occurs during the second half of June too, for the other LT intervals we find the maximum in the first half of June, one or two months earlier than in the previous cycle.

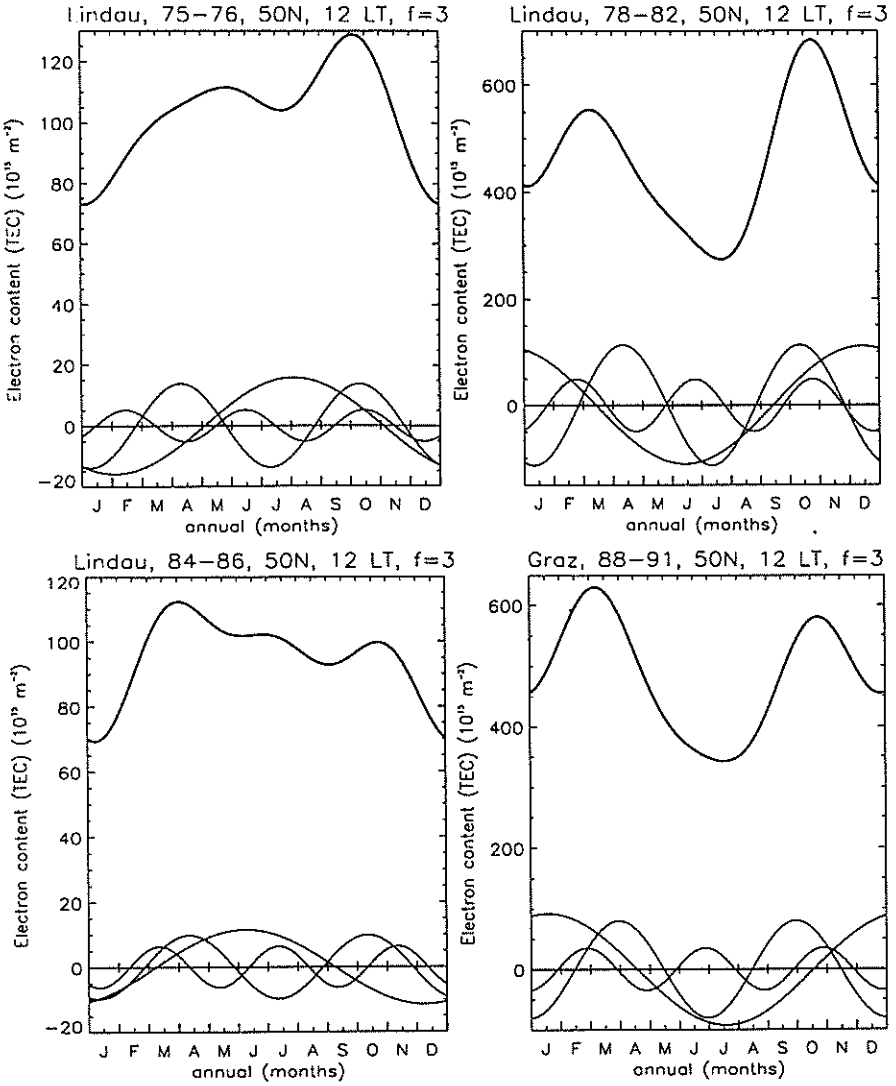

Figure 1: Annual variation of ionospheric electron content (TEC) from 4 Fourier components (mean, one year, half year, four months). Low sunspot numbers ($\overline{R} = 20$) (left hand side), high sunspot numbers ($\overline{R} = 150$) (right hand side), solar cycles 21 (top) and 22 (bottom). The one year, half year, four months components are shown separately (thin lines). Based on bi-hourly monthly medians from months selected according to sunspot numbers criterium.

For HS there is a change in phase from day to night (Figure 2). Cycle 21: from 0900–1700 LT the maximum of the annual component occurs between the first half of December and the second half of February. Cycle 22: from 0900–1700 LT the maximum of the annual component occurs between the second half of January and March, one or two months later than in the previous cycle (Figure 1). The interval 1700–1900 LT is a transition between nighttime and daytime behaviour (Figure 2). During 1978–82 (cycle 22) the phase of the annual component shows a clear leap from night to day but a smoother transition from day to night.

Semi annual component: For LS the maximum of the semi-annual part shows a different position for day and night. At night it occurs around the solstices, (1900–0700 LT second half of June) and during the day around the equinoxes (April, October). During the interval 0500–0700 LT there is a night to day change. The change from day to night behaviour is more distinct for cycle 22 than for cycle 21.
In latitudes <55°N during the time of HS the phase of the semi-annual component is stable (cycle 21: April, October, cycle 22: March/April, September/October, except for 01–05 LT [June, December]).

The change in the vernal-autumnal asymmetry does not appear in the Southern hemisphere (Titheridge et al., 1996) but there is some indication that it appears (perhaps in modified form) in North American West Coast data (Feichter and Leitinger, 1997).

3. VERNAL-AUTUMNAL ASYMMETRY IN THE SEASONAL VARIATION OF GEOMAGNETIC ACTIVITY

A double sunspot-cycle variation also occurs in terrestrial magnetic activity. In even-numbered cycles the last half of the sunspot-number-cycle is more active than the first half and the converse is true for the odd-numbered cycles (Chernosky, 1966). The curve of the 22-years cycle of magnetic activity is not symmetric relative to the minimum between two cycles.

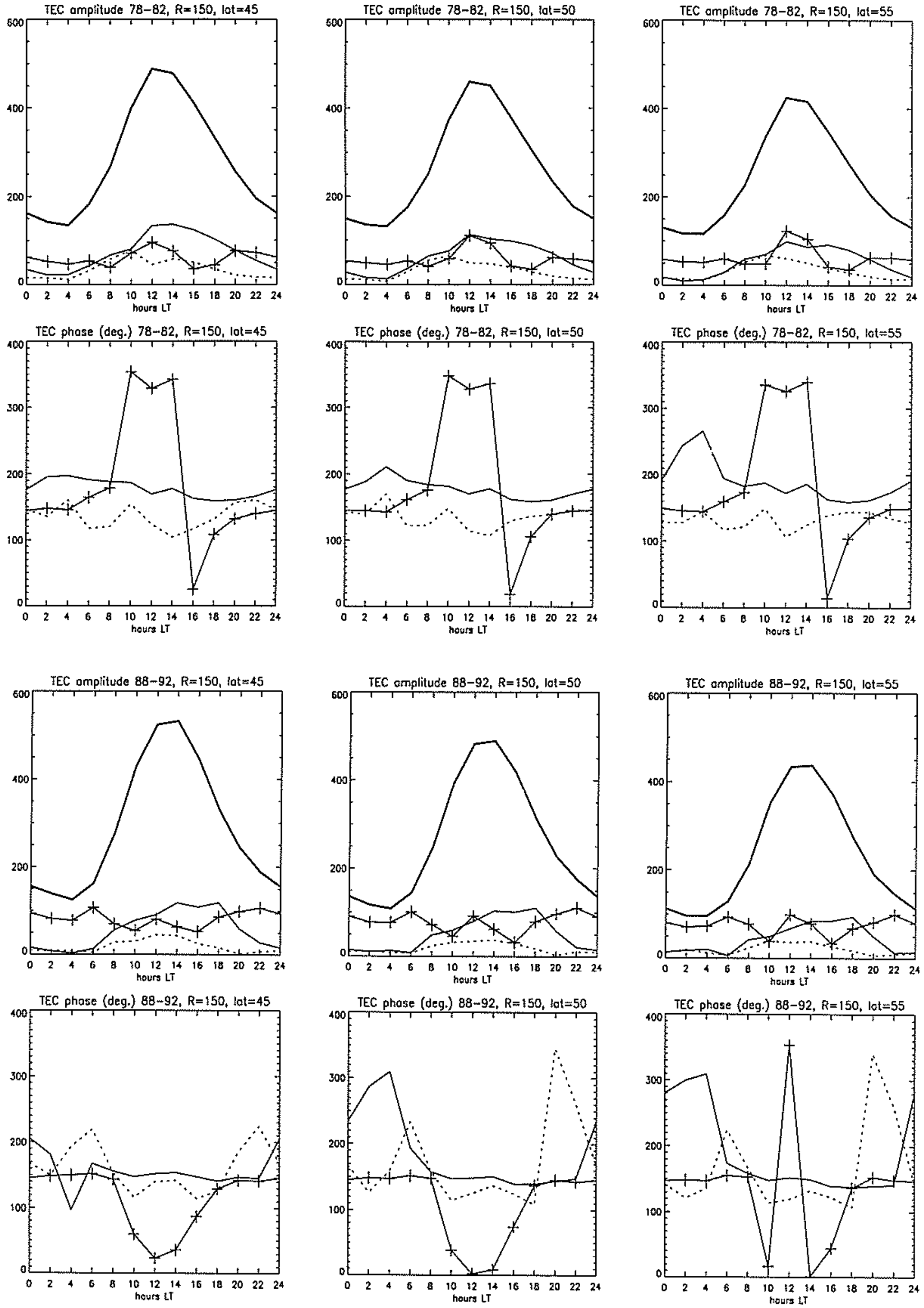

Figure 2: Diurnal variation of amplitudes (top and third row) and phases (second and bottom row) for 4 (3) Fourier components of the annual variation of ionospheric electron content (TEC): mean (heavy lines), one year (marked with crosses), half year (thin line), four months (dashed line). High sunspot numbers ($\overline{R} = 150$). Solar cycles 21 (top) and 22 (bottom). LT from 00 to 24 hours. Geographic latitude 45°N (left hand panels), 50°N (middle panels) and 55°N (right hand panels). Based on bi–hourly monthly medians from months selected according to sunspot numbers criterium.

Cycle 21, LS: Values for 52.5° N

	a0	a1	a2	b1	b2
A0	59.8	-31.7	5.0	-13.6	-0.8
A1	-19.4	1.7	6.2	5.1	5.8
A2	-2.0	7.9	-2.0	2.2	-0.8
B1	5.6	2.0	-5.2	-2.7	-0.0
B2	-1.2	-3.5	-0.4	-1.1	0.1

Slopes of regr. lines ($\Delta\phi = -5°$)

	a0	a1	a2	b1	b2
A0	5.7	-0.2	0.6	-1.4	-0.5
A1	1.0	0.9	-0.0	1.8	0.4
A2	-0.4	-0.2	-0.8	-0.0	-0.8
B1	-0.4	-0.3	-0.4	-1.1	0.1
B2	0.4	0.7	0.2	0.7	0.3

Cycle 21, HS: Values for 52.5° N

	a0	a1	a2	b1	b2
A0	254.8	-142.1	32.1	-61.6	9.7
A1	-5.0	-63.3	30.0	-19.5	19.2
A2	-56.3	38.5	-2.7	23.6	2.9
B1	10.8	35.8	-20.6	-5.2	-6.3
B2	4.9	-2.4	-5.4	-17.4	-1.2

Slopes of regr. lines ($\Delta\phi = -5°$)

	a0	a1	a2	b1	b2
A0	22.9	-10.2	1.7	-9.0	-1.9
A1	-0.8	-1.0	-1.3	2.7	-3.1
A2	-10.8	2.8	-1.9	5.0	-2.7
B1	2.2	0.3	2.6	-3.1	0.3
B2	3.3	-0.5	1.5	-2.4	1.9

Cycle 22, LS: Values for 52.5° N

	a0	a1	a2	b1	b2
A0	58.8	-27.7	5.8	-14.6	-1.2
A1	-21.8	-1.6	6.2	9.1	6.9
A2	-1.2	9.5	-2.0	-1.0	-0.5
B1	11.0	0.3	-2.0	-4.7	-2.8
B2	-2.0	-5.1	-1.8	-0.7	2.1

Slopes of regr. lines ($\Delta\phi = -5°$)

	a0	a1	a2	b1	b2
A0	5.5	0.3	0.8	-1.4	-0.4
A1	1.2	-0.4	0.3	2.8	0.3
A2	-0.6	0.8	-0.1	-1.2	-0.5
B1	-0.2	-0.2	-0.1	-0.5	-0.4
B2	0.2	0.7	0.4	0.9	0.6

Cycle 22, HS: Values for 52.5° N

	a0	a1	a2	b1	b2
A0	238.5	-147.2	33.4	-69.0	11.5
A1	-64.5	-39.6	27.9	-5.0	17.0
A2	-67.8	63.7	-3.3	41.3	-4.2
B1	20.5	-21.3	12.3	-11.8	4.8
B2	-18.7	16.9	-0.8	11.1	0.3

Slopes of regr. lines ($\Delta\phi = -5°$)

	a0	a1	a2	b1	b2
A0	25.0	-11.0	2.5	-8.4	-0.3
A1	-9.7	0.5	-2.3	3.6	-2.2
A2	-9.8	6.6	-2.1	3.5	-1.0
B1	5.8	-5.5	1.6	-2.9	-2.6
B2	-4.6	2.4	-1.5	2.3	-1.8

Table 1: Regional TEC models for cycle 21 (top half) and cycle 22 (bottom half): Regression line parameters (central values and slopes) for the 5 × 5 Fourier–coefficients. Horizontally: diurnal coeffients, vertically: annual coefficients. Left hand tables: low sunspot numbers (LS), right hand tables: high sunspot numbers (HS).

In 1988 the vernal – autumnal asymmetry in the seasonal variation of geomagnetic activity was investigated by L. Třisková using the *aa* index. Analysing the variation of geomagnetic activity, not from the viewpoint of sunspot cycles, but with respect to the polarity of the main solar dipole, she found an annual wave in the *aa* index with maxima alternatively around the vernal and the autumnal equinoxes (Triskova, 1989). This *aa* index behaviour might help explain the double sunspot cycle in total electron content of the ionosphere.

Assuming that a suitable geomagnetic index is an indicator for particle precipitation in higher latitudes the (statistical) effect of the annual variation of geomagnetic activity on the annual variation of F layer ionization could be based on the Joule heating effect of energetic particles reaching E and D layer heights. A widely accepted theory for F layer "negative storm effects" (e.g., Taeusch et al., 1971, Prölss, 1987, Prölss and Roemer, 1987) assumes changes of the thermospheric wind system and changes of thermospheric neutral gas composition. The wind change depresses F layer ionization in mid latitudes because the plasma is moved to lower altitudes resulting in increased recombination. The composition change decreases the number density ratio [0]/[N2] which also leads to a depression of ionization because recombination is enhanced compared with production. The "negative storm effect" is a typical phenomenon which is observed on the day following the day of the onset of a geomagnetic storm. In general it occurs in connection with moderate and severe geomagnetic storms. Usually, the mid latitude F–layer reaction to weak storms, and to substorms, is not directly observable because weak effects are masked by ionization variations unrelated to geomagnetic activity (day to day variability, TIDs, etc.). Experience with a large amount of European data (electron content, peak density) shows that "positive storm effects" which can occur in the afternoon, when the onset of the geomagnetic storm is in the (early) morning, does not cancel out the "negative effects". Except in winter, the statistical effect of geomagnetic disturbances on F–layer ionization in European mid latitudes, is a depression of ionization. Therefore, the annual asymmetry of F layer ionization in mid latitudes should be in antiphase with the vernal – autumnal asymmetry of geomagnetic activity: as we observed.

We do not want to rule out other possibilities to explain the double sunspot cycle observed in electron content and in peak density, but it is unlikely that a "purely solar activity" explanation can be found. There is no reason to believe in seasonal changes of the relation of a solar activity indicator to the solar EUV output.

4. MODELLING CONSEQUENCES

An easy way to construct local models for electron content (or for foF2) is to restrict the Fourier terms to a lower order. For many purposes restriction to 5 × 5 terms each for LS and HS and linear interpolation to account for varying solar activity is sufficient for TEC. (For foF2 one could use three levels of solar activity and quadratic interpolation.) The 5 × 5 terms comprise the average, the one day, the half day, the one year, the half year periods and combinations thereof.

In modelling efforts no true longitudinal variation appeared over Europe in the sector 10°W to 30°E. Therefore at least for this sector regional models need only a local time variation and a latitude variation. To cover the latitude range 40°N to 60°N it is sufficiently accurate to adapt a linear latitude dependence for all Fourier coefficients by means of linear regressions. Finally this leads to 4 sets of 5 × 5 coefficients: mid point (52.5°N) values and latitudinal slopes for LS and for HS. Table 1 gives the results for cycle 21 and cycle 22. Again comparison of the coefficients shows that the main cycle to cycle difference is found in the phases of the one year components (lines 2 and 4).

Of course it is an open question whether the solar cycle to solar cycle change in the vernal–autumnal asymmetry of the F layer ionization is considered to be strong enough to justify the complication of cycle dependent modelling. If not it is recommended to base models on data from two or from four complete cycles. The Fourier analysis approach is a purely linear process and therefore allows easy construction of an average model from the separate even cycle / odd cycle models (Table 1) simply by averaging for each coefficient.

REFERENCES

Chernosky, E. J. Double sunspot–cycle variation in terrestrial magnetic activity 1884–1963. *J. Geophys. Res.* **71**, 965–974, 1966

Feichter, E., R. Leitinger and G.K. Hartmann. Untersuchungen über die Halbjahres– und die Jahreswelle in F–Schicht–Parametern. *Kleinheubacher Ber.* **31**, 249–258, 1988

Feichter, E., R. Leitinger and G.K. Hartmann. Vergleich von Ionosphärenparametern aus zwei Sonnenfleckenzyklen. *Kleinheubacher Ber.* **33**, 93–102, 1990

Feichter, E., R. Leitinger and G.K. Hartmann. Die Halbjahresperiode in der Thermosphäre und in der Ionosphäre — ein Vergleich. *Kleinheubacher Ber.* **34**, 207–214, 1991

Feichter, E. and R. Leitinger. Longterm studies of ionospheric electron content. Wiss. Ber. 1/93, Institut für Meteorologie und Geophysik, Universität Graz, 1993

Feichter, E. and R. Leitinger. A 22–Years Cycle in the F layer ionization of the ionosphere. In press: *Ann. Geophys.*, 1997

Leitinger, R., G. Schmidt and A. Tauriainen. An evaluation method combining the differential Doppler measurements from two stations that enables the calculation of the electron content of the ionosphere. *J. Geophysics (Zs. Geophysik)* **41**, 201–213, 1975

Leitinger, R. and E. Putz. Die Auswertung von Differenz–Doppler–Messungen an den Signalen von Navigationssatelliten. Technischer Bericht, Universität Graz, 1978

Prölss, G. W. Storm–induced changes in the thermospheric composition at middle latitudes. *J. Planet. Space Sci.* **35**, 807–811, 1987

Prölss, G. W. and M. Roemer. Thermospheric storms. *Adv. Space Res.* **7**, (10)223–(10)235, 1987

Taeusch, D. R., G. R. Carignan and C. A. Reber. Neutral composition variations above 400 km during a magnetic storm. *J. Geophys. Res.* **76**, 8318–8325, 1971

Titheridge, J. E., R. Leitinger and E. Feichter. Comparison of the long term behaviour of the F layer of the ionosphere, Northern versus Southern hemisphere. *Kleinheubacher Ber.* **39**, 749–755, 1996

Triskova L. The vernal–autumnal asymmetry in the seasonal variation of the magnetic activity. *J. atm. terr. Phys.* **51**, 111–118, 1989

THE CONNECTION BETWEEN DAY-TO-DAY VARIATIONS OF THE IONOSPHERE AND SOLAR ACTIVITY CHANGES

Gordienko G.I., Kaliev M.Z., Institute of Ionosphere, Academy of Sciences, 480068, Almaty, Kazakstan. E-mail: gord@ionos.alma-ata.su

It has been shown in [1] the earth's ionosphere experiences not only sporadic and short-lived changes but also has regular variations with quasiperiods of to 27 (T1), 13 - 15 (T2), and 8 - 9 (T3) days. The last, T3, contributes to an ionospheric background level. These results have been found by investigating the frequency composition of ionospheric parameter variations at Alma-Ata, (43°25' N, 76°92' E). The studies [1,2] show that there are some spectra common to variations in the ionospheric F2 layer critical frequencies, the intensity of galactic cosmic rays, the 3340m atmospheric pressure, the intensity of solar activity (F10.7) and the ionospheric total electron content. The cause of these variations [1,2] is thought to be the solar activity modulating source.

However, when these studies were made, the question of the time evolution of separate spectral parts had not been considered and here their properties are investigated. As before [1,2], the Sun is assumed to play a leading role in the earth's climate. A qualitative analysis of ionospheric oscillations has been carried out. The absolute values of their amplitudes are not discussed (it is a separate question). From the beginning, it is important to clarify whether there is a connection between solar activity and the scale of ionospheric structures since often quasi-periodicities of 13 - 15 and 8 - 9 days are found in weather system statistics.

The initial data used are observations of noon foF2 made at Alma-Ata ionospheric observatory from November 1 1985 to February 28 1989 and the daily F10.7 flux obtained from the Solar Geophysical Data Summaries for the same period. A composite demodulation method [3], which makes it possible to select separate harmonic components from general quasi-periodic processes, has been used to analyse the data. The filter's characteristics were chosen to conform with the harmonics T1, T2 and T3. The results are calculated using a probability-statistical approach.

Figure 1 shows the results of digitally filtering the two data sets; the F10.7cm flux and Alma Ata foF2 (each data set is 1247 days long). The 0.1 MHz noise level in foF2 variations, caused by the measurement errors - foF2 is scaled to the nearest 0.1 MHz - is omitted. In Figure 1(a), the solid line is the distribution of the 27-day harmonic, or wave, for the F10.7 flux. The 60 day long filter is is moved 1 day at a time. The dashed lines are the upper and lower limits of the 27-day harmonic amplitude for the foF2 data. These lines form an envelope for the range of foF2 oscillation amplitudes for T1, T2 and T3. Figure 1(b, c) shows the upper and lower envelopes for the 14-day (Figure 1(b)) and 9-day (Figure 1(c)) harmonic amplitude, both for the F10.7cm flux (solid line) and foF2 (dashed line). The vertical amplitude scale in the figures is arbitrary.

For all F10.7cm flux estimates there are some regions (or episodes) containing waves that are, at first sight, invariant in space for some time intervals. These amplitudes reduce, become disturbed or irregular, and then regenerate again. These episodes appear co-ordinated. The picture of recurrent signs is observed for all foF2 estimates.

Comparing the features of the harmonic amplitude distributions, we conclude that,

(a) foF2 and F10.7 variations are correlated;

(b) foF2 oscillations do not depart significantly in amplitude from the noise level measurements if the solar F10.7cm flux oscillations are weak;

(c) the correlation between the F10.7cm flux and foF2 variations for T2 and T3 are high. If the periods T2 and T3 are simply the second and third order harmonics, related to the 27-day periodicity that differs from a sinusoidal shape, then the same relationships exist for both the F10.7cm flux and foF2;

(d) there are some features, in each case, where these features are within the recurrence episode limits;

(e) the results of similar research for night-time (00h, or midnight; 1.10.85 - 1.02.87) show that the T1, T2, T3 components are also correlated with variations of F10.7cm flux;

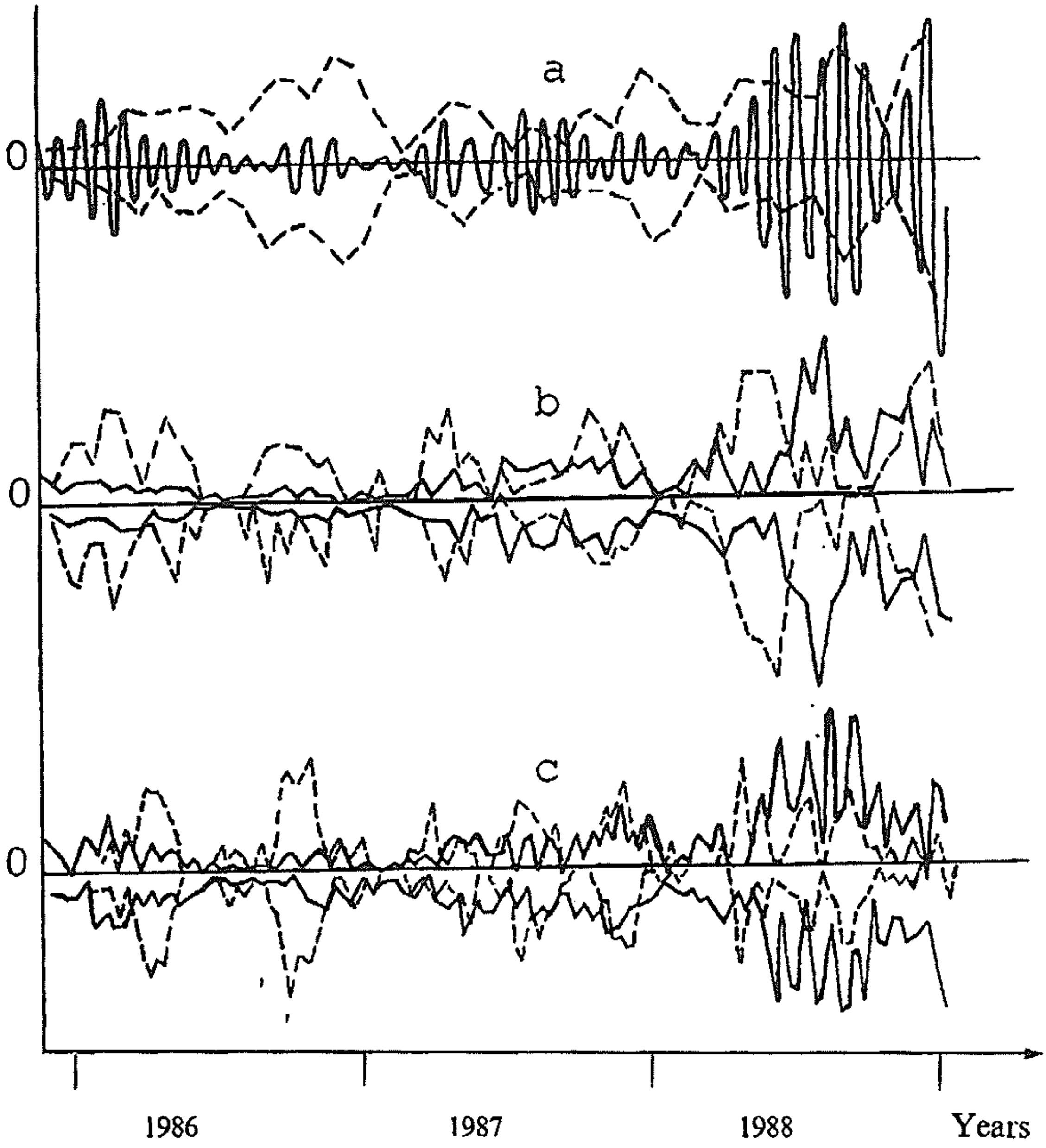

(f) the periods T1, T2 and T3 vary both over each episode, and from one episode to another, in roughly the 22-36, 13-15 and 8-10 day range;

(g) variations in T1, T2, and T3 about the main peaks for F10.7cm flux and foF2 differ.

The question of whether these variations exist in the ionosphere, naturally, is not a new one. This paper suggests that the quasi-periods, T2 and T3, are likely to be second and third order harmonics of the 27-day periodicity in solar activity. The correlation between foF2 variations with F10.7cm flux variations is evidence for this proposal.

REFERENCES

[1] Burlakova I. A., G. I. Gordienko, I. A. Zelenkova, M. Z. Kaliev, B.V.Troitsky, On methods for analysis of ionospheric disturbances, Proceedings of Kazakstan Academy of Sciences (physics - mathematics series), 4, pp. 93 - 99, 1994, (in Russian).

[2] Burlakova I. A., I. O. Gontarev, G. I. Gordienko, B. V. Troitsky, L. P. H. Churunova, Day-to-day variations of ionosphere conditions as given by satellite data registration, Geomagn. and Aeronomy, v. 32(2) pp. 160 - 162, 1992., (in Russian).

[3] Privalsky V. E., Complex demodulation of random processes and its application for the tides, Proceedings of 13th scientific Meeting at the Far East State University, 5, 4, p. 74, 1969, (in Russian).

COMPUTER AIDED PROCESSING OF IONOGRAMS AND IONOSONDE RECORDS

AUTHOR INDEX

UAG SERIES OF REPORTS

Fewer than four UAG Reports are published at irregular intervals each year. Copies of these publications may be purchased through the NATIONAL GEOPHYSICAL DATA CENTER, Solar-Terrestrial Physics Division (E/GC2) 325 Broadway, Boulder, Colorado 80303, USA. Please note that some reports are available on microfiche only at $4.00 a copy and that a $10.00 handling charge will be added. In this case orders must include check or money order payable in U.S. currency to Commerce, NOAA/NGDC.

UAG- 1	IQSY NIGHT AIRGLOW DATA, by L.L. Smith, F.E. Roach, and J.M. McKennan, ESSA Aeronomy Laboratory, Boulder, CO, July 1968, 305 pp.
UAG- 2	A REEVALUATION OF SOLAR FLARES, 1964-1966, by Helen W. Dodson and E. Ruth Hedeman, McMath-Hulbert Observatory, University of Michigan, Pontaic, MI, August 1968, 28 pp.
UAG- 3	OBSERVATIONS OF JUPITER'S SPORADIC RADIO EMISSION IN THE RANGE 7.6-41 MHZ, 6 JULY 1966 THROUGH 8 SEPTEMBER 1968, by James W. Warwick and George A. Dulk, University of Colorado, Boulder, CO, October 1968, 35 pp.
UAG- 4	ABBREVIATED CALENDAR RECORD 1966-1967, by J. Virginia Lincoln, Hope I. Leighton and Dorothy K. Kropp, ESSA [now NOAA], Aeronomy and Space Data Center, Boulder, CO, January 1969, 170 pp.
UAG- 5	DATA ON SOLAR EVENT OF MAY 23, 1967, AND ITS GEOPHYSICAL EFFECTS, compiled by J. Virginia Lincoln, World Data Center A, Upper Atmosphere Geophysics, ESSA [now NOAA], Boulder, CO, February 1969, 120 pp.
UAG- 6	INTERNATIONAL GEOPHYSICAL CALENDARS 1957-1969, by A.H. Shapley and J. Virginia Lincoln, ESSA Research Laboratories [now NOAA], Boulder, CO, March 1969, 25 pp.
UAG- 7	OBSERVATIONS OF THE SOLAR ELECTRON CORONA: FEBRUARY 1964 - JANUARY 1968, by Richard T. Hansen, High Altitude Observatory, NCAR, Boulder, CO, and Kamuela, HI, October 1969, 12 pp.
UAG- 8	DATA ON SOLAR-GEOPHYSICAL ACTIVITY OCTOBER 24 - NOVEMBER 6, 1968, Parts 1 and 2, compiled by J. Virginia Lincoln, World Data Center A, Upper Atmosphere Geophysics, ESSA [now NOAA], Boulder, CO, March 1970, 312 pp, (includes Parts 1 and 2).
UAG- 9	DATA ON COSMIC RAY EVENT OF NOVEMBER 18, 1968, AND ASSOCIATED PHENOMENA, compiled by J. Virginia Lincoln, World Data Center A, Upper Atmosphere Geophysics, ESSA [now NOAA], Boulder, CO, April 1970, 109 pp.
UAG-10	ATLAS OF IONOGRAMS, edited by A.H. Shapley, ESSA Research Laboratories [now NOAA], Boulder, CO, May 1970, 243 pp.
UAG-11	[Superseded by UAG-30]
UAG-12	SOLAR-GEOPHYSICAL ACTIVITY ASSOCIATED WITH THE MAJOR GEOMAGNETIC STORM OF MARCH 8, 1970, Parts 1, 2 and 3, compiled by J. Virginia Lincoln and Dale B. Bucknam, World Data Center A, Upper Atmosphere Geophysics, ESSA [now NOAA], Boulder, CO, April 1971, 466 pp, (includes 3 parts).
UAG-13	DATA ON THE SOLAR PROTON EVENT OF NOVEMBER 2, 1969, THROUGH THE GEOMAGNETIC STORM OF NOVEMBER 8-10, 1969, compiled by Dale B. Bucknam and J. Virginia Lincoln, World Data Center A, Upper Atmosphere Geophysics, ESSA [now NOAA], Boulder, CO, May 1971, 76 pp.
UAG-14	AN EXPERIMENTAL, COMPREHENSIVE FLARE INDEX AND ITS DERIVATION FOR 'MAJOR' FLARES, 1955-1969, by Helen W. Dodson and E. Ruth Hedeman, McMath-Hulbert Observatory, University of Michigan, Pontiac, MI, July 1971, 25 pp.
UAG-15	[Superseded by UAG-30]
UAG-16	TEMPORAL DEVELOPMENT OF THE GEOPHYSICAL DISTRIBUTION OF AURORAL ABSORPTION FOR 30 SUBSTORM EVENTS IN EACH OF IQSY (1964-65) AND IASY (1960), by F.T. Berkey, University of Alaska, Fairbanks, AK; V.M. Driatskiy, Arctic and Antarctic Research Institute, Leningrad, USSR; K. Henriksen, Auroral Observatory, Tromso, Norway; D.H. Jelly, Communications Research Center, Ottawa, Canada; T.I. Shchuka, Arctic and Antarctic Research Institute, Leningrad, USSR; A. Theander, Kiruna Geophysical Observatory, Kiruna, Sweden; and J. Yliniemi, University of Oulu, Oulu, Finland, September 1971, 131 pp, $4.00 (microfiche only).

UAG-17	IONOSPHERIC DRIFT VELOCITY MEASUREMENTS AT JICAMARCA, PERU (JULY 1967 - MARCH 1970), by Ben B. Balsley, NOAA Aeronomy Laboratory, Boulder, CO, and Ronald F. Woodman, Jicamarca Radar Observatory, Instituto Geofisico del Peru, Lima, Peru, October 1971, 45 pp, $4.00 (microfiche only).
UAG-18	A STUDY OF POLAR CAP AND AURORAL ZONE MAGNETIC VARIATIONS, by K. Kawasaki and S.-I. Akasofu, University of Alaska, Fairbanks, AK, June 1972, 21 pp.
UAG-19	REEVALUATION OF SOLAR FLARES 1967, by Helen W. Dodson and E. Ruth Hedeman, McMath-Hulbert Observatory, University of Michigan, Pontiac, MI, and Marta Rovira de Miceli, San Miguel Observatory, Argentina, June 1972, 15 pp.
UAG-20	[Superseded by UAG-30]
UAG-21	PRELIMINARY COMPILATION OF DATA FOR RETROSPECTIVE WORLD INTERVAL JULY 26 - AUGUST 14, 1972, by J. Virginia Lincoln and Hope I. Leighton, World Data Center A for Solar-Terrestrial Physics, NOAA, Boulder, CO, November 1972, 128 pp.
UAG-22	AURORAL ELECTROJET MAGNETIC ACTIVITY INDICES (AE) FOR 1970, by Joe Haskell Allen, National Geophysical and Solar-Terrestrial Data Center, Boulder, CO, November 1972, 146 pp.
UAG-23	U.R.S.I. HANDBOOK OF IONOGRAM INTERPRETATION AND REDUCTION, Second Edition, November 1972, edited by W.R. Piggott, Radio and Space Research Station, Slough, UK, and K. Rawer, Arbeitsgruppe fur Physikalische Weltraumforschung, Freiburg, GFR, November 1972, 324 pp.
UAG-23A	U.R.S.I. HANDBOOK OF IONOGRAM INTERPRETATION AND REDUCTION, Second Edition, Revision of Chapters 1-4, edited by W.R. Piggott, Radio and Space Research Station, Slough, UK, and K. Rawer, Arbeitsgruppe fur Physikalische Weltraumforschung, Freiburg, GFR, November 1972, 135 pp.
UAG-24	DATA ON SOLAR-GEOPHYSICAL ACTIVITY ASSOCIATED WITH THE MAJOR GROUND LEVEL COSMIC RAY EVENTS OF 24 JANUARY AND 1 SEPTEMBER 1971, Parts 1 and 2, compiled by Helen E. Coffey and J. Virginia Lincoln, World Data Center A for Solar-Terrestrial Physics, NOAA, Boulder, CO, December 1972, 462 pp, (includes Parts 1 and 2).
UAG-25	OBSERVATIONS OF JUPITER'S SPORADIC RADIO EMISSION IN THE RANGE 7.6-41 MHZ, 9 SEPTEMBER 1968 THROUGH 9 DECEMBER 1971, by James W. Warwick, George A. Dulk and David G. Swann, University of Colorado, Boulder, CO, February 1973, 35 pp.
UAG-26	DATA COMPILATION FOR THE MAGNETOSPHERICALLY QUIET PERIODS FEBRUARY 19-23 AND NOVEMBER 29 - DECEMBER 3, 1970, compiled by Helen E. Coffey and J. Virginia Lincoln, World Data Center A for Solar-Terrestrial Physics, NOAA, Boulder, CO, May 1973, 129 pp.
UAG-27	HIGH SPEED STREAMS IN THE SOLAR WIND, by D.S. Intriligator, University of Southern California, Los Angeles, CA, June 1973, 16 pp.
UAG-28	COLLECTED DATA REPORTS ON AUGUST 1972 SOLAR-TERRESTRIAL EVENTS, Parts 1, 2 and 3, edited by Helen E. Coffey, World Data Center A for Solar-Terrestrial Physics, NOAA, Boulder, CO, July 1973, 932 pp.
UAG-29	AURORAL ELECTROJET MAGNETIC ACTIVITY INDICES AE(11) FOR 1968, by Joe Haskell Allen, Carl C. Abston and Leslie D. Morris, National Geophysical and Solar-Terrestrial Data Center, Boulder, CO, October 1973, 148 pp.
UAG-30	CATALOGUE OF DATA ON SOLAR-TERRESTRIAL PHYSICS, prepared by NOAA Environmental Data Service, Boulder, CO, October 1973, 317 pp. Supersedes catalogs UAG-11, 15 and 20.
UAG-31	AURORAL ELECTROJET MAGNETIC ACTIVITY INDICES AE(11) FOR 1969, by Joe Haskell Allen, Carl C. Abston and Leslie D. Morris, National Geophysical and Solar-Terrestrial Data Center, Boulder, CO, February 1974, 142 pp.
UAG-32	SYNOPTIC RADIO MAPS OF THE SUN AT 3.3 MM FOR THE YEARS 1967-1969, by Earle B. Mayfield, Kennon P. White III, and Fred I. Shimabukuro, Aerospace Corp., El Segundo, CA, April 1974, 26 pp.
UAG-33	AURORAL ELECTROJET MAGNETIC ACTIVITY INDICES AE(10) FOR 1967, by Joe Haskell Allen, Carl C. Abston and Leslie D. Morris, National Geophysical and Solar-Terrestrial Data Center, Boulder, CO, May 1974, 142 pp.

UAG-34	ABSORPTION DATA FOR THE IGY/IGC AND IQSY, compiled and edited by A.H. Shapley, National Geophysical and Solar-Terrestrial Data Center, Boulder, CO; W.R. Piggott, Appleton Laboratory, Slough, UK; and K. Rawer, Arbeitsgruppe fur Physikalische Weltraumforschung, Freiburg, GFR, June 1974, 381 pp.
UAG-35	[Superseded by UAG-92]
UAG-36	AN ATLAS OF EXTREME ULTRAVIOLET FLASHES OF SOLAR FLARES OBSERVED VIA SUDDEN FREQUENCY DEVIATIONS DURING THE ATM-SKYLAB MISSIONS, by R.F. Donnelly and E.L. Berger, NOAA Space Environment Laboratory; Lt. J.D. Busman, NOAA Commissioned Corps; B. Henson, NASA Marshall Space Flight Center; T.B. Jones, University of Leicester, UK; G.M. Lerfald, NOAA Wave Propagation Laboratory; K. Najita, University of Hawaii; W.M. Retallack, NOAA Space Environment Laboratory and W.J. Wagner, Sacramento Peak Observatory, October 1974, 95 pp.
UAG-37	AURORAL ELECTROJET MAGNETIC ACTIVITY INDICES AE(10) FOR 1966, by Joe Haskell Allen, Carl C. Abston and Leslie D. Morris, National Geophysical and Solar-Terrestrial Data Center, Boulder, CO, December 1974, 142 pp.
UAG-38	MASTER STATION LIST FOR SOLAR-TERRESTRIAL PHYSICS DATA AT WDC-A FOR SOLAR-TERRESTRIAL PHYSICS, by R.W. Buhmann, World Data Center A for Solar-Terrestrial Physics, Boulder, CO; Juan D. Roederer, University of Denver, Denver, CO; and M.A. Shea and D.F. Smart, Air Force Cambridge Research Laboratories, Hanscom AFB, MA, December 1974, 110 pp.
UAG-39	AURORAL ELECTROJET MAGNETIC ACTIVITY INDICES AE(11) FOR 1971, by Joe Haskell Allen, Carl C. Abston and Leslie D. Morris, National Geophysical and Solar-Terrestrial Data Center, Boulder, CO, February 1975, 144 pp.
UAG-40	H-ALPHA SYNOPTIC CHARTS OF SOLAR ACTIVITY FOR THE PERIOD OF SKYLAB OBSERVATIONS, MAY 1973 MARCH 1974, by Patrick S. McIntosh, NOAA Space Environment Laboratory, Boulder, CO, February 1975, 32 pp.
UAG-41	H-ALPHA SYNOPTIC CHARTS OF SOLAR ACTIVITY DURING THE FIRST YEAR OF SOLAR CYCLE 20 OCTOBER 1964 AUGUST 1965, by Patrick S. McIntosh, NOAA Space Environment Laboratory, Boulder, CO, and Jerome T. Nolte, American Science and Engineering, Inc., Cambridge, MA, March 1975, 25 pp.
UAG-42	OBSERVATIONS OF JUPITER'S SPORADIC RADIO EMISSION IN THE RANGE 7.6-80 MHZ, 10 DECEMBER 1971 THROUGH 21 MARCH 1975, by James W. Warwick, George A. Dulk and Anthony C. Riddle, University of Colorado, Boulder, CO, April 1975, 49 pp.
UAG-43	CATALOG OF OBSERVATION TIMES OF GROUND-BASED SKYLAB-COORDINATED SOLAR OBSERVING PROGRAMS, compiled by Helen E. Coffey, World Data Center A for Solar-Terrestrial Physics, NOAA, Boulder, CO, May 1975, 159 pp.
UAG-44	SYNOPTIC MAPS OF SOLAR 9.1 CM MICROWAVE EMISSION FROM JUNE 1962 TO AUGUST 1973, by Werner Graf and Ronald N. Bracewell, Stanford University, Stanford, CA, May 1975, 183 pp.
UAG-45	AURORAL ELECTROJET MAGNETIC ACTIVITY INDICES AE(11) FOR 1972, by Joe Haskell Allen, Carl C. Abston and Leslie D. Morris, National Geophysical and Solar-Terrestrial Data Center, Boulder, CO, May 1975, 144 pp, $4.00 (microfiche only).
UAG-46	INTERPLANETARY MAGNETIC FIELD DATA 1963-1964, by Joseph H. King, National Space Science Data Center, NASA Goddard Space Flight Center, Greenbelt, MD, June 1975, 382 pp.
UAG-47	AURORAL ELECTROJET MAGNETIC ACTIVITY INDICES AE(11) FOR 1973, by Joe Haskell Allen, Carl C. Abston and Leslie D. Morris, National Geophysical and Solar-Terrestrial Data Center, Boulder, CO, June 1975, 144 pp, $4.00 (microfiche only).
UAG-48	[Superseded by UAG-48A]
UAG-48A	SYNOPTIC OBSERVATIONS OF THE SOLAR CORONA DURING CARRINGTON ROTATIONS 1580-1596 (11 OCTOBER 1971 - 15 JANUARY 1973), [Re-issue of UAG-48 with quality images], by R.A. Howard, M.J. Koomen, D.J. Michels, R. Tousey, C.R. Detwiler, D.E. Roberts, R.T. Seal, and J.D. Whitney, U.S. Naval Research Laboratory, Washington, DC; and R.T. Hansen and S.F. Hansen, C.J. Garcia and E. Yasukawa, High Altitude Observatory, NCAR, Boulder, CO, February 1976, 200 pp. Supersedes UAG-48.
UAG-49	[Superseded by UAG-92]

UAG-50	HIGH-LATITUDE SUPPLEMENT TO THE URSI HANDBOOK ON IONOGRAM INTERPRETATION AND REDUCTION, edited by W.R. Piggott, British Antarctic Survey, c/o Appleton Laboratory, Slough, UK, October 1975, 294 pp.
UAG-51	SYNOPTIC MAPS OF SOLAR CORONAL HOLE BOUNDARIES DERIVED FROM HE II 304A SPECTROHELIOGRAMS FROM THE MANNED SKYLAB MISSIONS, by J.D. Bohlin and D.M. Rubenstein, U.S. Naval Research Laboratory, Washington, DC, November 1975, 30 pp.
UAG-52	EXPERIMENTAL COMPREHENSIVE SOLAR FLARE INDICES FOR CERTAIN FLARES, 1970-1974, by Helen W. Dodson and E. Ruth Hedeman, McMath-Hulbert Observatory, University of Michigan, Pontiac, MI, November 1975, 27 pp.
UAG-53	DESCRIPTION AND CATALOG OF IONOSPHERIC F-REGION DATA, JICAMARCA RADIO OBSERVATORY (NOVEMBER 1966 - APRIL 1969), by W.L. Clark and T.E. Van Zandt, NOAA Aeronomy Laboratory, Boulder, CO, and J.P. McClure, University of Texas at Dallas, Dallas, TX, April 1976, 10 pp.
UAG-54	[Superseded by UAG-85]
UAG-55	EQUIVALENT IONOSPHERIC CURRENT REPRESENTATIONS BY A NEW METHOD, ILLUSTRATED FOR 8-9 NOVEMBER 1969 MAGNETIC DISTURBANCES, by Y. Kamide, Cooperative Institute for Research in Environmental Sciences, University of Colorado, Boulder, CO; H.W. Kroehl, Data Studies Division, National Geophysical and Solar-Terrestrial Data Center, Boulder, CO; M. Kanamitsu, Advanced Study Program, National Center for Atmospheric Research, Boulder, CO; Joe Haskell Allen, Data Studies Division, National Geophysical and Solar-Terrestrial Data Center, Boulder, CO; and S.-I. Akasofu, Geophysical Institute, University of Alaska, Fairbanks, AK, April 1976, 91 pp, $4.00 (microfiche only).
UAG-56	ISO-INTENSITY CONTOURS OF GROUND MAGNETIC H PERTURBATIONS FOR THE DECEMBER 16-18, 1971, GEOMAGNETIC STORM, Y. Kamide, Cooperative Institute for Research in Environmental Sciences, University of Colorado, Boulder, CO, April 1976, 37 pp.
UAG-57	MANUAL ON IONOSPHERIC ABSORPTION MEASUREMENTS, edited by K. Rawer, Institut fur Physikalische Weltraumforschung, Freiburg, GFR, June 1976, 302 pp.
UAG-58	ATS-6 RADIO BEACON ELECTRON CONTENT MEASUREMENTS AT BOULDER, JULY 1974 - MAY 1975, by R.B. Fritz, NOAA Space Environment Laboratory, Boulder, CO, September 1976, 61 pp.
UAG-59	AURORAL ELECTROJET MAGNETIC ACTIVITY INDICES AE(11) FOR 1974, by Joe Haskell Allen, Carl C. Abston and Leslie D. Morris, National Geophysical and Solar-Terrestrial Data Center, Boulder, CO, December 1976, 144 pp.
UAG-60	GEOMAGNETIC DATA FOR JANUARY 1976 [AE(7) INDICES AND STACKED MAGNETOGRAMS], by Joe Haskell Allen, Carl C. Abston and Leslie D. Morris, National Geophysical and Solar-Terrestrial Data Center, Boulder, CO, July 1977, 57 pp.
UAG-61	COLLECTED DATA REPORTS FOR STIP INTERVAL II 20 MARCH - 5 MAY 1976, edited by Helen E. Coffey and John A. McKinnon, World Data Center A for Solar-Terrestrial Physics, Boulder, CO, August 1977, 313 pp.
UAG-62	GEOMAGNETIC DATA FOR FEBRUARY 1976 [AE(7) INDICES AND STACKED MAGNETOGRAMS], by Joe Haskell Allen, Carl C. Abston and Leslie D. Morris, National Geophysical and Solar-Terrestrial Data Center, Boulder, CO, September 1977, 55 pp.
UAG-63	GEOMAGNETIC DATA FOR MARCH 1976 [AE(7) INDICES AND STACKED MAGNETOGRAMS], by Joe Haskell Allen, Carl C. Abston and Leslie D. Morris, National Geophysical and Solar-Terrestrial Data Center, Boulder, CO, September 1977, 57 pp.
UAG-64	GEOMAGNETIC DATA FOR APRIL 1976 [AE(8) INDICES AND STACKED MAGNETOGRAMS], by Joe Haskell Allen, Carl C. Abston and Leslie D. Morris, National Geophysical and Solar-Terrestrial Data Center, Boulder, CO, February 1978, 55 pp.
UAG-65	THE INFORMATION EXPLOSION AND ITS CONSEQUENCES FOR DATA ACQUISITION, DOCUMENTATION, PROCESSING, by G.K. Hartmann, Max-Planck-Institut fur Aeronomie, Lindau, GFR, May 1978, 36 pp.

UAG-66	SYNOPTIC RADIO MAPS OF THE SUN AT 3.3 MM 1970-1973, by Earle B. Mayfield and Fred I. Shimabukuro, Aerospace Corp., El Segundo, CA, May 1978, 30 pp.
UAG-67	IONOSPHERIC D-REGION PROFILE DATA BASE, A COLLECTION OF COMPUTER-ACCESSIBLE EXPERIMENTAL PROFILES OF THE D AND LOWER E REGIONS, by L.F. McNamara, Ionospheric Prediction Service, Sydney, Australia, August 1978, 30 pp, $4.00 (microfiche only).
UAG-68	A COMPARATIVE STUDY OF METHODS OF ELECTRON DENSITY PROFILE ANALYSIS, by L.F. McNamara, Ionospheric Prediction Service, Sydney, Australia, August 1978, 30 pp, $4.00 (microfiche only).
UAG-69	SELECTED DISTURBED D-REGION ELECTRON DENSITY PROFILES. THEIR RELATION TO THE UNDISTURBED D REGION, by L.F. McNamara, Ionospheric Prediction Service, Sydney, Australia, October 1978, 50 pp, $4.00 (microfice only).
UAG-70	ANNOTATED ATLAS OF H-ALPHA SYNOPTIC CHARTS FOR SOLAR CYCLE 20 (1964-1974) CARRINGTON SOLAR ROTATIONS 1487-1616, by Patrick S. McIntosh, NOAA Space Environment Laboratory, Boulder, CO, February 1979, 327 pp.
UAG-71	MAGNETIC POTENTIAL PLOTS OVER THE NORTHERN HEMISPHERE FOR 26-28 MARCH 1976, A.D. Richmond, NOAA Space Environment Laboratory, Boulder, CO; H.W. Kroehl, National Geophysical and Solar-Terrestrial Data Center, Boulder, CO; M.A. Henning, Lockheed Missiles and Space Co., Aurora, CO; and Y. Kamide, Kyoto Sangyo University, Kyoto, Japan, April 1979, 118 pp.
UAG-72	ENERGY RELEASE IN SOLAR FLARES, PROCEEDINGS OF THE WORKSHOP ON ENERGY RELEASE IN FLARES, 26 FEBRUARY - 1 MARCH 1979, CAMBRIDGE, MASSACHUSETTS, U.S.A., edited by David M. Rust, American Science and Engineering, Inc., Cambridge, MA; and A. Gordon Emslie, Harvard-Smithsonian Center for Astrophysics, Cambridge, MA, July 1979, 68 pp, $4.00 (microfiche only).
UAG-73	AURORAL ELECTROJET MAGNETIC ACTIVITY INDICES AE(11-12) FOR JANUARY - JUNE 1975, by Joe Haskell Allen, Carl C. Abston, J.E. Salazar and J.A. McKinnon, National Geophysical and Solar-Terrestrial Data Center, NOAA, Boulder, CO, August 1979, 114 pp, $4.00 (microfiche only).
UAG-74	ATS-6 RADIO BEACON ELECTRON CONTENT MEASUREMENTS AT OOTACAMUND, INDIA, OCTOBER - JULY 1976, by S.D. Bouwer, K. Davies, R.F. Donnelly, R.N. Grubb, J.E. Jones and J.H. Taylor, NOAA Space Environment Laboratory, Boulder, CO; and R.G. Rastogi, M.R. Deshpande, H. Chandra and G. Sethia, Physical Research Laboratory, Ahmedabad, India, March 1980, 58 pp.
UAG-75	THE ALASKA IMS MERIDIAN CHAIN: MAGNETIC VARIATIONS FOR 9 MARCH - 27 APRIL 1978, by H.W. Kroehl and G.P. Kosinski, National Geophysical and Solar-Terrestrial Data Center, Boulder, CO; S.-I. Akasofu, G.J. Romick, C.E. Campbell and G.K. Corrick, University of Alaska, Fairbanks, AK; and C.E. Hornback and A.M. Gray, NOAA Space Environment Laboratory, Boulder, CO, June 1980, 107 pp.
UAG-76	AURORAL ELECTROJET MAGNETIC ACTIVITY INDICES AE(12) FOR JULY - DECEMBER 1975, by Joe Haskell Allen, Carl C. Abston, J.E. Salazar and J.A. McKinnon, National Geophysical and Solar-Terrestrial Data Center, NOAA, Boulder, CO, August 1980, 116 pp.
UAG-77	SYNOPTIC SOLAR MAGNETIC FIELD MAPS FOR THE INTERVAL INCLUDING CARRINGTON ROTATIONS 1601-1680, MAY5, 1973 - APRIL 26, 1979, by J. Harvey, B. Gillespie, P. Miedaner and C. Slaughter, Kitt Peak National Observatory, Tucson, AZ, August 1980, 66 pp.
UAG-78	THE EQUATORIAL LATITUDE OF AURORAL ACTIVITY DURING 1972-1977, by N.R. Sheeley, Jr. and R.A. Howard, E.O. Hulbert Center for Space Research, U.S. Naval Research Laboratory, Washington, DC and B.S. Dandekar, Air Force Geophysics Laboratory, Hanscom AFB, MA, October 1980, 61 pp.
UAG-79	SOLAR OBSERVATIONS DURING SKYLAB, APRIL 1973 - FEBRUARY 1974, I. CORONAL X-RAY STRUCTURE, II. SOLAR FLARE ACTIVITY, by J.M. Hanson, University of Michigan, Ann Arbor, MI; and E.C. Roelof and and R.E. Gold, The Johns Hopkins University, Laurel, MD, December 1980, 43 pp.
UAG-80	EXPERIMENTAL COMPREHENSIVE SOLAR FLARE INDICES FOR 'MAJOR' AND CERTAIN LESSER FLARES, 1975-1979, compiled by Helen W. Dodson and E. Ruth Hedeman, The Johns Hopkins University, Laurel, MD, July 1981, 33 pp.
UAG-81	EVOLUTIONARY CHARTS OF SOLAR ACTIVITY (CALCIUM PLAGES) AS FUNCTIONS OF HELIOGRAPHIC LONGITUDE AND TIME, 1964-1979, by E. Ruth Hedeman, Helen W. Dodson and Edmond C. Roelof, The Johns Hopkins University, Laurel, MD, August 1981, 103 pp.

UAG-82	INTERNATIONAL REFERENCE IONOSPHERE - IRI 79, edited by J. Virginia Lincoln and Raymond O. Conkright, National Geophysical and Solar-Terrestrial Data Center, NOAA, Boulder, CO, November 1981, 243 pp.
UAG-83	SOLAR-GEOPHYSICAL ACTIVITY REPORTS FOR SEPTEMBER 7-24, 1977 AND NOVEMBER 22, 1977, Parts 1 and 2, compiled by John A. McKinnon and J. Virginia Lincoln, World Data Center A for Solar-Terrestrial Physics, NOAA, Boulder, CO, February 1982, 553 pp.
UAG-84	CATALOG OF AURORAL RADIO ABSORPTION DURING 1976-1979 AT ABISKO, SWEDEN, by J.K. Hargreaves, C.M. Taylor and J.M. Penman, Environmental Sciences Department, University of Lancaster, Lancaster, UK, July 1982, 69 pp.
UAG-85	[Superseded by UAG-91]
UAG-86	[Superseded by UAG-92]
UAG-87	CHANGES IN THE GLOBAL ELECTRIC FIELDS AND CURRENTS FOR MARCH 17-19, 1978, FROM SIX IMS MERIDIAN CHAINS OF MAGNETOMETERS, by Y. Kamide, Kyoto Sangyo University, Kyoto, Japan; H.W. Kroehl, National Geophysical Data Center, NOAA, Boulder, CO; and A.D. Richmond, NOAA Space Environment Laboratory, Boulder, CO, November 1982, 102 pp.
UAG-88	NUMERICAL MODELING OF IONOSPHERIC PARAMETERS FROM GLOBAL IMS MAGNETOMETER DATA FOR THE CDAW-6 INTERVALS, by Y. Kamide, Kyoto Sangyo University, Kyoto, Japan; H.W. Kroehl, National Geophysical Data Center, NOAA, Boulder, CO; and B.A. Hausman, National Geophysical Data Center, NOAA, Boulder, CO, November 1983, 197 pp.
UAG-89	ATMOSPHERIC HANDBOOK: ATMOSPHERIC DATA TABLES AVAILABLE ON COMPUTER TAPE, by V.E. Derr, NOAA Environmental Research Laboratories, Boulder, CO, July 1984, 56 pp.
UAG-90	EXPERIENCE WITH PROPOSED IMPROVEMENTS OF THE INTERNATIONAL REFERENCE IONOSPHERE (IRI): CONTRIBUTED PAPERS, MAINLY FROM THE URSI-COSPAR WORKSHOP HELD IN BUDAPEST IN 1980, edited by K. Rawer, University of Freiburg, Federal Republic of Germany, and C.M. Minnis, International Union of Radio Science (URSI), Brussels, Belgium, May 1984, 233 pp.
UAG-91	COMBINED CATALOG OF IONOSPHERE VERTICAL SOUNDINGS DATA, compiled by Raymond O. Conkright and Marcus O. Ertle, National Geophysical Data Center, NOAA, Boulder, CO, December 1984, 174 pp.
UAG-92	INTERNATIONAL CATALOG OF GEOMAGNETIC DATA, compiled by C.C. Abston, National Geophysical Data Center, NOAA, Boulder, CO; N.E. Papitashvili, Academy of Sciences of the USSR, World Data Center B2, Moscow, USSR; and V.O. Papitashvili, IZMIRAN, Moscow Region, USSR, August 1985, 291 pp. Supersedes UAG-35, 49, and 86.
UAG-93	IONOGRAM ANALYSIS WITH THE GENERALIZED PROGRAM POLAN, by J.E. Titheridge, University of Auck land, New Zealand, December 1985, 194 pp.
UAG-94	THE SOLAR MAGNETIC FIELD--1976 THROUGH 1985: AN ATLAS OF PHOTOSPHERIC MAGNETIC FIELD OBSERVATIONS AND COMPUTED CORONAL MAGNETIC FIELDS FROM THE JOHN M. WILCOX SOLAR OBSERVATORY AT STANFORD, by J. Todd Hoeksema and Philip H. Scherrer, Center for Space Science and Astrophysics, Stanford University, Stanford, CA, January 1986, 370 pp.
UAG-95	SUNSPOT NUMBERS: 1610-1985, (based on THE SUNSPOT-ACTIVITY IN THE YEARS 1610-1960, by Prof. M. Waldmeier, Copyright 1961, Swiss Federal Observatory, Zurich, Switzerland), revised by John A. McKinnon, National Geophysical Data Center, NOAA, Boulder, CO, January 1987, 112 pp.
UAG-96	SOLAR-GEOPHYSICAL ACTIVITY REPORTS FOR STIP INTERVAL XV, 12-21 February 1984 Ground Level Event, AND STIP INTERVAL XVI, 20 April - 4 May 1984 Forbush Decrease, compiled by Helen E. Coffey and Joe H. Allen, National Geophysical Data Center, NOAA, Boulder, CO, July 1987, 418 pp.
UAG-97	NUMERICAL MODELING OF POLAR IONOSPHERIC ELECTRODYNAMICS FOR JULY 23-24, 1983, UTILIZING IONOSPHERIC CONDUCTANCES DEDUCED FROM DMSP X-RAY IMAGES, by B.-H. Ahn, Kyungpook National University, Taegu, Korea; E. Friis-Christensen, Division of Geophysics, Danish Meteorological Institute, Copenhagen, Denmark; D.J. Gorney, Space Sciences Laboratory, The Aerospace Corporation, Los Angeles, CA; Y. Kamide, Kyoto Sangyo University, Kyoto, Japan; and H.W. Kroehl, National Geophysical Data Center, NOAA, Boulder, CO, April 1988, 133 pp.

UAG-98	TYPE II SOLAR RADIO BURSTS RECORDED AT WEISSENAU 1966-1987, by H.W. Urbarz, Astronomical Institute of Tubingen University, Weissenau Station, 7980 Rasthalde, Ravensburg, GFR, February 1990, 86 pp.
UAG-99	PROCEEDINGS OF THE WORKSHOP ON GEOPHYSICAL INFORMATICS, MOSCOW, AUGUST 14-18, 1988, edited by J.H. Allen, National Geophysical Data Center, NOAA, Boulder, CO; and V.A. Nechitailenko, Soviet Geophysical Committee, Academy of Sciences of the USSR, Moscow, USSR, January 1991, 304 pp.
UAG-100	CATALOGUE OF SOLAR FILAMENT DISAPPEARANCES 1964-1980, by C.S. Wright, Electronics Research Laboratory, Defence Science and Technology Organisation, Salisbury, South Australia 5108, Australia, February 1991, 62 pp.
UAG-101	ATLAS OF STACKPLOTS DERIVED FROM SOLAR SYNOPTIC CHARTS, Evolution of Large-Scale Magnetic Fields and Coronal Holes from H-alpha Synoptic Charts: 1966-1987, by P.S. McIntosh, NOAA Space Environment Laboratory, Boulder, CO; and E.C. Willock and R.J. Thompson, IPS Radio and Space Services, West Chatswood, New South Wales 2057, Australia, October 1991, 188 pp.
UAG-102	CATALOGUE OF CORONAL HOLES 1970-1991, A.Sanchez Ibarra, Centro de Investigacion en Fisica, Universidad de Sonora, Hermosillo, Sonora, Mexico; and M. Barraza-Paredes, Centro de Investigacion en Astronomia Solar, CIAS, Hermosillo, Sonora, Mexico, October 1992, 64 pp.
UAG-103	GEOMAGNETIC POLAR CAP (PC) INDEX, S. Vennerstrøm and E. Friis-Christensen, Division of Geophysics, Danish Meteorological Institute, Copenhagen, Denmark; O.A. Troshichev and V.G. Andresen, Department of Geophysics, Arctic and Antarctic Research Institute, St. Petersburg, Russia, April 1994, 274 pp.
UAG-104	IONOSONDE NETWORKS AND STATIONS--PROCEEDINGS OF SESSION G6 URSI MEETING, AUG.25-SEP. 2, 1993, Phil Wilkinson, Editor, IPS Radio and Space Services, P.O. Box 5606, West Chatswood, Australia. January, 1995, 155 pp.